PhD

PROGRAM IN TRANSLATIONAL
AND MOLECULAR MEDICINE

DIMET

University of Milano-Bicocca
School of Medicine and Faculty of Science

Chromatin structure alterations modulate muscle niche functionality in chronological aging

Coordinator: Prof. Andrea Biondi
Tutor: Prof. Chiara Lanzuolo

Dr. Philina Santarelli
Matr. No. 849339

XXXIV CYCLE
ACADEMIC YEAR
2021-2022

Chapter 1 GENERAL INTRODUCTION

1.1. Muscle Stem Cells

1.1.1. Muscle stem cell contribution in the postnatal and adult stage

Skeletal muscle, which composes about 40 percent of the body mass, is critical for the proper performance and maintenance of various daily body functions such as posture, balance maintenance, breathing and locomotion (Mukund & Subramaniam, 2020). Progressive loss of muscle mass and function is a hallmark of aging, known as sarcopenia (Cesari et al., 2014). To date, it is well recognized that improving balance and motility, through exercise, are important factors in the public health of the elderly in order to reduce fall-related consequences such as fractures, immobility and death (Campisi et al., 2019; Grevendonk et al., 2021; Morley et al., 2013).

Extensive research has elucidated the origin of skeletal muscle during embryonic and fetal development (Musumeci et al., 2015). In brief, during embryonic myogenesis, occurring between E10.5 – E12.5, $Pax3^{+}$/$Pax7^{+}$ progenitors allow the generation of primary fibers (Kassar-Duchossoy et al., 2005). This is followed by fetal myogenesis, occurring from E14.5 at E17.5, carried out by $Pax7^{+}$ progenitors with the generation of secondary myofibers either by the fusion of fetal myoblast between each other or with primary myofibers (Biressi et al., 2007; Duxson et al., 1989).

In skeletal muscle, like in other tissue, progenitors and adult stem cells are fundamental to the correct growth, preservation, and regeneration (Wagers & Weissman, 2004). In 1961 two distinct works in rat and frog muscles, reported by electron microscopy the discovery of the so-called “apparent quiescent cells”, lying beneath the basal lamina and leaning on the muscle fiber (Katz 1961; Mauro 1961). These cells were called Satellite cells for their peripheral localization in the muscle fiber and were morphologically described with a large nuclear to cytoplasm ratio, small nucleus, few organelles, and condensed interphase chromatin. In 1975, with the isolation of mouse myofibers, scientists demonstrated that satellite cells can give rise to myoblasts and fuse into myotubes (Bischoff, 1975; Konigsberg et al., 1975). Moreover, in the ’70, evidence based on ^{3}H-thymidine incorporation proved that dividing satellite cells can provide myonuclei to the already existent myofiber (Moss & Leblond, 1971) and that satellite cells return mitotically quiescent in adult muscle after muscle regeneration (Schultz et al., 1978).
Muscle growth and maintenance during the postnatal period in mammals, namely in mice, reveal at least five distinct stages after birth: nursing, pre-puberty, adolescence, or puberty, and early and late adulthood (Figure 1). During these periods muscle stem cells change in behaviour and competence.

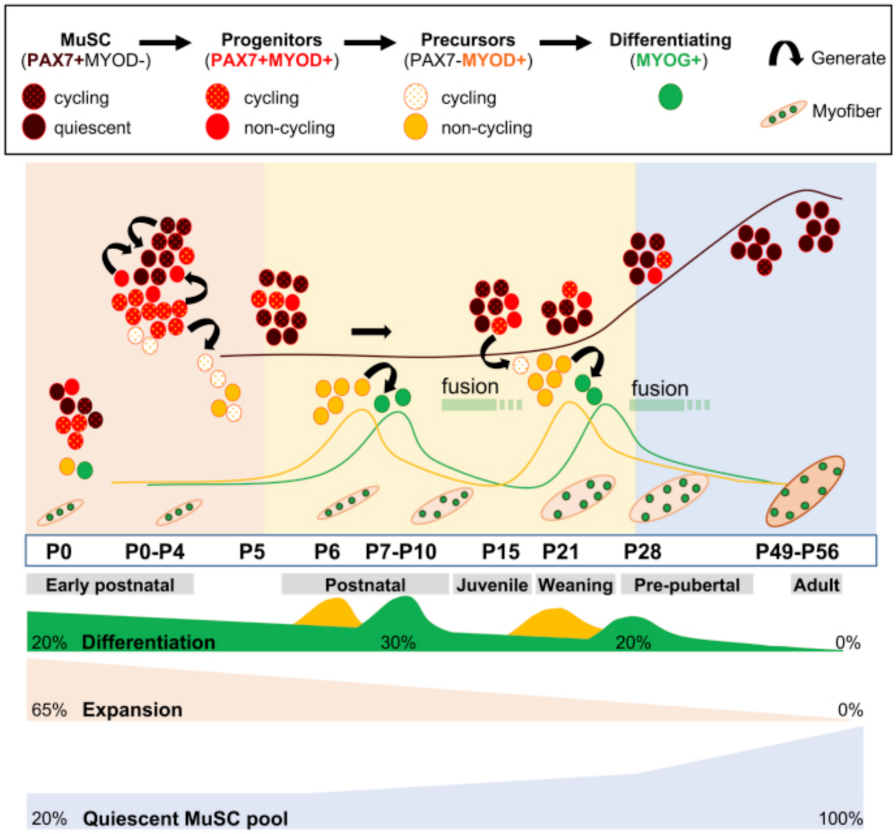

Figure 1. Postnatal myogenic development and establishment of the quiescent muscle stem cell pool. Postnatal myogenesis is characterized by two different myogenic waves at P7–P10 and P21–P28. The quiescence MuSC pool is established around 8 weeks. Each phase is described by a diverse percentage of MuSCs population. Adapted from (Rattazzi et al., 2020).

The nursing period in mice (0–3 weeks) is characterized by pronounced growth of muscle mass and size, with important metabolic and morphological changes, such as dynamic phenotypic changes of slow oxidative (type 1), fast oxidative (type IIa) and fast glycolytic (type IIb or type IIx) muscle myofiber type, an increased number of myonuclei per myofiber and a sustained rise of myofiber cross-sectional area (CSA) (Agbulut et al., 2003; Enesco & Puddy, 1964; White et al., 2010). In the first

three weeks of life, stem cells are required for myonuclei accretion (Lepper et al., 2009; White et al., 2010), whereas the number of myofibers remains stable. During the post-nursing period (> 3 weeks of life), the role of MuSCs in muscle growth was controversial, with seminal works demonstrating that after day 21 of postnatal life (P21) muscle growth was not due to nuclei accretion, but mainly by muscle hypertrophy (Lepper et al., 2009; White et al., 2010). More recently, it has been shown that muscle growth after P21 is sustained by the presence of cycling $Pax7^{+}$ stem cells until puberty is reached (Bachman et al., 2018; Gattazzo et al., 2020), while stimuli such as sex hormones and cell cycle inhibitors lay the path for the formation of the quiescent muscle stem cell pool (J. H. Kim et al., 2016). Although the dynamics of quiescent MuSC pool establishment is still under intense investigation, it is generally accepted that the steady state period of MuSCs fusion is reached around 8-12 weeks after birth, with substantial differences among different muscles. Pawlikowski et al. demonstrate that, for example, the extensor digitorum longus (EDL) muscle achieves maturation at 8 weeks after birth, while the Soleus at 12 weeks after birth (Pawlikowski et al., 2015). Whether these differences are dependent on intrinsic MuSC factors or muscle-specific requirements is unclear. In adulthood MuSCs are quiescent; however, in response to muscle trauma or stress, they can be activated to reconstitute damaged fibers or form new ones (Lepper et al., 2011). Finally, during physiological aging, it is possible to

observe a progressive deterioration in muscle stem cell number and function, driven by environmental and cell-autonomous factors (Hong et al., 2022).

1.1.2.Intrinsic and extrinsic factors that regulate the maintenance and activation of MuSCs

Quiescent MuSCs (QSCs) are characterized by the expression of PAX7, which not only defines the “stem pool” but also delineates the consequent myogenic fate and lineage (Seale et al., 2000). Following injury, QSCs activate, re-enter the cell cycle, and proliferate (Relaix et al., 2021). Activated MuSCs (ASCs), characterized by the myogenic regulatory factors (MRFs) upregulation (e.g., *Myf5*, *Myod1*), provide progeny for the muscle repair process, whereas a small population of self-renewal cells ensures the preservation of the stem cell pool (Zammit et al., 2004).

The quiescence of MuSCs is an “active” maintained state (Crist et al., 2012) defined by the G0 state of the cell (Coller et al., 2006) and adjuvanted by regulated mechanisms and properties (Lemons et al., 2010; Ryall et al., 2015). Quiescence MuSCs have a unique transcriptional signature characterized by an expression profile that suggests the need to inhibit cell proliferation, anchor the stem cell to its anatomical location, and provide the correct metabolic profile to keep the cell quiescent and ready for activation. Accordingly, they exhibit the expression

of genes involved in the negative regulation of the cell cycle (Shea et al., 2010) activation of the Notch signalling (Bjornson et al., 2012; Conboy et al., 2005), upregulation of genes involved in cell-cell adhesion (Goel et al., 2017) and extracellular matrix (ECM) (Baghdadi, Firmino, et al., 2018; Fry et al., 2017a), and the upregulation of genes controlling fatty acid oxidation and metabolism (Pala et al., 2018; Ryall et al., 2015). The fine-tuned combination of intrinsic and extrinsic factors is necessary for the maintenance of this cellular state. In MuSCs, several other cellular pathways have been described to be involved in the regulation of MuSCs quiescence, as p53 (Liu et al., 2018), retinoblastoma tumour suppressor protein (pRB) (Hosoyama et al. 2011), CDK inhibitors (Cheng et al., 2000; Sousa-Victor et al., 2014)and miRNAs (Castel et al., 2018; Cheung et al., 2012; Rodriguez-Outeiriño et al., 2022). Moreover, the skeletal muscle niche mediates a vast range of extrinsic mechanisms that regulate stem cell quiescence (Yin et al., 2013). Cell-cell receptors presented by the myofibers (Beauchamp et al., 2000; Bjornson et al., 2012; Mourikis et al., 2012), attachment to the basal lamina (Pisconti et al., 2016; Rozo et al., 2016), the composition of the ECM (Ghadiali et al., 2017; Noviello et al., 2022), and communication with different types of muscle-resident non-myogenic cells (Dell'Orso et al., 2019), such as fibro-adipogenic progenitors (FAPs) (Fry et al., 2017b; Uezumi et al., 2010), immune and endothelial cells (Arnold et al., 2007;

Verma et al., 2018) are fundamental characteristic for the proper maintenance of the quiescent MuSC pool.

After stimuli, such as injury, exercise, or pathological conditions, MuSCs begin to proliferate and give rise to muscle precursors characterized by the concomitant expression of *Pax7* and *Myod1* genes (PAX7+/MYOD+). Numerous growth factors released from the surrounding environment are involved at the beginning of the activation process, such as Fibroblast Growth Factor (FGF) (Pawlikowski et al. 2017), Tumor Necrosis Factor-alpha (TNF-α) (Moresi et al. 2008), Insulin-like Growth Factor (IGF-1)(Pelosi et al. 2007), Hepatocyte Growth factor (HGF) (Miller et al. 2000). These growth factors engage with QSC membrane receptors and activate the cell cycle process (Dumont et al. 2015). One of the first events that precede the protein expression of MYOD in MuSCs activation is the p38a/ß-MAPK signalling pathway activation (Jones et al. 2005), which leads to MYOD protein expression through the inactivation of Tristetrapolin (TTP) (Hausburg et al. 2015). In fact, TTP promotes mRNA decay of the *Myod1* transcript in QSCs whereas in activated MuSCs TTP translation is prevented by the interaction of STAUFEN1 with the 3' untranslated region of *Myod1* mRNA (de Morrée et al. 2017).

1.2. Epigenetic regulation of muscle stem cell

1.2.1. Euchromatin/Heterochromatin compartments

Chromatin exists at the nuclear level in two distinct functional and structural compartments, euchromatin (EC) and heterochromatin (HC) (Misteli 2007; Ou et al. 2017), historically defined through cytological differences evidenced by optical microscopy and, afterward, by electron microscopy (Belmont et al. 1989; Passarge 1979). EC is characterized by gene-rich, transcriptionally active regions and open chromatin fibers, localized at the nuclear interior, whereas HC allows the compaction of gene-poor and transcriptionally inactive regions, preferentially at telomeric/centromeric loci and at the nuclear periphery (Ou et al. 2017). Heterochromatin can be further divided into constitutive (cHC) and facultative (fHC), established on the occurrence of different histone marks: cHC is defined by the presence of di-methylation and tri-methylation of lysine 9 on histone H3 (H3K9me2/3) and fHC by the presence of tri-methylation of lysine 27 on histone H3 (H3K27me3) (Saksouk et al., 2015; Trojer & Reinberg, 2007). Constitutive heterochromatin includes repeat-rich sequences and prevents recombination of conserved genomic portions of chromosomes (Saksouk,

Simboeck, and Déjardin 2015). Facultative chromatin is enriched at developmental and lineage-specific genes that are expressed in determinate times and spaces in complex organisms (Lanzuolo and Orlando 2012).

Quiescence-to-activation transition in MuSCs goes along with a profound shift from condensed to open chromatin (Shi and Garry 2006), initially observed by electron microscopy (Figure 2).

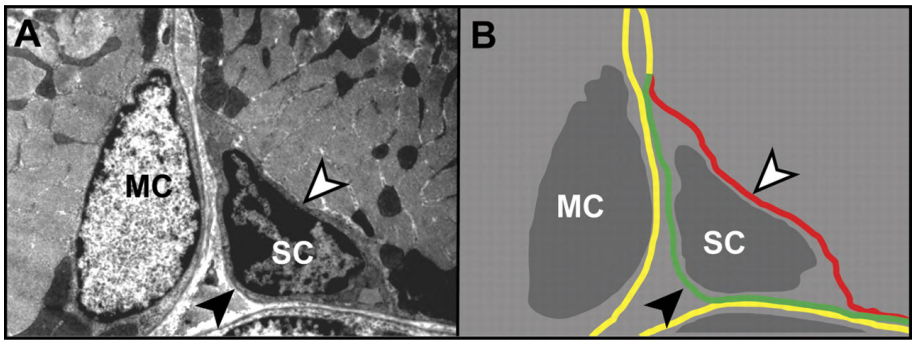

Figure 2. Electron microscopy visualization of the specialized MuSC niche in adult skeletal muscle. Electron micrograph of myocyte nucleus (MC) and the satellite cell nucleus (SC). (A) Schematic representation of A box, emphasizing the MuSC positioning between the basal lamina (black arrow or green line) and the sarcolemma (red line or white arrow) (B) (Shi & Garry, 2006).

In recent years, several studies pointed out the importance of heterochromatin in MuSC quiescence. Deletion of Suv4-20h1, an H4K20 dimethyl transferase involved in the formation of facultative heterochromatin, promotes MuSCs activation at the expense of the pool of quiescent MuSCs (Boonsanay et al. 2016). In vivo experiments where Suv4-20h1 is deleted specifically in MuSCs, show a dramatic decline in condensed chromatin content, followed by MYOD release from the nuclear periphery, a decrease in H3K27me3 deposition and, lastly, quiescence exit due to activation and proliferation of muscle stem

cell (Boonsanay et al. 2016). Thus, the Suv4-20h1-H4K20me2-MyoD-H3K27me3 axis safeguards the formation of facultative heterochromatin, highlighting the importance of heterochromatin remodeling and maintenance in muscle stem cells (Boonsanay et al. 2016). Indeed, additional evidence confirming the necessity of preservation of heterochromatin conformation in QSCs derived from recent work (Liu, Rodriguez-Mateo, et al., 2021) that identifies Hairless (Hr), a Jumanji Family member, as an important player in the maintenance of the correct level of H3K9me3 during quiescence. Hr competes with JMJD1A, an H3K9 demethylase, for the binding of tri-methylated lysine 9 to histone 3, preserving heterochromatin condensation and protecting DNA from genotoxic insult. Disruption of these mechanisms leads to the early activation of the MuSC pool and defects in regeneration and self-renewal (Liu, Rodriguez-Mateo, et al., 2021). Lastly, PAX7 itself is important for the maintenance of heterochromatin condensation (Günther et al. 2013). PAX7 conditional deletion in adult MuSCs, besides a significant loss of satellite cell, causes the appearance of atypical MuSCs, detect by electron microscopy, characterized by an important loss of compact heterochromatin, and increase cytoplasm and organelles volume (Günther et al. 2013). In this context, Schwoerer and colleagues, using a mass spectrometry-based proteomic strategy to quantify methylation and acetylation of histone proteins, described the trend of several histone markers during different days post injury (dpi) (0,2,3,5) in muscle stem cell

(Schwörer et al., 2016). Starting from day 3 after injury, the peak of MuSCs proliferation (Wosczyna & Rando, 2018), there is a decrease in the level of histone acetylation and a progressive increase in di-trimethylation of H3K9 between day 3 and 5 dpi. In contrast, no changes in the levels of H3K273 are shown. The researchers stated that activation was accompanied by a progressive movement toward a heterochromatin state during activation (Schwörer et al., 2016), a statement in contrast to the studies reported above. The different models and methods of analysis and quantification of histone modifications are probably behind the differences achieved. Despite the conflicting results, these studies highlighted how proper chromatin compaction is fundamental to healthy muscle stem cell biology.

Consistent with these findings, the correct H3K27 and H3K9 demethylation of muscle-specific gene promoters (described below in the paragraph: Safeguard of cell identity by remodelers action) ensures the correct differentiation of muscle progenitors, thereby preventing the expression of genes related to other lineage programs (Caretti et al., 2004; Choi et al., 2010; Tosic et al., 2018). For example, the histone demethylase LSD1 looks to participate in the restriction of muscle-specific gene expression by demethylating H3K4me2 in promoters such as *Glis1*, associated with adipose tissue, preventing transcription and differentiation toward brown-like adipocytes (Tosic et al. 2018). On other targets as *Myog* and *Ckm*, LSD1 is necessary for H3K9me2 demethylation to trigger transcriptional activation.

Indeed, disruption of LSD1 activity leads to an inability to promote myogenic differentiation (Choi et al. 2010).

1.2.2. From chromatin compartmentalization to topological associated domains (TADs)

Chromatin organization discloses hierarchical levels ranging from the basis of repeated nucleosome units to higher-order structures (Ghosh & Meyer, 2021) (Figure 3).

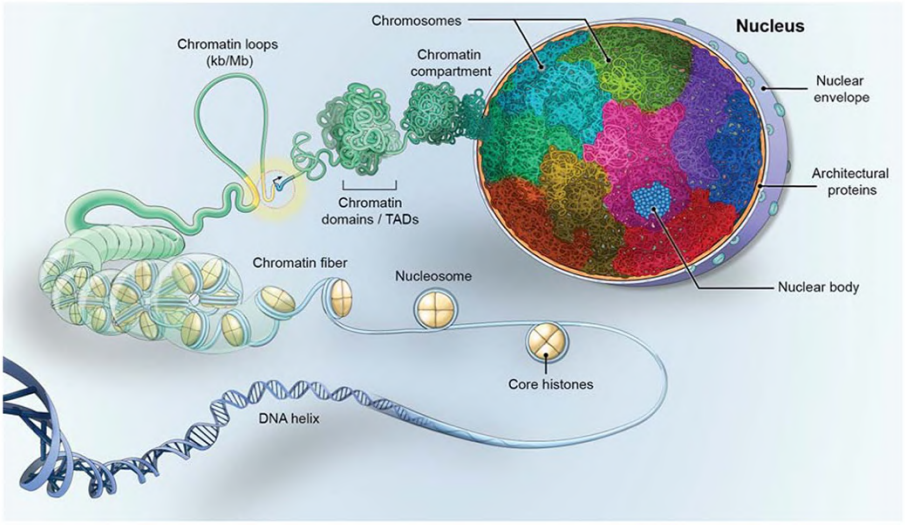

Figure 3. The hierarchical organization of the genome. Chromatin needs fine compaction to fit in the nucleus. Chromosomes occupy specific nuclear regions known as chromosome territories (CT). Chromatin compartments originate from the interaction of multiple chromatin domains, otherwise called topologically associated domains (TADs), generated by the association, and looping of chromatin fibers. The latter is represented by DNA wrapped around the nucleosome and maintained in 10-nm beads-on-a-string fibers by coupling with other nuclear proteins (Misteli, 2020).

Starting from the higher degree of arrangement, each chromosome occupies a distinct subnuclear area, constituting chromosome territories (Cremer and Cremer 2010; Tanabe et al. 2002). The interaction between chromosomal DNA and the nuclear envelope, interceded by intermediate filament proteins

called Lamins and transmembrane proteins, allows the conservation of chromosome positioning (Bianchi and Lanzuolo 2015). The development of high-throughput chromosome conformation capture (HI-C) (Lieberman-Aiden et al., 2009) has allowed the identification of two multi-megabase (Mb) domains, namely A and B compartment, that reflect the spatial segregation of the genome in active, or euchromatin, and silent, or heterochromatin, compartment (Cremer et al., 2015), respectively. Topological Associated Domains (TADs), on a scale of 500 kilobases (kb) to 1 megabase (Mb), ensure distal DNA/DNA interactions (Dixon et al. 2012; Naumova et al. 2012; Nora et al. 2012). In particular, within TADs such interactions are favoured and the chromatin forms DNA loops that contain one or more genes bound at the basis by CCTC-binding factor (CTCF) homodimer and Cohesin, (Bauer et al. 2021). The CTCF loops are termed insulated neighbourhoods (INs) and regulate gene expression by constraining enhancer-promoter interactions (Bianchi & Lanzuolo, 2015; Sun et al., 2019).

TADs are mostly conserved between different species and different cell types (Dixon et al. 2012) and are characterized by a central region enriched with tissue-specific genes (Bianchi and Lanzuolo 2015), surrounded by regions bearing housekeeping genes and binding sites for the CTCF protein (Cuddapah et al. 2009). It is becoming increasingly clear that intra-TAD connections, which include promoter-promoter, enhancer-enhancer and promoter-enhancer interactions define cellular

specificity during development and differentiation (Barrington et al., 2019; Hu et al., 2018). Recent works have highlighted specific factors driving chromatin organization in muscle progenitors (Wang et al. 2022; N. Zhang et al. 2020). Interestingly, in these works authors reported that during activation processes less than 5-7 % of the genome presented a compartment switching, confirming the overall stability of chromatin compartments. The substantial difference was detected within TADs: this rewiring of genomic topology is carried out by two TFs critical for lineage identity and specification, PAX7 and MYOD (Wang et al., 2022; N. Zhang et al., 2020). Initially, using an embryonic stem cells (ESC) model in which PAX7 expression is induced to generate skeletal muscle progenitors *in vitro*, it has been described how PAX7 acts as a pioneer factor, binds preferentially at enhancers and allows the maintenance of open and active chromatin (Lilja et al. 2017). Subsequently, the same group demonstrated that PAX7 is critical for the maintenance of muscle-specific promoter-enhancer (P-En) interactions, which are necessary for the proper initiation of the myogenic program (N. Zhang et al., 2020). Two subclasses of P-En PAX7-dependent interaction have been defined: the first loose PAX7 binding, concomitant with the differentiation-dependent Pax7 transcriptional inhibition; in the second class, an epigenetic memory is maintained, associated with the persistence of enhancer and loop features, thanks to the recruitment of several transcription factors, which have already been shown to be critical for muscular differentiation (Jun/Fos,

bHLH, Six and Runx family) (N. Zhang et al. 2020). In a parallel work, Wang et al. have shown that MYOD together with CTCF, regulates chromatin loops, suggesting that also MYOD could be a key organizer in establishing the unique 3D genomic architecture of myoblasts (Wang et al. 2022).

1.2.3. Safeguard of cell identity by remodelers action

At the transcriptional level, epigenetic factors determine the fate choices of MuSCs and influence the maintenance of cell identity. Evolutionarily conserved epigenetic players involved in the regulation of muscle cells are Polycomb group (PcG) proteins. These large multimers proteins act mainly as repressors of gene transcription at different levels of the epigenome, from histone modification to chromatin remodeling, ensuring the establishment and maintenance of cell identity (J. J. Kim & Kingston, 2022). The two main PcG complexes identified in mammals are the Polycomb Repressive Complex1 (PRC1), composed of Ring1a/b catalytic subunit and Polycomb Repressive Complex2 (PRC2), constituted by the methyltransferase Enhancer of zeste homolog 2 (EZH2) (Lanzuolo and Orlando 2012). PRC1, through the Ring1 associated E3 ligase activity, monoubiquitinates the histone H2A at lysine 119 (H2Aub119) (H. Wang et al., 2004), whereas PRC2 mediates the deposition of H3K27me3 through EZH2 (Bender et

al., 2004). In skeletal muscle, PcG proteins keep muscle-specific genes repressed in undifferentiated MuSCs while, at the onset of differentiation, their repositioning from muscle genes to stemness genes allows the correct progression of the myogenic program (Caretti et al. 2004; Juan et al. 2009, 2011; Palacios et al. 2010; Woodhouse et al. 2013). However, PRCs can assemble into multiple complexes with distinct components and stoichiometry, finally giving rise to diverse functions. This plasticity ensures a key role of PcG multimers in various cell types and contexts. In muscle, one example is represented by the appropriate maintenance of the transcriptional program of MuSCs under physiological and environmental stress (Bodega et al., 2017; Stojic et al., 2011). *Ezh1* is highly expressed in quiescent MuSCs (Boonsanay et al., 2016; Fukada et al., 2007; Shcherbina et al., 2020), whereas *Ezh2* is quickly upregulated upon proliferation and activation (Boonsanay et al., 2016; Juan et al., 2011; Shcherbina et al., 2020) in MuSCs. *Ex-vivo* and *in vivo* loss-of-function studies have highlighted the biological importance of EZH2 in ensuring appropriate muscle stem cell differentiation (Palacios et al., 2010) and self-renewal (Juan et al., 2011). But how the loss of EZH1 *in vivo*, specifically in MuSCs may impact muscle homeostasis and regeneration remains to be investigated. A possible role of EZH1 in maintaining an active and specific transcription in quiescent MuSCs has previously been proposed by Sartorelli's group (Mousavi et al., 2012), based on its lower methyltransferase activity (Margueron et al., 2008).

This hypothesis was further supported by other independent studies showing the ability of EZH1 to act as a positive regulator of transcription (Mousavi et al., 2012; Su et al., 2016). An additional role of these proteins in transcriptional regulation, beyond the methyltransferase activity, was suggested by a recent work: Bodega et al., working on post-mitotic muscle cells, identify a cytosolic isoform of EZH1, EZH1β, where the histone methyltransferase SET domain is missing and that interact with the PRC2 subunit EED. In presence of atrophy oxidative stress, EZH1β is targeted for proteasomal degradation, allowing the translocation of EED in the nucleus, where it assembles a functional PRC2-EZH1 complex redistributed on muscle-specific genes, such as *Myog* and *Myh3*. The maintenance of EED in the cytosol prevents the H3K27 trimethylation of target genes in absence of stress stimuli, thereby sustaining the correct expression of the myogenic program (Bodega et al., 2017).

At the microscopic level, PcG proteins form aggregates (also named PcG bodies) (Lanzuolo et al. 2007; Saurin et al. 1998), an intranuclear architecture required to mediate long-range chromatin interactions and clustering of their targets (Wani et al., 2016). PcG bodies are correctly maintained by the interplay with Lamin A/C (Briand et al., 2018; Cesarini et al., 2015; Marullo et al., 2016; Salvarani et al., 2019), one of the major proteins of the Nuclear Lamina, that is also present in in the nucleoplasm. Lamin A/C depletion in muscle myoblast leads to the nuclear diffusion of Polycomb bodies, with a subsequent de-repression of genes

fundamental for the correct progression of the myogenic program (Cesarini et al. 2015). Furthermore, knock out (KO) of *Lmna* in postnatal mice leads to a genome-wide redistribution of H3K27me3 and to an alteration of the proper 3D genome organization (Bianchi et al. 2020). Specifically, $Lmna^{\Delta 8-11-/-}$ MuSCs exhibit dysregulation of PcG target genes, like adipocyte-specific genes (i.e., *pparg, plin)* and cell cycle inhibitors ($p16^{ink4a}$). This will ultimately impact the confidence of lineage decision, promoting the acquisition of features peculiar to senescence and heading to cause the exhaustion of MuSC pool (Bianchi et al., 2020).

One of the major groups of Polycomb targets are the bivalent genes. The simultaneous presence at the promoter level of the histone modifications H3K27me3 and H3K4me3 – respectively associated with transcriptional repression and activation – defines what is generally called a 'bivalent domain' (Bernstein et al. 2006). Bivalence was initially hypothesized to be a chromatin state specific to ESCs. During ESC differentiation, bivalence is thought to resolve to an H3K4me3-only or H3K27me3-only state, depending on whether the gene is activated or silenced, respectively (Bernstein et al. 2006). However, subsequent observations have confirmed the existence of bivalent domains in adult stem cells and terminally differentiated cell types (Burney et al. 2013; Chiacchiera et al. 2016; Mikkelsen et al. 2007).

The chromatin of quiescent MuSCs is characterized by the presence, at the transcription start site (TSS) level, of H3K4me3

on approximately 50% of the annotated genes (L. Liu et al. 2013), including *Myod1* and *Myf5*. After MuSCs activation, there's the acquisition of H3K27me through PcG protein, but the number and identity of genes characterized by the presence of H3K4me3 do not change. The authors concluded that trimethylation of H3K4 is needed for gene activation, but not sufficient to define its expression state (L. Liu et al. 2013). Interestingly, 90% of the genes marked by H3K27me3 in quiescent MuSCs – around 2,000 – display a bivalent state at the TSS. Many of these bivalent TSS belong to non-myogenic regulators of the development processes, suggesting a potentiality of MuSC to enter other differentiation programs (L. Liu et al. 2013). In agreement with this hypothesis, recent data indicate that HIRA, involved in the H3.3 incorporation required for acetylation and promoter-enhancer activity, is essential for the proper accessibility and H3K27 acetylation of the *Pax7* promoter. This fine-tuned regulation allows the proper signal balance at bivalent domains, avoiding the expression of alternative lineage genes (Esteves de Lima et al. 2021). *Hira* KO in MuSCs leads to an upregulation of genes involved in neuronal, endothelial, mesenchymal, and osteogenic lineage and to downregulation of *Pax7* and muscle-related genes, that in the end cause a loss of MuSCs and defect in muscle regeneration.

1.3. Aging of muscle stem cell pool

1.3.1. Macro and micro alteration in physiological aging

Aging is a complex phenomenon that is difficult to define and can be conceptualized as a process of deficit accumulation, which occurs in different individuals in different ways, depending on the interaction of intrinsic and extrinsic factors (Mitnitski, Mogilner, and Rockwood 2001). The most widely accepted functional definition is that aging is a decrease in physiological reserves with acceptable steady-state functioning that cannot adapt to any further stress, even physiological (Lipsitz 2004; Yates 2002).

Although there are many driving causes of age-related functional decline, certainly one of the main drivers is reduced skeletal muscle performance. Sarcopenia, i.e., the loss of muscle mass and strength, is normally associated with a progressive increase in age (Cesari et al. 2014). Longitudinal studies show that in people over 75 years old, muscle mass is lost at a rate of 0.64-0.7% per year in women and 0.8-0.98% per year in men. Muscle strength, on the other hand, is lost more quickly; at an age of approximately 75 years, strength is lost at a rate of 3-4% per year in men and 2.5-3% per year in women (Mitchell et al. 2012). Sarcopenic muscle shows increased heterogeneity in muscle fiber size, decreased oxidative capacity, and increased

intramuscular connective and adipose tissue (Taylor-Jones et al. 2002; Woo 2017).

In particular, the ability to store lipids is critical for skeletal muscle metabolic demand (Goodpaster et al. 2001). Physical activity, a disease condition, or an injury influences the dynamic ability of the muscle to store energy in the form of fat (Liu, Zhong, et al., 2021; Miljkovic-Gacic et al., 2008; Ryan et al., 2011). The different localization of lipids at the muscle level goes to define intramyocellular lipids (IMCL) and extramyocellular lipids (EMCL): respectively, IMCLs are cytoplasmic lipid droplets within the muscle cells, while EMCLs define lipid layers stored in adipocytes between myofibers and fascicles (Addison et al., 2014). The two types of accumulations, in addition to different depot kinetics, mirror different physiological and pathological states (Gepner et al. 2017; Takashima et al. 2018). The increased number and size of IMCL during endurance exercise is known as the “athlete-obesity” paradox (Goodpaster et al., 2001): skeletal muscle of athletes is, in fact, characterized by a high mitochondrial volume and increased oxidation capacity, coupled with the presence of intracellular lipids located near the mitochondrial surface, allowing optimal energy movement at the time of physical exertion (Tarnopolsky et al., 2007). Moreover, exercise prevents age-associated muscle fat infiltration (Goodpaster et al. 2008). In pathological conditions, such as obesity and Type II diabetes, increased inter- and intramuscular fat mass has been associated with decreased muscle strength,

power, and quality (Beasley et al. 2009; Gorgey and Dudley 2007). Aging is associated with increased deposition of fat at the skeletal muscle level: increased deposition of IMCL during aging was correlated to insulin sensitivity and obesity, which are common in the elderly (Goodpaster et al., 2001). With respect to the extramyocellular depot, associations with aging have not yet been elucidated. In the end, the molecular mechanisms and cell populations involved in the different depot maintenance still need to be elucidated. To date, it is commonly accepted that an active lifestyle and physical activity alleviates sarcopenia and prevents inflammation and body fat accumulation (Bori et al., 2012; H.-T. Chen et al., 2017; Pence et al., 2016).

Currently, it has become clear that aging muscle dysfunction, together with loss of muscle mass, is not only caused by contractile impairment, but also by metabolic and endocrine abnormalities, together with a state of low-grade systemic inflammation (Biolo, Cederholm, and Muscaritoli 2014). Compromised regenerative capacity, production of reactive oxygen species, altered mitochondrial function, muscle innervation alterations and attenuated stress response capacity has been proposed as key factors in sarcopenia (Phillips and Leeuwenburgh 2005; Riuzzi et al. 2018; Romanello and Sandri 2016).

1.3.2. Disruption of muscle stem cell number and function

Aging leads to alterations in the intrinsic and extrinsic mechanisms of regulation of adult stem cells, with consequent impairment in regenerative potential and maintenance of the stem cell pool (Almada and Wagers, 2016). Strict regulation of quiescence is essential for the long-term maintenance of the stem cell pool, and the loss of these regulatory mechanisms leads to a reduction in the stem pool underlying various diseases and aging (Chang et al., 2016; Choudhury et al., 2007; Kalamakis et al., 2019). In line with these observations, muscle aging is marked by a decrease in the number and function of MuSCs (Brack, Bildsoe and Hughes, 2005; Carlson and Conboy, 2007). The causes that can be associated with the reduction in the MuSCs pool are both related to the niche and cell-autonomous alteration that in concurrence cause an imbalance between the processes of quiescence, activation, and self-renewal (Chakkalakal et al., 2012; Bernet et al., 2014; Sousa-Victor et al., 2014). The role of the environment/muscle niche in influencing MuSCs alteration during aging was suggested by early heterochronic tissue transplantation experiments (Carlson and Faulkner, 1989; Roberts, McGeachie and Grounds, 1997), supported afterward by heterochronic parabiosis studies (Conboy et al., 2005; Brack et al., 2007). By combining the circulatory systems of young and old animals in both sets of

studies, it was shown that the regenerative capacity of old MuSC can be rejuvenated by exposure to a young myogenic environment. In further evidence of the role of circulating and environmental molecules in influencing aging processes, the regenerative capacity of young MuSCs in the heterochronic pair was also negatively affected, supporting the idea that there are factors derived from aged serum that drive MuSCs dysfunction (Conboy et al., 2005; Brack et al., 2007).

The seminal work published by Brack's group demonstrates how the myofiber, acting as a niche, can influence the activation of MuSCs: the increased expression of Fibroblast growth factor 2 (FGF2) in aged myofiber leads to quiescence exit of MuSCs, increase proliferation and exhaustion of the MuSC pool, highlighting the importance of fiber-derived factors for the proper preservation of MuSCs (Chakkalakal et al., 2012).

Early events of muscle aging depend mainly by external stimuli, however, at some point stem cells begin to accumulate intrinsic defects that drive them into a state of pre-senescence (Sousa-Victor et al., 2014) (Figure 4).

Loss of MuSCs with age may also occur through processes that affect cell survival, such as apoptosis or senescence (Bernet et al., 2014; Cosgrove et al., 2014; Sousa-Victor et al., 2014; Fry et al., 2015). Senescence allows cells to remain alive; however, an irreversible cell cycle block in the G0 state, renders them incapable of mitotic division. The implication is that the ability of the geriatric MuSCs to cope with the transition from G0

quiescence to activation is impaired, with the inability to provide new progenitors to participate in muscle regeneration.

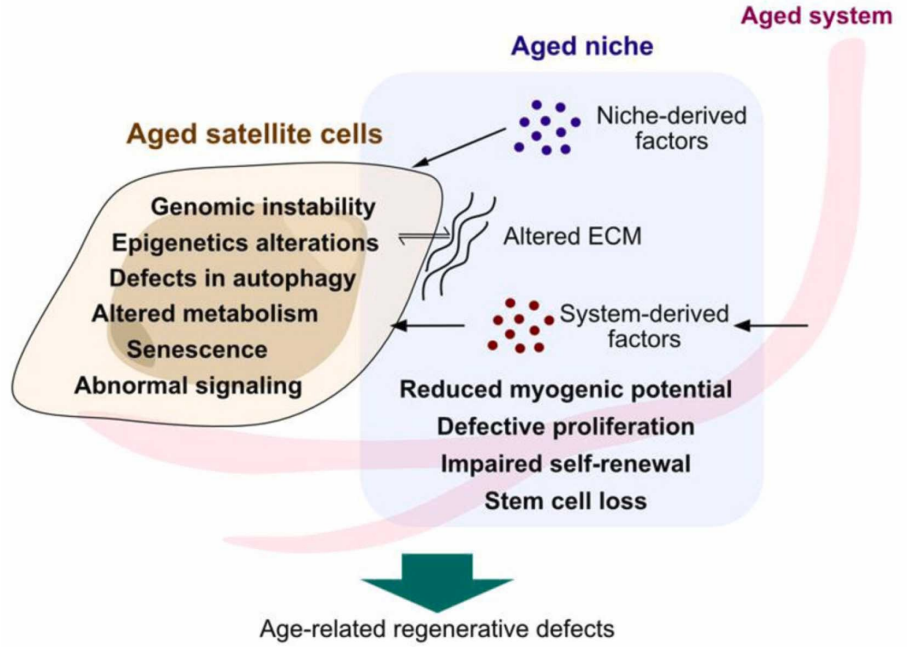

Figure 4. Intrinsic and extrinsic defect in aged MuSCs. The aging of MuSCs is characterized by the alteration of multiple factors starting from the environment surrounding the stem cell, such as factors released from the niche or at a systemic level, to intrinsic issues, like epigenetic dysregulation, genomic instability, etc., which together lead to defects concerning muscle stem cell quiescence, activation, and renewal (Hong et al., 2022).

In the skeletal muscle of geriatric mice, MuSCs were found in a pre-senescence state, which was partially caused by the de-repression of the cell cycle inhibitor *p16* ^{ink4a} (Sousa-Victor et al., 2014), a target of EZH2 and BMI1 (Agherbi et al., 2009). In line with these observations, progeroid mice, which are characterized by a phenotype of premature aging due to a truncated form of Lamin A called progerin, show reduced levels of muscle stem cells that express *p16* ^{ink4a} and have senescent traits (Sousa-Victor et al., 2014).

Several other factors have been described to have a role in regulation of aging of muscle stem cells. The transcription factor Slug, a member of the zinc-finger transcription factor of the Slug/Snail superfamily, was shown to be highly expressed in quiescent muscle stem cells and downregulated in aged muscle stem cells (Zhu et al., 2019). MuSC-specific *Slug* knockout in vivo influences the self-renewal capacity of the stem cell pool by derepression of genes related to cell cycle and muscle differentiation. Interestingly, *Slug* KO causes also an upregulation of *p16* ^{ink4a} at the mRNA level, apparently in contrast with previous findings, even though the protein level was unaffected.

Elevated activity of the p38/MAPK and JAK/STAT signalling pathways were related to defects in asymmetric division and enhanced myogenic differentiation in aged MuSCs that finally lead to muscle regeneration impairment and the exhaustion of the muscle stem cell pool (Bernet et al., 2014; Price et al., 2014). Concomitantly, during aging MuSCs display an alteration of the Notch signalling (Liu et al., 2018), important for quiescence maintenance in MuSCs (Baghdadi, Castel, et al., 2018; Baghdadi, Firmino, et al., 2018; Bjornson et al., 2012). The alteration of the Notch-p53 axis causes a defect in the cell cycle of aged muscle stem cells, that upon activation leads to a mitotic catastrophe, impairing the regenerative and self-renewal potential of the aged MuSCs (Liu et al., 2018). MuSCs function is also impaired by other age-related alterations including

autophagy, metabolism, and epigenetic mechanism (García-Prat et al., 2016, 2020; Kollu et al., 2015; Liu et al., 2013; Pala et al., 2018; Sahu et al., 2018).

1.3.3. Epigenetic features

A tight and precise epigenetic state in quiescent stem cells establishes a safe, poised state, that allows prompt stimulation in emergency situations but provides the necessary stability to prevent precocious or unintentional activation (Wagers and Weissman, 2004). As reported above, aging is accompanied by loss of tissue integrity and homeostasis of the body in part due to stem cell exhaustion (López-Otín et al., 2013). However, molecular mechanisms that in muscular senescence trigger the alteration of stem cell niche are still unknown. The close relationship between aging and epigenetic mechanisms has been highlighted by multiple studies in the field of adult stem cells (Brown et al., 2013; R. Kim et al., 2016; Li et al., 2020). Aging-associated alterations affect all levels of epigenome organization, including histone marker deposition and loss of chromatin compartmentalization integrity (Haithcock et al., 2005; Ikegami et al., 2020; Jung et al., 2010; Larson et al., 2012; Ocampo et al., 2016; H. Zhang et al., 2016).

DNA methylation impairment with age was described to happen in several organs in different species (Stubbs et al., 2017; Gavery

et al., 2019; Voisin et al., 2021). These studies were further corroborated in mice by recent developments in single-cell Omics techniques that shed a light on the correlation between DNA methylation and transcriptional changes (Hernando-Herraez et al., 2019). By single-cell transcriptome and methylome sequencing, in PAX7-positive cells derived from young and old mice, it has been delineated how progressive acquisition of promoter methylation heterogeneity correlates with transcription during muscle stem cell aging (Hernando-Herraez et al., 2019). To further underline the importance of locus-specific promoter methylation, a study carried out by Bigot et al. in young and old myoblast, showed that DNA hypermethylation of the *Spry1* and *Notch1* genes, important for self-renewal and quiescence maintenance and exit in MuSCs, was associated with transcriptional down-regulation and a failure in the re-establishment the stem cell pool in aged myoblasts (Bigot et al., 2015).

Various studies agree in finding in old MuSCs with respect to young MuSCs, a general increase in chromatin accessibility: using ATAC-seq (assay for transposase-accessible chromatin with high-throughput sequencing), alterations in the expression of factors important for the regulation of histone mark deposition and removal, followed by a change in the profile of histone modifications have been described (Shcherbina et al., 2020; Larouche et al., 2021; Dong et al., 2022). These observations are in line with the loss of heterochromatin in aging that results in

impaired gene expression and dysfunction of cellular functioning(Larson et al., 2012; Becker, Nicetto and Zaret, 2016; Ocampo et al., 2016). The "model of heterochromatin loss in aging" (Villeponteau, 1997), which traces its roots back to 1997, proposed that loss of heterochromatin compactness at developmentally important gene domains, defined during embryogenesis, causes changes in chromatin structure and gene expression that border on the problems of aging. Aging-associated loss or re-localization of heterochromatin has been demonstrated in several organisms (Haithcock et al., 2005; Larson et al., 2012) and in diseases related to premature aging such as progeria (Chandra et al., 2015; Sebestyén et al., 2020; H. Zhang et al., 2016). Other works, using transcriptomics and proteomics methods applied to young and old MuSCs, have shown a dysregulation of histone mark profile during aging (Schwörer et al., 2016; Shcherbina et al., 2020). Mass-spectrometry-base analysis in old and young MuSCs highlighted increased global levels of H3K9me2 and H3K27me3 in old cells, confirming Liu's noteworthy paper in muscle aging (Liu et al., 2013). This data, apparently in contrast with the heterochromatin lost, is accompanied by an increase in open chromatin marks during activation, such as H3 and H4 acetylation (Schwörer et al., 2016), suggesting a remodeling in both euchromatin and heterochromatin compartments.

Overall, the old muscle stem cell appears to be characterized by a concomitant loss of constitutive heterochromatin, abnormal

propagation of facultative heterochromatin, and increased accessibility, which overall determine the aberrant stem cell transcription and subsequent inability to adequately provide for the maintenance of muscle homeostasis and regeneration.

1.4. Fibroadipogenic progenitors and Aging

Among the different cell populations that sustain skeletal muscle homeostasis, fibro adipogenic progenitors, or FAPs (Joe et al., 2010; Uezumi et al., 2010), have received consistent interest due to their high phenotypic plasticity, which has been discovered to be crucial for effective muscle homeostasis and regeneration (W. Chen et al., 2022; Contreras et al., 2021). Indeed, the depletion of FAPs, in two different works, led to muscle atrophy and reduced muscle force (E. W. Roberts et al., 2013; Uezumi et al., 2021).

The expression of surface markers, such as stem cell antigen-1 (Sca1 or Ly6A/E) and platelet-derived growth factor receptor α (PDGFRα), shared also by mesenchymal stem cells bring these cells into the wide world of mesenchymal multipotent cells (Joe et al., 2010; Petrilli et al., 2020). Indeed, FAPs could differentiate, *in vivo*, into fibroblasts and adipocytes (Kopinke et al., 2017; Murphy et al., 2011), whereas it was recently shown that under defined culture conditions faps can also give rise to chondrocytes and osteoblasts (Lees-Shepard et al., 2018; Wosczyna et al., 2012).

In resting muscle, FAPs are quiescent and localized in the interstitial space near blood vessels (Contreras et al., 2021). Multiple single-cell RNA-seq studies have led to the elucidation of the cell type composition in non-injured skeletal muscle

(Camps et al., 2020; Malecova et al., 2018; Oprescu et al., 2020; Scott et al., 2019). Although there are dissimilarities, probably due to different isolation protocol and bioinformatic analyses, most studies come to define, mainly, two sub-populations of FAPs in resting muscle with similar gene expression characteristics: one population with pronounced tendencies toward ECM-associated transcripts (*Col4a1, Col6a1, Smoc2*) and the other subpopulation enriched in transcripts related to biological processes and signalling pathways (*Igfbp5, Sema3c, Wnt2*). In general, these studies highlight the heterogeneity of the FAP cell population as well as the importance played in maintaining muscle homeostasis and regeneration.

To date, it has become clear how not only MuSC but also FAPs play a key role in aging: the number of FAPs and their proliferative capacity decrease with time, increasing their predisposition to fibrogenic differentiation, whereas there's a decrease in the adipogenic potential (Lukjanenko et al., 2019; Uezumi et al., 2021). Various intrinsic and extrinsic cellular defects have been shown to contribute to the impairment of FAP activity: during aging, the secretion capacity of paracrine factors by FAPs decreases, e.g., IL-33, WISP, important factors for the regulation of innate type 2 immunity and dividing asymmetric MuSCs, respectively (Kuswanto et al., 2016; Lukjanenko et al., 2019). Other studies have shown how intrinsic factors and variation in the niche environment led to altered proliferation and differentiation capabilities of FAPs (Lukjanenko et al., 2019;

Quinn et al., 2005; Sugihara et al., 2018; Uezumi et al., 2021) However, the epigenetic changes in dysfunctional FAPs were not described yet.

1.5. Scope of the thesis

The proper functioning of cardiac and skeletal muscles is essential throughout life. A delicate balance between environment and cellular mechanisms allows striated muscles to perform successfully. The intimate liaison between environmental encounters and epigenetics is emerging in the field of muscle aging as an important modulator of muscle stem cell function. My work has aimed to investigate the complex phenotypic and nuclear organization changes that occur at the striated muscle level, under physiological and pathological conditions, with widely recognized techniques and others developed in our laboratory. Chapter 2 and 3 refer to two papers published during my doctoral period that were of fundamental importance to my preparation of *in vivo* working ability and to improve the experimental conditions that led to the development of my main doctoral work set forth in Chapter 4.

Chapter 2 – We focused on the cardiac muscle tissue in a mouse model of Emery Dreifuss muscular dystrophy (EDMD) lacking the structural protein Lamin A/C. We show that the deletion of the *Cdkn2a* locus, required for the cell cycle control during development, improved the cardiac function of dystrophic mice increasing life expectancy. This is accompanied by decreased apoptosis events at the level of cardiomyocytes that overall lead to an improved contractile function of the heart.

Chapter 3 – We presented an optimized method to simultaneously isolate fibromuscular stromal populations from different tissues (muscle, aorta, skin) of progeria mice. With this protocol, we were able to preserve the nuclear and chromatin integrity of the cells.

Chapter 4 – We set up an advanced version of our chromatin fractionation technique, named 4 fractions Sequential Analysis of MacroMolecules accessibilitY (4fSAMMY-seq), capable of distinguishing soluble-associated fractions of euchromatin and heterochromatin. We used the novel 4fSAMMY-seq technique to dissect the chromatin structure re-organization during the murine life course in Muscle Stem Cells. In parallel, we characterized the muscle environment to define changes in the muscle niche during aging and to understand the delicate balance between intrinsic and extrinsic cellular signals.

1.6. References To Chapter 1

Addison, O., Marcus, R. L., Lastayo, P. C., & Ryan, A. S. (2014). Intermuscular Fat: A Review of the Consequences and Causes. *International Journal of Endocrinology*, *2014*. https://doi.org/10.1155/2014/309570

Agherbi, H., Gaussmann-Wenger, A., Verthuy, C., Chasson, L., Serrano, M., & Djabali, M. (2009). Polycomb Mediated Epigenetic Silencing and Replication Timing at the INK4a/ARF Locus during Senescence. *PLoS ONE*, *4*(5), e5622. https://doi.org/10.1371/journal.pone.0005622

Almada, A. E., & Wagers, A. J. (2016). Molecular circuitry of stem cell fate in skeletal muscle regeneration, ageing and disease. *Nature Reviews Molecular Cell Biology*, *17*(5), 267–279. https://doi.org/10.1038/nrm.2016.7

Arnold, L., Henry, A., Poron, F., Baba-Amer, Y., van Rooijen, N., Plonquet, A., Gherardi, R. K., & Chazaud, B. (2007). Inflammatory monocytes recruited after skeletal muscle injury switch into antiinflammatory macrophages to support myogenesis. *Journal of Experimental Medicine*, *204*(5), 1057–1069. https://doi.org/10.1084/jem.20070075

Bachman, J. F., Klose, A., Liu, W., Paris, N. D., Blanc, R. S., Schmalz, M., Knapp, E., & Chakkalakal, J. v. (2018). Prepubertal skeletal muscle growth requires pax7-expressing satellite cell-derived myonuclear contribution. *Development (Cambridge)*, *145*(20). https://doi.org/10.1242/dev.167197

Baghdadi, M. B., Castel, D., Machado, L., Fukada, S. I., Birk, D. E., Relaix, F., Tajbakhsh, S., & Mourikis, P. (2018). Reciprocal signalling by Notch-Collagen V-CALCR retains muscle stem cells in their niche. *Nature*, *557*(7707), 714–718. https://doi.org/10.1038/s41586-018-0144-9

Baghdadi, M. B., Firmino, J., Soni, K., Evano, B., di Girolamo, D., Mourikis, P., Castel, D., & Tajbakhsh, S. (2018). Notch-Induced miR-708 Antagonizes Satellite Cell Migration and Maintains Quiescence. *Cell Stem Cell*, *23*(6), 859-868.e5. https://doi.org/10.1016/j.stem.2018.09.017

Barrington, C., Georgopoulou, D., Pezic, D., Varsally, W., Herrero, J., & Hadjur, S. (2019). Enhancer accessibility and CTCF

occupancy underlie asymmetric TAD architecture and cell type specific genome topology. *Nature Communications*, *10*(1), 2908. https://doi.org/10.1038/s41467-019-10725-9

Bauer, B. W., Davidson, I. F., Canena, D., Wutz, G., Tang, W., Litos, G., Horn, S., Hinterdorfer, P., & Peters, J.-M. (2021). Cohesin mediates DNA loop extrusion by a “swing and clamp” mechanism. *Cell*, *184*(21), 5448-5464.e22. https://doi.org/10.1016/j.cell.2021.09.016

Beasley, L. E., Koster, A., Newman, A. B., Javaid, M. K., Ferrucci, L., Kritchevsky, S. B., Kuller, L. H., Pahor, M., Schaap, L. A., Visser, M., Rubin, S. M., Goodpaster, B. H., & Harris, T. B. (2009). Inflammation and Race and Gender Differences in Computerized Tomography-measured Adipose Depots. *Obesity*, *17*(5), 1062–1069. https://doi.org/10.1038/oby.2008.627

Beauchamp, J. R., Heslop, L., Yu, D. S., Tajbakhsh, S., Kelly, R. G., Wernig, A., Buckingham, M. E., Partridge, T. A., & Zammit, P. S. (2000). Expression of CD34 and Myf5 defines the majority of quiescent adult skeletal muscle satellite cells. *The Journal of Cell Biology*, *151*(6), 1221–1234. http://www.ncbi.nlm.nih.gov/pubmed/11121437

Becker, J. S., Nicetto, D., & Zaret, K. S. (2016). H3K9me3-Dependent Heterochromatin: Barrier to Cell Fate Changes. *Trends in Genetics*, *32*(1), 29–41. https://doi.org/10.1016/j.tig.2015.11.001

Belmont, A. S., Braunfeld, M. B., Sedat, J. W., & Agard, D. A. (1989). Large-scale chromatin structural domains within mitotic and interphase chromosomes in vivo and in vitro. *Chromosoma*, *98*(2), 129–143. https://doi.org/10.1007/BF00291049

Bender, L. B., Cao, R., Zhang, Y., & Strome, S. (2004). The MES-2/MES-3/MES-6 Complex and Regulation of Histone H3 Methylation in C. elegans. *Current Biology*, *14*(18), 1639–1643. https://doi.org/10.1016/j.cub.2004.08.062

Bernet, J. D., Doles, J. D., Hall, J. K., Kelly Tanaka, K., Carter, T. A., & Olwin, B. B. (2014). P38 MAPK signaling underlies a cell-autonomous loss of stem cell self-renewal in skeletal muscle of aged mice. *Nature Medicine*, *20*(3), 265–271. https://doi.org/10.1038/nm.3465

Bernstein, B. E., Mikkelsen, T. S., Xie, X., Kamal, M., Huebert, D. J., Cuff, J., Fry, B., Meissner, A., Wernig, M., Plath, K., Jaenisch, R., Wagschal, A., Feil, R., Schreiber, S. L., & Lander, E. S. (2006). A Bivalent Chromatin Structure Marks Key Developmental Genes in Embryonic Stem Cells. *Cell*, *125*(2), 315–326. https://doi.org/10.1016/j.cell.2006.02.041

Bianchi, A., & Lanzuolo, C. (2015). Into the chromatin world: Role of nuclear architecture in epigenome regulation. *AIMS Biophysics*, *2*(4), 585–612. https://doi.org/10.3934/biophy.2015.4.585

Bianchi, A., Mozzetta, C., Pegoli, G., Lucini, F., Valsoni, S., Rosti, V., Petrini, C., Cortesi, A., Gregoretti, F., Antonelli, L., Oliva, G., de Bardi, M., Rizzi, R., Bodega, B., Pasini, D., Ferrari, F., Bearzi, C., & Lanzuolo, C. (2020). Dysfunctional polycomb transcriptional repression contributes to lamin A/C-dependent muscular dystrophy. *Journal of Clinical Investigation*, *130*(5), 2408–2421. https://doi.org/10.1172/JCI128161

Bigot, A., Duddy, W. J., Ouandaogo, Z. G., Negroni, E., Mariot, V., Ghimbovschi, S., Harmon, B., Wielgosik, A., Loiseau, C., Devaney, J., Dumonceaux, J., Butler-Browne, G., Mouly, V., & Duguez, S. (2015). Age-Associated Methylation Suppresses SPRY1, Leading to a Failure of Re-quiescence and Loss of the Reserve Stem Cell Pool in Elderly Muscle. *Cell Reports*, *13*(6), 1172–1182. https://doi.org/10.1016/j.celrep.2015.09.067

Biolo, G., Cederholm, T., & Muscaritoli, M. (2014). Muscle contractile and metabolic dysfunction is a common feature of sarcopenia of aging and chronic diseases: from sarcopenic obesity to cachexia. *Clinical Nutrition (Edinburgh, Scotland)*, *33*(5), 737–748. https://doi.org/10.1016/j.clnu.2014.03.007

Biressi, S., Tagliafico, E., Lamorte, G., Monteverde, S., Tenedini, E., Roncaglia, E., Ferrari, S., Ferrari, S., Cusella-De Angelis, M. G., Tajbakhsh, S., & Cossu, G. (2007). Intrinsic phenotypic diversity of embryonic and fetal myoblasts is revealed by genome-wide gene expression analysis on purified cells. *Developmental Biology*, *304*(2), 633–651. https://doi.org/10.1016/j.ydbio.2007.01.016

Bischoff, R. (1975). Regeneration of single skeletal muscle fibers in vitro. *The Anatomical Record*, *182*(2), 215–235. https://doi.org/10.1002/ar.1091820207

Bjornson, C. R. R., Cheung, T. H., Liu, L., Tripathi, P. v., Steeper, K. M., & Rando, T. A. (2012). Notch Signaling Is Necessary to Maintain Quiescence in Adult Muscle Stem Cells. *Stem Cells*, *30*(2), 232–242. https://doi.org/10.1002/stem.773

Bodega, B., Marasca, F., Ranzani, V., Cherubini, A., della Valle, F., Neguembor, M. V., Wassef, M., Zippo, A., Lanzuolo, C., Pagani, M., & Orlando, V. (2017). A cytosolic Ezh1 isoform modulates a PRC2-Ezh1 epigenetic adaptive response in postmitotic cells. *Nature Structural and Molecular Biology*, *24*(5), 444–452. https://doi.org/10.1038/nsmb.3392

Boonsanay, V., Zhang, T., Georgieva, A., Kostin, S., Qi, H., Yuan, X., Zhou, Y., & Braun, T. (2016). Regulation of Skeletal Muscle Stem Cell Quiescence by Suv4-20h1-Dependent Facultative Heterochromatin Formation. *Cell Stem Cell*, *18*(2), 229–242. https://doi.org/10.1016/j.stem.2015.11.002

Bori, Z., Zhao, Z., Koltai, E., Fatouros, I. G., Jamurtas, A. Z., Douroudos, I. I., Terzis, G., Chatzinikolaou, A., Sovatzidis, A., Draganidis, D., Boldogh, I., & Radak, Z. (2012). The effects of aging, physical training, and a single bout of exercise on mitochondrial protein expression in human skeletal muscle. *Experimental Gerontology*, *47*(6), 417–424. https://doi.org/10.1016/j.exger.2012.03.004

Brack, A. S., Bildsoe, H., & Hughes, S. M. (2005). Evidence that satellite cell decrement contributes to preferential decline in nuclear number from large fibres during murine age-related muscle atrophy. *Journal of Cell Science*, *118*(20), 4813–4821. https://doi.org/10.1242/JCS.02602

Brack, A. S., Conboy, M. J., Roy, S., Lee, M., Kuo, C. J., Keller, C., & Rando, T. A. (2007). Increased Wnt Signaling During Aging Alters Muscle Stem Cell Fate and Increases Fibrosis. *Science*, *317*(5839), 807–810. https://doi.org/10.1126/science.1144090

Briand, N., Guénantin, A.-C., Jeziorowska, D., Shah, A., Mantecon, M., Capel, E., Garcia, M., Oldenburg, A., Paulsen, J., Hulot, J.-S., Vigouroux, C., & Collas, P. (2018). The lipodystrophic hotspot lamin A p.R482W mutation deregulates the mesodermal inducer T/Brachyury and early vascular differentiation gene networks. *Human Molecular Genetics*, *27*(8), 1447–1459. https://doi.org/10.1093/hmg/ddy055

Brown, K., Xie, S., Qiu, X., Mohrin, M., Shin, J., Liu, Y., Zhang, D., Scadden, D. T., & Chen, D. (2013). SIRT3 Reverses Aging-Associated Degeneration. *Cell Reports*, *3*(2), 319–327. https://doi.org/10.1016/j.celrep.2013.01.005

Burney, M. J., Johnston, C., Wong, K.-Y., Teng, S.-W., Beglopoulos, V., Stanton, L. W., Williams, B. P., Bithell, A., & Buckley, N. J. (2013). An epigenetic signature of developmental potential in neural stem cells and early neurons. *Stem Cells*, *31*(9), 1868–1880. https://doi.org/10.1002/stem.1431

Camps, J., Breuls, N., Sifrim, A., Giarratana, N., Corvelyn, M., Danti, L., Grosemans, H., Vanuytven, S., Thiry, I., Belicchi, M., Meregalli, M., Platko, K., MacDonald, M. E., Austin, R. C., Gijsbers, R., Cossu, G., Torrente, Y., Voet, T., & Sampaolesi, M. (2020). Interstitial Cell Remodeling Promotes Aberrant Adipogenesis in Dystrophic Muscles. *Cell Reports*, *31*(5), 107597. https://doi.org/10.1016/j.celrep.2020.107597

Caretti, G., Padova, M. di, Micales, B., Lyons, G., & Sartorelli, V. (2004). The Polycomb Ezh2 methyltransferase regulates muscle gene expression and skeletal muscle differentiation. *Genes & Development*, *18*, 2627–2638. https://doi.org/10.1101/gad.1241904.netic

Carlson, B. M., & Faulkner, J. A. (1989). Muscle transplantation between young and old rats: age of host determines recovery. *American Journal of Physiology-Cell Physiology*, *256*(6), C1262–C1266. https://doi.org/10.1152/ajpcell.1989.256.6.C1262

Carlson, M. E., & Conboy, I. M. (2007). Loss of stem cell regenerative capacity within aged niches. *Aging Cell*, *6*(3), 371–382. https://doi.org/10.1111/J.1474-9726.2007.00286.X

Castel, D., Baghdadi, M. B., Mella, S., Gayraud-Morel, B., Marty, V., Cavaillé, J., Antoniewski, C., & Tajbakhsh, S. (2018). Small-RNA sequencing identifies dynamic microRNA deregulation during skeletal muscle lineage progression. *Scientific Reports*, *8*(1), 4208. https://doi.org/10.1038/s41598-018-21991-w

Cesari, M., Landi, F., Vellas, B., Bernabei, R., & Marzetti, E. (2014). Sarcopenia and Physical Frailty: Two Sides of the Same Coin. *Frontiers in Aging Neuroscience*, *6*. https://doi.org/10.3389/fnagi.2014.00192

Cesarini, E., Mozzetta, C., Marullo, F., Gregoretti, F., Gargiulo, A., Columbaro, M., Cortesi, A., Antonelli, L., di Pelino, S., Squarzoni, S., Palacios, D., Zippo, A., Bodega, B., Oliva, G., & Lanzuolo, C. (2015). Lamin A/C sustains PcG protein architecture, maintaining transcriptional repression at target genes. *Journal of Cell Biology*, *211*(3), 533–551. https://doi.org/10.1083/jcb.201504035

Chakkalakal, J. v., Jones, K. M., Basson, M. A., & Brack, A. S. (2012). The aged niche disrupts muscle stem cell quiescence. *Nature*, *490*(7420), 355–360. https://doi.org/10.1038/nature11438

Chandra, T., Ewels, P. A., Schoenfelder, S., Furlan-Magaril, M., Wingett, S. W., Kirschner, K., Thuret, J.-Y., Andrews, S., Fraser, P., & Reik, W. (2015). Global Reorganization of the Nuclear Landscape in Senescent Cells. *Cell Reports*, *10*(4), 471–483. https://doi.org/10.1016/j.celrep.2014.12.055

Chang, J., Wang, Y., Shao, L., Laberge, R.-M., Demaria, M., Campisi, J., Janakiraman, K., Sharpless, N. E., Ding, S., Feng, W., Luo, Y., Wang, X., Aykin-Burns, N., Krager, K., Ponnappan, U., Hauer-Jensen, M., Meng, A., & Zhou, D. (2016). Clearance of senescent cells by ABT263 rejuvenates aged hematopoietic stem cells in mice. *Nature Medicine*, *22*(1), 78–83. https://doi.org/10.1038/nm.4010

Chen, H.-T., Chung, Y.-C., Chen, Y.-J., Ho, S.-Y., & Wu, H.-J. (2017). Effects of Different Types of Exercise on Body Composition, Muscle Strength, and IGF-1 in the Elderly with Sarcopenic Obesity. *Journal of the American Geriatrics Society*, *65*(4), 827–832. https://doi.org/10.1111/jgs.14722

Chen, W., You, W., Valencak, T. G., & Shan, T. (2022). Bidirectional roles of skeletal muscle fibro-adipogenic progenitors in homeostasis and disease. *Ageing Research Reviews*, *80*, 101682. https://doi.org/10.1016/j.arr.2022.101682

Cheng, T., Rodrigues, N., Dombkowski, D., Stier, S., & Scadden, D. T. (2000). Stem cell repopulation efficiency but not pool size is governed by p27kip1. *Nature Medicine*, *6*(11), 1235–1240. https://doi.org/10.1038/81335

Cheung, T. H., Quach, N. L., Charville, G. W., Liu, L., Park, L., Edalati, A., Yoo, B., Hoang, P., & Rando, T. A. (2012). Maintenance of muscle stem-cell quiescence by microRNA-

489. *Nature*, *482*(7386), 524–528. https://doi.org/10.1038/nature10834
Chiacchiera, F., Rossi, A., Jammula, S., Piunti, A., Scelfo, A., Ordóñez-Morán, P., Huelsken, J., Koseki, H., & Pasini, D. (2016). Polycomb Complex PRC1 Preserves Intestinal Stem Cell Identity by Sustaining Wnt/β-Catenin Transcriptional Activity. *Cell Stem Cell*, *18*(1), 91–103. https://doi.org/10.1016/j.stem.2015.09.019
Choi, J., Jang, H., Kim, H., Kim, S.-T., Cho, E.-J., & Youn, H.-D. (2010). Histone demethylase LSD1 is required to induce skeletal muscle differentiation by regulating myogenic factors. *Biochemical and Biophysical Research Communications*, *401*(3), 327–332. https://doi.org/10.1016/j.bbrc.2010.09.014
Choudhury, A. R., Ju, Z., Djojosubroto, M. W., Schienke, A., Lechel, A., Schaetzlein, S., Jiang, H., Stepczynska, A., Wang, C., Buer, J., Lee, H.-W., von Zglinicki, T., Ganser, A., Schirmacher, P., Nakauchi, H., & Rudolph, K. L. (2007). Cdkn1a deletion improves stem cell function and lifespan of mice with dysfunctional telomeres without accelerating cancer formation. *Nature Genetics*, *39*(1), 99–105. https://doi.org/10.1038/ng1937
Coller, H. A., Sang, L., & Roberts, J. M. (2006). A new description of cellular quiescence. *PLoS Biology*, *4*(3), 0329–0349. https://doi.org/10.1371/journal.pbio.0040083
Conboy, I. M., Conboy, M. J., Wagers, A. J., Girma, E. R., Weissman, I. L., & Rando, T. A. (2005). Rejuvenation of aged progenitor cells by exposure to a young systemic environment. *Nature*, *433*(7027), 760–764. https://doi.org/10.1038/nature03260
Contreras, O., Rossi, F. M. v., & Theret, M. (2021). Origins, potency, and heterogeneity of skeletal muscle fibro-adipogenic progenitors—time for new definitions. *Skeletal Muscle*, *11*(1), 16. https://doi.org/10.1186/s13395-021-00265-6
Cosgrove, B. D., Gilbert, P. M., Porpiglia, E., Mourkioti, F., Lee, S. P., Corbel, S. Y., Llewellyn, M. E., Delp, S. L., & Blau, H. M. (2014). Rejuvenation of the muscle stem cell population restores strength to injured aged muscles. *Nature Medicine*, *20*(3), 255–264. https://doi.org/10.1038/nm.3464

Cremer, T., & Cremer, M. (2010). Chromosome Territories. *Cold Spring Harbor Perspectives in Biology*, *2*(3), a003889–a003889. https://doi.org/10.1101/cshperspect.a003889

Cremer, T., Cremer, M., Hübner, B., Strickfaden, H., Smeets, D., Popken, J., Sterr, M., Markaki, Y., Rippe, K., & Cremer, C. (2015). The 4D nucleome: Evidence for a dynamic nuclear landscape based on co-aligned active and inactive nuclear compartments. *FEBS Letters*, *589*(20PartA), 2931–2943. https://doi.org/10.1016/j.febslet.2015.05.037

Crist, C. G., Montarras, D., & Buckingham, M. (2012). Muscle Satellite Cells Are Primed for Myogenesis but Maintain Quiescence with Sequestration of Myf5 mRNA Targeted by microRNA-31 in mRNP Granules. *Cell Stem Cell*, *11*(1), 118–126. https://doi.org/10.1016/j.stem.2012.03.011

Cuddapah, S., Jothi, R., Schones, D. E., Roh, T.-Y., Cui, K., & Zhao, K. (2009). Global analysis of the insulator binding protein CTCF in chromatin barrier regions reveals demarcation of active and repressive domains. *Genome Research*, *19*(1), 24–32. https://doi.org/10.1101/gr.082800.108

de Morrée, A., van Velthoven, C. T. J., Gan, Q., Salvi, J. S., Klein, J. D. D., Akimenko, I., Quarta, M., Biressi, S., & Rando, T. A. (2017). Staufen1 inhibits MyoD translation to actively maintain muscle stem cell quiescence. *Proceedings of the National Academy of Sciences of the United States of America*, *114*(43), E8996–E9005. https://doi.org/10.1073/pnas.1708725114

Dell'Orso, S., Juan, A. H., Ko, K.-D., Naz, F., Gutierrez-Cruz, G., Feng, X., & Sartorelli, V. (2019). Single-cell analysis of adult skeletal muscle stem cells in homeostatic and regenerative conditions. *Development*, *146*(12). https://doi.org/10.1242/dev.174177

Dixon, J. R., Selvaraj, S., Yue, F., Kim, A., Li, Y., Shen, Y., Hu, M., Liu, J. S., & Ren, B. (2012). Topological domains in mammalian genomes identified by analysis of chromatin interactions. *Nature*, *485*(7398), 376–380. https://doi.org/10.1038/nature11082

Dong, A., Liu, J., Lin, K., Zeng, W., So, W.-K., Hu, S., & Cheung, T. H. (2022). Global chromatin accessibility profiling analysis reveals a chronic activation state in aged muscle stem cells.

IScience, *25*(9), 104954. https://doi.org/10.1016/j.isci.2022.104954
Dumont, N. A., Wang, Y. X., von Maltzahn, J., Pasut, A., Bentzinger, C. F., Brun, C. E., & Rudnicki, M. A. (2015). Dystrophin expression in muscle stem cells regulates their polarity and asymmetric division. *Nature Medicine*, *21*(12), 1455–1463. https://doi.org/10.1038/nm.3990
Duxson, M. J., Usson, Y., & Harris, A. J. (1989). The origin of secondary myotubes in mammalian skeletal muscles: Ultrastructural studies. *Development*, *107*(4), 743–750. https://doi.org/10.1242/dev.107.4.743
Enesco, M., & Puddy, D. (1964). INCREASE IN THE NUMBER OF NUCLEI AND WEIGHT IN SKELETAL MUSCLE OF RATS OF VARIOUS AGES. *The American Journal of Anatomy*, *114*(2), 235–244. https://doi.org/10.1002/AJA.1001140204
Esteves de Lima, J., Bou Akar, R., Machado, L., Li, Y., Drayton-Libotte, B., Dilworth, F. J., & Relaix, F. (2021). HIRA stabilizes skeletal muscle lineage identity. *Nature Communications 2021 12:1*, *12*(1), 1–13. https://doi.org/10.1038/s41467-021-23775-9
Fry, C. S., Kirby, T. J., Kosmac, K., McCarthy, J. J., & Peterson, C. A. (2017a). Myogenic Progenitor Cells Control Extracellular Matrix Production by Fibroblasts during Skeletal Muscle Hypertrophy. *Cell Stem Cell*, *20*(1), 56–69. https://doi.org/10.1016/j.stem.2016.09.010
Fry, C. S., Kirby, T. J., Kosmac, K., McCarthy, J. J., & Peterson, C. A. (2017b). Myogenic Progenitor Cells Control Extracellular Matrix Production by Fibroblasts during Skeletal Muscle Hypertrophy. *Cell Stem Cell*, *20*(1), 56–69. https://doi.org/10.1016/j.stem.2016.09.010
Fry, C. S., Lee, J. D., Mula, J., Kirby, T. J., Jackson, J. R., Liu, F., Yang, L., Mendias, C. L., Dupont-Versteegden, E. E., McCarthy, J. J., & Peterson, C. A. (2015). Inducible depletion of satellite cells in adult, sedentary mice impairs muscle regenerative capacity without affecting sarcopenia. *Nature Medicine*, *21*(1), 76–80. https://doi.org/10.1038/nm.3710
Fukada, S., Uezumi, A., Ikemoto, M., Masuda, S., Segawa, M., Tanimura, N., Yamamoto, H., Miyagoe-Suzuki, Y., & Takeda, S. (2007). Molecular Signature of Quiescent Satellite Cells in Adult

Skeletal Muscle. *Stem Cells*, *25*(10), 2448–2459. https://doi.org/10.1634/stemcells.2007-0019
García-Prat, L., Martínez-Vicente, M., Perdiguero, E., Ortet, L., Rodríguez-Ubreva, J., Rebollo, E., Ruiz-Bonilla, V., Gutarra, S., Ballestar, E., Serrano, A. L., Sandri, M., & Muñoz-Cánoves, P. (2016). Autophagy maintains stemness by preventing senescence. *Nature*, *529*(7584), 37–42. https://doi.org/10.1038/nature16187
García-Prat, L., Perdiguero, E., Alonso-Martín, S., Dell'Orso, S., Ravichandran, S., Brooks, S. R., Juan, A. H., Campanario, S., Jiang, K., Hong, X., Ortet, L., Ruiz-Bonilla, V., Flández, M., Moiseeva, V., Rebollo, E., Jardí, M., Sun, H.-W., Musarò, A., Sandri, M., … Muñoz-Cánoves, P. (2020). FoxO maintains a genuine muscle stem-cell quiescent state until geriatric age. *Nature Cell Biology*, *22*(11), 1307–1318. https://doi.org/10.1038/s41556-020-00593-7
Gattazzo, F., Laurent, B., Relaix, F., Rouard, H., & Didier, N. (2020). Distinct Phases of Postnatal Skeletal Muscle Growth Govern the Progressive Establishment of Muscle Stem Cell Quiescence. *Stem Cell Reports*, *15*(3), 597–611. https://doi.org/10.1016/j.stemcr.2020.07.011
Gavery, M. R., Nichols, K. M., Berejikian, B. A., Tatara, C. P., Goetz, G. W., Dickey, J. T., van Doornik, D. M., & Swanson, P. (2019). Temporal Dynamics of DNA Methylation Patterns in Response to Rearing Juvenile Steelhead (Oncorhynchus mykiss) in a Hatchery versus Simulated Stream Environment. *Genes*, *10*(5), 356. https://doi.org/10.3390/genes10050356
Gepner, Y., Shelef, I., Schwarzfuchs, D., Cohen, N., Bril, N., Rein, M., Tsaban, G., Zelicha, H., Yaskolka Meir, A., Tene, L., Sarusy, B., Rosen, P., Hoffman, J. R., Stout, J. R., Thiery, J., Ceglarek, U., Stumvoll, M., Blüher, M., Stampfer, M. J., & Shai, I. (2017). Intramyocellular triacylglycerol accumulation across weight loss strategies; Sub-study of the CENTRAL trial. *PLOS ONE*, *12*(11), e0188431. https://doi.org/10.1371/journal.pone.0188431
Ghadiali, R. S., Guimond, S. E., Turnbull, J. E., & Pisconti, A. (2017). Dynamic changes in heparan sulfate during muscle differentiation and ageing regulate myoblast cell fate and FGF2

signalling. *Matrix Biology*, *59*, 54–68. https://doi.org/10.1016/j.matbio.2016.07.007
Ghosh, R. P., & Meyer, B. J. (2021). Spatial Organization of Chromatin: Emergence of Chromatin Structure During Development. *Annual Review of Cell and Developmental Biology*, *37*(1), 199–232. https://doi.org/10.1146/annurev-cellbio-032321-035734
Goel, A. J., Rieder, M.-K., Arnold, H.-H., Radice, G. L., & Krauss, R. S. (2017). Niche Cadherins Control the Quiescence-to-Activation Transition in Muscle Stem Cells. *Cell Reports*, *21*(8), 2236–2250. https://doi.org/10.1016/j.celrep.2017.10.102
Goodpaster, B. H., Chomentowski, P., Ward, B. K., Rossi, A., Glynn, N. W., Delmonico, M. J., Kritchevsky, S. B., Pahor, M., & Newman, A. B. (2008). Effects of physical activity on strength and skeletal muscle fat infiltration in older adults: a randomized controlled trial. *Journal of Applied Physiology*, *105*(5), 1498. https://doi.org/10.1152/JAPPLPHYSIOL.90425.2008
Goodpaster, B. H., He, J., Watkins, S., & Kelley, D. E. (2001). Skeletal Muscle Lipid Content and Insulin Resistance: Evidence for a Paradox in Endurance-Trained Athletes. *The Journal of Clinical Endocrinology & Metabolism*, *86*(12), 5755–5761. https://doi.org/10.1210/jcem.86.12.8075
Gorgey, A. S., & Dudley, G. A. (2007). Skeletal muscle atrophy and increased intramuscular fat after incomplete spinal cord injury. *Spinal Cord*, *45*(4), 304–309. https://doi.org/10.1038/sj.sc.3101968
Grevendonk, L., Connell, N. J., McCrum, C., Fealy, C. E., Bilet, L., Bruls, Y. M. H., Mevenkamp, J., Schrauwen-Hinderling, V. B., Jörgensen, J. A., Moonen-Kornips, E., Schaart, G., Havekes, B., de Vogel-van den Bosch, J., Bragt, M. C. E., Meijer, K., Schrauwen, P., & Hoeks, J. (2021). Impact of aging and exercise on skeletal muscle mitochondrial capacity, energy metabolism, and physical function. *Nature Communications*, *12*(1), 4773. https://doi.org/10.1038/s41467-021-24956-2
Günther, S., Kim, J., Kostin, S., Lepper, C., Fan, C.-M., & Braun, T. (2013). Myf5-Positive Satellite Cells Contribute to Pax7-Dependent Long-Term Maintenance of Adult Muscle Stem Cells. *Cell Stem Cell*, *13*(5), 590–601. https://doi.org/10.1016/j.stem.2013.07.016

Haithcock, E., Dayani, Y., Neufeld, E., Zahand, A. J., Feinstein, N., Mattout, A., Gruenbaum, Y., & Liu, J. (2005). Age-related changes of nuclear architecture in Caenorhabditis elegans. *Proceedings of the National Academy of Sciences of the United States of America*, *102*(46), 16690–16695. https://doi.org/10.1073/PNAS.0506955102

Hausburg, M. A., Doles, J. D., Clement, S. L., Cadwallader, A. B., Hall, M. N., Blackshear, P. J., Lykke-Andersen, J., & Olwin, B. B. (2015). Post-transcriptional regulation of satellite cell quiescence by TTP-mediated mRNA decay. *ELife*, *4*(4). https://doi.org/10.7554/eLife.03390

Hernando-Herraez, I., Evano, B., Stubbs, T., Commere, P.-H., Jan Bonder, M., Clark, S., Andrews, S., Tajbakhsh, S., & Reik, W. (2019). Ageing affects DNA methylation drift and transcriptional cell-to-cell variability in mouse muscle stem cells. *Nature Communications*, *10*(1), 4361. https://doi.org/10.1038/s41467-019-12293-4

Hong, X., Campanario, S., Ramírez-Pardo, I., Grima-Terrén, M., Isern, J., & Muñoz-Cánoves, P. (2022). Stem cell aging in the skeletal muscle: The importance of communication. *Ageing Research Reviews*, *73*, 101528. https://doi.org/10.1016/j.arr.2021.101528

Hosoyama, T., Nishijo, K., Prajapati, S. I., Li, G., & Keller, C. (2011). Rb1 gene inactivation expands satellite cell and postnatal myoblast pools. *Journal of Biological Chemistry*, *286*(22), 19556–19564. https://doi.org/10.1074/jbc.M111.229542

Hu, G., Cui, K., Fang, D., Hirose, S., Wang, X., Wangsa, D., Jin, W., Ried, T., Liu, P., Zhu, J., Rothenberg, E. v., & Zhao, K. (2018). Transformation of Accessible Chromatin and 3D Nucleome Underlies Lineage Commitment of Early T Cells. *Immunity*, *48*(2), 227-242.e8. https://doi.org/10.1016/j.immuni.2018.01.013

Ikegami, K., Secchia, S., Almakki, O., Lieb, J. D., Moskowitz, I. P., C, S. L. A., Ikegami, K., Secchia, S., Almakki, O., Lieb, J. D., & Moskowitz, I. P. (2020). Phosphorylated Lamin A / C in the Nuclear Interior Binds Active Enhancers Associated with Abnormal Transcription in Progeria Article Phosphorylated Lamin A / C in the Nuclear Interior Binds Active Enhancers Associated with Abnormal Transcription in Proger.

Developmental Cell, *52*(6), 699-713.e11. https://doi.org/10.1016/j.devcel.2020.02.011

Joe, A. W. B., Yi, L., Natarajan, A., le Grand, F., So, L., Wang, J., Rudnicki, M. A., & Rossi, F. M. v. (2010). Muscle injury activates resident fibro/adipogenic progenitors that facilitate myogenesis. *Nature Cell Biology*, *12*(2), 153–163. https://doi.org/10.1038/ncb2015

Jones, N. C., Tyner, K. J., Nibarger, L., Stanley, H. M., Cornelison, D. D. W., Fedorov, Y. v, & Olwin, B. B. (2005). The p38alpha/beta MAPK functions as a molecular switch to activate the quiescent satellite cell. *The Journal of Cell Biology*, *169*(1), 105–116. https://doi.org/10.1083/jcb.200408066

Juan, A. H., Derfoul, A., Feng, X., Ryall, J. G., Dell'Orso, S., Pasut, A., Zare, H., Simone, J. M., Rudnicki, M. A., & Sartorelli, V. (2011). Polycomb EZH2 controls self-renewal and safeguards the transcriptional identity of skeletal muscle stem cells. *Genes and Development*, *25*(8), 789–794. https://doi.org/10.1101/gad.2027911

Juan, A. H., Kumar, R. M., Marx, J. G., Young, R. A., & Sartorelli, V. (2009). Mir-214-Dependent Regulation of the Polycomb Protein Ezh2 in Skeletal Muscle and Embryonic Stem Cells. *Molecular Cell*, *36*(1), 61–74. https://doi.org/10.1016/j.molcel.2009.08.008

Jung, J.-W., Lee, S., Seo, M.-S., Park, S.-B., Kurtz, A., Kang, S.-K., & Kang, K.-S. (2010). Histone deacetylase controls adult stem cell aging by balancing the expression of polycomb genes and jumonji domain containing 3. *Cellular and Molecular Life Sciences : CMLS*, *67*(7), 1165–1176. https://doi.org/10.1007/s00018-009-0242-9

Kalamakis, G., Brüne, D., Ravichandran, S., Bolz, J., Fan, W., Ziebell, F., Stiehl, T., Catalá-Martinez, F., Kupke, J., Zhao, S., Llorens-Bobadilla, E., Bauer, K., Limpert, S., Berger, B., Christen, U., Schmezer, P., Mallm, J. P., Berninger, B., Anders, S., … Martin-Villalba, A. (2019). Quiescence Modulates Stem Cell Maintenance and Regenerative Capacity in the Aging Brain. *Cell*, *176*(6), 1407-1419.e14. https://doi.org/10.1016/j.cell.2019.01.040

Kassar-Duchossoy, L., Giacone, E., Gayraud-Morel, B., Jory, A., Gomès, D., & Tajbakhsh, S. (2005). Pax3/Pax7 mark a novel population of primitive myogenic cells during development.

Genes and Development, *19*(12), 1426–1431. https://doi.org/10.1101/gad.345505
Katz, B. (1961). The termination of the afferent nerve fibre in the muscle spindle of the frog. *Philosophical Transactions of the Royal Society of London. Series B, Biological Sciences*, *243*(703), 221–240. https://doi.org/10.1098/rstb.1961.0001
Kim, J. H., Han, G. C., Seo, J. Y., Park, I., Park, W., Jeong, H. W., Lee, S. H., Bae, S. H., Seong, J., Yum, M. K., Hann, S. H., Kwon, Y. G., Seo, D., Choi, M. H., & Kong, Y. Y. (2016). Sex hormones establish a reserve pool of adult muscle stem cells. *Nature Cell Biology*, *18*(9), 930–940. https://doi.org/10.1038/ncb3401
Kim, J. J., & Kingston, R. E. (2022). Context-specific Polycomb mechanisms in development. *Nature Reviews Genetics*, *23*(11), 680–695. https://doi.org/10.1038/s41576-022-00499-0
Kim, R., Sheaffer, K. L., Choi, I., Won, K. J., & Kaestner, K. H. (2016). Epigenetic regulation of intestinal stem cells by Tet1-mediated DNA hydroxymethylation. *Genes & Development*, *30*(21), 2433–2442. https://doi.org/10.1101/GAD.288035.116
Kollu, S., Abou-Khalil, R., Shen, C., & Brack, A. S. (2015). The Spindle Assembly Checkpoint Safeguards Genomic Integrity of Skeletal Muscle Satellite Cells. *Stem Cell Reports*, *4*(6), 1061–1074. https://doi.org/10.1016/j.stemcr.2015.04.006
Konigsberg, U. R., Lipton, B. H., & Konigsberg, I. R. (1975). The regenerative response of single mature muscle fibers isolated in vitro. *Developmental Biology*, *45*(2), 260–275. https://doi.org/10.1016/0012-1606(75)90065-2
Kopinke, D., Roberson, E. C., & Reiter, J. F. (2017). Ciliary Hedgehog Signaling Restricts Injury-Induced Adipogenesis. *Cell*, *170*(2), 340-351.e12. https://doi.org/10.1016/j.cell.2017.06.035
Kuswanto, W., Burzyn, D., Panduro, M., Wang, K. K., Jang, Y. C., Wagers, A. J., Benoist, C., & Mathis, D. (2016). Poor Repair of Skeletal Muscle in Aging Mice Reflects a Defect in Local, Interleukin-33-Dependent Accumulation of Regulatory T Cells. *Immunity*, *44*(2), 355–367. https://doi.org/10.1016/j.immuni.2016.01.009

Lanzuolo, C., & Orlando, V. (2012). Memories from the Polycomb Group Proteins. *Annual Review of Genetics*, *46*(1), 561–589. https://doi.org/10.1146/annurev-genet-110711-155603

Lanzuolo, C., Roure, V., Dekker, J., Bantignies, F., & Orlando, V. (2007). Polycomb response elements mediate the formation of chromosome higher-order structures in the bithorax complex. *Nature Cell Biology*, *9*(10), 1167–1174. https://doi.org/10.1038/ncb1637

Larouche, J. A., Mohiuddin, M., Choi, J. J., Ulintz, P. J., Fraczek, P., Sabin, K., Pitchiaya, S., Kurpiers, S. J., Castor-Macias, J., Liu, W., Hastings, R. L., Brown, L. A., Markworth, J. F., de Silva, K., Levi, B., Merajver, S. D., Valdez, G., Chakkalakal, J. v, Jang, Y. C., … Aguilar, C. A. (2021). Murine muscle stem cell response to perturbations of the neuromuscular junction are attenuated with aging. *ELife*, *10*. https://doi.org/10.7554/eLife.66749

Larson, K., Yan, S.-J., Tsurumi, A., Liu, J., Zhou, J., Gaur, K., Guo, D., Eickbush, T. H., & Li, W. X. (2012). Heterochromatin Formation Promotes Longevity and Represses Ribosomal RNA Synthesis. *PLoS Genetics*, *8*(1), e1002473. https://doi.org/10.1371/journal.pgen.1002473

Lees-Shepard, J. B., Yamamoto, M., Biswas, A. A., Stoessel, S. J., Nicholas, S.-A. E., Cogswell, C. A., Devarakonda, P. M., Schneider, M. J., Cummins, S. M., Legendre, N. P., Yamamoto, S., Kaartinen, V., Hunter, J. W., & Goldhamer, D. J. (2018). Activin-dependent signaling in fibro/adipogenic progenitors causes fibrodysplasia ossificans progressiva. *Nature Communications*, *9*(1), 471. https://doi.org/10.1038/s41467-018-02872-2

Lemons, J. M. S., Feng, X.-J., Bennett, B. D., Legesse-Miller, A., Johnson, E. L., Raitman, I., Pollina, E. A., Rabitz, H. A., Rabinowitz, J. D., & Coller, H. A. (2010). Quiescent Fibroblasts Exhibit High Metabolic Activity. *PLoS Biology*, *8*(10), e1000514. https://doi.org/10.1371/journal.pbio.1000514

Lepper, C., Conway, S. J., & Fan, C. M. (2009). Adult satellite cells and embryonic muscle progenitors have distinct genetic requirements. *Nature*, *460*(7255), 627–631. https://doi.org/10.1038/nature08209

Lepper, C., Partridge, T. A., & Fan, C.-M. (2011). An absolute requirement for Pax7-positive satellite cells in acute injury-

induced skeletal muscle regeneration. *Development*, *138*(17), 3639–3646. https://doi.org/10.1242/dev.067595

Li, G., Tang, X., Zhang, S., Jin, M., Wang, M., Deng, Z., Liu, Z., Qian, M., Shi, W., Wang, Z., Xie, H., Li, J., & Liu, B. (2020). <scp>SIRT</scp> 7 activates quiescent hair follicle stem cells to ensure hair growth in mice. *The EMBO Journal*, *39*(18). https://doi.org/10.15252/embj.2019104365

Lieberman-Aiden, E., van Berkum, N. L., Williams, L., Imakaev, M., Ragoczy, T., Telling, A., Amit, I., Lajoie, B. R., Sabo, P. J., Dorschner, M. O., Sandstrom, R., Bernstein, B., Bender, M. A., Groudine, M., Gnirke, A., Stamatoyannopoulos, J., Mirny, L. A., Lander, E. S., & Dekker, J. (2009). Comprehensive mapping of long-range interactions reveals folding principles of the human genome. *Science*, *326*(5950), 289–293. https://doi.org/10.1126/SCIENCE.1181369/SUPPL_FILE/LIEBERMAN-AIDEN.SOM.PDF

Lilja, K. C., Zhang, N., Magli, A., Gunduz, V., Bowman, C. J., Arpke, R. W., Darabi, R., Kyba, M., Perlingeiro, R., & Dynlacht, B. D. (2017). Pax7 remodels the chromatin landscape in skeletal muscle stem cells. *PLOS ONE*, *12*(4), e0176190. https://doi.org/10.1371/journal.pone.0176190

Lipsitz, L. A. (2004). Physiological Complexity, Aging, and the Path to Frailty. *Science of Aging Knowledge Environment*, *2004*(16), pe16–pe16. https://doi.org/10.1126/sageke.2004.16.pe16

Liu, L., Charville, G. W., Cheung, T. H., Yoo, B., Santos, P. J., Schroeder, M., & Correspondence, T. A. R. (2018). *Impaired Notch Signaling Leads to a Decrease in p53 Activity and Mitotic Catastrophe in Aged Muscle Stem Cells*. https://doi.org/10.1016/j.stem.2018.08.019

Liu, L., Cheung, T. H., Charville, G. W., Hurgo, B. M. C., Leavitt, T., Shih, J., Brunet, A., & Rando, T. A. (2013). Chromatin Modifications as Determinants of Muscle Stem Cell Quiescence and Chronological Aging. *Cell Reports*, *4*(1), 189–204. https://doi.org/10.1016/j.celrep.2013.05.043

Liu, Rodriguez-Mateo, C., Huang, P., Huang, A., Lieu, A., Mao, M., Chung, M., Yang, S., Yu, K., Charville, G. W., Gan, Q., & Rando, T. A. (2021). Hairless regulates heterochromatin maintenance and muscle stem cell function as a histone

demethylase antagonist. *Proceedings of the National Academy of Sciences*, *118*(37). https://doi.org/10.1073/pnas.2025281118
Liu, Zhong, J., Ruan, Y., Zhang, Z., Sun, J., & Chen, H. (2021). The association between fat-to-muscle ratio and metabolic disorders in type 2 diabetes. *Diabetology & Metabolic Syndrome*, *13*(1), 129. https://doi.org/10.1186/s13098-021-00748-y
López-Otín, C., Blasco, M. A., Partridge, L., Serrano, M., & Kroemer, G. (2013). The Hallmarks of Aging. *Cell*, *153*(6), 1194–1217. https://doi.org/10.1016/j.cell.2013.05.039
Lukjanenko, L., Karaz, S., Stuelsatz, P., Gurriaran-Rodriguez, U., Michaud, J., Dammone, G., Sizzano, F., Mashinchian, O., Ancel, S., Migliavacca, E., Liot, S., Jacot, G., Metairon, S., Raymond, F., Descombes, P., Palini, A., Chazaud, B., Rudnicki, M. A., Bentzinger, C. F., & Feige, J. N. (2019). Aging Disrupts Muscle Stem Cell Function by Impairing Matricellular WISP1 Secretion from Fibro-Adipogenic Progenitors. *Cell Stem Cell*, *24*(3), 433-446.e7. https://doi.org/10.1016/j.stem.2018.12.014
Malecova, B., Gatto, S., Etxaniz, U., Passafaro, M., Cortez, A., Nicoletti, C., Giordani, L., Torcinaro, A., de Bardi, M., Bicciato, S., de Santa, F., Madaro, L., & Puri, P. L. (2018). Dynamics of cellular states of fibro-adipogenic progenitors during myogenesis and muscular dystrophy. *Nature Communications*, *9*(1), 3670. https://doi.org/10.1038/s41467-018-06068-6
Margueron, R., Li, G., Sarma, K., Blais, A., Zavadil, J., Woodcock, C. L., Dynlacht, B. D., & Reinberg, D. (2008). Ezh1 and Ezh2 Maintain Repressive Chromatin through Different Mechanisms. *Molecular Cell*, *32*(4), 503–518. https://doi.org/10.1016/j.molcel.2008.11.004
Marullo, F., Cesarini, E., Antonelli, L., Gregoretti, F., Oliva, G., & Lanzuolo, C. (2016). Nucleoplasmic Lamin A/C and Polycomb group of proteins: An evolutionarily conserved interplay. *Nucleus*, *7*(2), 103–111. https://doi.org/10.1080/19491034.2016.1157675
Mauro, A. (1961). Satellite cell of skeletal muscle fibers. *The Journal of Biophysical and Biochemical Cytology*, *9*, 493–495. https://doi.org/10.1083/jcb.9.2.493
Mikkelsen, T. S., Ku, M., Jaffe, D. B., Issac, B., Lieberman, E., Giannoukos, G., Alvarez, P., Brockman, W., Kim, T.-K., Koche, R. P., Lee, W., Mendenhall, E., O'Donovan, A., Presser, A.,

Russ, C., Xie, X., Meissner, A., Wernig, M., Jaenisch, R., … Bernstein, B. E. (2007). Genome-wide maps of chromatin state in pluripotent and lineage-committed cells. *Nature*, *448*(7153), 553–560. https://doi.org/10.1038/nature06008

Miljkovic-Gacic, I., Wang, X., Kammerer, C. M., Gordon, C. L., Bunker, C. H., Kuller, L. H., Patrick, A. L., Wheeler, V. W., Evans, R. W., & Zmuda, J. M. (2008). Fat Infiltration in Muscle: New Evidence for Familial Clustering and Associations With Diabetes. *Obesity*, *16*(8), 1854–1860. https://doi.org/10.1038/oby.2008.280

Miller, K. J., Thaloor, D., Matteson, S., & Pavlath, G. K. (2000). Hepatocyte growth factor affects satellite cell activation and differentiation in regenerating skeletal muscle. *American Journal of Physiology-Cell Physiology*, *278*(1), C174–C181. https://doi.org/10.1152/ajpcell.2000.278.1.C174

Misteli, T. (2007). Beyond the Sequence: Cellular Organization of Genome Function. *Cell*, *128*(4), 787–800. https://doi.org/10.1016/j.cell.2007.01.028

Mitchell, W. K., Williams, J., Atherton, P., Larvin, M., Lund, J., & Narici, M. (2012). Sarcopenia, dynapenia, and the impact of advancing age on human skeletal muscle size and strength; a quantitative review. *Frontiers in Physiology*, *3*, 260. https://doi.org/10.3389/fphys.2012.00260

Mitnitski, A. B., Mogilner, A. J., & Rockwood, K. (2001). Accumulation of deficits as a proxy measure of aging. *TheScientificWorldJournal*, *1*, 323–336. https://doi.org/10.1100/tsw.2001.58

Moresi, V., Pristerà, A., Scicchitano, B. M., Molinaro, M., Teodori, L., Sassoon, D., Adamo, S., & Coletti, D. (2008). Tumor necrosis factor-alpha inhibition of skeletal muscle regeneration is mediated by a caspase-dependent stem cell response. *Stem Cells (Dayton, Ohio)*, *26*(4), 997–1008. https://doi.org/10.1634/STEMCELLS.2007-0493

Morley, J. E., Vellas, B., Kan, G. A. van, Anker, S. D., Bauer, J. M., Bernabei, R., Cesari, M., Chumlea, W. C., Doehner, W., Evans, J., Fried, L. P., Guralnik, J. M., Katz, P. R., Malmstrom, T. K., McCarter, R. J., Gutierrez Robledo, L. M., Rockwood, K., von Haehling, S., Vanderwoude, M. F., & Walston, J. (2013). Frailty conensus: a call to action. *Journal of the American Medical*

Directors Assocation, *14*(6), 392–397. https://doi.org/10.1016/j.jamda.2013.03.022.Frailty
Moss, F. P., & Leblond, C. P. (1971). Satellite cells as the source of nuclei in muscles of growing rats. *The Anatomical Record*, *170*(4), 421–435. https://doi.org/10.1002/ar.1091700405
Mourikis, P., Gopalakrishnan, S., Sambasivan, R., & Tajbakhsh, S. (2012). Cell-autonomous Notch activity maintains the temporal specification potential of skeletal muscle stem cells. *Development*, *139*(24), 4536–4548. https://doi.org/10.1242/dev.084756
Mousavi, K., Zare, H., Wang, A. H., & Sartorelli, V. (2012). Polycomb Protein Ezh1 Promotes RNA Polymerase II Elongation. *Molecular Cell*, *45*(2), 255–262. https://doi.org/10.1016/j.molcel.2011.11.019
Mukund, K., & Subramaniam, S. (2020). Skeletal muscle: A review of molecular structure and function, in health and disease. *WIREs Systems Biology and Medicine*, *12*(1). https://doi.org/10.1002/wsbm.1462
Murphy, M. M., Lawson, J. A., Mathew, S. J., Hutcheson, D. A., & Kardon, G. (2011). Satellite cells, connective tissue fibroblasts and their interactions are crucial for muscle regeneration. *Development*, *138*(17), 3625–3637. https://doi.org/10.1242/dev.064162
Musumeci, G., Castrogiovanni, P., Coleman, R., Szychlinska, M. A., Salvatorelli, L., Parenti, R., Magro, G., & Imbesi, R. (2015). Somitogenesis: From somite to skeletal muscle. *Acta Histochemica*, *117*(4–5), 313–328. https://doi.org/10.1016/j.acthis.2015.02.011
Naumova, N., Smith, E. M., Zhan, Y., & Dekker, J. (2012). Analysis of long-range chromatin interactions using Chromosome Conformation Capture. *Methods*, *58*(3), 192–203. https://doi.org/10.1016/j.ymeth.2012.07.022
Nora, E. P., Lajoie, B. R., Schulz, E. G., Giorgetti, L., Okamoto, I., Servant, N., Piolot, T., van Berkum, N. L., Meisig, J., Sedat, J., Gribnau, J., Barillot, E., Blüthgen, N., Dekker, J., & Heard, E. (2012). Spatial partitioning of the regulatory landscape of the X-inactivation centre. *Nature*, *485*(7398), 381–385. https://doi.org/10.1038/nature11049

Noviello, C., Kobon, K., Delivry, L., Guilbert, T., Britto, F., Julienne, F., Maire, P., Randrianarison-Huetz, V., & Sotiropoulos, A. (2022). RhoA within myofibers controls satellite cell microenvironment to allow hypertrophic growth. *IScience*, *25*(1), 103616. https://doi.org/10.1016/j.isci.2021.103616

Ocampo, A., Reddy, P., Martinez-Redondo, P., Platero-Luengo, A., Hatanaka, F., Hishida, T., Li, M., Lam, D., Kurita, M., Beyret, E., Araoka, T., Vazquez-Ferrer, E., Donoso, D., Roman, J. L., Xu, J., Rodriguez Esteban, C., Nuñez, G., Nuñez Delicado, E., Campistol, J. M., … Izpisua Belmonte, J. C. (2016). In Vivo Amelioration of Age-Associated Hallmarks by Partial Reprogramming. *Cell*, *167*(7), 1719-1733.e12. https://doi.org/10.1016/j.cell.2016.11.052

Oprescu, S. N., Yue, F., Qiu, J., Brito, L. F., & Kuang, S. (2020). Temporal Dynamics and Heterogeneity of Cell Populations during Skeletal Muscle Regeneration. *IScience*, *23*(4), 100993. https://doi.org/10.1016/j.isci.2020.100993

Ou, H. D., Phan, S., Deerinck, T. J., Thor, A., Ellisman, M. H., & O'Shea, C. C. (2017). ChromEMT: Visualizing 3D chromatin structure and compaction n interphase and mitotic cells. *Science (New York, N.Y.)*, *357*(6349). https://doi.org/10.1126/SCIENCE.AAG0025

Pala, F., di Girolamo, D., Mella, S., Yennek, S., Chatre, L., Ricchetti, M., & Tajbakhsh, S. (2018). Distinct metabolic states govern skeletal muscle stem cell fates during prenatal and postnatal myogenesis. *Journal of Cell Science*, *131*(14). https://doi.org/10.1242/jcs.212977

Palacios, D., Mozzetta, C., Consalvi, S., Caretti, G., Saccone, V., Proserpio, V., Marquez, V. E., Valente, S., Mai, A., Forcales, S. v., Sartorelli, V., & Puri, P. L. (2010). TNF/p38α/Polycomb Signaling to Pax7 Locus in Satellite Cells Links Inflammation to the Epigenetic Control of Muscle Regeneration. *Cell Stem Cell*, *7*(4), 455–469. https://doi.org/10.1016/j.stem.2010.08.013

Passarge, E. (1979). Emil Heitz and the concept of heterochromatin: longitudinal chromosome differentiation was recognized fifty years ago. *American Journal of Human Genetics*, *31*(2), 106–115. http://www.ncbi.nlm.nih.gov/pubmed/377956

Pawlikowski, B., Pulliam, C., Betta, N. D., Kardon, G., & Olwin, B. B. (2015). Pervasive satellite cell contribution to uninjured adult

muscle fibers. *Skeletal Muscle*, *5*(1). https://doi.org/10.1186/S13395-015-0067-1

Pawlikowski, B., Vogler, T. O., Gadek, K., & Olwin, B. B. (2017). Regulation of skeletal muscle stem cells by fibroblast growth factors. *Developmental Dynamics : An Official Publication of the American Association of Anatomists*, *246*(5), 359–367. https://doi.org/10.1002/DVDY.24495

Pelosi, L., Giacinti, C., Nardis, C., Borsellino, G., Rizzuto, E., Nicoletti, C., Wannenes, F., Battistini, L., Rosenthal, N., Molinaro, M., & Musar, A. (2007). Local expression of IGF-1 accelerates muscle regeneration by rapidly modulating inflammatory cytokines and chemokines. *The FASEB Journal*, *21*(7), 1393–1402. https://doi.org/10.1096/fj.06-7690com

Pence, B. D., Gibbons, T. E., Bhattacharya, T. K., Mach, H., Ossyra, J. M., Petr, G., Martin, S. A., Wang, L., Rubakhin, S. S., Sweedler, J. v., McCusker, R. H., Kelley, K. W., Rhodes, J. S., Johnson, R. W., & Woods, J. A. (2016). Effects of exercise and dietary epigallocatechin gallate and β-alanine on skeletal muscle in aged mice. *Applied Physiology, Nutrition, and Metabolism*, *41*(2), 181–190. https://doi.org/10.1139/apnm-2015-0372

Petrilli, L. L., Spada, F., Palma, A., Reggio, A., Rosina, M., Gargioli, C., Castagnoli, L., Fuoco, C., & Cesareni, G. (2020). High-Dimensional Single-Cell Quantitative Profiling of Skeletal Muscle Cell Population Dynamics during Regeneration. *Cells*, *9*(7). https://doi.org/10.3390/CELLS9071723

Phillips, T., & Leeuwenburgh, C. (2005). Muscle fiber-specific apoptosis and TNF-α signaling in sarcopenia are attenuated by life-long calorie restriction. *The FASEB Journal*, *19*(6), 1–33. https://doi.org/10.1096/fj.04-2870fje

Pisconti, A., Banks, G. B., Babaeijandaghi, F., Betta, N. D., Rossi, F. M. v., Chamberlain, J. S., & Olwin, B. B. (2016). Loss of niche-satellite cell interactions in syndecan-3 null mice alters muscle progenitor cell homeostasis improving muscle regeneration. *Skeletal Muscle*, *6*(1), 34. https://doi.org/10.1186/s13395-016-0104-8

Price, F. D., von Maltzahn, J., Bentzinger, C. F., Dumont, N. A., Yin, H., Chang, N. C., Wilson, D. H., Frenette, J., & Rudnicki, M. A. (2014). Inhibition of JAK-STAT signaling stimulates adult

satellite cell function. *Nature Medicine*, *20*(10), 1174–1181. https://doi.org/10.1038/nm.3655

Quinn, L. S., Strait-Bodey, L., Anderson, B. G., Argilés, J. M., & Havel, P. J. (2005). Interleukin-15 stimulates adiponectin secretion by 3T3-L1 adipocytes: evidence for a skeletal muscle-to-fat signaling pathway. *Cell Biology International*, *29*(6), 449–457. https://doi.org/10.1016/j.cellbi.2005.02.005

Relaix, F., Bencze, M., Borok, M. J., der Vartanian, A., Gattazzo, F., Mademtzoglou, D., Perez-Diaz, S., Prola, A., Reyes-Fernandez, P. C., Rotini, A., & Taglietti. (2021). Perspectives on skeletal muscle stem cells. *Nature Communications 2021 12:1*, *12*(1), 1–11. https://doi.org/10.1038/s41467-020-20760-6

Riuzzi, F., Sorci, G., Arcuri, C., Giambanco, I., Bellezza, I., Minelli, A., & Donato, R. (2018). Cellular and molecular mechanisms of sarcopenia: the S100B perspective. *Journal of Cachexia, Sarcopenia and Muscle*, *9*(7), 1255–1268. https://doi.org/10.1002/jcsm.12363

Roberts, E. W., Deonarine, A., Jones, J. O., Denton, A. E., Feig, C., Lyons, S. K., Espeli, M., Kraman, M., McKenna, B., Wells, R. J. B., Zhao, Q., Caballero, O. L., Larder, R., Coll, A. P., O'Rahilly, S., Brindle, K. M., Teichmann, S. A., Tuveson, D. A., & Fearon, D. T. (2013). Depletion of stromal cells expressing fibroblast activation protein-α from skeletal muscle and bone marrow results in cachexia and anemia. *Journal of Experimental Medicine*, *210*(6), 1137–1151. https://doi.org/10.1084/jem.20122344

Roberts, P., McGeachie, J. K., & Grounds, M. D. (1997). The host environment determines strain-specific differences in the timing of skeletal muscle regeneration : cross-transplantation studies between SJL/J and BALB/c mice. In *J. Anat* (Vol. 191).

Rodriguez-Outeiriño, L., Hernandez-Torres, F., Ramirez de Acuña, F., Rastrojo, A., Creus, C., Carvajal, A., Salmeron, L., Montolio, M., Soblechero-Martin, P., Arechavala-Gomeza, V., Franco, D., & Aranega, A. E. (2022). miR-106b is a novel target to promote muscle regeneration and restore satellite stem cell function in injured Duchenne dystrophic muscle. *Molecular Therapy - Nucleic Acids*, *29*, 769–786. https://doi.org/10.1016/j.omtn.2022.08.025

Romanello, V., & Sandri, M. (2016). Mitochondrial Quality Control and Muscle Mass Maintenance. *Frontiers in Physiology*, *6*(JAN). https://doi.org/10.3389/fphys.2015.00422

Rozo, M., Li, L., & Fan, C.-M. (2016). Targeting β1-integrin signaling enhances regeneration in aged and dystrophic muscle in mice. *Nature Medicine*, *22*(8), 889–896. https://doi.org/10.1038/nm.4116

Ryall, J. G., Dell'Orso, S., Derfoul, A., Juan, A., Zare, H., Feng, X., Clermont, D., Koulnis, M., Gutierrez-Cruz, G., Fulco, M., & Sartorelli, V. (2015). The NAD+-dependent sirt1 deacetylase translates a metabolic switch into regulatory epigenetics in skeletal muscle stem cells. *Cell Stem Cell*, *16*(2), 171–183. https://doi.org/10.1016/j.stem.2014.12.004

Ryan, A. S., Buscemi, A., Forrester, L., Hafer-Macko, C. E., & Ivey, F. M. (2011). Atrophy and Intramuscular Fat in Specific Muscles of the Thigh. *Neurorehabilitation and Neural Repair*, *25*(9), 865–872. https://doi.org/10.1177/1545968311408920

Sahu, A., Mamiya, H., Shinde, S. N., Cheikhi, A., Winter, L. L., Vo, N. v, Stolz, D., Roginskaya, V., Tang, W. Y., St Croix, C., Sanders, L. H., Franti, M., van Houten, B., Rando, T. A., Barchowsky, A., & Ambrosio, F. (2018). Age-related declines in α-Klotho drive progenitor cell mitochondrial dysfunction and impaired muscle regeneration. *Nature Communications*, *9*(1), 4859. https://doi.org/10.1038/s41467-018-07253-3

Saksouk, N., Simboeck, E., & Déjardin, J. (2015). Constitutive heterochromatin formation and transcription in mammals. *Epigenetics & Chromatin*, *8*(1), 3. https://doi.org/10.1186/1756-8935-8-3

Salvarani, N., Crasto, S., Miragoli, M., Bertero, A., Paulis, M., Kunderfranco, P., Serio, S., Forni, A., Lucarelli, C., Dal Ferro, M., Larcher, V., Sinagra, G., Vezzoni, P., Murry, C. E., Faggian, G., Condorelli, G., & di Pasquale, E. (2019). The K219T-Lamin mutation induces conduction defects through epigenetic inhibition of SCN5A in human cardiac laminopathy. *Nature Communications*, *10*(1), 2267. https://doi.org/10.1038/s41467-019-09929-w

Saurin, A. J., Shiels, C., Williamson, J., Satijn, D. P. E., Otte, A. P., Sheer, D., & Freemont, P. S. (1998). The Human Polycomb Group Complex Associates with Pericentromeric

Heterochromatin to Form a Novel Nuclear Domain. *Journal of Cell Biology*, *142*(4), 887–898. https://doi.org/10.1083/jcb.142.4.887

Schultz, E., Gibson, M. C., & Champion, T. (1978). Satellite cells are mitotically quiescent in mature mouse muscle: An EM and radioautographic study. *Journal of Experimental Zoology*, *206*(3), 451–456. https://doi.org/10.1002/JEZ.1402060314

Schwörer, S., Becker, F., Feller, C., Baig, A. H., Köber, U., Henze, H., Kraus, J. M., Xin, B., Lechel, A., Lipka, D. B., Varghese, C. S., Schmidt, M., Rohs, R., Aebersold, R., Medina, K. L., Kestler, H. A., Neri, F., von Maltzahn, J., Tümpel, S., & Rudolph, K. L. (2016). Epigenetic stress responses induce muscle stem-cell ageing by Hoxa9 developmental signals. *Nature 2016 540:7633*, *540*(7633), 428–432. https://doi.org/10.1038/nature20603

Scott, R. W., Arostegui, M., Schweitzer, R., Rossi, F. M. V., & Underhill, T. M. (2019). Hic1 Defines Quiescent Mesenchymal Progenitor Subpopulations with Distinct Functions and Fates in Skeletal Muscle Regeneration. *Cell Stem Cell*, *25*(6), 797-813.e9. https://doi.org/10.1016/j.stem.2019.11.004

Seale, P., Sabourin, L. A., Girgis-Gabardo, A., Mansouri, A., Gruss, P., & Rudnicki, M. A. (2000). Pax7 Is Required for the Specification of Myogenic Satellite Cells. *Cell*, *102*(6), 777–786. https://doi.org/10.1016/S0092-8674(00)00066-0

Sebestyén, E., Marullo, F., Lucini, F., Petrini, C., Bianchi, A., Valsoni, S., Olivieri, I., Antonelli, L., Gregoretti, F., Oliva, G., Ferrari, F., & Lanzuolo, C. (2020). SAMMY-seq reveals early alteration of heterochromatin and deregulation of bivalent genes in Hutchinson-Gilford Progeria Syndrome. *Nature Communications*, *11*(1). https://doi.org/10.1038/S41467-020-20048-9

Shcherbina, A., Larouche, J., Fraczek, P., Yang, B. A., Brown, L. A., Markworth, J. F., Chung, C. H., Khaliq, M., de Silva, K., Choi, J. J., Fallahi-Sichani, M., Chandrasekaran, S., Jang, Y. C., Brooks, S. v., & Aguilar, C. A. (2020). Dissecting Murine Muscle Stem Cell Aging through Regeneration Using Integrative Genomic Analysis. *Cell Reports*, *32*(4), 107964. https://doi.org/10.1016/J.CELREP.2020.107964

Shea, K. L., Xiang, W., LaPorta, V. S., Licht, J. D., Keller, C., Basson, M. A., & Brack, A. S. (2010). Sprouty1 Regulates Reversible Quiescence of a Self-Renewing Adult Muscle Stem Cell Pool during Regeneration. *Cell Stem Cell*, *6*(2), 117–129. https://doi.org/10.1016/j.stem.2009.12.015

Shi, X., & Garry, D. J. (2006). Muscle stem cells in development, regeneration, and disease. *Genes & Development*, *20*(13), 1692–1708. https://doi.org/10.1101/gad.1419406

Sousa-Victor, P., Gutarra, S., García-Prat, L., Rodriguez-Ubreva, J., Ortet, L., Ruiz-Bonilla, V., Jardí, M., Ballestar, E., González, S., Serrano, A. L., Perdiguero, E., & Muñoz-Cánoves, P. (2014). Geriatric muscle stem cells switch reversible quiescence into senescence. *Nature*, *506*(7488), 316–321. https://doi.org/10.1038/nature13013

Stojic, L., Jasencakova, Z., Prezioso, C., Stützer, A., Bodega, B., Pasini, D., Klingberg, R., Mozzetta, C., Margueron, R., Puri, P., Schwarzer, D., Helin, K., Fischle, W., & Orlando, V. (2011). Chromatin regulated interchange between polycomb repressive complex 2 (PRC2)-Ezh2 and PRC2-Ezh1 complexes controls myogenin activation in skeletal muscle cells. *Epigenetics & Chromatin*, *4*(1), 16. https://doi.org/10.1186/1756-8935-4-16

Stubbs, T. M., Bonder, M. J., Stark, A.-K., Krueger, F., von Meyenn, F., Stegle, O., & Reik, W. (2017). Multi-tissue DNA methylation age predictor in mouse. *Genome Biology*, *18*(1), 68. https://doi.org/10.1186/s13059-017-1203-5

Su, S.-K., Li, C.-Y., Lei, P.-J., Wang, X., Zhao, Q.-Y., Cai, Y., Wang, Z., Li, L., & Wu, M. (2016). The EZH1-SUZ12 complex positively regulates the transcription of NF-κB target genes through interaction with UXT. *Journal of Cell Science*, *129*(12), 2343–2353. https://doi.org/10.1242/jcs.185546

Sugihara, H., Teramoto, N., Yamanouchi, K., Matsuwaki, T., & Nishihara, M. (2018). Oxidative stress-mediated senescence in mesenchymal progenitor cells causes the loss of their fibro/adipogenic potential and abrogates myoblast fusion. *Aging*, *10*(4), 747–763. https://doi.org/10.18632/aging.101425

Sun, F., Chronis, C., Kronenberg, M., Chen, X. F., Su, T., Lay, F. D., Plath, K., Kurdistani, S. K., & Carey, M. F. (2019). Promoter-Enhancer Communication Occurs Primarily within Insulated

Neighborhoods. *Molecular Cell*, *73*(2), 250-263.e5. https://doi.org/10.1016/j.molcel.2018.10.039
Takashima, H., Takebayashi, T., Ogon, I., Yoshimoto, M., Morita, T., Imamura, R., Nakanishi, M., Nagahama, H., Terashima, Y., & Yamashita, T. (2018). Analysis of intra and extramyocellular lipids in the multifidus muscle in patients with chronic low back pain using MR spectroscopy. *The British Journal of Radiology*, 20170536. https://doi.org/10.1259/bjr.20170536
Tanabe, H., Müller, S., Neusser, M., von Hase, J., Calcagno, E., Cremer, M., Solovei, I., Cremer, C., & Cremer, T. (2002). Evolutionary conservation of chromosome territory arrangements in cell nuclei from higher primates. *Proceedings of the National Academy of Sciences*, *99*(7), 4424–4429. https://doi.org/10.1073/pnas.072618599
Tarnopolsky, M. A., Rennie, C. D., Robertshaw, H. A., Fedak-Tarnopolsky, S. N., Devries, M. C., & Hamadeh, M. J. (2007). Influence of endurance exercise training and sex on intramyocellular lipid and mitochondrial ultrastructure, substrate use, and mitochondrial enzyme activity. *American Journal of Physiology-Regulatory, Integrative and Comparative Physiology*, *292*(3), R1271–R1278. https://doi.org/10.1152/ajpregu.00472.2006
Taylor-Jones, J. M., McGehee, R. E., Rando, T. A., Lecka-Czernik, B., Lipschitz, D. A., & Peterson, C. A. (2002). Activation of an adipogenic program in adult myoblasts with age. *Mechanisms of Ageing and Development*, *123*(6), 649–661. https://doi.org/10.1016/S0047-6374(01)00411-0
Tosic, M., Allen, A., Willmann, D., Lepper, C., Kim, J., Duteil, D., & Schüle, R. (2018). Lsd1 regulates skeletal muscle regeneration and directs the fate of satellite cells. *Nature Communications*, *9*(1), 366. https://doi.org/10.1038/s41467-017-02740-5
Trojer, P., & Reinberg, D. (2007). Facultative Heterochromatin: Is There a Distinctive Molecular Signature? *Molecular Cell*, *28*(1), 1–13. https://doi.org/10.1016/j.molcel.2007.09.011
Uezumi, A., Fukada, S., Yamamoto, N., Takeda, S., & Tsuchida, K. (2010). Mesenchymal progenitors distinct from satellite cells contribute to ectopic fat cell formation in skeletal muscle. *Nature Cell Biology*, *12*(2), 143–152. https://doi.org/10.1038/ncb2014

Uezumi, A., Ikemoto-Uezumi, M., Zhou, H., Kurosawa, T., Yoshimoto, Y., Nakatani, M., Hitachi, K., Yamaguchi, H., Wakatsuki, S., Araki, T., Morita, M., Yamada, H., Toyoda, M., Kanazawa, N., Nakazawa, T., Hino, J., Fukada, S. I., & Tsuchida, K. (2021). Mesenchymal Bmp3b expression maintains skeletal muscle integrity and decreases in age-related sarcopenia. *The Journal of Clinical Investigation*, *131*(1). https://doi.org/10.1172/JCI139617

Verma, M., Asakura, Y., Murakonda, B. S. R., Pengo, T., Latroche, C., Chazaud, B., McLoon, L. K., & Asakura, A. (2018). Muscle Satellite Cell Cross-Talk with a Vascular Niche Maintains Quiescence via VEGF and Notch Signaling. *Cell Stem Cell*, *23*(4), 530-543.e9. https://doi.org/10.1016/j.stem.2018.09.007

Villeponteau, B. (1997). THE HETEROCHROMATIN LOSS MODEL OF AGING. In *Experimental Gerontology* (Vol. 32).

Voisin, S., Jacques, M., Landen, S., Harvey, N. R., Haupt, L. M., Griffiths, L. R., Gancheva, S., Ouni, M., Jähnert, M., Ashton, K. J., Coffey, V. G., Thompson, J. M., Doering, T. M., Gabory, A., Junien, C., Caiazzo, R., Verkindt, H., Raverdy, V., Pattou, F., … Eynon, N. (2021). Meta-analysis of genome-wide DNA methylation and integrative omics of age in human skeletal muscle. *Journal of Cachexia, Sarcopenia and Muscle*, *12*(4), 1064–1078. https://doi.org/10.1002/jcsm.12741

Wagers, A. J., & Weissman, I. L. (2004). Plasticity of adult stem cells. *Cell*, *116*(5), 639–648. https://doi.org/10.1016/S0092-8674(04)00208-9

Wang, H., Wang, L., Erdjument-Bromage, H., Vidal, M., Tempst, P., Jones, R. S., & Zhang, Y. (2004). Role of histone H2A ubiquitination in Polycomb silencing. *Nature*, *431*(7010), 873–878. https://doi.org/10.1038/nature02985

Wang, R., Chen, F., Chen, Q., Wan, X., Shi, M., Chen, A. K., Ma, Z., Li, G., Wang, M., Ying, Y., Liu, Q., Li, H., Zhang, X., Ma, J., Zhong, J., Chen, M., Zhang, M. Q., Zhang, Y., Chen, Y., & Zhu, D. (2022). MyoD is a 3D genome structure organizer for muscle cell identity. *Nature Communications*, *13*(1), 205. https://doi.org/10.1038/s41467-021-27865-6

Wani, A. H., Boettiger, A. N., Schorderet, P., Ergun, A., Münger, C., Sadreyev, R. I., Zhuang, X., Kingston, R. E., & Francis, N. J. (2016). Chromatin topology is coupled to Polycomb group

protein subnuclear organization. *Nature Communications*, *7*(1), 10291. https://doi.org/10.1038/ncomms10291
White, R. B., Biérinx, A. S., Gnocchi, V. F., & Zammit, P. S. (2010). Dynamics of muscle fibre growth during postnatal mouse development. *BMC Developmental Biology*, *10*. https://doi.org/10.1186/1471-213X-10-21
Woo, J. (2017). Sarcopenia. *Clinics in Geriatric Medicine*, *33*(3), 305–314. https://doi.org/10.1016/j.cger.2017.02.003
Woodhouse, S., Pugazhendhi, D., Brien, P., & Pell, J. M. (2013). Ezh2 maintains a key phase of muscle satellite cell expansion but does not regulate terminal differentiation. *Journal of Cell Science*, *126*(2), 565–579. https://doi.org/10.1242/jcs.114843
Wosczyna, M. N., Biswas, A. A., Cogswell, C. A., & Goldhamer, D. J. (2012). Multipotent progenitors resident in the skeletal muscle interstitium exhibit robust BMP-dependent osteogenic activity and mediate heterotopic ossification. *Journal of Bone and Mineral Research*, *27*(5), 1004–1017. https://doi.org/10.1002/jbmr.1562
Wosczyna, M. N., & Rando, T. A. (2018). A Muscle Stem Cell Support Group: Coordinated Cellular Responses in Muscle Regeneration. *Developmental Cell*, *46*(2), 135–143. https://doi.org/10.1016/j.devcel.2018.06.018
Yates, F. E. (2002). Complexity of a human being: changes with age. *Neurobiology of Aging*, *23*(1), 17–19. https://doi.org/10.1016/S0197-4580(01)00261-5
Yin, H., Price, F., & Rudnicki, M. A. (2013). Satellite Cells and the Muscle Stem Cell Niche. *Physiological Reviews*, *93*(1), 23–67. https://doi.org/10.1152/physrev.00043.2011
Zammit, P. S., Golding, J. P., Nagata, Y., Hudon, V., Partridge, T. A., & Beauchamp, J. R. (2004). Muscle satellite cells adopt divergent fates: A mechanism for self-renewal? *Journal of Cell Biology*, *166*(3), 347–357. https://doi.org/10.1083/jcb.200312007
Zhang, H., Sun, L., Wang, K., Wu, D., Trappio, M., Witting, C., & Cao, K. (2016). Loss of H3K9me3 Correlates with ATM Activation and Histone H2AX Phosphorylation Deficiencies in Hutchinson-Gilford Progeria Syndrome. *PLOS ONE*, *11*(12), e0167454. https://doi.org/10.1371/journal.pone.0167454

Zhang, N., Mendieta-Esteban, J., Magli, A., Lilja, K. C., Perlingeiro, R. C. R., Marti-Renom, M. A., Tsirigos, A., & Dynlacht, B. D. (2020). Muscle progenitor specification and myogenic differentiation are associated with changes in chromatin topology. *Nature Communications*, *11*(1). https://doi.org/10.1038/S41467-020-19999-W

Zhu, P., Zhang, C., Gao, Y., Wu, F., Zhou, Y., & Wu, W. S. (2019). The transcription factor Slug represses p16Ink4a and regulates murine muscle stem cell aging. *Nature Communications*, *10*(1). https://doi.org/10.1038/s41467-019-10479-4

Chapter 2 Role of *Cdkn2a* in the Emery–Dreifuss Muscular Dystrophy Cardiac Phenotype

Gloria Pegoli [1], Marika Milan [1], Pierluigi Giuseppe Manti [2], Andrea Bianchi [1], Federica Lucini [1,3], Philina Santarelli [1], Claudia Bearzi [1,4], Roberto Rizzi [1,5] and Chiara Lanzuolo [1,5],*

***Biomolecules* 2021, *11*(4), 538;**

https://doi.org/10.3390/biom11040538

Received: 8 September 2020

Revised: 23 March 2021

Accepted: 23 March 2021

Published: 6 April 2021

Role of Cdkn2a in the Emery–Dreifuss Muscular Dystrophy Cardiac Phenotype

Gloria Pegoli [1], Marika Milan [1], Pierluigi Giuseppe Manti [2], Andrea Bianchi [1], Federica Lucini [1,3], Philina Santarelli [1], Claudia Bearzi [1,4], Roberto Rizzi [1,5] and Chiara Lanzuolo [1,5]*

1 Istituto Nazionale di Genetica Molecolare "Romeo ed Enrica Invernizzi", 20122 Milan, Italy;
pegoli@ingm.org (G.P.); milan@ingm.org (M.M.); andrea.bianchi89@libero.it (A.B.); lucini@ingm.org (F.L.); santarelli@ingm.org (P.S.); claudia.bearzi@cnr.it (C.B.); roberto.rizzi@cnr.it (R.R.)
2 Department of Oncology and Hemato-Oncology, University of Milan, 20122 Milan, Italy;
pierluigi.manti@unimi.it
3 IFOM, the FIRC Institute of Molecular Oncology, 20139 Milan, Italy
4 Consiglio Nazionale delle Ricerche (CNR), Istituto di Ricerca Genetica e Biomedica, 20138 Milan, Italy
5 Consiglio Nazionale delle Ricerche (CNR), Institute of Biomedical Technologies (ITB), 20054 Milan, Italy
* Correspondence: chiara.lanzuolo@cnr.it; Tel.: +39-02-00660358

Keywords: Emery–Dreifuss muscular dystrophy; Cdkn2a locus; Lamin A/C; p16INK4a; heart; dilated cardiomyopathy; cellular senescence

2.1. Abstract

The Cdkn2a locus is one of the most studied tumor suppressor loci in the context of several cancer types. However, in the last years, its expression has also been linked to terminal differentiation and the activation of the senescence program in different cellular subtypes. Knock-out (KO) of the entire locus enhances the capability of stem cells to proliferate in some tissues and respond to severe physiological and non-physiological damages in different organs, including the heart. Emery–Dreifuss muscular dystrophy (EDMD) is characterized by severe contractures and muscle loss at the level of skeletal muscles of the elbows, ankles and neck, and by dilated cardiomyopathy. We have recently demonstrated, using the LMNA Δ8–11 murine model of Emery–Dreifuss muscular dystrophy (EDMD), that dystrophic muscle stem cells prematurely express non-lineage-specific genes early on during postnatal growth, leading to rapid exhaustion of the muscle stem cell pool. Knock-out of the Cdkn2a locus in EDMD dystrophic mice partially restores muscle stem cell properties. In the present study, we describe the cardiac phenotype of the LMNA Δ8–11 mouse model and functionally characterize the effects of KO of the Cdkn2a locus on heart functions and life expectancy.

2.2. Introduction

The protein p16INK4a is part of the INK4 family of proteins (INhibitor of Cyclin-Dependent Kinase 4) together with p15INK4b, p18INK4c and p19INK4d [1]. This group of regulators plays a crucial role in cell cycle inhibition and tumor suppression [2,3]. In humans, p16INK4a is transcribed from the Cdkn2a locus, alternatively called INK4/ARF (ARF, Alternative Reading Frame) on chromosome 9p21.3 [1,4,5] (Figure 1). The locus contains two genes, p16INK4a and ARF (the latter is named p19 in mice and p14 in humans), that, although endowed with their promoter and first exons (E1α for p16INK4a and E1β for ARF), share Exons 2 and 3 (E2 and E3). E1α is spliced to E2 and E3 to produce p16INK4a, while E1β, upon splicing to E2 and E3, imposes a frameshift that generates p19ARF (p14ARF in human), a protein with different amino acid sequence. p15INK4b, transcribed from the flanking CDKN2B locus, shares 85% identity in its amino acid sequences with p16INK4a [2] and both negatively regulate the pRB–E2F (retinoblastoma-Transcription Factor E2) pathway involved in cell cycle control [4] (Figure 1).

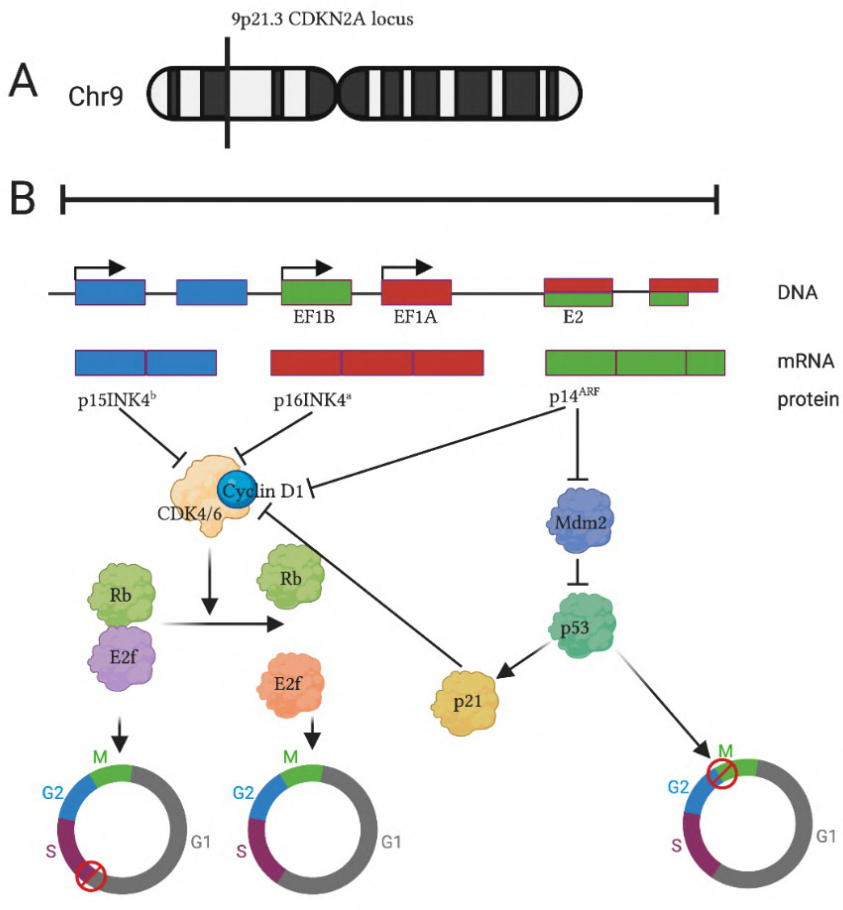

Figure 5. The CDKN2A/B loci and regulated pathways. (A) Localization of the locus of interest on human chromosome 9. (B) The products of the locus collaborate to block the cell cycle by inhibiting the retinoblastoma (RB)–E2F pathway.

During the G1 phase, hypo-phosphorylated RB aggregates with E2F, preventing the activation of genes involved in cell proliferation [1]. In the late G1 phase, cyclin-dependent kinase 4 or 6 (CDK4/6) phosphorylates RB, provoking E2F release and S phase entry. Expression of p16INK4a results in CDK4/6 inhibition and leads to cell cycle arrest at G1 phase [2,4].

ARF stops the cell cycle acting in response to aberrant cell growth or oncogenic stresses. Upon activation of several oncogenes such as Rat Sarcoma (Ras), Adenovirus early region 1A (E1A), E2F and cellular- Myelocytomatosis (c-MYC), the intracellular levels of ARF increase, causing Mouse Double Minute 2 (MDM2) inhibition and the activation of a p53-dependent transcriptional program. This molecular cascade leads to an arrest in both the G1 and G2 phase mediated by the upregulation of p21, a p53 target that is able to inhibit cyclin-dependent kinases [2,4,6,7].

Cdkn2a is one of the most intensively studied tumor suppressor loci, as several malignant tumors show abnormalities in the Cdkn2a sequence and expression status [2–5]. Specifically, in the case of p16INK4a, the most frequent genetic alterations are homozygous deletions, while epigenetic alterations are mediated by the Polycomb group of proteins (PcG), evolutionarily conserved epigenetic repressors that regulate higher-order chromatin structures [3,4,8–11]. Notably, even though the most common hypothesis is that the reduced expression of p16INK4a is the leading cause of neoplastic progression, p16INK4a overexpression has been frequently found to be associated with a poor prognosis in cancer patients [1,3,12], suggesting that p16INK4a levels are tightly regulated in healthy tissues.

In parallel with the role of Cdkn2a in cell cycle control, p16INK4a has been intensively studied for its role in cellular senescence [12] and cell differentiation [13]. Elevated levels of p16INK4a

induce senescence of progenitor stem cells [14,15], characterized by cell cycle blockage, DNA damage accumulation and decreased capability to remove free radicals [14,16]. Growing pieces of evidence point out the importance of p16INK4a in muscle senescence, a process called sarcopenia, the age-dependent loss of muscle mass and function that can worsen the standard quality of life [17]. In later stages of mouse aging (28–32 months), subsequent to p21 expression, p16INK4a expression increases and establishes the irreversible senescence program [6,18,19]. In line with recent reports showing that suppression of the Cdkn2a locus improves cell and tissue regeneration properties [20–25], Cdkn2a knock-out (KO) or knock-down (KD) [18] allow the better capacity of muscle stem cells (MuSCs) to regenerate and proliferate when occasional or chronic injuries occur in senescent skeletal muscles [18,24,26].

Senescence and Cyclin-Dependent Kinase Inhibitors (CDKI) expression in muscle stem cells are typical traits of Emery–Dreifuss muscular dystrophy (EDMD) [24,27,28], a form of muscular dystrophy affecting 1–9 in 1,000,000 patients worldwide, presenting slowly progressive muscle weakness and atrophy (ORPHA:261). The autosomal dominant form of EDMD (EDMD2) is due to heterozygous mutations in the LMNA gene encoding for Lamin A/C protein [29,30]. Different mechanisms have been proposed as a driving force for EDMD pathogenesis and progression [31]; among them are the epigenetic mechanisms that involve Lamin A/C and the PcG proteins,

whose interplay is paving the way to understand why EDMD displays a broad spectrum of symptom variability and uncorrelated genotype–phenotype in patients [24,31–35].

The cardiomyopathy occurring in EDMD2 is correlated with high incidence of heart blockage and ventricular arrhythmias, resulting in a more aggressive phenotype than other inherited ones [36]. Surprisingly, heart failure without prior cardiac symptoms can be the first manifestation of the disease [37–39]. Dilated cardiomyopathy (DCM) [40–42] is interrelated with cardiac electrophysiologic defects, like sinus node dysfunction, progressive atrioventricular blockage, paroxysmal atrial fibrillation and ventricular arrhythmias [37,43–47]. The penetrance and expressivity of these symptoms show both inter- and intra-familial variability [48].

The cardiac phenotype of EDMD has been deeply investigated in the LaminH222P/H222P mouse model [49,50], a model of EDMD carrying the same H222P genetic mutation found in patients. In this specific murine model, the heart dynamics associated with EDMD pathology are partially recapitulated: dilated cardiomyopathy and arrhythmias are the most evident phenotype, although no sudden deaths have been observed. Before the appearance of the severe cardiac phenotype, several signaling pathways strongly activated under stress conditions are abnormally regulated: levels of Wingless-related integration site (WNT) and β-catenin are decreased [51], while the Mitogen-Activated Protein Kinase (MAPK) proteins Extracellular signal-

Regulated Kinase 1/2 (ERK1/2), p38α and Jun Nuclear Kinase (JNK) are hyperactivated [52–59], together with the a serine/threonine protein kinase- mammalian Target of Rapamycin Complex 1 (AKT-mTORC1) pathway [52]. Interestingly, by using bioinformatical tools, it has been demonstrated that even the Transforming growth factor beta (TGF-β) pathway, linked to fibrosis, is upregulated [49,52].

Molecular alterations that could affect heart functions, however, are not a prerogative of the LaminH222P/H222P model: it has been recently reported that patient-specific induced pluripotent stem cell (iPSC)-derived cardiomyocytes (carrying mutations in the LMNA gene) display aberrant calcium homeostasis, leading to arrhythmias at the single-cell level that could be partially rescued by pharmacological and molecular inhibition of the Platelet-derived growth factor (PDGF) [60]. In another mouse model of DCM, tet-off bigenic mice expressing lamin (D300N) mutant protein in cardiac myocytes [61], a significant downregulation of retinoblastoma (RB) expression has been found, accompanied by transcriptional upregulation of other loci, Cdkn2a included, supporting the role of p16INK4a in heart dysfunction [62].

Few cardiac studies have been conducted on another EDMD mouse model, the LMNA Δ8-11, due to the shorter life of the homozygous mutant mice that encounter premature death. While at birth, wild-type, heterozygous and homozygous LMNA Δ8-11 mice are indistinguishable, after 2–3 weeks from birth, LMNA Δ8-

11 –/– mice show a reduction in growth and display typical traits of muscular dystrophy, dying before 8 weeks of age [63]. The cardiac phenotype of dystrophic LMNA Δ8-11 –/– mice at 4–6 weeks of postnatal age has been classified as DCM with limited compensatory hypertrophy [64]. Furthermore, some LMNA Δ8-11 –/– mice show sudden death in the first 20 days of life, recapitulating all heart-associated defects reported in human EDMD. It is also known that heterozygous LMNA Δ8-11 +/– mice, even in the absence of skeletal myopathy, display some cardiac abnormalities late in adulthood, i.e., at approximately 50 weeks [65], which strictly recapitulate the progression of the disease in EDMD patients. Altogether, this evidence confirms that Lamin A's absence or haploinsufficiency influences cardiac performance and can generate DCM.

In this work, we present the possible beneficial effects of genetic Cdkn2a locus ablation on the cardiac functions of the most severely affected EDMD mice (LMNA Δ8-11 –/–).

2.3. Materials and Methods

Ethical Approval

Heterozygous B6.129S1(Cg)-Lmnatm1Stw/BkknJ mice (LMNA Δ8-11 +/–) [63] and Cdkn2a +/– mice [66] (in which both p16INK4a and p19ARF were ablated) were used to obtain our model of interest. The relevant genotypes were obtained by crossing double heterozygous mice LMNA Δ8-11 +/– Cdkn2a +/–. Pup genotyping was performed within the first 7 days after birth on a small part of the skin, under general anesthesia. All the experimental procedures were performed under the ethical approval of the Italian Ministry of Health and the Institutional Animal Care and Use Committee (authorization No. 83/2019-PR). The animals were maintained in an authorized animal facility at San Raffaele Hospital, Milan (authorization No. N. 127/2012-A).

Mice Genotyping

DNA was extracted from a small amount of skin, obtained after ear tagging, using Phire tissue direct PCR master mix (Thermo Scientific, F170L, Waltham, MA, USA), then amplified using the following primers spanning the Lamin A locus: Fw-Lmna: 5′-GCTTCGAGTGACTGTGACAC-3′; Rev-Lmna: 5′-GTCCCCATCACTTGGTTGTC-3′; Rev-mutLmna: 5′-

ACCGGTGGATGTGGAATGTG-3′. Primers for the Cdkn2a locus were previously described in Serrano et al. [66].

Survival and Weight Control

Mice were monitored daily and weighted starting from Day 5 after birth to death. For weight assessment, we considered 3–5 mice for each time point. After 30 days, the number of weight measurements dropped due to premature death.

Immunohistochemistry

Hearts were collected from anesthetized 30-day-old (P30) mice after being perfused with 50 mM KCl (Sigma, P9333, St. Louis, MO, USA), according to the experimental protocol approved by the Italian Ministry of Health. Hearts were embedded in Killik medium for inclusion (Bio-optica, 05-9801), frozen in pre-cooled isopentane (Sigma, 277258) and sectioned into pieces with 8 µm thickness (Leica CM1850 cryostat, Wetzlar, Germany). Before proceeding with the immunofluorescence protocol, samples were warmed at room temperature (RT) for 30 min and then fixed in ice-cold acetone for 10 min. After 2 washes in Phosphate-buffered saline (PBS), sections were permeabilized with 0.1% Triton x-100 (Sigma, T8787) for 10 min at RT and washed again in PBS. Samples were later blocked using 5% Bovine Serum Albumin (BSA) (Sigma, A7030) for 1 h prior to over/night (O/N) incubation at 4 °C with primary antibodies diluted in 0.5% BSA.

The primary antibodies anti-cardiac troponin T (cTNNT, 1:100 dilution, Abcam, ab33589), anti-α-smooth muscle actin (α-SMA, 1:200 dilution, Sigma-Aldrich, A2547), anti-Connexin43 (Cx43, 1:100 dilution, Cell Signaling CST, #3512), anti- Marker Of Proliferation Ki-67 (Ki67, 1:100 dilution; Abcam, ab15580) and anti-N-Cadherin (N-Cadherin, 1:800 dilution, BD, 610921) were used. The following day, the slides were washed in PBS for 10 min before the incubation with fluorescent-conjugated secondary antibodies (1:1000 dilution) for 2 hours at RT. Fluorescent phalloidin, tetramethyl-rhodamine B isothiocyanate-conjugated (Sigma, P1951), was used at 50 µg/mL concentration. To quantify the number of capillaries, the sections were stained with isolectin B4 Fluorescein isothiocyanate (FITC)-conjugated antibody for 1 h at 37 °C (ISO/B4, 1:50 dilution; Sigma-Aldrich, L2140). The apoptotic index was evaluated by a Terminal deoxynucleotidyl transferase-mediated dUTP nick-end labeling (TUNEL) assay following the protocol given by the manufacturer (ApoAlert DNA Fragmentation assay kit, 630107). Cell nuclei were counterstained with 4′,6-diamidino-2-phenylindole (DAPI) (1:1000, Sigma, D9542) before mounting the slides with Prolong Glass Antifade (Thermo, P36984). All the images were acquired with a confocal microscope (Leica SP5 using LAS AF software) and processed using ImageJ software. The fibrotic area was assessed by Masson′s Trichrome assay (Bio-Optica, 04-010802) according to the manufacturer′s protocol. The images of all sections were acquired using a Leica optical time-lapse

microscope. The fibrotic area size was expressed (in percentages) as a ratio of the fibrotic area (stained in blue) on the total area. To quantify the number of vessels, α-SMA-positive cells were divided by the total area of the section. Differently from vessels, capillary density was expressed as the number of isolectin B4-positive capillaries divided by the number of nuclei. For Connexin43 or N-Cadherin localization analysis, both signals were processed from every field with Fiji (Fiji Is Just ImageJ) software for background removal and transformation into a binary mask. The total area of singly positive Connexin43 or N-Cadherin and doubly positive Connexin43/N-Cadherin signals was measured and then a ratio between the co-localizing area and the total Connexin43 area was used as a quantification of Connexin43 localization on intercalated discs (IDs). For the TUNEL assay and Ki67 labeling, the positive nuclei were normalized on the total number of nuclei in the tissue field.

Real-Time PCR

Murine hearts were collected post mortem at Day 0 (P0) and Day 30 (P30) after birth. Total RNA was extracted from the whole heart using Tissue Ruptor (Qiagen, 9002755) and TriReagent (Sigma, T9424) following the standard procedure: 1 µg of RNA from each sample was retrotranscribed into cDNA using the QuantiTect reverse transcription kit (Qiagen, 205313) and amplified in the presence of 5 µL of SYBR select master mix

(Thermo Fisher, 4472908) using the Quant Studio 5 Real-Time PCR System (Thermo Scientific, A28140). All the reactions were performed in a final volume of 10 µL and with a technical triplicate. Expression was calculated by normalizing Threshold Cycle (Ct) values on Glyceraldehyde 3-phosphate dehydrogenase (GAPDH) and relative to the average of the wild type (LMNA Δ8-11 +/+ Cdkn2a +/+) control samples. The primer sequences used for transcriptional analyses were the following: GAPDH: 5′-GTATGTCGTGGAGTCTACTGG-3′, 5′-TCGTGGTTCACACCCATCAC-3′; TGFβ: 5′-CAACCCAGGTCCTTCCTAAA-3′, 5′-GGAGAGCCCTGGATACCAAC-3′; Collagen 1a1: 5′-CCTCAGGGTATTGCTGGACA-3′, 5′-GAAGGACCTTGTTTGCCAGG-3′; Collagen 1a2: 5′-GGAACAAATGGGCTCACTGG-3′, 5′-CAAGTCCTCTGGCACCTGTA-3′; Collagen 3a1: 5′-CCCAACCCAGAGATCCCATT-3′, 5′-GGTCACCATTTCTCCCAGGA-3′; Fibronectin1: 5′-CCCCATTCCAGGACACTTCT-3′, 5′-AGGGTTCTTCATCAGTGCCA-3′; αSMA: 5′-CCTCTGGACGTACAACTGGT-3′, 5′-GGTAGTCGGTGAGATCTCGG-3′; αFAP: 5′-CACCTGATCGGCAATTTGTG-3′, 5′-CCCATTCTGAAGGTCGTAGATGT-3′; Connexin43: 5′-CAATTCCTCCTGCCGCAAT-3′, 5′-GCCCCATTCGATTTTGCTCT-3′.

Ecocardiography Measurements

Transthoracic echocardiography was performed on 15-day-old (P15) and 30-day-old (P30) mice using the Visual Sonic-Vevo 2100 imaging system and a MS-400 transducer, which was optimized for mice cardiovascular imaging. Before the procedure, the mice were anesthetized using 0.5–1% isoflurane according to the experimental protocol approved by the Italian Ministry of Health and kept under a hot lamp for proper thermoregulation, keeping their heartbeat at approximately 500 bpm (beat per minute). Parameters and data were obtained from M-mode recordings of at least 3 consecutive measurements along the parasternal short axis and considering the mean measures of 3 or more cardiac cycles. Data were analyzed using Vevo lab 3.2.0 software. Considering the typical pathology of EDMD, we consider the measure of fractional shortening (FS) as a significant comparison parameter that measures heart contraction, calculated as follows:

$$FS = \frac{(LVID;d - LVID;s)}{LVID;d}\ x\ 100, \qquad (1)$$

where left ventricular interior diameter during diastole is LVID;d and left ventricular diameter during systole is LVID;s. Other measurements performed are as reported in the formulae below: Equation (2): ejection fraction (EF); Equation (3): wall thickness during systole and diastole (WT;s and WT;d, respectively); Equation (4): left ventricle volume during systole and diastole (LV

Vol;s and LV Vol;d, respectively); Equation (5): left ventricle mass (LV Mass AW).

$$EF = \frac{(LV\ Vol;d - LV\ Vol;s)}{LV\ Vol;d}\ x\ 100, \quad (2)$$

$$WT;s,d = \frac{(LVAW;s,d + LVPW;s,d)}{2}, \quad (3)$$

$$LV\ Vol;s,d = \frac{7.0}{2.4 + LVID;s,d}\ x\ LVID;s,d^3, \quad (4)$$

$$LV\ Mass\ AW = ((LVID;d + LVPW;d + IVS;d)^3 - LVID;d^3)\ x\ 1.053, \quad (5)$$

where left ventricular anterior wall during systole or diastole is LVAW;s,d, left ventricular posterior wall during systole or diastole is LVPW;s,d and interventricular septum during diastole is IVS;d.

Statistics

All the data are represented using Graph Pad Prism 6. The sample size (n) for each experiment is described in the relative figure legend. All the statistical analyses were performed with parametric tests (one-way or two-way ANOVA) with Graph Pad Prism 6 (3–7 animals per group). When the datasets did not follow the normal distribution, we chose the non-parametric Kruskal–Wallis test. For Supplementary Figure S1, we evaluated the normal distribution of data with D′Agostino and Pearson, and Shapiro–Wilk tests. Statistical analysis of survival curves was performed with the Gehan–Breslow–Wilcoxon test.

Graphics

Figure 1 was generated by using a regularly licensed version of Biorender.

2.4. Results

2.4.1.Cdkn2a KO Ameliorates Life Span of Dystrophic LMNA Δ8-11 –/– Mice

We recently demonstrated that the absence of Lamin A in LMNA Δ8-11 –/– mice during postnatal growth causes aberrant transcriptional programs at the level of MuSCs, leading to defective identity [24,26]. We also reported that Cdkn2a genetic ablation restores MuSCs' properties [24]. Here, we investigated the impact of Cdkn2a KO on LMNA Δ8-11 –/– heart dysfunctions. We first monitored growth and muscle loss in mice by measuring their body weight on a daily basis (Figure S1). We found only slight differences between LMNA Δ8-11 –/– Cdkn2a+/+ and LMNA Δ8-11 –/– Cdkn2a–/– genotypes during the early stages of postnatal growth. Analyzing the number of premature deaths, we noticed that the survival rate of dystrophic LMNA Δ8-11 –/– mice rapidly decreased, being 83% at Day 20 and 57% at Day 30 of postnatal growth. On the other hand, no sudden deaths could be found in the Cdkn2a mutated background (Figure 2) and the survival rate remained at 100% until Day 30 of postnatal growth. Altogether, these data suggest that a putative deregulation of the cell cycle during late heart development in LMNA Δ8-11 –/– mice might be at the origin of sudden death by heart failure during postnatal growth.

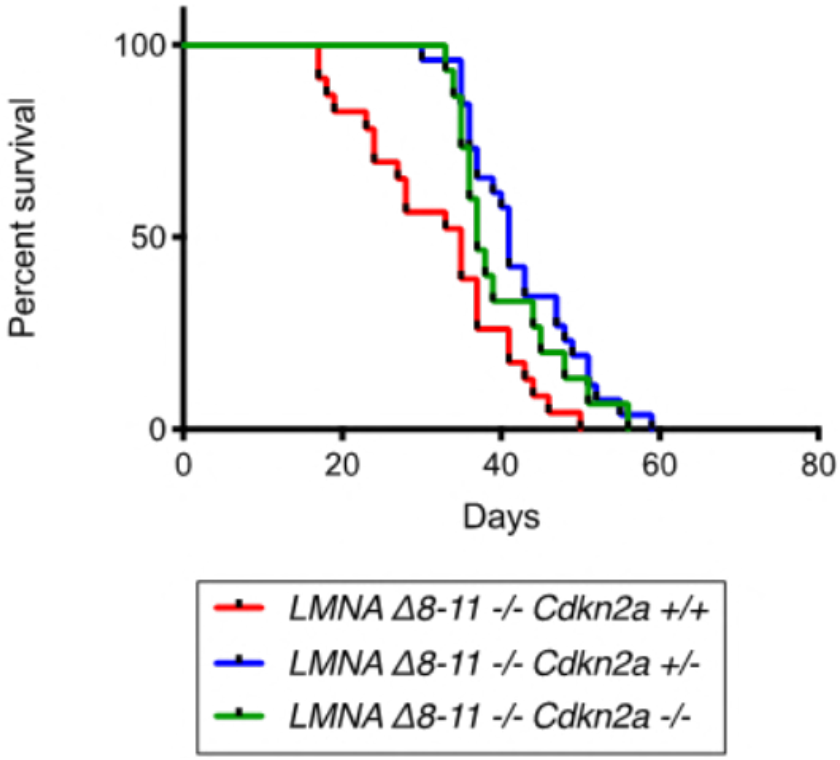

Figure 6. Survival curves of LMNA Δ8-11 –/– mice with different Cdkn2a backgrounds. Survival curves of the LMNA Δ8-11 –/– Cdkn2a +/+ (red), LMNA Δ8-11 –/– Cdkn2a +/– (blue) and LMNA Δ8-11 –/– Cdkn2a –/– (green). n = 15–26. Statistical tests were performed by the Gehan–Breslow–Wilcoxon test. p-values: LMNA Δ8-11 –/– Cdkn2a +/+ vs. LMNA Δ8-11 –/– Cdkn2a +/– *** p = 0.0004; LMNA Δ8-11 –/– Cdkn2a +/+ vs. LMNA Δ8-11 –/– Cdkn2a –/– * p = 0.025.

2.4.2.Cdkn2a KO Improves the Cardiac Function of Dystrophic LMNA Δ8-11 –/– Mice

To evaluate cardiac function in vivo, we performed trans-thoracic echocardiography. Mice were monitored at 15 days of postnatal growth, the timepoint when the skeletal muscle dystrophic symptoms started to appear, and 1 month after birth (Videos S1–

S5), when mice were proximal to death as seen by the excessive muscle loss and cardiac involvement.

We compared the measures of fractional shortening (FS), a parameter that measures contraction performance that is widely used to assess left ventricular dysfunction (LVdys) (Figure 3A,B) (see Methods). The echocardiographic analysis 15 days after birth showed slight impairment of FS in the LMNA Δ8-11 –/– background animals compared with the LMNA Δ8-11 +/+ (control groups) (Figure 3A). The average value of FS found in the two control groups was 40%, while it decreased to 35% in the LMNA Δ8-11 –/– mice. The contraction deficit was also confirmed by measurement of the ejection fraction (EF)(Figure S2), a measure of the pumping efficiency of the heartbeat. At 30 days after birth, both FS and EF parameters showed a further decrease in LMNA Δ8-11 –/– Cdkn2a +/+ animals, dropping to 24% (Figures 3B,C and S2). On the other hand, the average value of FS was relatively compensated in LMNA Δ8-11 –/– Cdkn2a +/– and LMNA Δ8-11 –/– Cdkn2a –/– mice, resulting in a less drastic cardiac phenotype (Figures 3B,C and S2). Other M-mode measurements performed on 30-day-old mice (Videos S1–S5) showed (i) a decrease in the wall thickness in systole in dystrophic LMNA Δ8-11 –/– Cdkn2a +/+ mice partially recovered in Cdkn2a KO backgrounds (Figure S2), (ii) a reduction of the left ventricular volume in diastole and (iii) a significant drop of the Left Ventricular (LV) mass in a LMNA Δ8-11 –/– background not recovered in the absence of the Cdkn2a locus (Figure S2). These

data are compatible with the smaller dimensions and weight of LMNA Δ8-11 –/– mice compared with the LMNA wild-type (wt) background. Taken together, these findings suggest the coexistence of multiple heart defects in mice lacking the LMNA gene. Hearts from LMNA Δ8-11 –/– Cdkn2a +/– and LMNA Δ8-11 –/– Cdkn2a –/– double mutants, despite presenting the same morphological defects as dystrophic LMNA Δ8-11 –/– Cdkn2a +/+ mice, display partially restored functionality.

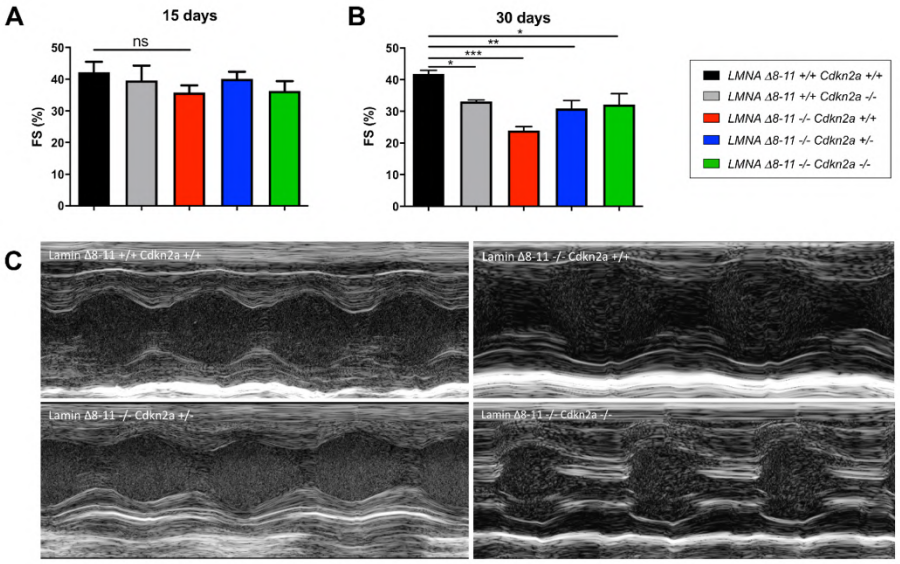

Figure 7. Echocardiographic results of LMNA Δ8-11 –/– mice with different Cdkn2a backgrounds. (A) Fractional shortening measures obtained at 15 days. n = 3–6. (B) Fractional shortening measures obtained at 1 month. n = 3–5. (C) Representative images of indicated genotypes of M-mode acquisitions in 1-month-old mice. Error bars represent ± Stanbdard Error of the Mean (SEM). Statistical tests were performed with one-way ANOVA with multiple comparisons. * $p < 0.05$; ** $p < 0.01$; *** $p < 0.001$. ns, not significant.

2.4.3.LMNA Δ8-11 –/– Mice Accumulate Fibrosis during Postnatal Heart Development

Myocardial fibrosis is the most common feature of dystrophic hearts [67] and one of the leading causes of any later cardiac pathology [68]. Considering the key Cdkn2a role in cell cycle control, we decided to test the progression of fibrotic infiltration by studying the transcript profile of the whole hearts of newborn mice, when cardiomyocytes are still able to replicate, and 30-day-old mice, when cardiomyocytes are entirely differentiated.

We tested our samples for the most common stress and fibrosis markers known in the literature: Tgfβ, a cytokine that regulates fibroblast activation during inflammation [69]; Fibronectin 1, a protein necessary for proper collagen deposition in the heart [70]; Collagen 1a1, Collagen 1a2 and Collagen 3a1, three different subunits of collagen that confer more or less elasticity on muscle tissue [71]; and α-SMA and α-FAP, both markers of fibroblast activation [72]. We highlighted a peculiar fibrosis dynamic in which LMNA Δ8-11 –/– Cdkn2a +/+ mice at 0 days presented a slightly, non-significant increase in the expression of fibrotic markers (Figure 4A), which was rescued in Cdkn2a +/– or –/– mutated backgrounds. On the other hand, in 1-month-old animals, LMNA Δ8-11 –/– Cdkn2a +/+ exhibited a trend of downregulation of all fibrotic-related genes, which was recovered in the Cdkn2a KO backgrounds. Unexpectedly, the histological analysis revealed a different picture with an increase in both perivascular and interstitial fibrosis in 1-month-old dystrophic LMNA Δ8-11 –/– Cdkn2a +/+ mice (Figure 4B). The percentage of fibrotic area was reduced and was rescued only in the

complete absence of the Cdkn2a locus. The accumulated fibrosis observed in 1-month-old LMNA Δ8-11 –/– Cdkn2a +/+ mice could result from the initial upregulation seen at birth (Figure 4A).

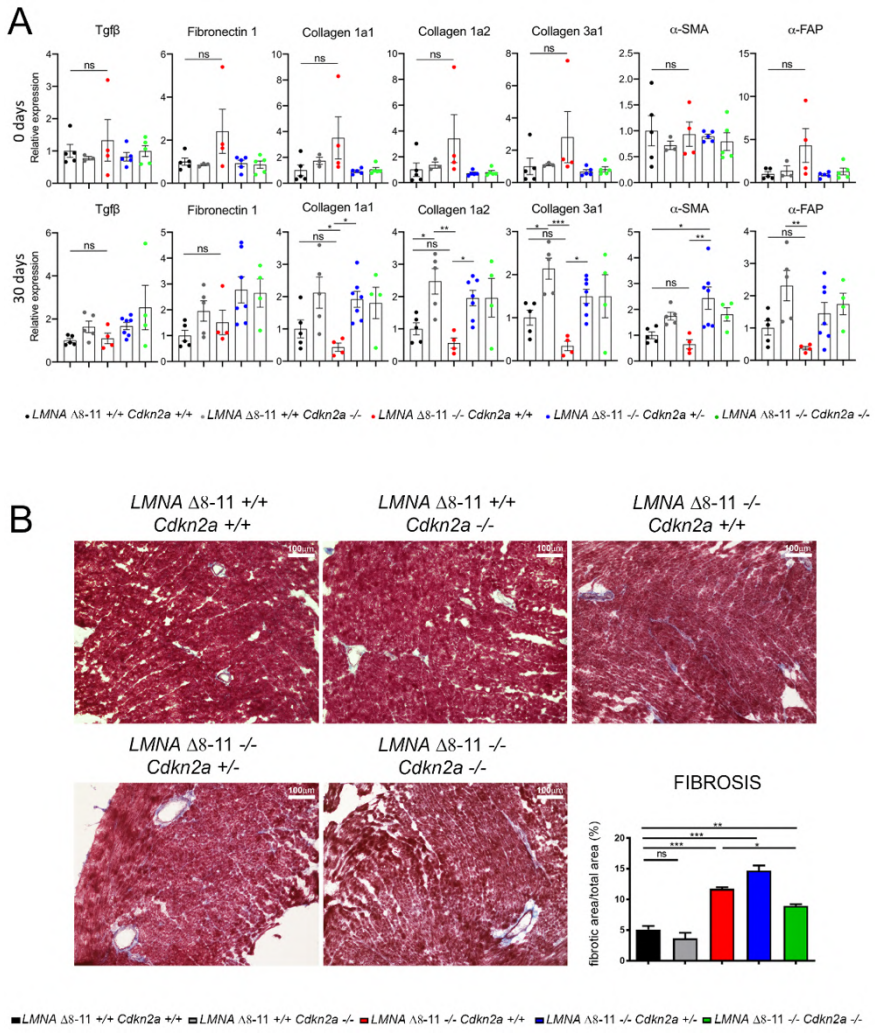

Figure 8. Evaluation of heart fibrosis. (A) Quantitative real-time analysis of fibrosis- and stress condition-related genes in the heart. The upper line represents the data obtained from newborn mice (n = 3–5); the lower line represents the data obtained from 1-month-old mice (n=4–7). (B) Representative images of Masson′s trichrome staining on 1-month-old mice. The graph illustrates the fibrotic index calculated as fibrotic area/total area × 100. Scale bar represents 100 µm. Error bars represent ± SEM.

Statistical tests were performed with one-way ANOVA with multiple comparisons. *p < 0.05; **p < 0.01; ***p < 0.001. ns, not significant.

Alternatively, but not mutually exclusively, LMNA Δ8-11 –/– dysfunctional hearts may activate, at the transcriptional level, some compensatory repressive mechanisms to counteract the deposition of fibrosis.

2.4.4.Alteration of LMNA Δ8-11 –/– Cardiac Tissue is Partially Recovered in a Cdkn2a KO Background

To further analyze the molecular pathways altered in LMNA Δ8-11 –/– mice and possibly recovered in the absence of Cdkn2a, we performed immunofluorescence staining. We first examined the number of α-SMA- (smooth muscle actin-) and vWF- (von Willebrand factor-) positive vessels and the capillary density, generally involved in the amount of oxygen and nutrients that support the repair process of the damaged tissue. We did not find significant differences between wt and LMNA Δ8-11 –/– mice (Figure 5A,B), even though we detected a slight decrease in capillary density in the dystrophic LMNA Δ8-11 –/– mice. These data corroborate previous reports showing that EDMD dystrophy is not accompanied by tissue degeneration [73]. Delocalization of CX43, with consequent alteration of heart contractile function, was observed in cardiomyopathies of multiple origin [74, 75]. Thus, we decided to monitor the distribution of Connexin43 (CX43) on the fibers. In healthy hearts, this protein preferentially

localizes at intercalated discs between adjacent cardiomyocytes, where it constitutes the gap junctions, essential for the propagation of action potentials and maintenance of the correct heartbeat [76]. Together with gap junctions, intercalated discs also host adheren junctions, enabling force transmission across the sarcolemma, which are easily recognizable by their principal protein component N-cadherin [77]. Although we did not find significant transcriptional differences in the CX43 gene across distinct genotypes (Figure S3A), we observed a general increase in CX43 staining in the LMNA Δ8-11 –/– mice (Figure S3B), suggesting an alteration of post-transcriptional or post-translational regulation of protein levels in the absence of Lamin A. Furthermore, we observed a slight decrease in the proportion of CX43 localizing at N-cadherin-positive intercalated discs in LMNA Δ8-11 –/– mice, which was partially recovered upon ablation of the Cdkn2a locus (Figure 6A,B).

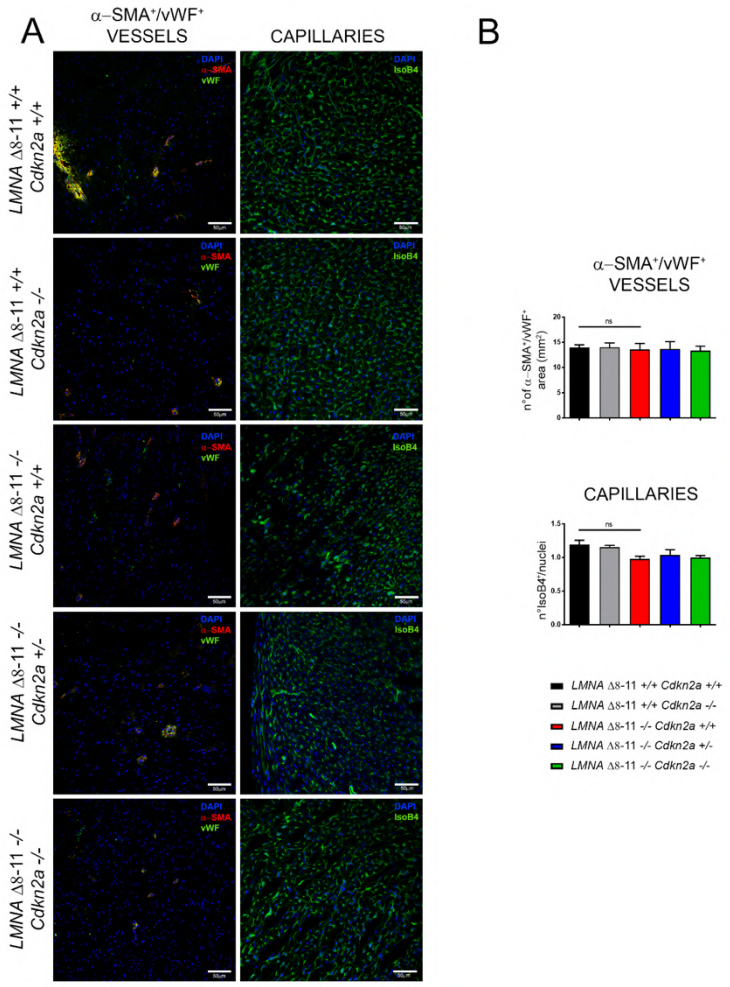

Figure 9. Histological analysis on heart sections. (A) Representative confocal images for smooth muscle actin- (α-SMA-) and von Willebrand factor- (vWF-) positive vessels (red and green; left panels) and isolectin B4-positive capillaries (green; right panels) in 1-month-old mice. Nuclei were counterstained with DAPI. The scale bar represents 50 µm. (B) The graphs show the ratio of α-SMA- and vWF-positive vessels on the total area (mm^2) (upper panel)(n = 4–5) and capillary density as the number of isolectin B4-positive capillaries divided by the number of nuclei (lower panel)(n = 3–5). Error bars represent ±SEM. Statistical tests were performed with one-way ANOVA with multiple comparisons. ns, not significant.

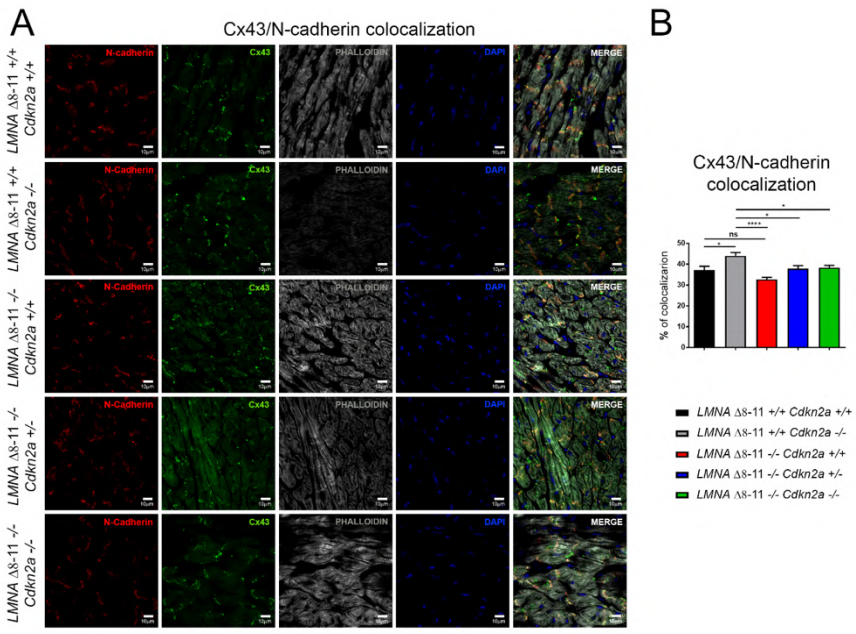

Figure 10. Histological analysis of heart sections on 1-month-old mice. (A) Representative confocal images for N-Cadherin-positive intercalated discs (IDs) (red; left panels), transmembrane gap junction Connexin43 (green; middle panels) and the F-actin cardiomyocyte cytoskeleton (White; right panels). Nuclei were counterstained with DAPI. The scale bar represents 10 µm. (B) Graph showing the proportion of Connexin43 localized at IDs. Error bars represent ±SEM. n = 4–5. Statistical analysis was performed with one-way ANOVA with multiple comparisons. * $p < 0.05$; *** $p < 0.001$. ns, not significant.

Finally, we quantified the apoptotic rate of cardiomyocytes by assessing the presence of fragmented DNA with a TUNEL assay. All LMNA Δ8-11 –/– Cdkn2a +/+ mice showed a significantly higher apoptotic index compared with healthy littermates, confirming a premature and aberrant blockage in the cell cycle (Figure 7A,B). The absence of one or two alleles of Cdkn2a is sufficient to significantly reduce the number of apoptotic cardiomyocytes (Figure 7A,B). These results were further confirmed by staining with Ki67, a marker of active proliferation. In fact, the quantification of Ki67 staining showed a substantial

decrease in cardiomyocyte proliferation in dystrophic LMNA Δ8-11 –/– hearts and recovery in the Cdkn2a KO background (Figure 7A,B). Importantly, LMNA Δ8-11+/+ Cdkn2a –/– mice did not exhibit an increase in cell proliferation, suggesting that in a non-dystrophic condition, the lack of Cdkn2a function does not necessarily activate cell proliferation. Taken together, these results reveal that Cdkn2a plays an essential role in the regulation of cardiomyocyte fitness in the heart, and its ablation in LMNA Δ8-11 –/– dystrophic mice is enough to restore the physiological number of cardiomyocytes.

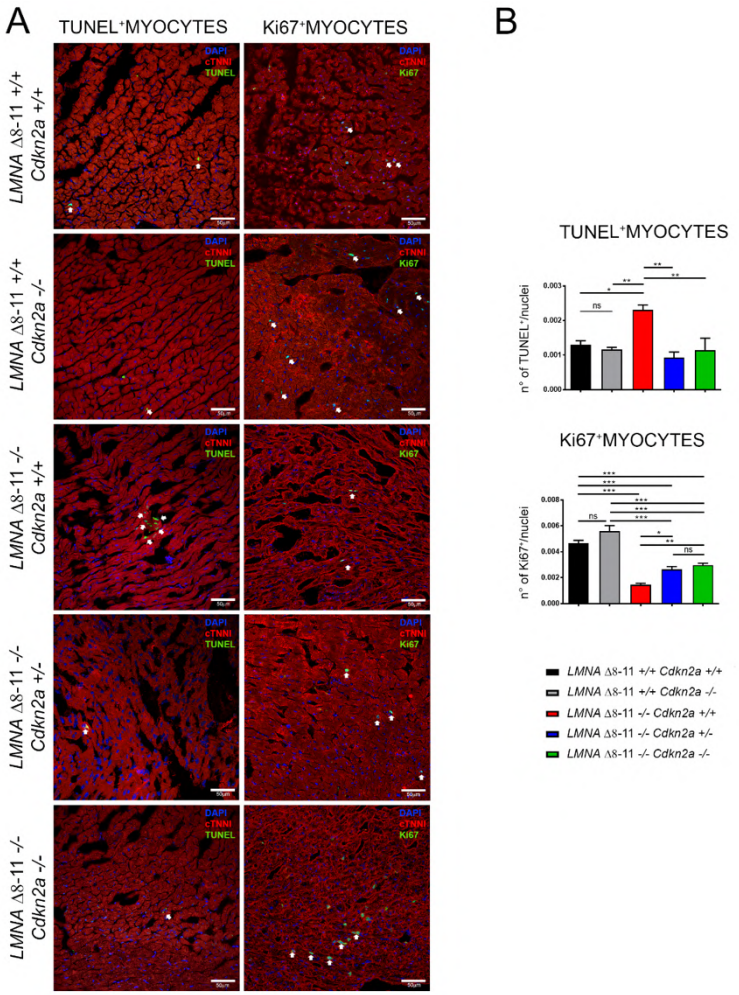

Figure 11. Apoptotic and proliferation assay on heart sections. (A) Confocal images of cTNNi-positive cardiomyocytes (red) and apoptotic (green; left panels) or proliferative nuclei stained for Ki67 (Green; right panels). Nuclei were counterstained with DAPI. The scale bar represents 50 µm. (B) The graphs show the ratio between TUNEL (upper panel) or Ki67-positive (lower panel) cardiomyocytes and total nuclei. Error bars represent ±SEM. n = 3–5. Statistical tests were performed with one-way ANOVA with multiple comparisons. * $p < 0.05$; ** $p < 0.01$; *** $p < 0.001$. ns, not significant.

2.5. Discussion

Shortly after birth, cardiomyocytes enter a cell proliferation block. This event, together with the lack of a resident stem cell population in the heart, determines the low regeneration capability of this organ. Cardiac regenerative strategies, from the induction of cardiomyocyte proliferation to cardiac cell reprogramming and transplantation, represent a vast field of study aimed at recovering myocardial performance [78–80].

In recent years, several pieces of evidence have pointed out the increased capability of Cdkn2a KO cells to regenerate after injury [20–23]. Strikingly, these observations were extended to cardiac contractile cells, where the inactivation of p16INK4a and ARF increased the capability of the whole heart in vivo and cardiomyocytes in vitro to regenerate or proliferate after ischemia, showing a functional recovery after injury, a smaller scars size and enhanced myocardial repair [21,22,81].

Emery–Dreifuss muscular dystrophy (EDMD) is a syndrome caused by Lamin A mutations. Most patients present a significant heart pathology, mainly caused by electrical conduction defects [73]. It is estimated that 10% of EDMD patients die of sudden heart failure with no prior cardiac symptoms, turning the study of asymptomatic hearth defects into an unmet clinical need [65,82]. The penetrance and expressivity of DCM-associated cardiac electrophysiological defects show both inter- and intra-familial variability, suggesting an involvement of the individual epigenetic

background in the severity of the disease [44,73,83–85]. We recently demonstrated that Lamin A haploinsufficiency causes epigenetic transcriptional aberrancies, leading to a dysfunctional muscle stem cell niche [24,26]. As part of this work, we report that Cdkn2a genetic ablation alleviates Lamin A-dependent skeletal muscular dystrophy [24]. Here we show that before the 30th day of life, no sudden deaths were registered in LMNA Δ8-11 –/– Cdkn2a–/– mice (Figure 2). These data, supported by immunohistochemical analyses showing aberrant proliferation and apoptotic death in dystrophic hearts (Figure 7), suggest that a deregulated cell cycle in late heart development (both in pre- and postnatal phases) could culminate in sudden heart failure.

The heart′s capability to regenerate and substitute cardiomyocytes in adulthood after any kind of injury has long been debated, but a univocal truth has not been reached yet. Different studies have proposed several molecular mechanisms that cardiomyocytes could undertake to re-enter the replicative cell cycle but have never demonstrated heart regeneration in physiological conditions [78–80].

It is known that during development, there is a phase known as hyperplastic growth [86,87], when cardiomyocytes increase in number, then, during hypertrophic growth, only 0.5–2% of cardiomyocytes can replicate, while the others grow only in dimension. In mice, after the very first heartbeat at E7.5 (embryonic development Day 7.5), the precursors of

cardiomyocytes actively replicate until Day E11.5 and, at 12 days after birth, stop proliferating [87] (Table 1).

Table 1. Key characteristics of human and mouse hearts.

	Human	Mouse
First heartbeat	3 weeks	E7.5
Four chambers visible	1.5 months	E9.5
Decline in proliferation	2 months	E11.5
Lamin A/C expression	Not addressed	E12.5
Stop proliferation	1 week after birth	12 days after birth

The role of Lamin A during heart development has been rarely addressed, as, for a long time, it has been thought that Lamin A was expressed only after birth. Lamin A expression in prenatal heart development at E12.5 was discovered only in 2011 [88]. Thus, reasonably, Cdkn2a defects in Lamin dystrophy will manifest between E12.5, when LMNA starts to be expressed, and 12 days after birth, when cardiomyocyte proliferation stops. We believe that this time window is fundamental for physiological heart development, and lack of Lamin A, causing a premature block in the cell cycle, does not allow the complete maturation of the heart.

Although the abnormal proliferation of fibroblasts in the heart is described as pathological when associated with muscular dystrophy or myocardial infarction, reparative fibrosis is an essential early compensatory mechanism to preserve the structural heart integrity and to regulate tissue stiffness [89]. In

physiological conditions, the presence of fibroblasts in the cardiac tissue is required to coordinate the electrical stimulation of cardiomyocytes [90–92]. Nevertheless, the excessive accumulation of interstitial fibrosis generates a barrier between cardiomyocytes, impairing normal heart electrical communication.

The role of Cdkn2a locus in heart myofibroblasts regulation is under debate, with findings indicating that both Cdkn2 haploinsufficiency and overexpression can result in induction of fibrosis [93,94]. This indicates that fine-tuned regulation of the Cdkn2a locus is a key factor in determining the right amount of cardiac myofibroblasts. In dystrophic LMNA Δ8-11 –/– Cdkn2a +/+ mice, we found an accumulation of perivascular and interstitial fibrosis accompanied by an unexpected transcriptional downregulation of fibrosis-related pathways (Figure 4), suggesting the presence of counteracting mechanisms participating in fibrosis activation.

2.6. Conclusions

According to the World Health Organization (WHO), cardiovascular diseases are the leading cause of death globally. The discovery of new molecular and epigenetic mechanisms at the basis of different cardiac pathologies may give an advantage to the development of new therapies. Even if related to a rare

disease such as EDMD, any further information on dilated cardiomyopathy may be eventually useful for new promising treatments for diseases with similar progression. Although further studies will be needed to translate these results into clinical practice, our findings, revealing in dystrophic LMNA Δ8-11 –/– mice the role of the cell cycle in the postnatal heart development might contribute to the identification of new pathways that could be used for the classification of individual risk for sudden cardiac death.

Supplementary Materials: The following are available online at www.mdpi.com/xxx/s1. Figure S1, S2, S3: Supplementary data, Figure S2:, Figure S3:, Video S1: supplementary video 1, Video S2: supplementary video 2, Video S3: supplementary video 3, Video S4: supplementary video 4, Video S5: supplementary video 5.

Author Contributions: Conceptualization, C.L. and R.R.; methodology, G.P., M.M., P.G.M., A.B., F.L., P.S. and C.B.; validation, G.P., M.M. and C.B. formal analysis, G.P., M.M., A.B. and F.L.; investigation, G.P., M.M., P.G.M., A.B., F.L., P.S. and C.B; writing—original draft preparation, C.L. and G.P.; writing—review and editing, all authors; supervision, C.L., R.R.; project administration, C.L.; funding acquisition, C.L. We are thankful to Roche Foundation for the support to M.M. All authors have read and agreed to the published version of the manuscript.

Funding: This research was funded by the My First AIRC Grant (MFAG) (n. 18535), AFM-Telethon (No.. 21030) and Fondazione Cariplo (No.. 2017-0649) to C.L.

Institutional Review Board Statement:
All the experimental procedures were performed under the ethical approval of the Italian Ministry of Health and the Institutional Animal Care and Use Committee (authorization No. 83/2019-PR).

Acknowledgments: We thank the members of the laboratory for their precious support and constructive discussions. We are grateful to Chiara Cordiglieri and Alessandra Fasciani from the Isttuto Nazionale Genetica Molecolare (INGM) Imaging Facility for their assistance in image acquisition and in the setting up of plugins for co-localization analysis. We thank Laura Perani and the Preclinical Imaging facility of San Raffaele Hospital for the help with the echographer. We thank Eva Pinatel for the help in drawing Figure 1.

Conflicts of Interest: The authors declare no conflict of interest.

2.7. References to Chapter 2

1. Serra, S.; Chetty, R. p16. *J. Clin. Pathol.* **2018**, *71*, 853–858, doi:10.1136/jclinpath-2018-205216.
2. Kim, W.Y.; Sharpless, N.E. The Regulation of INK4/ARF in Cancer and Aging. *Cell* **2006**, *127*, 265–275, doi:10.1016/j.cell.2006.10.003.
3. Romagosa, C.; Simonetti, S.; López-Vicente, L.; Mazo, A.; Lleonart, M.E.; Castellvi, J.; Ramon y Cajal, S. p16Ink4a overexpression in cancer: A tumor suppressor gene associated with senescence and high-grade tumors. *Oncogene* **2011**, *30*, 2087–2097, doi:10.1038/onc.2010.614.
4. Li, J.; Poi, M.J.; Tsai, M.-D. Regulatory Mechanisms of Tumor Suppressor P16 INK4A and Their Relevance to Cancer. *Biochemistry* **2011**, *50*, 5566–5582, doi:10.1021/bi200642e.
5. Sharpless, N.E.; DePinho, R.A. The INK4A/ARF locus and its two gene products. *Curr. Opin. Genet. Dev.* **1999**, *9*, 22–30, doi:10.1016/S0959-437X(99)80004-5.
6. Stein, G.H.; Drullinger, L.F.; Soulard, A.; Dulić, V. Differential Roles for Cyclin-Dependent Kinase Inhibitors p21 and p16 in the Mechanisms of Senescence and Differentiation in Human Fibroblasts. *Mol. Cell. Biol.* **1999**, *19*, 2109–2117, doi:10.1128/mcb.19.3.2109.
7. Fontana, R.; Ranieri, M.; La Mantia, G.; Vivo, M. Dual Role of the Alternative Reading Frame ARF Protein in Cancer. *Biomolecules* **2019**, *9*, 87, doi:10.3390/biom9030087.
8. Molofsky, A.V.; He, S.; Bydon, M.; Morrison, S.J.; Pardal, R. Bmi-1 promotes neural stem cell self-renewal and neural development but not mouse growth and survival by repressing the p16Ink4a and p19Arf senescence pathways. *Genes Dev.* **2005**, *19*, 1432–1437, doi:10.1101/gad.1299505.
9. Heenan, P.R.; Wang, X.; Gooding, A.R.; Cech, T.R.; Perkins, T.T. Bending and looping of long DNA by Polycomb repressive complex 2 revealed by AFM imaging in liquid. *Nucleic Acids Res.* **2020**, *48*, 2969–2981, doi:10.1093/nar/gkaa073.
10. Ito, T.; Teo, Y.V.; Evans, S.A.; Neretti, N.; Sedivy, J.M. Regulation of Cellular Senescence by Polycomb Chromatin Modifiers through Distinct DNA Damage- and Histone Methylation-Dependent Pathways. *Cell Rep.* **2018**, *22*, 3480–3492, doi:10.1016/j.celrep.2018.03.002.
11. Lanzuolo, C.; Roure, V.; Dekker, J.; Bantignies, F.; Orlando, V. Polycomb response elements mediate the formation of chromosome higher-order structures in the bithorax complex. *Nat. Cell Biol.* **2007**, *9*, 1167–1174, doi:10.1038/ncb1637.
12. Gonzalez, S.; Serrano, M. A New Mechanism of Inactivation of the INK4/ARF Locus. *Cell Cycle* **2006**, *5*, 1382–1384, doi:10.1111/j.1440-1746.2006.04137.x.
13. Minami, R.; Muta, K.; Umemura, T.; Motomura, S.; Abe, Y.; Nishimura, J.; Nawata, H. p16INK4a induces differentiation and apoptosis in erythroid lineage cells. *Exp. Hematol.* **2003**, *31*, 355–362, doi:10.1016/S0301-472X(03)00040-7.
14. Rayess, H.; Wang, M.B.; Srivatsan, E.S. Cellular senescence and tumor suppressor gene p16. *Int. J. Cancer* **2012**, *130*, 1715–1725, doi:10.1002/ijc.27316.
15. Sherr, C.J. Ink4-Arf locus in cancer and aging. *Wiley Interdiscip. Rev. Dev. Biol.* **2012**, *1*, 731–741, doi:10.1002/wdev.40.
16. Gan, Q.; Huang, J.; Zhou, R.; Niu, J.; Zhu, X.; Wang, J.; Zhang, Z.; Tong, T. PPAR accelerates cellular senescence by inducing p16INK4 expression in human diploid fibroblasts. *J. Cell Sci.* **2008**, *121*, 2235–2245, doi:10.1242/jcs.026633.
17. Bengal, E.; Perdiguero, E.; Serrano, A.L.; Muñoz-Cánoves, P. Rejuvenating stem cells to restore muscle regeneration in aging. *F1000Research* **2017**, *6*, 1–10, doi:10.12688/f1000research.9846.1.

18. Sousa-Victor, P.; Gutarra, S.; García-Prat, L.; Rodriguez-Ubreva, J.; Ortet, L.; Ruiz-Bonilla, V.; Jardí, M.; Ballestar, E.; González, S.; Serrano, A.L.; et al. Geriatric muscle stem cells switch reversible quiescence into senescence. *Nature* **2014**, *506*, 316–321, doi:10.1038/nature13013.
19. Carlson, M.E.; Hsu, M.; Conboy, I.M. Imbalance between pSmad3 and Notch induces CDK inhibitors in old muscle stem cells. *Nature* **2008**, *454*, 528–532, doi:10.1038/nature07034.
20. Cosgrove, B.D.; Gilbert, P.M.; Porpiglia, E.; Mourkioti, F.; Lee, S.P.; Corbel, S.Y.; Llewellyn, M.E.; Delp, S.L.; Blau, H.M. Rejuvenation of the muscle stem cell population restores strength to injured aged muscles. *Nat. Med.* **2014**, *20*, 255–264, doi:10.1038/nm.3464.
21. Hatzistergos, K.E.; Williams, A.R.; Dykxhoorn, D.; Bellio, M.A.; Yu, W.; Hare, J.M. Tumor Suppressors RB1 and CDKN2a Cooperatively Regulate Cell-Cycle Progression and Differentiation During Cardiomyocyte Development and Repair. *Circ. Res.* **2019**, *124*, 1184–1197, doi:10.1161/circresaha.118.314063.
22. An, S.; Chen, Y.; Gao, C.; Qin, B.; Du, X.; Meng, F.; Qi, Y. Inactivation of INK4a and ARF induces myocardial proliferation and improves cardiac repair following ischemia.reperfusion. *Mol. Med. Rep.* **2015**, *12*, 5911–5916, doi:10.3892/mmr.2015.4133.
23. Lewis, J.L.; Chinswangwatanakul, W.; Zheng, B.; Marley, S.B.; Nguyen, D.X.; Cross, N.C.P.; Banerji, L.; Glassford, J.; Thomas, N.S.B.; Goldman, J.M.; et al. The influence of INK4 proteins on growth and self-renewal kinetics of hematopoietic progenitor cells. *Blood* **2001**, *97*, 2604–2610, doi:10.1182/blood.V97.9.2604.
24. Bianchi, A.; Mozzetta, C.; Pegoli, G.; Lucini, F.; Valsoni, S.; Rosti, V.; Petrini, C.; Cortesi, A.; Gregoretti, F.; Antonelli, L.; et al. Dysfunctional polycomb transcriptional repression contributes to lamin A/C–dependent muscular dystrophy. *J. Clin. Investig.* **2020**, *130*, 2408–2421, doi:10.1172/JCI128161.
25. Pajcini, K.V.; Corbel, S.Y.; Sage, J.; Pomerantz, J.H.; Blau, H.M. Transient inactivation of Rb and ARF yields regenerative cells from postmitotic mammalian muscle. *Cell Stem Cell* **2010**, *7*, 198–213, doi:10.1016/j.stem.2010.05.022.
26. Pegoli, G.; Lucini, F.; Mozzetta, C.; Lanzuolo, C. Single myofiber isolation and culture from a murine model of emery-dreifuss muscular dystrophy in early post-natal development. *J. Vis. Exp.* **2020**, doi:10.3791/61516.
27. Kandert, S.; Wehnert, M.; Müller, C.R.; Buendia, B.; Dabauvalle, M.-C. Impaired nuclear functions lead to increased senescence and inefficient differentiation in human myoblasts with a dominant p.R545C mutation in the LMNA gene. *Eur. J. Cell Biol.* **2009**, *88*, 593–608, doi:10.1016/j.ejcb.2009.06.002.
28. Cohen, T.V.; Gnocchi, V.F.; Cohen, J.E.; Aditi, P.; Liu, H.; Ellis, J.A.; Foisner, R.; Stewart, C.L.; Zammit, P.S.; Partridge, T.A. Defective skeletal muscle growth in lamin A/C-deficient mice is rescued by loss of lap2α. *Hum. Mol. Genet.* **2013**, *22*, 2852–2869, doi:10.1093/hmg/ddt135.
29. Bonne, G.; Quijano-roy, S. Emery-Dreifuss Muscular Dystrophy, Laminopathies, and Other Nuclear Envelopathies. *Handb. Clin. Neurol.* **2013**, *113*, 1367–1376, doi:10.1016/B978-0-444-59565-2.00007-1.
30. Bonne, G.; Di Barletta, M.R.; Varnous, S.; Bécane, H.-M.; Hammouda, E.-H.; Merlini, L.; Muntoni, F.; Greenberg, C.R.; Gary, F.; Urtizberea, J.-A.; et al. Mutations in the gene encoding lamin A/C cause autosomal dominant Emery-Dreifuss muscular dystrophy. *Nat. Genet.* **1999**, *21*, 285–288, doi:10.1038/6799.
31. Bianchi, A.; Manti, P.G.; Lucini, F.; Lanzuolo, C. Mechanotransduction, nuclear architecture and epigenetics in Emery Dreifuss Muscular Dystrophy: Tous pour un, un pour tous. *Nucleus* **2018**, *9*, 276–290, doi:10.1080/19491034.2018.1460044.
32. Cesarini, E.; Mozzetta, C.; Marullo, F.; Gregoretti, F.; Gargiulo, A.; Columbaro, M.; Cortesi, A.; Antonelli, L.; Di Pelino, S.; Squarzoni, S.; et al. Lamin A/C sustains

PcG protein architecture, maintaining transcriptional repression at target genes. *J. Cell Biol.* **2015**, *211*, 533–551, doi:10.1083/jcb.201504035.
33. Marullo, F.; Cesarini, E.; Antonelli, L.; Gregoretti, F.; Oliva, G.; Lanzuolo, C. Nucleoplasmic Lamin A/C and Polycomb group of proteins: An evolutionarily conserved interplay. *Nucleus* **2016**, *7*, 130–111, doi:10.1080/19491034.2016.1157675.
34. Salvarani, N.; Crasto, S.; Miragoli, M.; Bertero, A.; Paulis, M.; Kunderfranco, P.; Serio, S.; Forni, A.; Lucarelli, C.; Dal Ferro, M.; et al. The K219T-Lamin mutation induces conduction defects through epigenetic inhibition of SCN5A in human cardiac laminopathy. *Nat. Commun.* **2019**, *10*, 1–16, doi:10.1038/s41467-019-09929-w.
35. Sebestyén, E.; Marullo, F.; Lucini, F.; Petrini, C.; Bianchi, A.; Valsoni, S.; Olivieri, I.; Antonelli, L.; Gregoretti, F.; Oliva, G.; et al. SAMMY-seq reveals early alteration of heterochromatin and deregulation of bivalent genes in Hutchinson-Gilford Progeria Syndrome. *Nat. Commun.* **2020**, *11*, 6274, doi:10.1038/s41467-020-20048-9.
36. Lu, J.T.; Muchir, A.; Nagy, P.L.; Worman, H.J. LMNA cardiomyopathy: Cell biology and genetics meet clinical medicine. *Dis. Model. Mech.* **2011**, *4*, 562–568, doi:10.1242/dmm.006346.
37. Becane, H.-M.; Bonne, G.; Varnous, S.; Muchir, A.; Ortega, V.; Hammouda, E.H.; Urtizberea, J.-A.; Lavergne, T.; Fardeau, M.; Eymard, B.; et al. High Incidence of Sudden Death with Conduction System and Myocardial Disease Due to Lamins A and C Gene Mutation. *Pacing Clin. Electrophysiol.* **2000**, *23*, 1661–1666, doi:10.1046/j.1460-9592.2000.01661.x.
38. KARKKAINEN, S. A novel mutation, Ser143Pro, in the lamin A/C gene is common in finnish patients with familial dilated cardiomyopathy. *Eur. Heart J.* **2004**, *25*, 885–893, doi:10.1016/j.ehj.2004.01.020.
39. De Backer, J.; Van Beeumen, K.; Loeys, B.; Duytschaever, M. Expanding the phenotype of sudden cardiac death—An unusual presentation of a family with a Lamin A/C mutation. *Int. J. Cardiol.* **2010**, *138*, 97–99, doi:10.1016/j.ijcard.2008.06.008.
40. van der Kooi, A.J.; Ledderhof, T.M.; DeVoogt, W.G.; Res, J.C.J.; Bouwsma, G.; Troost, D.; Busch, H.F.M.; Becker, A.E.; DeVisser, M. A newly recognized autosomal dominant limb girdle muscular dystrophy with cardiac involvement. *Ann. Neurol.* **1996**, *39*, 636–642, doi:10.1002/ana.410390513.
41. Van Der Kooi, A.J.; Van Meegen, M.; Ledderhof, T.M.; McNally, E.M.; De Visser, M.; Bolhuis, P.A. Genetic localization of a newly recognized autosomal dominant limb- girdle muscular dystrophy with cardiac involvement (LGMD1B) to chromosome 1q11-21. *Am. J. Hum. Genet.* **1997**, *60*, 891–895.
42. Rudnik-Schöneborn, S.; Botzenhart, E.; Eggermann, T.; Senderek, J.; Schoser, B.G.H.; Schröder, R.; Wehnert, M.; Wirth, B.; Zerres, K. Mutations of the LMNA gene can mimic autosomal dominant proximal spinal muscular atrophy. *Neurogenetics* **2007**, *8*, 137–142, doi:10.1007/s10048-006-0070-0.
43. Boriani, G.; Wollmann, C.; Biffi, M.; Kuhl, M.; Schuchert, A.; Sperzel, J.; Stiller, S.; Gasparini, G.; Bocker, D. Evaluation of a Dual Chamber Implantable Cardioverter Defibrillator for the Treatment of Atrial and Ventricular Arrhythmias. *Pacing Clin. Electrophysiol.* **2003**, *26*, 461–465, doi:10.1046/j.1460-9592.2003.00072.x.
44. Sanna, T.; Dello Russo, A.; Toniolo, D.; Vytopil, M.; Pelargonio, G.; De Martino, G.; Ricci, E.; Silvestri, G.; Giglio, V.; Messano, L.; et al. Cardiac features of Emery-Dreifuss muscular dystrophy caused by lamin A/C gene mutations. *Eur. Heart J.* **2003**, doi:10.1016/j.ehj.2003.09.020.
45. Sakata, K.; Shimizu, M.; Ino, H.; Yamaguchi, M.; Terai, H.; Fujino, N.; Hayashi, K.; Kaneda, T.; Inoue, M.; Oda, Y.; et al. High incidence of sudden cardiac death with conduction disturbances and atrial cardiomyopathy caused by a nonsense

mutation in the STA gene. *Circulation* **2005**, *111*, 3352–3358, doi:10.1161/circulationaha.104.527184.
46. Astejada, M.N.; Goto, K.; Nagano, A.; Ura, S.; Noguchi, S.; Nonaka, I.; Nishino, I.; Hayashi, Y.K. Emerinopathy and laminopathy clinical, pathological and molecular features of muscular dystrophy with nuclear envelopathy in Japan. *Acta Myol.* **2007**, *26*, 159–164.
47. Carboni, N.; Mura, M.; Mercuri, E.; Marrosu, G.; Manzi, R.C.; Cocco, E.; Nissardi, V.; Isola, F.; Mateddu, A.; Solla, E.; et al. Cardiac and muscle imaging findings in a family with X-linked Emery–Dreifuss muscular dystrophy. *Neuromuscul. Disord.* **2012**, *22*, 152–158, doi:10.1016/j.nmd.2011.09.001.
48. Bonne, G.; Mercuri, E.; Muchir, A.; Urtizberea, A.; Becane, H.M.; Recan, D.; Merlini, L.; Wehnert, M.; Boor, R.; Reuner, U.; et al. Clinical and molecular genetic spectrum of autosomal dominant Emery-Dreifuss muscular dystrophy due to mutations of the lamin A/C gene. *Ann. Neurol.* **2000**, *48*, 170–180.
49. Arimura, T.; Helbling-Leclerc, A.; Massart, C.; Varnous, S.; Niel, F.; Lacène, E.; Fromes, Y.; Toussaint, M.; Mura, A.M.; Kelle, D.I.; et al. Mouse model carrying H222P-Lmna mutation develops muscular dystrophy and dilated cardiomyopathy similar to human striated muscle laminopathies. *Hum. Mol. Genet.* **2005**, *14*, 155–169, doi:10.1093/hmg/ddi017.
50. Vignier, N.; Mougenot, N.; Bonne, G.; Muchir, A. Effect of genetic background on the cardiac phenotype in a mouse model of Emery-Dreifuss muscular dystrophy. *Biochem. Biophys. Reports* **2019**, *19*, 100664, doi:10.1016/j.bbrep.2019.100664.
51. Le Dour, C.; Macquart, C.; Sera, F.; Homma, S.; Bonne, G.; Morrow, J.P.; Worman, H.J.; Muchir, A. Decreased WNT/β-catenin signalling contributes to the pathogenesis of dilated cardiomyopathy caused by mutations in the lamin a/C gene. *Hum. Mol. Genet.* **2017**, *26*, ddw389, doi:10.1093/hmg/ddw389.
52. Muchir, A.; Wu, W.; Choi, J.C.; Iwata, S.; Morrow, J.; Homma, S.; Worman, H.J. Abnormal p38 mitogen-activated protein kinase signaling in dilated cardiomyopathy caused by lamin A/C gene mutation. *Hum. Mol. Genet.* **2012**, *21*, 4325–4333, doi:10.1093/hmg/dds265.
53. Muchir, A.; Pavlidis, P.; Decostre, V.; Herron, A.J.; Arimura, T.; Bonne, G.; Worman, H.J. Activation of MAPK pathways links LMNA mutations to cardiomyopathy in Emery-Dreifuss muscular dystrophy. *J. Clin. Investig.* **2007**, *117*, doi:10.1172/JCI29042.
54. Muchir, A.; Wu, W.; Worman, H.J. Mitogen-Activated Protein Kinase Inhibitor Regulation of Heart Function and Fibrosis in Cardiomyopathy Caused by Lamin A/C Gene Mutation. *Trends Cardiovasc. Med.* **2010**, *20*, 217–221, doi:10.1016/j.tcm.2011.11.002.
55. Chatzifrangkeskou, M.; Le Dour, C.; Wu, W.; Morrow, J.P.; Joseph, L.C.; Beuvin, M.; Sera, F.; Homma, S.; Vignier, N.; Mougenot, N.; et al. ERK1/2 directly acts on CTGF/CCN2 expression to mediate myocardial fibrosis in cardiomyopathy caused by mutations in the lamin A/C gene. *Hum. Mol. Genet.* **2016**, *25*, 2220–2233, doi:10.1093/hmg/ddw090.
56. Wu, W.; Shan, J.; Bonne, G.; Worman, H.J.; Muchir, A. Pharmacological inhibition of c-Jun N-terminal kinase signaling prevents cardiomyopathy caused by mutation in LMNA gene. *Biochim. Biophys. Acta* **2010**, *1802*, 632–638, doi:10.1016/j.bbadis.2010.04.001.
57. Wu, W.; Muchir, A.; Shan, J.; Bonne, G.; Worman, H.J. Mitogen-Activated Protein Kinase Inhibitors Improve Heart Function and Prevent Fibrosis in Cardiomyopathy Caused by Mutation in Lamin A/C Gene. *Circulation* **2011**, *123*, 53–61, doi:10.1161/circulationaha.110.970673.
58. Wu, W.; Chordia, M.D.; Hart, B.P.; Kumarasinghe, E.S.; Ji, M.K.; Bhargava, A.; Lawlor, M.W.; Shin, J.; Sera, F.; Homma, S.; et al. Macrocyclic MEK1/2 inhibitor with efficacy in a mouse model of cardiomyopathy caused by lamin A/C gene

mutation. *Bioorg. Med. Chem.* **2017**, *25*, 1004–1013, doi:10.1016/j.bmc.2016.12.014.
59. Muchir, A.; Wu, W.; Sera, F.; Homma, S.; Worman, H.J. Mitogen-activated protein kinase kinase 1/2 inhibition and angiotensin II converting inhibition in mice with cardiomyopathy caused by lamin A/C gene mutation. *Biochem. Biophys. Res. Commun.* **2014**, *452*, 958–961, doi:10.1016/j.bbrc.2014.09.020.
60. Lee, J.; Termglinchan, V.; Diecke, S.; Itzhaki, I.; Lam, C.K.; Garg, P.; Lau, E.; Greenhaw, M.; Seeger, T.; Wu, H.; et al. Activation of PDGF pathway links LMNA mutation to dilated cardiomyopathy. *Nature* **2019**, *572*, 335–340, doi:10.1038/s41586-019-1406-x.
61. Chen, S.N.; Lombardi, R.; Karmouch, J.; Tsai, J.-Y.; Czernuszewicz, G.; Taylor, M.R.G.; Mestroni, L.; Coarfa, C.; Gurha, P.; Marian, A.J. DNA Damage Response/TP53 Pathway Is Activated and Contributes to the Pathogenesis of Dilated Cardiomyopathy Associated With LMNA (Lamin A/C) Mutations. *Circ. Res.* **2019**, *124*, 856–873, doi:10.1161/CIRCRESAHA.118.314238.
62. Chen, S.N.; Sbaizero, O.; Taylor, M.R.G.; Mestroni, L. Lamin A/C Cardiomyopathy: Implications for Treatment. *Curr. Cardiol. Rep.* **2019**, *21*, 160, doi:10.1007/s11886-019-1224-7.
63. Sullivan, T.; Escalante-Alcalde, D.; Bhatt, H.; Anver, M.; Bhat, N.; Nagashima, K.; Stewart, C.L.; Burke, B. Loss of a-Type Lamin Expression Compromises Nuclear Envelope Integrity Leading to Muscular Dystrophy. *J. Cell Biol.* **1999**, *147*, 913–920, doi:10.1083/jcb.147.5.913.
64. Nikolova, V.; Leimena, C.; McMahon, A.C.; Tan, J.C.; Chandar, S.; Jogia, D.; Kesteven, S.H.; Michalicek, J.; Otway, R.; Verheyen, F.; et al. Defects in nuclear structure and function promote dilated cardiomyopathy in lamin A/C–deficient mice. *J. Clin. Investig.* **2004**, *113*, 357–369, doi:10.1172/JCI200419448.
65. Wolf, C.M.; Wang, L.; Alcalai, R.; Pizard, A.; Burgon, P.G.; Ahmad, F.; Sherwood, M.; Branco, D.M.; Wakimoto, H.; Fishman, G.I.; et al. Lamin A/C haploinsufficiency causes dilated cardiomyopathy and apoptosis-triggered cardiac conduction system disease. *J. Mol. Cell. Cardiol.* **2008**, *44*, 293–303, doi:10.1016/j.yjmcc.2007.11.008.
66. Serrano, M.; Lee, H.W.; Chin, L.; Cordon-Cardo, C.; Beach, D.; DePinho, R.A. Role of the INK4a locus in tumor suppression and cell mortality. *Cell* **1996**, *85*, 27–37, doi:10.1016/S0092-8674(00)81079-X.
67. Silva, M.C.; Magalhães, T.A.; Meira, Z.M.A.; Rassi, C.H.R.E.; Andrade, A.C.D.S.; Gutierrez, P.S.; Azevedo, C.F.; Gurgel-Giannetti, J.; Vainzof, M.; Zatz, M.; et al. Myocardial Fibrosis Progression in Duchenne and Becker Muscular Dystrophy. *JAMA Cardiol.* **2017**, *2*, 190, doi:10.1001/jamacardio.2016.4801.
68. Travers, J.G.; Kamal, F.A.; Robbins, J.; Yutzey, K.E.; Blaxall, B.C. Cardiac Fibrosis. *Circ. Res.* **2016**, *118*, 1021–1040, doi:10.1161/CIRCRESAHA.115.306565.
69. Meng, X.; Nikolic-Paterson, D.J.; Lan, H.Y. TGF-β: The master regulator of fibrosis. *Nat. Rev. Nephrol.* **2016**, *12*, 325–338, doi:10.1038/nrneph.2016.48.
70. Valiente-Alandi, I.; Potter, S.J.; Salvador, A.M.; Schafer, A.E.; Schips, T.; Carrillo-Salinas, F.; Gibson, A.M.; Nieman, M.L.; Perkins, C.; Sargent, M.A.; et al. Inhibiting Fibronectin Attenuates Fibrosis and Improves Cardiac Function in a Model of Heart Failure. *Circulation* **2018**, *138*, 1236–1252, doi:10.1161/circulationaha.118.034609.
71. Kong, P.; Christia, P.; Frangogiannis, N.G. The pathogenesis of cardiac fibrosis. *Cell. Mol. Life Sci.* **2014**, *71*, 549–574, doi:10.1007/s00018-013-1349-6.
72. Borriello, L.; Nakata, R.; Sheard, M.A.; Fernandez, G.E.; Sposto, R.; Malvar, J.; Blavier, L.; Shimada, H.; Asgharzadeh, S.; Seeger, R.C.; et al. Cancer-Associated Fibroblasts Share Characteristics and Protumorigenic Activity with Mesenchymal Stromal Cells. *Cancer Res.* **2017**, *77*, 5142–5157, doi:10.1158/0008-5472.CAN-16-2586.

73. Madej-Pilarczyk, A. Clinical aspects of emery-dreifuss muscular dystrophy. *Nucleus* **2018**, *9*, 314–320, doi:10.1080/19491034.2018.1462635.
74. Himelman, E.; Lillo, M.A.; Nouet, J.; Patrick Gonzalez, J.; Zhao, Q.; Xie, L.H.; Li, H.; Liu, T.; Wehrens, X.H.T.; Lampe, P.D.; et al. Prevention of connexin-43 remodeling protects against Duchenne muscular dystrophy cardiomyopathy. *J. Clin. Investig.* **2020**, *130*, 1713–1727doi:10.1172/JCI128190.
75. Macquart, C.; Jüttner, R.; Morales Rodriguez, B.; Le Dour, C.; Lefebvre, F.; Chatzifrangkeskou, M.; Schmitt, A.; Gotthardt, M.; Bonne, G.; Muchir, A. Microtubule cytoskeleton regulates Connexin 43 localization and cardiac conduction in cardiomyopathy caused by mutation in A-type lamins gene. *Hum. Mol. Genet.* **2019**, doi:10.1093/hmg/ddy227.
76. Duffy, H.S. The molecular mechanisms of gap junction remodeling. *Hear. Rhythm* **2012**, doi:10.1016/j.hrthm.2011.11.048.
77. Hertig, C.M.; Eppenberger-Eberhardt, M.; Koch, S.; Eppenberger, H.M. N-cadherin in adult rat cardiomyocytes in culture. I. Functional role of N-cadherin and impairment of cell-cell contact by a truncated N-cadherin mutant. *J. Cell Sci.* **1996**, *109*, 1–10.
78. Laflamme, M.A.; Murry, C.E. Heart regeneration. *Nature* **2011**, *473*, 326–335, doi:10.1038/nature10147.
79. Eschenhagen, T.; Bolli, R.; Braun, T.; Field, L.J.; Fleischmann, B.K.; Frisén, J.; Giacca, M.; Hare, J.M.; Houser, S.; Lee, R.T.; et al. Cardiomyocyte Regeneration: A Consensus Statement. *Circulation* **2017**, *136*, 680–686, doi:10.1161/CIRCULATIONAHA.117.029343.
80. Weinberger, F.; Eschenhagen, T. Heart regeneration: From mouse to human. *Curr. Opin. Physiol.* **2020**, *14*, 7–12, doi:10.1016/j.cophys.2019.10.010.
81. Cui, M.; Wang, Z.; Chen, K.; Shah, A.M.; Tan, W.; Duan, L.; Sanchez-Ortiz, E.; Li, H.; Xu, L.; Liu, N.; et al. Dynamic Transcriptional Responses to Injury of Regenerative and Non-regenerative Cardiomyocytes Revealed by Single-Nucleus RNA Sequencing. *Dev. Cell* **2020**, *53*, 102–116, doi:10.1016/j.devcel.2020.02.019.
82. Pillers, D.A.M.; Von Bergen, N.H. Emery–dreifuss muscular dystrophy: A test case for precision medicine. *Appl. Clin. Genet.* **2016**, doi:10.2147/TACG.S75028.
83. Blagova, O.; Nedostup, A.; Shumakov, D.; Poptsov, V.; Shestak, A.; Zaklyasminskaya, E. Dilated cardiomyopathy with severe arrhythmias in emery-dreifuss muscular dystrophy from ablation to heart transplantation. *J. Atr. Fibrillation* **2016**, doi:10.4022/jafib.1468.
84. Russo, V.; Rago, A.; Politano, L.; Papa, A.A.; Di Meo, F.; Russo, M.G.; Golino, P.; Calabrò, R.; Nigro, G. Increased dispersion of ventricular repolarization in emery dreifuss muscular dystrophy patients. *Med. Sci. Monit.* **2012**, *18*, 643–647, doi:10.12659/MSM.883541.
85. Bialer, M.G.; Mcdaniel, N.L.; Kelly, T.E. Progression of cardiac disease in emery-dreifuss muscular dystrophy. *Clin. Cardiol.* **1991**, *14*, 411–416, doi:10.1002/clc.4960140509.
86. Asp, M.; Giacomello, S.; Larsson, L.; Wu, C.; Fürth, D.; Qian, X.; Wärdell, E.; Custodio, J.; Reimegård, J.; Salmén, F.; et al. A Spatiotemporal Organ-Wide Gene Expression and Cell Atlas of the Developing Human Heart. *Cell* **2019**, *179*, 1647–1660, doi:10.1016/j.cell.2019.11.025.
87. Günthel, M.; Barnett, P.; Christoffels, V.M. Development, Proliferation, and Growth of the Mammalian Heart. *Mol. Ther.* **2018**, *26*, 1599–1609, doi:10.1016/j.ymthe.2018.05.022.
88. Kubben, N.; Voncken, J.W.; Konings, G.; van Weeghel, M.; van den Hoogenhof, M.M.G.; Gijbels, M.; van Erk, A.; Schoonderwoerd, K.; van den Bosch, B.; Dahlmans, V.; et al. Post-natal myogenic and adipogenic developmental. *Nucleus* **2011**, *2*, 195–207, doi:10.4161/nucl.2.3.15731.

89. Segura, A.M.; Frazier, O.H.; Buja, L.M. Fibrosis and heart failure. *Heart Fail. Rev.* **2014**, *19*, 173–185, doi:10.1007/s10741-012-9365-4.
90. Zhang, J.; Tao, R.; Campbell, K.F.; Carvalho, J.L.; Ruiz, E.C.; Kim, G.C.; Schmuck, E.G.; Raval, A.N.; da Rocha, A.M.; Herron, T.J.; et al. Functional cardiac fibroblasts derived from human pluripotent stem cells via second heart field progenitors. *Nat. Commun.* **2019**, *10*, 2238, doi:10.1038/s41467-019-09831-5.
91. Furtado, M.B.; Nim, H.T.; Boyd, S.E.; Rosenthal, N.A. View from the heart: Cardiac fibroblasts in development, scarring and regeneration. *Development* **2016**, *143*, 387–397, doi:10.1242/dev.120576.
92. Lajiness, J.D.; Conway, S.J. The Dynamic Role of Cardiac Fibroblasts in Development and Disease. *J. Cardiovasc. Transl. Res.* **2012**, *5*, 739–748, doi:10.1007/s12265-012-9394-3.
93. Meng, X.; Wang, H.; Song, X.; Clifton, A.C.; Xiao, J. The potential role of senescence in limiting fibrosis caused by aging. *J. Cell. Physiol.* **2020**, *235*, 4046–4059, doi:10.1002/jcp.29313.
94. Meyer, K.; Hodwin, B.; Ramanujam, D.; Engelhardt, S.; Sarikas, A. Essential Role for Premature Senescence of Myofibroblasts in Myocardial Fibrosis. *J. Am. Coll. Cardiol.* **2016**, *67*, 2018–2028, doi:10.1016/j.jacc.2016.02.047.

Chapter 3 Polycomb bodies detection in murine fibromuscular stroma from skin, skeletal muscles and aortic tissues

Valentina Rosti[1,2*], Francesca Gorini[2*], Philina Santarelli[2], Maria Lucia Sarnicola[2] Silvia Magnani[3] and Chiara Lanzuolo[1, 2, 4]

In press

Polycomb bodies detection in murine fibromuscular stroma from skin, skeletal muscles and aortic tissues

Valentina Rosti[1], [2*], Francesca Gorini[2*], Philina Santarelli[2], Maria Lucia Sarnicola[2] Silvia Magnani[3] and Chiara Lanzuolo[1, 2]

[1] *Institute of Biomedical Technologies, National Research Council, Milan, Italy.*

[2] *Istituto Nazionale di Genetica Molecolare "Romeo ed Enrica Invernizzi", INGM, Milan, Italy.*

[3] *Charles River Laboratories Italia S.r.l.*

[4] Corresponding author: chiara.lanzuolo@cnr.it

*Equal contribution

Keywords: Emery–Dreifuss muscular dystrophy; Cdkn2a locus; Lamin A/C; p16INK4a; heart; dilated cardiomyopathy; cellular senescence

3.1. Abstract

The regulation of chromatin structure depends on a dynamic, multiple mechanisms that modulate gene expression and constitute the epigenome. The Polycomb group (PcG) of proteins are epigenetic factors involved in the transcriptional repression. Among their multilevel, chromatin-associated functions, PcG proteins mediate the establishment and maintenance of higher-order structures at target genes, allowing the transmission of transcriptional programs throughout the cell cycle.

In the nucleus, PcG proteins localize close to the pericentric heterochromatin forming microscopically foci, called Polycomb bodies. Here, to visualize the tissue-specific PcG distribution in the aorta, dorsal skin and hindlimb muscles, we combine a fluorescence-activated cell sorter (FACS)-based method with an immunofluorescence staining.

3.2. Introduction

The epigenome is constituted by a plethora of components and intricate mechanisms which modulate the transcriptional state of genomic regions to establish lineage-specific patterns of gene expression.

One of the key epigenetic mechanisms is the transcriptional repression exerted by the Polycomb group (PcG) of proteins, epigenetic factors essential for the development, differentiation and cellular-identity maintenance [1]. Extensive studies described PcG's role in organism development and adult homeostasis, with the identification of Polycomb Repressive Complex 1 and 2 (PRC1 and PRC2), characterized by different multiprotein assemble, catalytic activities and cellular functions [2]. PRC1 is responsible for the mono-ubiquitination of lysine 119 of histone H2A (H2AK119ub), via the catalytic activity of Ring1A/B combined with Bmi-1 [3], while PRC2 complex establishes tri-methylation on H3K27 (H3K27me3) through the catalytic subunit EZH1/2 [4]-[5]. The two different PRCs show an intimate relationship, as, for example, the PRC2-mediated H3K27me3 acts as a docking site for PRC1 recruitment [6]-[7] to a subset of common regions [8]. PRC1 has been shown to act upstream of PRC2 to trigger its activity in a positive feedback loop [9].

A major role of PcG in epigenetic regulation is through the formation of higher order chromatin structures [10,11] at PcG

binding sites which not only regulate gene expression but also allow the transmission of the transcriptional program throughout the cell cycle [12,13].

In the nucleus, PcG proteins form microscopically visible disseminated foci, called Polycomb bodies, localized close to the pericentric heterochromatin [14]. Alterations in PcG bodies localization affect PcG transcriptional repression, as shown by our group upon depletion of Lamin A, one of the main component of the nuclear lamina [15] and later corroborated by other authors [16–19]. Further, studying two distinct Lamin A-dependent pathologies, Emery Dreifuss Muscular Dystrophy and Hutchinson Gilford Progeria Syndrome, we described how mutation of Lamin A can impact the PcG architecture and generate a dysfunctional Polycomb program leading to a defect in cell identity maintenance [15,20,21].

The nuclear organization of PcG proteins, dependent or not by Lamin A, is an area of intense interest, because besides playing pivotal roles in embryo development, with several null mutants resulting in embryo-lethality [22], the Polycomb function is crucial for maintaining homeostatic and regenerative balances in adult tissues [23–25]. Indeed, increasingly growing evidence highlighted the importance of both PRC1 and PRC2 in the pathophysiologic processes of aortic tissue [26,27], in muscle regeneration capability [28]-[29] and in skin homeostasis [30,31]. In all mentioned tissues, the structural stromal compartment, containing fibroblasts and muscle cells, has received recent

attention due to its capacity to be sensitive and dynamically responsive to external cues [32,33]. The resident fibromuscular stromal cells are tissue-specific and influence the characteristic phenotype of cells present in each district [34]-[35]. By contributing substantially to the extracellular mechanical–chemical properties of the microenvironment, stromal cells not only define the physical integrity of tissue-resident cells but also have key roles in numerous physiological and pathological processes like wound healing, fibrosis and cancer [36,37].

However, adequate experimental conditions are required to preserve integrity of nuclear architecture during the stromal cells extraction protocol and minimize in vitro manipulations which induce homogenizing effect and transcriptional reprogramming [38].

Here, we report a fluorescence activated cell sorter (FACS)-based method to isolate the murine fibromuscular stromal subset which resides in whole aorta, dorsal skin and hindlimb muscles tissues. Moreover, using a combination of characteristic skin fibroblast surface markers, we set up a flow- cytometry gating strategy to separate the papillary and reticular dermis fibroblasts that differentially contribute to tissue homeostasis in the cute [39]. The downstream immunofluorescence staining provides useful tool to visualize the PcG distribution in tissue-specific stromal compartments (*Figure 1*).

3.3. 2. Materials

Mice

Male and female C57BL/6 mice were bred in an authorized facility at San Raffaele Hospital, Milan, Italy (authorization n. N. 11/2022-PR). All mouse experimental procedures were performed in compliance with animal welfare laws and guidelines under the ethical approval of the Italian Ministry of Health and the Institutional Animal Care and Use Committee.

Reagents

1. Hanks′ Balanced Salt solution (HBSS), calcium, magnesium, no phenol red
2. Dulbecco's Phosphate-buffered saline (PBS) w/o calcium and magnesium 1X
3. 1 U/mg Dispase II
4. DNase I grade II, from bovine pancreas
5. Collagenase A from Clostridium histolyticum
6. Collagenase D from Clostridium histolyticum
7. Collagenase type II
8. Fetal Bovine Serum (FBS)

9. Trypan Blue Stain
10. Bovine Serum Albumin, lyophilized powder (BSA)
11. Ethanol absolute
12. 50 mM CaCl2
13. 1 M MgCl2
14. Glycerol
15. Paraformaldehyde (PFA), powder
16. Triton X100
17. 100X Penicillin-streptomycin solution
18. TO-PRO™-3 stain (eBiosciencab, cat. no. T3605)
19. Anti-TER119 (eBioscience, cat. no. 48-5921-82)
20. Anti-CD45 (eBioscience, cat. no. 48-0451-82)
21. Anti-CD326 (eBioscience, cat. no. 48-5791-82)
22. Anti-TIE2 (eBioscience, cat. no. 13-5987-82)
23. Anti-CD31 (eBioscience, cat. no. 48-0311-82)
24. Anti-CD140b (Miltenyi Biotec, cat. no. 130-105-118)
25. Anti-ER-TR7 (Santa Cruz Biotechnology, cat. no. sc-73355)
26. Anti-SCA1 (Invitrogen, cat. no. 11-5981-82)
27. Anti-α7 Integrin (ABLAB, cat. no. 67001005)
28. Tween®20
29. Dulbecco's Modified Eagle's Medium (DMEM) high glucose

30. Mounting medium
31. Alexa Fluor 488 goat anti-rabbit
32. Alexa Fluor 647 goat anti-mouse
33. 4',6-diamidin-2-fenilindolo (DAPI)
34. Anti-Ring1b Rabbit monoclonal antibody (Cell Signaling Technology, cat. no. 5694S)
35. Anti-Lamib B Mouse monoclonal antibody (Atlas Antibodies, cat. no. AMAb 91251)
36. Anti-PHAL
37. TO-PRO™-3 (APC, eBiosciencab, T3605)

Solutions

1. Dermis digestion cocktail: HBSS containing 600 units/mL Collagenase type II, 2,4 units/mL Dispase II and 100 µg/mL DNase (See **Note 1**).
2. Aorta digestion cocktail: HBSS containing 300 units/mL Collagenase D, 2,4 units/mL Dispase II and 100 µg/mL DNase (See **Note 1)**.
3. Muscle digestion cocktail: 1X PBS containing 2 mg/mL Collagenase A, 2,4 U/mL Dispase II, 0,1 mg/mL DNase I, 0,4 mM $CaCl_2$ and 5 mM $MgCl_2$ (See **Note 1**).

4. Blocking digestion solution 10% (vol/vol): 1X PBS supplemented with 1% penicillin/streptomycin, 10% FBS and 10 µg/mL DNase.
5. HBSS+: HBSS supplemented with 0,2% BSA.
6. HBSS+++: HBSS supplemented with 0,2% BSA, 1x penicillin/streptomycin, 1x DNase I.
7. FACS staining solution: 1X PBS containing 1% penicillin/streptomycin, 0,2% BSA and 10 µg/mL DNase (See **Note 1**).
8. Murine muscle staining mix: 1:50 anti-CD45 Pacific blue, 1:50 anti-CD31 Pacific blue, 1:50 anti-Ter119 Pacific blue, 1:50 anti-SCA1 FITC and 1:100 anti-α7 integrin in FACS staining solution (See **Note 1**).
9. Murine aorta staining mix: 1:100 Anti-CD45 Pacific blue, 1:100 anti-CD31 Pacific blue, 1:100 anti-Ter119 Pacific blue, 1:100 anti-Tie2 Pacific blue, 1:100 anti-CD326 Pacific blue in FACS staining solution. Use a final volume of 100 uL per each 500K-1M of cells (See **Note 1**).
10. Murine dermis staining mix: 1:100 anti-CD45 Pacific blue, 1:100 anti-CD31 Pacific blue, 1:100 anti-Ter119 Pacific blue, 1:100 anti-Tie2 Pacific blue, 1:100 anti-CD326 Pacific blue, 1:25 anti-CD140b

PE-Vio770, 1:100 anti-ER-TR7 FITC FACS staining solution. Use a final volume of 100 uL per 500K-1M of cells (See **Note 1**).

11. Formaldehyde Fixative Solution: 4% w/v PFA in 1X PBS (See **Note 2**).
12. Permeabilization solution: 0.5% Triton X100 in 1X PBS.
13. Blocking buffer: 4% (w / v) BSA and 2% of secondary specie-specific serum in 1X PBS.

Equipment and Supplies

1. 15- and 50- mL Falcon tubes
2. 1,5- and 2- mL Microcentrifuge tubes
3. Refrigerated swing-bucket rotor centrifuge for 15- and 50- mlLFalcon tubes
4. Refrigerated microcentrifuge
5. 37°C water bath
6. 0.40 µm cell strainer
7. 0.70 µm cell strainer
8. Cell culture plate (24-well)
9. Cells counting chamber
10. Sterile hood for cell culture
11. Parafilm

12. Laboratory water bath

13. Sterile scissors for dissection

14. Stereoscopic microscope

15. Fume hood

16. Precision Weighing Balances

17. Autoclaved surgical tweezers/forceps

18. Light microscope

19. Tilting shaker

20. Bürker Counting Chambers

21. 30-µm Sterile Syringe Filcon

22. Sterile Syringe 3cc

23. 5 mL Polypropilene Tubes

24. FACS machine

25. CO_2 incubator (5% CO_2, 37 °C)

26. Glass Pasteur pipettes

27. Humidified chamber

28. Microscope glass slides (26x 76 mm)

29. Laser scanning confocal microscope

30. 10 mm Glass coverslip

3.4. Methods

Equipment preparation

1. Sanitize with 70% ethanol all the laboratory surfaces and surgical instruments which will be used during the experimental procedure.
2. Perform coating of 60 mm Petri dishes, 5 mL Polypropilene Tubes, 15-mLFalcon tubes and microcentrifuge tubes using a proper FBS volume for at least 5 minutes at RT (See **Note 3**).
3. Remove excess FBS.
4. To work under sterile conditions, it is recommended to perform all the steps in a laminar flow hood.

Tissue collection I TIMING: 30 minutes per mouse

1. Prepare 60 mm petri dishes with 2-3 mL of in ice-cold saline (three dishes per each mouse) and put in on ice.
2. Weight the mouse.
3. Sacrifice mouse by cervical dislocation according to proper national IACUC recommendation (See **Note 4**).
4. Shave the dorsal mouse skin and spray the mouse liberally with 70% ethanol before cutting the skin.

5. Place the mouse in a prone position on a clean and sterile dissection area to dry.
6. Carefully remove the skin, avoid including any subcutaneous fat, without touching the tendons/muscles as described in [40] (See **Note 5**).
7. Harvest dorsal mouse skin in the petri dish and rinse it in betadine followed by twice 1X PBS washes on ice.
8. Cut the two legs of the mouse and rapidly proceed with the collection of the hindlimb muscles as described in [41,42].
9. Place the mouse in a supine position, incise the midline of the abdomen and open the abdominal and chest cavities.
10. Cut the abdominal aorta at the middle and perfuse it with 1X PBS to remove blood from the aortic tissues.
11. Dissect the aorta from the aortic arch to the abdominal aorta and immersed it in ice-cold saline in a 60 mm Petri dish (See **Note 6**).
12. Fresh surgical collected tissues should be placed in 1X ice-cold PBS and kept in a refrigerator (4-8°C) until they can be transported to the laboratory on ice (See **Note 7**).

Enzymatical digestion and Preparation of a Single-Cell Suspension I TIMING: Murine Dermis-4 hours

1. Mince the skin using dissecting scissors until a uniform consistency with 2-3 mm^3 pieces by keeping the 60 mm petri dish always on ice (Figure 2A) (See **Note 8**).
2. Transfer the minced tissue into a 15-mL Falcon tubes and wash carefully with 2-3 mL of 1X PBS the 60 mm petri dish to retrieve all the tissue pieces.
3. Centrifuge the minced tissue at 300g for 5 minutes at 4°C. Carefully discard the supernatant.
4. Measure the weight of tissue with a precision balance.
5. Rinse twice with 10 mL of ice-cold sterile 1X PBS.
6. Add 1 mL of dermis digestion cocktail to each 30 mg of minced tissue (See **Note 9**).
7. Seal well the 15-mL Falcon tube with Parafilm, agitate sample vigorously and incubate at 37°C in water bath for 60-90 minutes. Tube should be positioned horizontally and completely submerged in water.
8. Shake the tube for 10 seconds every 10 minutes while incubating at 37 °C.
9. Stop the digestion reaction by topping up to 15 mL with ice-cold Blocking solution. Gently invert a few times to mix (See **Note 10**).

10. Place a 70-µm Nylon cell strainer into a new 50-mL Falcon tube.
11. Rinse the cell strainer with 5 mL of 1X PBS (See **Note 11**).
12. Transfer the tissue digestion on the cell strainer and allow to filter by gravity (See **Note 12**).
13. Rinse strainer with an additional 15mL ice-cold blocking digestion solution and bring the total volume to 30 mL.
14. Centrifuge at 300g for 5 minutes at 4°C and remove the supernatant by aspiration immediately after centrifugation taking caution to primary remove the upper layer of fat contamination (See **Note 13**).
15. Wash cells once with 10 mL of 1X PBS and then centrifuge the tube at 300g for 5 minutes at 4 °C.
16. Remove carefully the supernatant.
17. Resuspend single-cell suspension in 5mL of 1X PBS and count cells with Burker Counting Chamber. Usually, around 14K viable cells are recovered per mg of skin tissue (Figure 2D-E).
18. Centrifuge at 300g for 5 minutes at 4°C and remove carefully the supernatant.
19. Resuspend the pellet in 600µL of ice-cold staining solution and place the cell suspension in a 5-mL Polypropylene tube at 4 °C

overnight. Continue to 3.6 for FACS staining protocol (See **Note 14)**.

Enzymatical digestion and Preparation of a Single-Cell Suspension I TIMING: Murine Aorta-2 hours

1. Measure the weight of aortic tissue with a precision balance.
2. Use autoclaved surgical tweezers to rapidly transfer aorta tissue into 2 mL microcentrifuge tube and rinse twice with 1 mL of ice-cold sterile 1X PBS (See **Note 15**).
3. Mince the tissue into small pieces (~1 mm^3) inserting the autoclaved surgical scissors directly in the 2 mL microcentrifuge tube (Figure 2B).
4. Enzymatically digest the tissue by adding aorta digestion cocktail. Use 1 mL of solution per ~ 30 mg of minced tissue (See **Note 9**).
5. Cap the tube tightly with parafilm to seal the top and incubate in a water bath at 37 °C shaking vigorously for 10 seconds every 10 minutes (See **Note 16**).
6. Stop the digestion reaction by topping up to 2 mL with ice-cold blocking digestion solution.
7. Place a 30-µm sterile syringe falcon cells strainer on a top of a 5-mL polypropylene tube, prewet the strainer with 1X PBS to prime it (See **Note 11**).

8. Pass the cells through the primed strainer by pressing with the plunger of a sterile 3 cc syringe to facilitate filtering.
9. Pass another 2 mL of cold blocking solution throughout the same filter to maximize cell yield and bring the total volume to 4 ml.
10. Centrifuge the tube at 300g for 5 minutes at 4 °C. After centrifugation remove carefully the supernatant by aspiration.
11. Wash single-cells suspension once with 3 mL of 1X PBS and then centrifuge the tube at 300g for 5 minutes at 4 °C. Remove the supernatant without disturbing the pellet (See **Note 17**).
12. Resuspend cells in 1mL of 1X PBS for counting with Burker Counting Chamber. Usually, around 9K viable cells are recovered per mg of mouse aortic tissue (Figure 2D-E).
13. Centrifuge at 300g for 5 minutes at 4°C and remove carefully the supernatant.
14. Resuspend the pellet in 300µL of ice-cold staining solution and place the cell suspension in a 5-mL Polypropylene tube at 4 °C overnight. Continue to 3.6 for FACS staining protocol (See **Note 14)**.

Enzymatical digestion and Preparation of a Single-Cell Suspension I TIMING: Murine Muscle-2 hours

1. Mince the muscle using dissecting scissors until a uniform consistency with 2-3 mm3 pieces by keeping the 60 mm petri dish always on ice (Figure 2C) (See **Note 8**).
2. Transfer the minced tissue into a 15-mL Falcon tubes and wash carefully with 2-3 mL of 1X PBS the 60 mm petri dish to retrieve all the tissue pieces.
3. Centrifuge the minced tissue at 340g for 8 minutes at 4°C. Carefully discard the supernatant.
4. Rinse twice with 10 mL of ice-cold sterile 1X PBS.
5. Add 8 mL of muscle digestion cocktail to each ½ mouse (4mL for pups) (See **Note 9**).
6. Seal well the 15-mL Falcon tube with Parafilm, agitate sample vigorously and incubate at 37°C in water bath for 60-90 minutes. Tube should be positioned horizontally and completely submerged in water.
7. Shake the tube for 10 seconds every 15 minutes while incubating at 37 °C.
8. Stop the digestion reaction by topping up to 15 mL with ice-cold Blocking solution. Gently invert a few times to mix (See **Note 10**).
9. Place a 70-µm Nylon cell strainer into a new 50-mL Falcon tube.

10. Rinse the cell strainer with 5 mL of cold HBSS+.
11. Transfer the tissue digestion on the cell strainer and allow to filter by gravity.
12. Rinse strainer with an additional 10mL ice-cold HBSS+ solution and bring the total volume to 40 mL.
13. Centrifuge at 340g for 10 minutes at 4°C and remove the supernatant by aspiration immediately after centrifugation taking caution to primary remove the upper layer of fat contamination (See **Note 18**).
14. Resuspend the pellet with 10 mL of cold HBSS+.
15. Place a 40-µm Nylon cell strainer into a new 50-mL Falcon tube.
16. Rinse the cell strainer with 5 mL of cold HBSS+.
17. Transfer the tissue digestion on the cell strainer and allow to filter by gravity.
18. Wash the 15-ml falcon with 10 ml cold HBSS+ and transfer on the cell strainer.
19. Rinse strainer with an additional 10mL ice-cold HBSS+ solution and bring the total volume to 35 mL.
20. Centrifuge at 340g for 10 minutes at 4°C and discard the supernatant.

21. Resuspend single-cell suspension in in 1mL of cold HBSS++ and count cells with Burker Counting Chamber.
22. Centrifuge at 300g for 5 minutes at 4°C and remove carefully the supernatant.
23. Resuspend the pellet in 300µL of ice-cold staining solution and place the cell suspension in a 5-mL Polypropylene tube at 4 °C overnight. Continue to 3.6 for FACS staining protocol (See **Note 14)**.

Antibody staining and Cell Sorting | TIMING 90 minutes + 45 minutes sorting (per mouse)

The following steps should be performed in a sterile tissue culture hood and in the dark.

1. Centrifuge at 340g for 10 minutes at 4°C and discard the supernatant.
2. Adjust the cell suspension to a concentration of 500K-1M cells/100 µl with cold staining solution (*Table1,2,3*).
3. Mix thoroughly and incubate sample on ice (See **Note 19**) covered by an aluminum foil for 30-40 minutes.
4. Wash cells with 2 mL of cold 1X PBS (for Murine Dermis and Aorta) or HBSS+ (for Murine Muscle) and centrifuge at 300g for 8 minutes at 4°C.

5. Discard the supernatant and collect cells thought a 32µm cells strainer in 200µL of cold 1X PBS (See **Note 20**).
6. Stain cells with viability dye making 1/10000x dilutions of TO-PRO™-3 stain in 1X PBS, and adding 1µl of the diluted stain to each 100 µl of the cell suspension 10 minutes prior to FACS sorting (See **Note 21, 22)**.
7. Perform FACS to isolate fibromuscular stromal subset for TO-PRO™-3$^-$/CD45$^-$/CD31$^-$/Ter-119$^-$/ Tie2$^-$/EpCAM$^-$ cells in murine dermis and aorta (Figure 3-4).
8. Dermis papillary (PDGFRβ $^+$/ ER-TR7$^-$) and reticular fibroblasts (PDGFRβ $^+$/ ER-TR7$^-$) are isolated for stromal populations expressing either one or both of the two cell surface fibroblast markers PDGFRβ and ER-TR7 respectively (Figure 3).
9. Perform FACS gating strategy for muscle-digested cells and isolate fibromuscular subset excluding MuSCs and FAPs (Figure 5).

Immunofluorescence

1. Sterilize 10-mm round glass coverslips in 100% ethanol and let them air-dry (See **Note 23**).

2. Place each sterilized coverslip at the centre of a well of a 24-well culture plate.
3. Count the sorted cells and resuspended the desired concentration in a small volume of medium (20uL) (See **Note 24).**
4. Incubate for 1 hour at 37°C in a CO_2 incubator to let the cells sit on the coverslip.
5. Add 1mL of DMEM medium and incubate at 37°C overnight to allow cells attachment on the coverslip (See **Note 25**).
6. Remove the medium from each well avoiding cell displacement or clumping (See **Note 26).**
7. Under chemical-hood add 500µL 4% (w/v) PFA (pH 7,4) to each well and incubate for 10 minutes at RT (See **Note 27**).
8. Remove PFA solution and rapidly wash the cells twice with 1X PBS.
9. Rinse in 0.1% Tween/PBS for 5 minutes at RT on a tilting shaker with low speed.
10. Repeat 3 times (See **Note 28)**.
11. Out of the chemical-hood, add 1 mL of permeabilizing solution for 10 minutes at RT in mild agitation.
12. Remove permeabilizing solution and rinse cells with 1X PBS for 5 minutes on a tilting shaker.

13. Repeat 3 times.
14. Block non-specific staining by adding 1 mL of blocking solution
15. Incubate for 1 hour at RT on a tilting shaker.
16. Discard the blocking buffer.
17. Dilute the unconjugated primary antibodies in blocking buffer and incubate cells in a humidified chamber overnight at 4 °C or 2 hours at RT as indicated in Table 4 (See **Note 29)**.
18. Place the coverslip into a well with the cell-side upwards and rinse cells with 1X PBS for 5 minutes on a tilting shaker.
19. Repeat twice.
20. Stain the cytoskeleton adding diluted PHAL solution and incubate 2h at RT
21. Wash cells with 1X PBS for 5 minutes on a tilting shaker.
22. Repeat 3 times
23. Dilute the fluorescence-conjugated secondary antibodies of interest 1:500 in 4% (w / v) BSA and incubate the coverslip with the cells-side facing towards the antibody solution for 1 hour in the dark (See **Note 30)**.
24. Rinse cells with 1X PBS for 5 minutes on a tilting shaker.
25. Repeat 3 times

26. Counterstain the nuclei of cells using diluted DAPI solution and incubate for 10 minutes at RT protected from light
27. Rinse cells with 0.1% Tween/PBS for 5 minutes on a tilting shaker
28. Repeat twice
29. Mont the coverslip on a microscope slide (See **Note 31**).
30. Imaging acquisition (Figure 6)

3.5. Notes

1. Prepare fresh at each experiment.
2. Paraformaldehyde is extremely harmful, thus it is necessary to manage PFA carefully. We recommended to prepare and use PFA only in fume hood, wearing gloves to avoid fumes and air-borne powder.
3. FBS coating prevents attachment of the cells to the plastic surfaces and maximizes final single-cell suspension yield.
4. Different ages and genetically engineered mouse models can be used. We successfully applied this protocol on the following strains: C57BL/6 and progeric C57BL/6 Lmna G609G/G609G (data not shown).

5. Approximately can be harvested a piece of dorsal skin of 30mm x 100mm from pups (19 days after birth) and 60mm x 100mm from mice of 4-12 weeks of age.
6. Examine the harvested aorta and carefully remove the fat using surgical scissors under a stereoscopic microscope.
7. To ensure optimal cell populations recovery, fresh specimen should preferentially be processed immediately. However, at occurrence tissues can be store at 4-8°C up to 8 hours before digestion.
8. We recommend to mince tissue holding one end of a piece with forceps and cutting into small pieces maintaining them well moist. Finally, gather all pieces at the center of the 60mm petri dish and cut for an additional 1-2 minutes. At the end of this step, the preparation should yield a slurry of well-minced tissue which facilitate enzymatic digestion.
9. Prewarm the digestion cocktail in a 37 °C water bath for ~10 minutes before adding it to the minced tissue.
10. Digestion can be considered finished when large pieces are no longer present, and the solution appears turbid. Avoid over-digestion and determine the correct incubation time in each experiment by checking cell viability with Trypan Blue staining.

11. Priming the strainer reduces cell adhesion to the nylon surface.
12. The undigested tissue pieces may be disaggregated by addition to fresh dermis digestion solution and further incubation at 37°C.
13. The skin-derived digestion is grey. Cells suspension derived from cute of C57BL/6 pups appear darker than one derived from adult mice.
14. The overnight step at low temperature is strictly required, because reduces the cellular stress response associated with enzymatic tissue digestion. Thus, it is essential for preserving the nuclear structure and the expression of cell surface antigens.
15. Each wash can be performed with mild shaking for 5 sec. After shaking, the tissue sinks to the bottom of the microcentrifuge tube. Remove the supernatant carefully.
16. Given the little size of aortic tissues, particular care should be taken in order to avoid the over-digestion of tissue. Thus, every 10 minutes it is important to check cell viability, cell debris and aggregates to determine the optimal incubation time in each experiment.

17. For enhanced cell recovery, it is recommended to collect the discarded supernatants. These can be recentrifuged and combined with the newly prepared single cell suspension.
18. The pellet at the bottom after centrifugation is loose and can be easily disturbed. Control the aspiration strength and always aspirate only from the surface of the supernatant.
19. We recommend staining on ice to prevent the internalization of surface antigens.
20. Filter the sample right before the cell sorting.
21. Keep the cells on ice in the dark until your scheduled time for sorting. In our experience the cells and antigens are stable maximum for 24 hours.
22. Set up the FACS sorter in accordance with the manufacturer's specifications with the 100-µm nozzle and adjust the volume based on the number of events/second at the cell sorter (ideally ~200 events/second). We recommend including a non-stained control to exclude auto-fluorescent events and, at least the first time, a set of single-color staining to configurate and validate the staining pattern. Sort directly in 1,5 mL microcentrifuge tube pre-coated.

23. Primary cells are notoriously difficult to seed on coverslips. We recommend the use of round 10mm coverslips to ensure that a sufficient number of cells is achieved for immunostaining
24. We recommend viable cells seeding density that ranges from 10–50 thousands of cells for each coverslip.
25. If the cells are not completely attached on coverslip, we recommended to change medium with freshly one and leave the cells for another day at 37°C in a CO_2 incubator.
26. Be very gentle since the cells are not stable attached on the coverslip and the changes in surface tension that occur when the DMEM medium is entirely removed can damaged them.
27. The fixation is a critical step since the procedure is dependent on incubation time, temperature and pH. All these parameters should be kept constant among replicates.
28. At this step, the coverslips can be cover with 400µL of 10% glycerol/1X PBS and stored at 4 °C for up to 2 months.
29. Aliquot a small drop of diluted antibody (30 µL) on a microscope slide dressed in parafilm. Using forceps, take the coverslip with the cells out of the well, remove any drops on absorbent paper and put it on the antibody solution with the cells-side toward the solution.

30. From this step, carry out all the following procedures by protecting samples by light.
31. Dispense 8µL of mounting medium onto the microscope slide per 10-mm round glass coverslip. Keep the slides at 4°C protected from light in a slide box for later image acquisition through a confocal microscopy system.

3.6. Acknowledgment

We would like to thank Chiara Cordiglieri and Alessandra Fasciani from the INGM Imaging Facility for assistance during image acquisition and Maria Cristina Crosti for the INGM FACS Facility for assistance in cell sorting. We are grateful to Jessica Cassarà and Charles River service for mice maintenance and dissections.
This work is supported by FRRB (CP2_14/2018), Cariplo Foundation (2017-0649), CNR and Progeria Research Foundation (PRF 2021-81). FG is supported by AIRC fellowship.

3.7. Tables

ANTIBODY	FLUOROCHROME	IDENTIFIER	SPECIFICITY	DILUTION
TER119	PB	eBioscience, 48-5921-82	Erythrocytes	1:50
CD45	PB	eBioscience, 48-0451-82	Leukocyte	1:50
SCA1	FITC	eBioscience, 48-1159-81	FAPs	1:50
α7 Integrin	APC	AbLab, 67-001-05	MuSC	1:100
CD31	PB	eBioscience, 48-0311-82	Endothelia	1:50

Table–1 - Fluorochrome-conjugated antibodies used for the FACS-based isolation of mouse muscle digested cells. Viability staining is performed using TO-PRO™-3.

ANTIBODY	FLUOROCHROME	IDENTIFIER	SPECIFICITY	DILUTION
TER119	PB	eBioscience, 48-5921-82	Erythrocytes	1:100
CD45	PB	eBioscience, 48-0451-82	Leukocyte	1:100
CD326 (EpCAM)	PB	eBioscience, 48-5791-82	Epithelia	1:100
TIE2	PB	eBioscience, 13-5987-82	Pericyte	1:100
CD31	PB	eBioscience, 48-0311-82	Endothelia	1:100

Table–2 - Fluorochrome-conjugated antibodies used for the FACS-based isolation of mouse aortic fibromuscular stroma. Viability staining is performed using TO-PRO™-3.

ANTIBODY	FLUOROCHROME	IDENTIFIER	SPECIFICITY	DILUTION
TER119	PB	eBioscience, 48-5921	Erythrocytes	1:100
CD45	PB	eBioscience, 48-0451	Leukocyte	1:100
CD326 (EpCAM)	PB	eBioscience, 48-5791-82	Epithelia	1:100
TIE2	PB	eBioscience, 13-5987-82	Pericyte	1:100
CD31	PB	eBioscience, 48-0311-82	Endothelia	1:100
CD140b (PDGFRB)	PE-Vio® 770	Miltenyi Biotec, 130-105118	Pan Fibroblast	1:25
ER-TR7	FITC	cod	Reticular-Fibroblast	1:100

Table 3.- Fluorochrome-conjugated antibodies used to identify different cell populations present in mouse dermis. Viability staining is performed using TO-PRO™-3.

Antibody	Code	Host Species	Dilution	Incubation	Temperature
RING1B		rabbit	1:250	O/N	4°C
LAMB		mouse	1:100	2h	RT

Table 4 – List of primary antibodies used for immunofluorescence staining.

3.8. Legends

Figure 1 – Overview of murine FACS-based stroma isolation

Schematic diagram of the main steps involved in this protocol. Briefly, aorta, dermis and muscles fresh tissues are harvested from each mouse. The single cell suspensions derived from collagenase-dependent tissue-specific digestion protocols are stained to isolate murine stroma by FACS. immunofluorescence imaging technique are used to analyze the PcG architecture in the fibromuscular stroma (created with bio- render.com).

Figure 2 – Dissociation of murine tissues into single-cell suspensions

(A) Representative image of murine minced dermis, (**B**) whole aorta including ascending, aortic arch, descending, thoracic, and abdominal portions and (**C**) minced muscle sample in a petri dish (60x15mm). Bar length=1 cm. (**D**) Number of viable cells recovered per mg of each murine dermis (n=10) and aorta (n=10) specimens. (**E**) Table showing viable cells (second column) quantified using Trypan Blue staining, normalized to the initial tissue weight (first column), and reported as thousands of live cells per mg of tissue (third column) in murine dermis and aorta.

Figure 3 – Flow Cytometry gating strategy for murine dermal fibroblast isolation

A) Forward and side scatter gating (FSC-A vs SSC-A) to identify tissue-digested dermal cells and to remove debris. (**B**) FSC-A vs FSC-W plot allows doublets removal. (**C**) FSC-W vs TO-PRO-3 plot excludes low viability cells. (**D**) Immune cells ($CD45^+$), endothelial cells ($CD31^+$), Pericyte ($TIE2^+$), Erythrocytes ($TER119^+$), epithelial cells ($CD326^+$) are excluded to isolate the stromal cell fraction. (**E**) Pacific blue negative

cells are analyzed for their membrane PDGFRβ (CD140b) and ER-TR7 expression to isolate papillary (PDGFRβ $^{+}$/ ER-TR7^{-}, orange), reticular (PDGFRβ $^{+}$/ ER-TR7^{+}, brown) fibroblasts and the remaining double negative stromal cells (green).

Figure 4 – FACS gating strategy for murine aortic fibromuscular stroma isolation

A) Aortic cells are gated on forward and side scatter gating (FSC-A vs SSC-A). (**B**) Doublets and low viability cells are excluded using FSC-A vs FSC-W and (**C**) FSC-W vs TO-PRO-3 respectively. (**D**) Leukocyte (CD45+), Endothelia (CD31+), Pericyte (TIE2+), Erythrocytes (TER119+), are excluded to isolate stromal aortic subset.

Figure 5 – FACS gating strategy of murine muscle-associated stroma isolation

A) Cells selection by plotting SSC-A against the FSC-A. (**B**) Selection of the singlets executed by plotting FSC-W against the FSC-A. (**C**) Selection of PB-CD31^{-}/Ter119^{-}/CD45^{-} cells executed by plotting the Pacific Blue (PB) fluorescence against FSC-W. (**D**) PB negative cells were distinguished based on α7-integrin and Sca-1 expression in

MuSCs (Sca1-/α7-integrin), FAP (Sca1+/α7-integri-) and fibromuscular stromal cells (Sca1-/α7-integrin-, green).

Figure 6 – Immunofluorescence detection of Polycomb bodies

(**A**) Confocal microscope images from stroma cells in dermis, (**B**) aorta and (**C**) muscle specimens. Cells are stained using anti-RING1B, anti-LAMB and anti-PHALLOIDIN. Nuclei are stained with DAPI (blue). Scale bar, 20 µm.

3.9. Figure

Figure 1

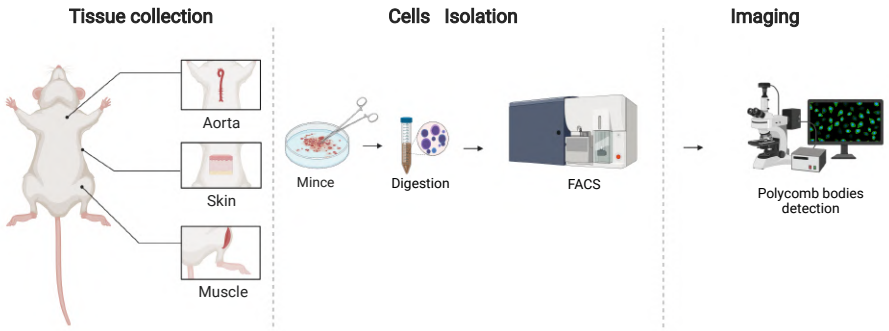

Figure 2

A.

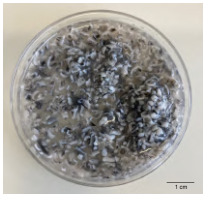

B.

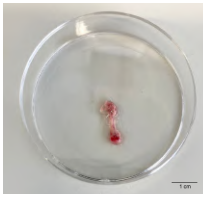

C.

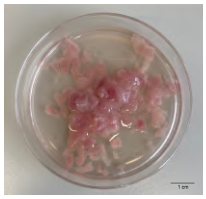

D.

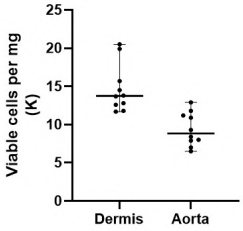

E.

Tissue	Weight [mg] **Median** (Range)	Viable Cells **Median** (Range)	Viable Cells per mg [K] **Median** (Range)
Dermis	**270** (220-340)	**3M** (2,5M-3,7M)	**14** (11,7-20,5)
Aorta	**35** (25-40)	**290 K** (250K-425K)	**9** (6,5-12,8)

Figure 3

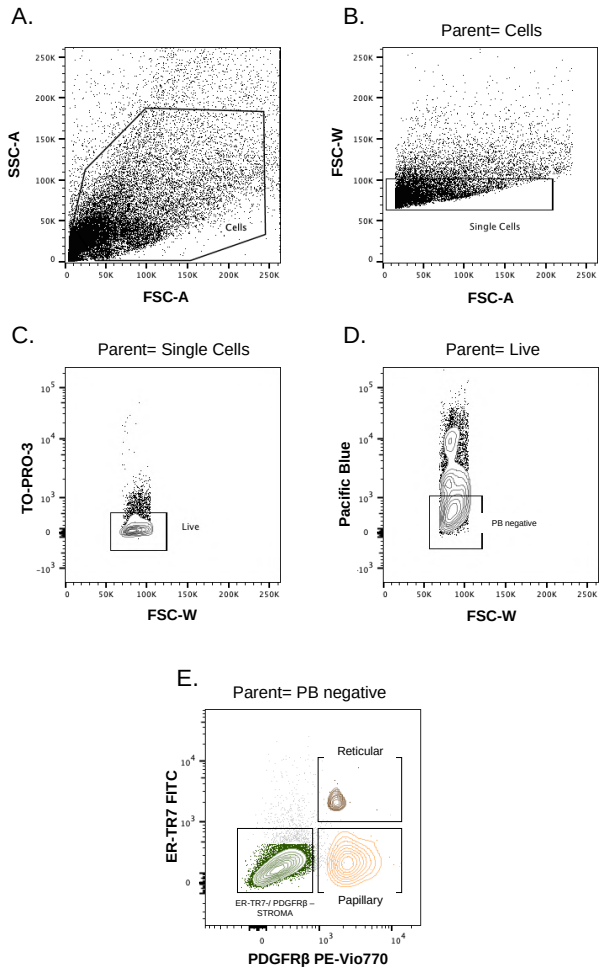
A.
SSC-A
FSC-A
Cells
B.
Parent= Cells
FSC-W
FSC-A
Single Cells
C.
Parent= Single Cells
TO-PRO-3
FSC-W
Live
D.
Parent= Live
Pacific Blue
FSC-W
PB negative
E.
Parent= PB negative
ER-TR7 FITC
PDGFRβ PE-Vio770
Reticular
Papillary
ER-TR7+/ PDGFRβ – STROMA

Figure 4

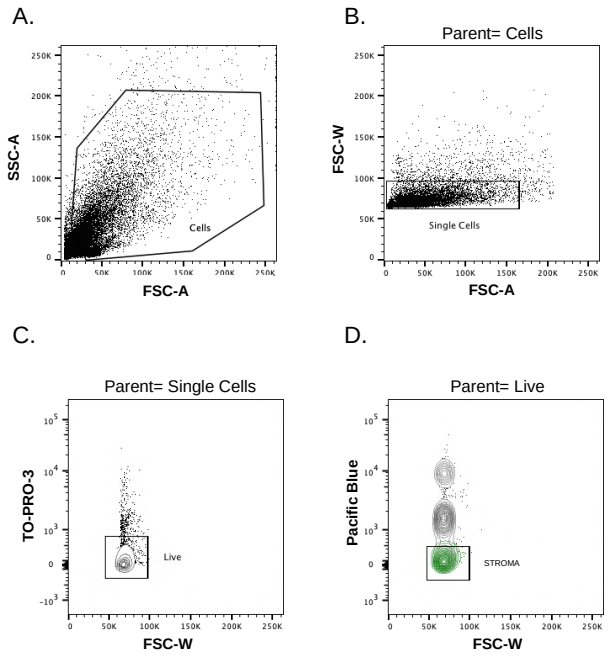
A.
B.
Parent= Cells
SSC-A
FSC-A
Cells
FSC-W
FSC-A
Single Cells
C.
D.
Parent= Single Cells
Parent= Live
TO-PRO-3
FSC-W
Live
Pacific Blue
FSC-W
STROMA

Figure 5

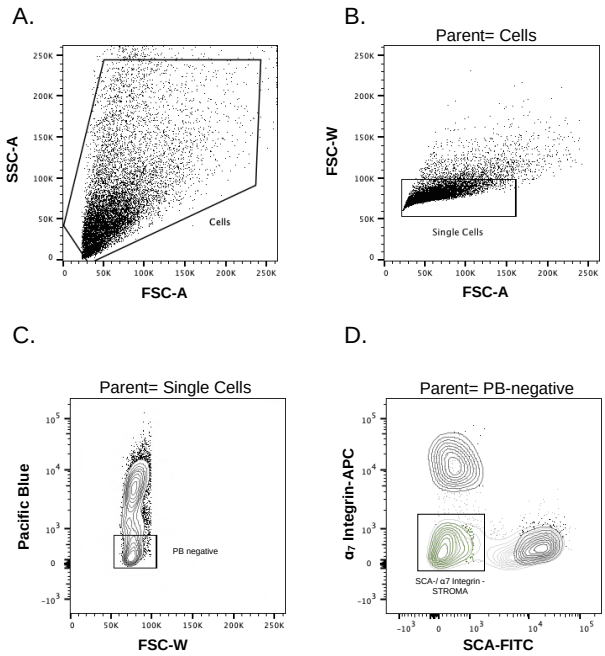
A.
SSC-A
FSC-A
Cells
B.
Parent= Cells
FSC-W
FSC-A
Single Cells
C.
Parent= Single Cells
Pacific Blue
FSC-W
PB negative
D.
Parent= PB-negative
α7 Integrin-APC
SCA-FITC
SCA-/ α7 Integrin - STROMA

Figure 6

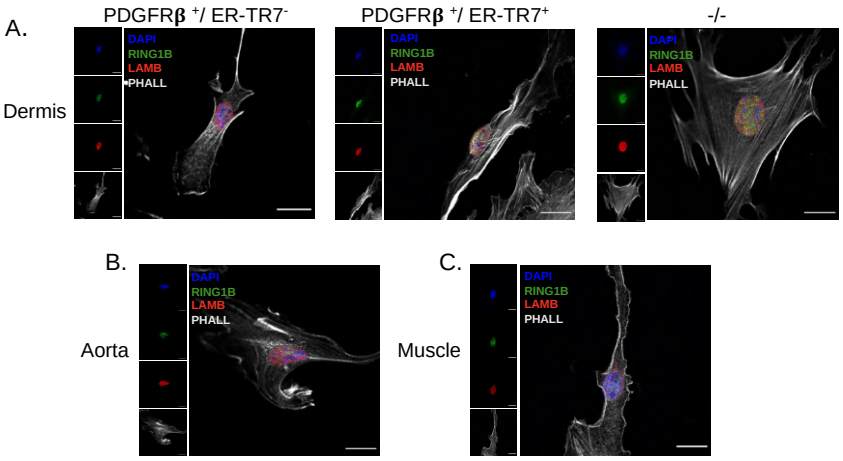
A.
PDGFRβ +/ ER-TR7-
PDGFRβ +/ ER-TR7+
-/-
Dermis
DAPI
RING1B
LAMB
PHALL
B.
Aorta
C.
Muscle

3.10. Reference to Chapter 3

[1] S. Levine, A. Weiss, H. Erdjument-Bromag, Z. Shao, P. Tempst, R. Kingston, The core of the polycomb repressive complex is compositionally and functionally conserved in flies and humans, Molecular and Cellular Biology. 22 (2002). https://doi.org/10.1128/MCB.22.17.6070-6078.2002.

[2] C. Lanzuolo, V. Orlando, Memories from the polycomb group proteins, Annu Rev Genet. 46 (2012) 561–589. https://doi.org/10.1146/annurev-genet-110711-155603.

[3] H. Wang, L. Wang, H. Erdjument-Bromage, M. Vidal, P. Tempst, R.S. Jones, Y. Zhang, Role of histone H2A ubiquitination in Polycomb silencing, Nature. 431 (2004) 873–878. https://doi.org/10.1038/nature02985.

[4] R. Cao, L. Wang, H. Wang, L. Xia, H. Erdjument-Bromage, P. Tempst, R.S. Jones, Y. Zhang, Role of histone H3 lysine 27 methylation in Polycomb-group silencing, Science. 298 (2002) 1039–1043. https://doi.org/10.1126/science.1076997.

[5] A. Laugesen, J.W. Højfeldt, K. Helin, Molecular Mechanisms Directing PRC2 Recruitment and H3K27 Methylation, Mol Cell. 74 (2019) 8–18. https://doi.org/10.1016/j.molcel.2019.03.011.

[6] W. Zhou, P. Zhu, J. Wang, G. Pascual, K.A. Ohgi, J. Lozach, C.K. Glass, M.G. Rosenfeld, Histone H2A monoubiquitination represses transcription by inhibiting RNA polymerase II transcriptional elongation, Mol Cell. 29 (2008) 69–80. https://doi.org/10.1016/j.molcel.2007.11.002.

[7] C.Y. Zhen, R. Tatavosian, T.N. Huynh, H.N. Duc, R. Das, M.

Kokotovic, J.B. Grimm, L.D. Lavis, J. Lee, F.J. Mejia, Y. Li, T. Yao, X. Ren, Live-cell single-molecule tracking reveals co-recognition of H3K27me3 and DNA targets polycomb Cbx7-PRC1 to chromatin, Elife. 5 (2016) e17667. https://doi.org/10.7554/eLife.17667.

[8] A.P. Bracken, N. Dietrich, D. Pasini, K.H. Hansen, K. Helin, Genome-wide mapping of Polycomb target genes unravels their roles in cell fate transitions, Genes Dev. 20 (2006) 1123–1136. https://doi.org/10.1101/gad.381706.

[9] R. Kalb, S. Latwiel, H.I. Baymaz, P.W.T.C. Jansen, C.W. Müller, M. Vermeulen, J. Müller, Histone H2A monoubiquitination promotes histone H3 methylation in Polycomb repression, Nat Struct Mol Biol. 21 (2014) 569–571. https://doi.org/10.1038/nsmb.2833.

[10] C. Lanzuolo, V. Roure, J. Dekker, F. Bantignies, V. Orlando, Polycomb response elements mediate the formation of chromosome higher-order structures in the bithorax complex, Nat Cell Biol. 9 (2007) 1167–1174. https://doi.org/10.1038/ncb1637.

[11] F. Bantignies, V. Roure, I. Comet, B. Leblanc, B. Schuettengruber, J. Bonnet, V. Tixier, A. Mas, G. Cavalli, Polycomb-dependent regulatory contacts between distant Hox loci in Drosophila, Cell. 144 (2011) 214–226. https://doi.org/10.1016/j.cell.2010.12.026.

[12] C. Lanzuolo, F. Lo Sardo, V. Orlando, Concerted epigenetic signatures inheritance at PcG targets through replication, Cell Cycle. 11 (2012) 1296–1300. https://doi.org/10.4161/cc.19710.

[13] C. Lanzuolo, F.L. Sardo, A. Diamantini, V. Orlando, PcG Complexes

Set the Stage for Epigenetic Inheritance of Gene Silencing in Early S Phase before Replication, PLOS Genetics. 7 (2011) e1002370. https://doi.org/10.1371/journal.pgen.1002370.

[14] T. Cheutin, G. Cavalli, Progressive polycomb assembly on H3K27me3 compartments generates polycomb bodies with developmentally regulated motion, PLoS Genet. 8 (2012) e1002465. https://doi.org/10.1371/journal.pgen.1002465.

[15] E. Cesarini, C. Mozzetta, F. Marullo, F. Gregoretti, A. Gargiulo, M. Columbaro, A. Cortesi, L. Antonelli, S. Di Pelino, S. Squarzoni, D. Palacios, A. Zippo, B. Bodega, G. Oliva, C. Lanzuolo, Lamin A/C sustains PcG protein architecture, maintaining transcriptional repression at target genes, J Cell Biol. 211 (2015) 533–551. https://doi.org/10.1083/jcb.201504035.

[16] N. Salvarani, S. Crasto, M. Miragoli, A. Bertero, M. Paulis, P. Kunderfranco, S. Serio, A. Forni, C. Lucarelli, M. Dal Ferro, V. Larcher, G. Sinagra, P. Vezzoni, C.E. Murry, G. Faggian, G. Condorelli, E. Di Pasquale, The K219T-Lamin mutation induces conduction defects through epigenetic inhibition of SCN5A in human cardiac laminopathy, Nat Commun. 10 (2019) 2267. https://doi.org/10.1038/s41467-019-09929-w.

[17] X. Zheng, J. Hu, S. Yue, L. Kristiani, M. Kim, M. Sauria, J. Taylor, Y. Kim, Y. Zheng, Lamins Organize the Global Three-Dimensional Genome from the Nuclear Periphery, Mol Cell. 71 (2018) 802-815.e7. https://doi.org/10.1016/j.molcel.2018.05.017.

[18] N. Briand, A.-C. Guénantin, D. Jeziorowska, A. Shah, M. Mantecon, E. Capel, M. Garcia, A. Oldenburg, J. Paulsen, J.-S. Hulot, C. Vigouroux, P.

Collas, The lipodystrophic hotspot lamin A p.R482W mutation deregulates the mesodermal inducer T/Brachyury and early vascular differentiation gene networks, Hum Mol Genet. 27 (2018) 1447–1459. https://doi.org/10.1093/hmg/ddy055.

[19] A. Oldenburg, N. Briand, A.L. Sørensen, I. Cahyani, A. Shah, J.Ø. Moskaug, P. Collas, A lipodystrophy-causing lamin A mutant alters conformation and epigenetic regulation of the anti-adipogenic MIR335 locus, J Cell Biol. 216 (2017) 2731–2743. https://doi.org/10.1083/jcb.201701043.

[20] A. Bianchi, C. Mozzetta, G. Pegoli, F. Lucini, S. Valsoni, V. Rosti, C. Petrini, A. Cortesi, F. Gregoretti, L. Antonelli, G. Oliva, M. De Bardi, R. Rizzi, B. Bodega, D. Pasini, F. Ferrari, C. Bearzi, C. Lanzuolo, Dysfunctional polycomb transcriptional repression contributes to lamin A/C-dependent muscular dystrophy, J Clin Invest. 130 (2020) 2408–2421. https://doi.org/10.1172/JCI128161.

[21] E. Sebestyén, F. Marullo, F. Lucini, C. Petrini, A. Bianchi, S. Valsoni, I. Olivieri, L. Antonelli, F. Gregoretti, G. Oliva, F. Ferrari, C. Lanzuolo, SAMMY-seq reveals early alteration of heterochromatin and deregulation of bivalent genes in Hutchinson-Gilford Progeria Syndrome, Nat Commun. 11 (2020) 6274. https://doi.org/10.1038/s41467-020-20048-9.

[22] D. O'Carroll, S. Erhardt, M. Pagani, S.C. Barton, M.A. Surani, T. Jenuwein, The polycomb-group gene Ezh2 is required for early mouse development, Mol Cell Biol. 21 (2001) 4330–4336. https://doi.org/10.1128/MCB.21.13.4330-4336.2001.

[23] P. Vizán, M. Beringer, L. Di Croce, Polycomb-dependent control of

cell fate in adult tissue, EMBO J. 35 (2016) 2268–2269. https://doi.org/10.15252/embj.201695694.

[24] J.J. Kim, R.E. Kingston, Context-specific Polycomb mechanisms in development, Nat Rev Genet. (2022). https://doi.org/10.1038/s41576-022-00499-0.

[25] F. Chiacchiera, A. Rossi, S. Jammula, A. Piunti, A. Scelfo, P. Ordóñez-Morán, J. Huelsken, H. Koseki, D. Pasini, Polycomb Complex PRC1 Preserves Intestinal Stem Cell Identity by Sustaining Wnt/β-Catenin Transcriptional Activity, Cell Stem Cell. 18 (2016) 91–103. https://doi.org/10.1016/j.stem.2015.09.019.

[26] P. Delgado-Olguín, L.T. Dang, D. He, S. Thomas, L. Chi, T. Sukonnik, N. Khyzha, M.-W. Dobenecker, J.E. Fish, B.G. Bruneau, Ezh2-mediated repression of a transcriptional pathway upstream of Mmp9 maintains integrity of the developing vasculature, Development. 141 (2014) 4610–4617. https://doi.org/10.1242/dev.112607.

[27] R. Li, X. Yi, X. Wei, B. Huo, X. Guo, C. Cheng, Z.-M. Fang, J. Wang, X. Feng, P. Zheng, Y.-S. Su, J.F. Masau, X.-H. Zhu, D.-S. Jiang, EZH2 inhibits autophagic cell death of aortic vascular smooth muscle cells to affect aortic dissection, Cell Death Dis. 9 (2018) 1–15. https://doi.org/10.1038/s41419-017-0213-2.

[28] A.H. Juan, A. Derfoul, X. Feng, J.G. Ryall, S. Dell'Orso, A. Pasut, H. Zare, J.M. Simone, M.A. Rudnicki, V. Sartorelli, Polycomb EZH2 controls self-renewal and safeguards the transcriptional identity of skeletal muscle stem cells, Genes Dev. 25 (2011) 789–794.

https://doi.org/10.1101/gad.2027911.

[29] S. Woodhouse, D. Pugazhendhi, P. Brien, J.M. Pell, Ezh2 maintains a key phase of muscle satellite cell expansion but does not regulate terminal differentiation, J Cell Sci. 126 (2013) 565–579. https://doi.org/10.1242/jcs.114843.

[30] C. Blanpain, E. Fuchs, Epidermal homeostasis: a balancing act of stem cells in the skin, Nat Rev Mol Cell Biol. 10 (2009) 207–217. https://doi.org/10.1038/nrm2636.

[31] I. Cohen, D. Zhao, C. Bar, V.J. Valdes, K.L. Dauber-Decker, M.B. Nguyen, M. Nakayama, M. Rendl, W.A. Bickmore, H. Koseki, D. Zheng, E. Ezhkova, PRC1 Fine-tunes Gene Repression and Activation to Safeguard Skin Development and Stem Cell Specification, Cell Stem Cell. 22 (2018) 726-739.e7. https://doi.org/10.1016/j.stem.2018.04.005.

[32] P. Lee, J. Decker, L. Shea, D.A. Beard, Plasticity of fibroblast transcriptional response to physical and biochemical cues revealed by dynamic network analysis, (2021) 2020.12.13.422572. https://doi.org/10.1101/2020.12.13.422572.

[33] B. Hinz, D. Lagares, Evasion of apoptosis by myofibroblasts: a hallmark of fibrotic diseases, Nat Rev Rheumatol. 16 (2020) 11–31. https://doi.org/10.1038/s41584-019-0324-5.

[34] J.L. Rinn, C. Bondre, H.B. Gladstone, P.O. Brown, H.Y. Chang, Anatomic demarcation by positional variation in fibroblast gene expression programs, PLoS Genet. 2 (2006) e119. https://doi.org/10.1371/journal.pgen.0020119.

[35] D.E. Discher, P. Janmey, Y.-L. Wang, Tissue cells feel and respond to the stiffness of their substrate, Science. 310 (2005) 1139–1143. https://doi.org/10.1126/science.1116995.

[36] V. Koliaraki, A. Prados, M. Armaka, G. Kollias, The mesenchymal context in inflammation, immunity and cancer, Nat Immunol. 21 (2020) 974–982. https://doi.org/10.1038/s41590-020-0741-2.

[37] B. Hinz, S.H. Phan, V.J. Thannickal, A. Galli, M.-L. Bochaton-Piallat, G. Gabbiani, The myofibroblast: one function, multiple origins, Am J Pathol. 170 (2007) 1807–1816. https://doi.org/10.2353/ajpath.2007.070112.

[38] G.G. Walmsley, Y. Rinkevich, M.S. Hu, D.T. Montoro, D.D. Lo, A. McArdle, Z.N. Maan, S.D. Morrison, D. Duscher, A.J. Whittam, V.W. Wong, I.L. Weissman, G.C. Gurtner, M.T. Longaker, Live fibroblast harvest reveals surface marker shift in vitro, Tissue Eng Part C Methods. 21 (2015) 314–321. https://doi.org/10.1089/ten.TEC.2014.0118.

[39] S. Mine, N.O. Fortunel, H. Pageon, D. Asselineau, Aging alters functionally human dermal papillary fibroblasts but not reticular fibroblasts: a new view of skin morphogenesis and aging, PLoS One. 3 (2008) e4066. https://doi.org/10.1371/journal.pone.0004066.

[40] G.G. Walmsley, Z.N. Maan, M.S. Hu, D.A. Atashroo, A.J. Whittam, D. Duscher, R. Tevlin, O. Marecic, H.P. Lorenz, G.C. Gurtner, M.T. Longaker, Murine Dermal Fibroblast Isolation by FACS, J Vis Exp. (2016). https://doi.org/10.3791/53430.

[41] C. Mozzetta, Isolation and Culture of Muscle Stem Cells, Methods Mol Biol. 1480 (2016) 311–322. https://doi.org/10.1007/978-1-4939-6380-

5_27.

[42] Single Myofiber Isolation and Culture from a Murine Model of Emery-Dreifuss Muscular Dystrophy in Early Post-Natal Development | Protocol (Translated to Italian), (n.d.). https://www.jove.com/it/v/61516/single-myofiber-isolation-culture-from-murine-model-emery-dreifuss?language=Italian (accessed July 25, 2022).

Chapter 4 Chromatin structure alterations modulate muscle niche functionality in chronological aging

4.1. Abstract

The correct 3D organization of the genome is known to influence the spatiotemporal expression of lineage-specific genes during stem cell differentiation and aging processes. We introduce a novel evolution of the SAMMY-seq technique to precisely map genomic regions separated by their biochemical properties. This single-handedly technique enables the identification of heterochromatic and euchromatic domains and their compartmentalization in the nuclear space. Crucial practical advantages of this method include: its applicability on as little as 10K cells; reduced costs; few manipulation steps and short execution time. In postnatal Muscle Stem Cells (MuSCs) we observed a reproducible distribution of euchromatic and heterochromatic genomic domains, in line with known epigenetic signatures. Our findings highlight how MuSCs over life exhibit a global steady chromatin organization, accompanied by solubility changes that favour processes such as MuSCs activation but may become obstacles during aging for proper pool maintenance. Still, we describe environmental alterations of the muscle niche, emphasizing a supportive population of MuSCs, namely Fibroadipogenic progenitors (FAPs), which exhibit dramatic transcriptional alterations during aging. Our extensive characterization of the environment and chromatin organization in MuSCs expands our understanding of quiescence, activation

and aging processes, laying the groundwork for the study of the role of the epigenome in pathological conditions.

4.2. Results

4.2.1.Postnatal and adult Muscle Stem Cells (MuSCs) exhibit different grades of activation and proliferation

Skeletal muscle tissue is characterized by great regenerative potential, permitted by the subsistence of muscle stem cells (Relaix et al., 2021; Sambasivan et al., 2011).

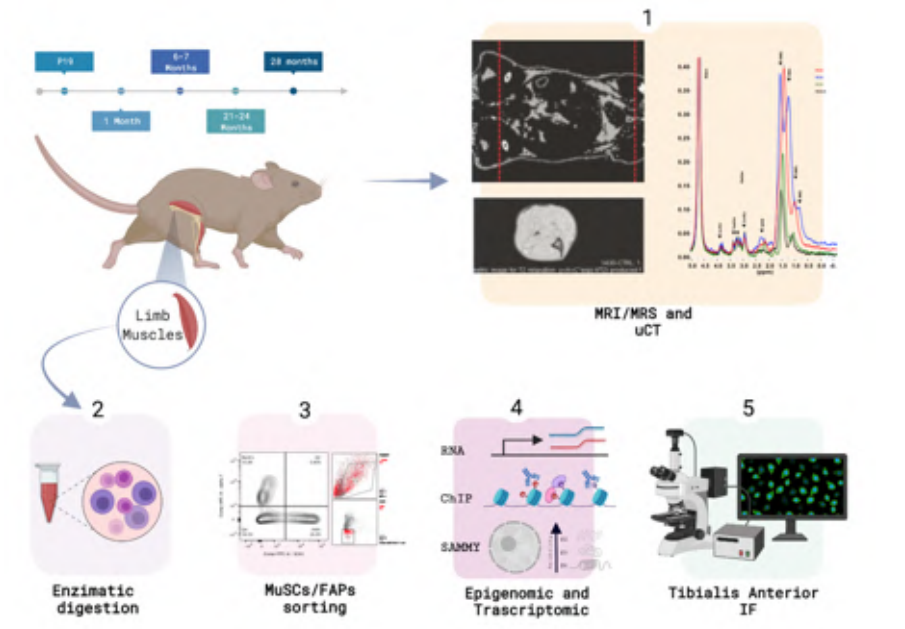

Figure 12. Experimental Design: Mice of different ages were subjected to MRI/MRS and µCT (1). Limb muscles were excised and enzymatically digested to obtain a cell suspension (2). The cell suspension was then stained and FACS-sorted to obtain two cell populations, MuSCs and FAPs (3). These populations were further divided to perform RNA-seq and SAMMY-seq (4). A pool of satellite cells extracted from 10-15 mice was used to perform ChIP-seq (4). The tibialis anterior was embedded in OCT and flash-frozen for immunofluorescence analysis (5). This schematic representation is created with BioRender.com

The MuSCs cell state changes during the life period, adapting to the physiological request over the time (Bachman et al., 2018b; Gattazzo et al., 2020; Lepper et al., 2009; Sousa-Victor et al., 2014). To investigate the MuSCs function and dysfunction we focused our attention on four different stages: postnatal (P19), adult (6-7 months), old (21-24 months), and geriatric (27-28 months) (Fig. 1). Briefly, before harvesting limb muscle tissue, adult, old, and geriatric mice were subjected to micro-computed tomography (μCT) and magnetic resonance imaging/spectroscopy (MRI/MRS). Due to the small body size, we were not able to perform the same examinations on postnatal mice. After limb muscle collection and enzymatic digestion, the cell suspension was stained, and fluorescence-activated cell sorting (FACS) was used to obtain two different populations: muscle stem cells (MuSCs) and fibro-adipogenic progenitors (FAPs) (Suppl. Fig. 1). Both freshly isolated cell types were subjected to genome-wide analyses such as RNA-seq and SAMMY-seq. From the same mouse, before the limb muscle

collection, Tibialis Anterior (TA) muscle was collected and embedded for immunofluorescence analysis (Fig.1).

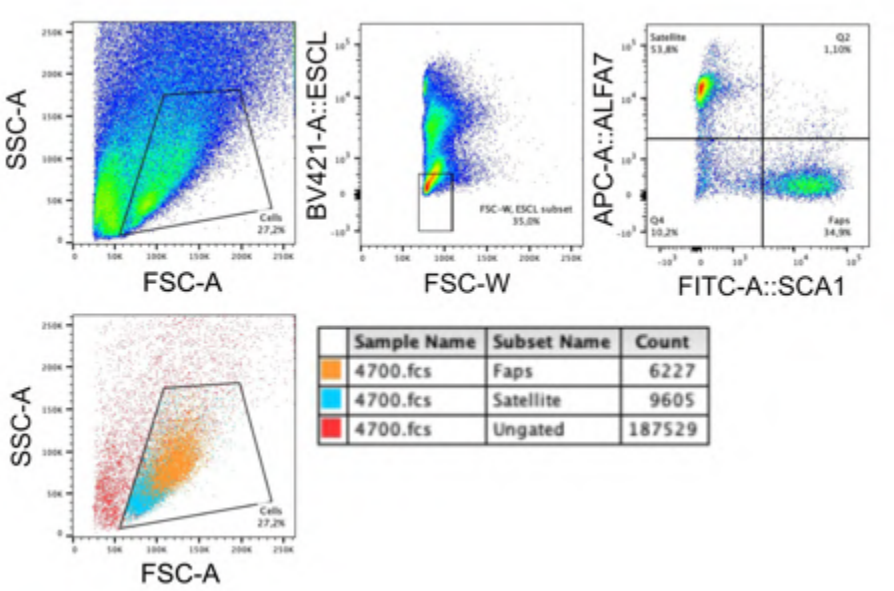

Supplementary Figure 1. Flow Cytometry Gating Strategy. Cell suspension from muscle-digested tissue was stained with PB-CD45/ PB-CD31/ PB-Ter119/ FITC-Sca1/APC-alpha 7 integrin antibodies. Firstly, debris was eliminated through forward and side scatter gating (FSC-A vs SSC-A). FSC-W versus PB - CD45/CD31/ter119 allows lineage negative exclusion. Finally, FAPs were sorted as Sca-1+ while MuSCs were sorted as alpha 7 integrin+.

For ChIP-seq experiments, we used a pool of MuSCs extracted from 10-15 mice. Initially, we focused on defining the MuSCs niche composition at different life stages (Fig. 2, 3). As already reported (Gattazzo et al., 2020), the postnatal period is marked by a high proportion of activated (PAX7+/MYOD+) (Fig. 2a, 2b) and proliferative (PAX7+/KI67+) MuSCs (Fig. 3a, 3b). The percentage of activated MuSCs decreased significantly in adulthood and old age, dropping in the geriatric stage (Fig. 2b). Whereas we could see proliferative MuSCs in postnatal stage,

we did not detect proliferation in observed stages of adult life

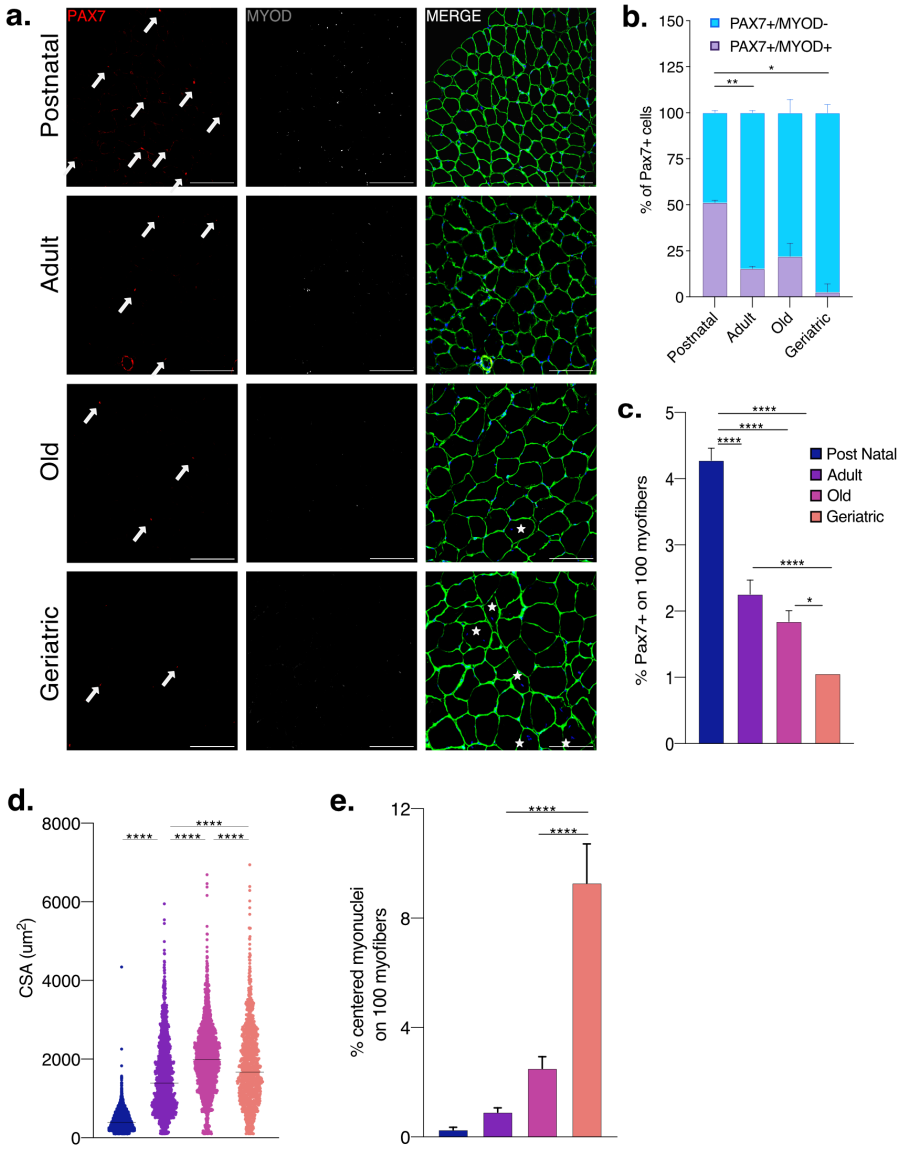

Figure 13. Activated and quiescent Muscle Stem Cells during the life course. Immunofluorescence on Tibialis Anterior (TA) sections at different ages for Pax7/MyoD/Laminin/Dapi (a) and relative quantification (b). White arrow identify PAX7 positive cells, whereas white star identify centered nuclei. Data are shown as mean ± SEM; *p<0.05, **p<0,001, calculated by 2way ANOVA and Bonferroni's multiple comparison test. Evaluation of the total percentage of Pax7 positive cells every 100 myofibers (c). Quantification of mean fiber cross-sectional area (d). Centered

nucleated myofiber count (e). Data are shown as mean ± SEM; *p<0.05, ****p<0,0001, calculated by 1way ANOVA, Tukey's multiple comparison test (c, d, e). (Scale bar, 100um)

(Brack et al., 2005; Carlson & Conboy, 2007; Sousa-Victor et al., 2014)(Fig. 3b). Consistent with the establishment of the stem pool, the overall number of MuSCs decreased significantly in the adult compared with the postnatal period and progressively declined in old and geriatric ages (Fig. 2c).

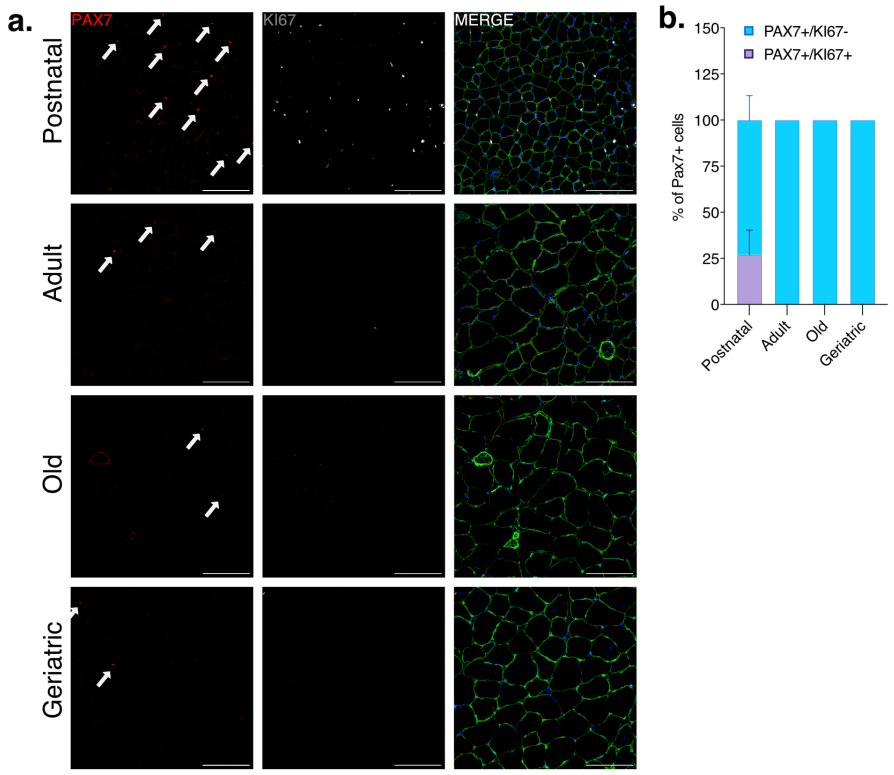

Figure 3. Muscle Stem Cells proliferation status during the life course. Immunofluorescence on Tibialis Anterior (TA) sections at different ages for Pax7/KI67/Laminin/Dapi (a) and relative quantification (b). White arrow identify PAX7 positive cells. Data are shown as mean ± SEM. (Scale bar, 100um)

As expected, the Cross-Sectional Area (CSA) of the adult murine muscle fibers was in average higher than the postnatal (Fig. 2d). Old mice showed a significant increase in CSA compared with adult mice (Fig. 2d), accompanied by a slight increase in the percentage of activated PAX7+/MYOD+ MuSCs (Fig. 2b), suggesting muscle accretion due to hyperplasia rather than hypertrophy. Geriatric compared with old mice exhibited a CSA decrease (Fig. 2d). Of note, we also found an increase of center-nucleated myofibers (Fig. 2e), that suggests the presence of muscle regeneration.

To study at the molecular level the age dependent MuSCs states, we analysed total RNA sequencing using the iDEP tool (Ge et al., 2018), for Differential Expression (DE) analysis the significance threshold was set to False Discovery Rate (FDR) ≤ 0.05 and minimum Fold Change as 2. We sequenced at least three replicates for each time point, with an acceptable sequencing minimum of approximately fifteen million uniquely mapped reads (Suppl. Fig. 2a). We observed high correlation degree ($r > 0.87$) across all biological replicates, confirming the purity of our samples (Suppl. Fig. 2b).

Firstly, we decided to focus our analysis on the Postnatal-Adult comparison. Principal Component Analysis (PCA) clearly showed that postnatal and adult MuSCs segregate into two distinct groups (Fig. 4a). DE analysis highlighted that 1.970 genes (1067 upregulated and 903 downregulated) change their expression during the passage from the postnatal to the adult

stage (Fig. 4b). Reactome pathway-based enrichment analysis was performed to understand the functional significance of the genes specific for Postnatal and Adult MuSCs (Fig. 4c).

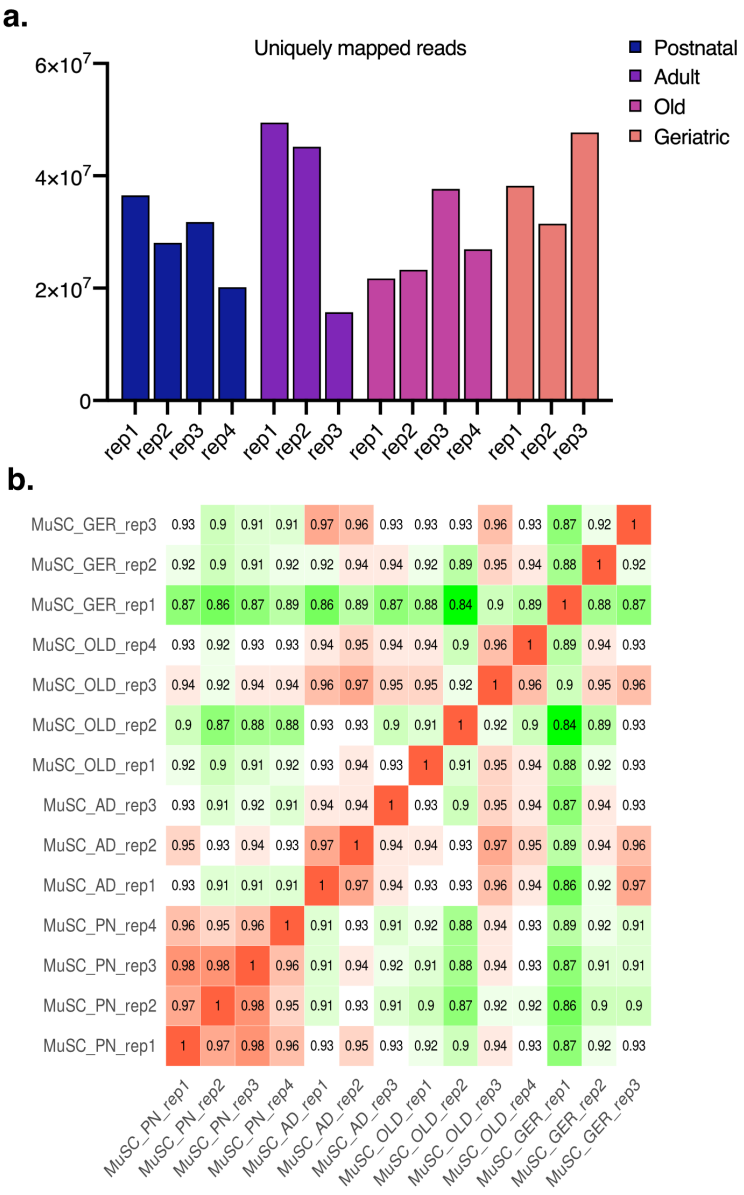

Supplementary Figure 2. RNA-seq quality control. Millions of RNA-seq uniquely mapped reads per sequenced sample (a). Spearman Correlation Analysis between replicates and samples (b).

Up-regulated genes in the postnatal stage were enriched mainly in terms related to Cell Cycle (*Cdc20, Cdc45, Ccnd2, Ccne1 Mcm2, Mcm5*) and Nucleosome Assembly, reflecting their proliferative activity (Fig. 4c).

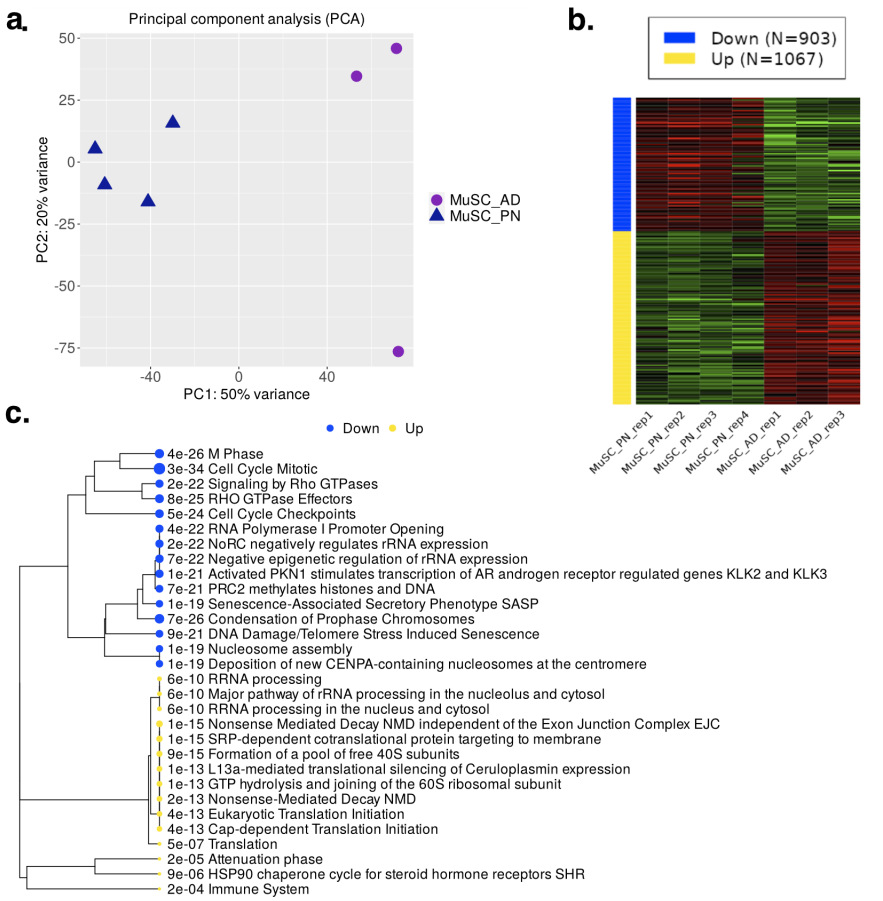

Figure 4. Transcriptional profile of Adult and Postnatal MuSCs. Principal Component Analysis (PCA) of the values of gene expression among the two indicated groups: 4 postnatal samples and 3 adult samples. Each dot represents a mouse (a). Heatmap of Differentially Expressed Genes (DEG) in the comparison of Adult versus Postnatal MuSCs. The blue bar represents down-regulated genes (894), the yellow bar represents up-regulated genes (995) (b). Enriched pathways analysis using the Reactome database for unique genes. Gene sets closer to the tree share more genes. Sizes of the dot corresponding to adjusted P-values (c).

On the other hand, adult up-regulated genes were enriched in terms related to translation Initiation, signalling in the immune system (*Stat3, Fos, Nfkb2, Il6*) and Nonsense-mediated RNA Decay (NMD), an important pathway necessary for the selective degradation of RNA transcript in stem cells (Lou et al., 2016) (Fig. 4c). Interestingly, it has been demonstrated that in C2C12 myoblasts the *myogenin* RNA is a direct target of NDM (Gong et al., 2009).

Then, we shifted our focus to examine the transcriptional profile between adulthood and aging (Fig. 5). We identified a total of 82 differentially enriched genes (DEGs) in old MuSCs (Fig. 5a), 52 upregulated (Fig. 5b) and 30 downregulated genes (Fig 5c). Enrichment pathway analysis of biological process reveals that upregulated genes were enriched for terms related to muscle process and contraction (*Myl2, Trpc3, Tnni2, Acta1, Tnnt3*) (Fig 5d), echo of the slight increase in the number of activated MuSCs at 22-24 months and for term linked to detoxification (*Hbb-bs, Hbb-bt*), suggesting a transcriptional response of the old MuSCs to the environment of the evolving niche (Fig. 5d). The number of differentially expressed genes exhibits an incremental trajectory with age (Fig 5 b, c). Geriatric MuSCs exhibit 329 DEGs with respect to old muscle stem cells (Fig. 5a), 134 upregulated (Fig. 5b) and 197 downregulated genes (Fig.5c). Up-regulated genes show enrichment for genes related to ECM and collagen organization (*Adamts2, Mmp13, Fn1, Fmod, Col1a1, Col1a2,*

Col14a1, Col27a1) (Fig 5e), together with development of vascular system.

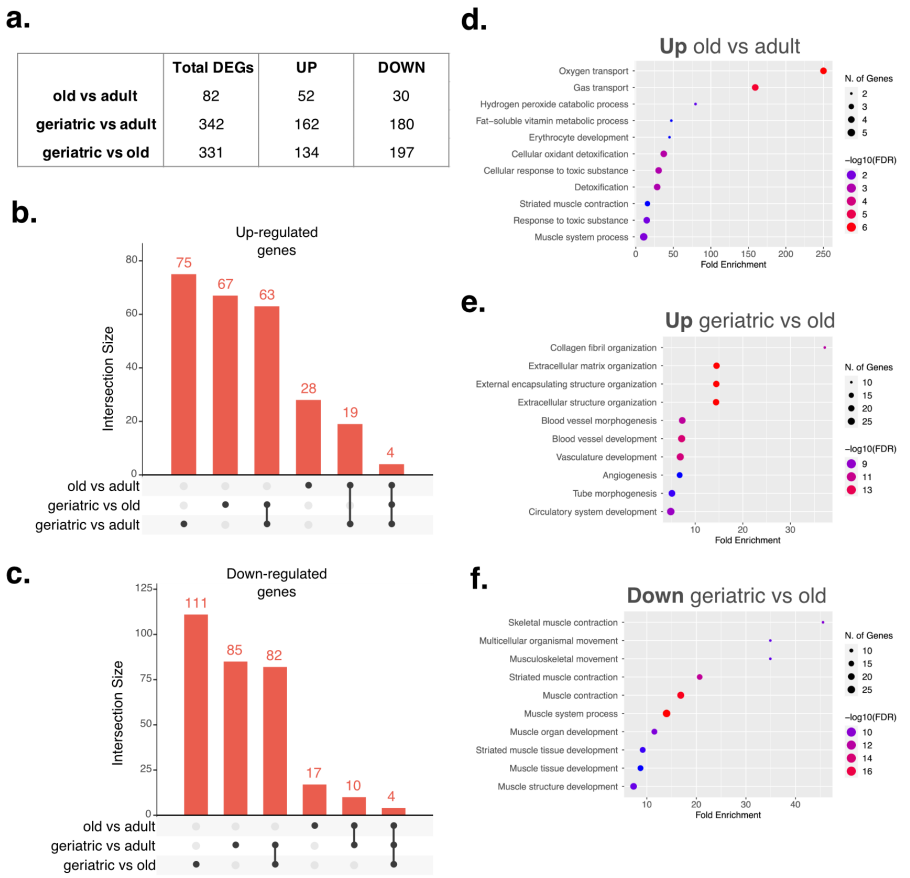

	Total DEGs	UP	DOWN
old vs adult	82	52	30
geriatric vs adult	342	162	180
geriatric vs old	331	134	197

Figure 5. Transcriptional profile of adult, old and geriatric MuSCs. Table of the number of DEGs (a). The upSet plot shows the intersections of the three datasets of up/down-regulated genes in the combination matrix (bottom) and the columns show how many genes are in each intersection (b, c). Enriched pathways of biological process for unique genes in the comparison old vs adult MuSCs, geriatric vs old (d, e, f). Gene sets closer to the tree share more genes. Sizes of the dot corresponding to adjusted P-values.

On the other hand, downregulated genes were enriched uniquely for terms related to muscle development and contraction (*Pax7, Myf5, Hey1, Myh2, Myh1, Myh4, Ryr3, Myl3, Tnnt3*) (Fig. 5f),

suggesting a defect in the maintenance of the transcriptional program proper for the cell identity of the muscle stem cell.

In summary, immunofluorescence analysis of TA muscle and gene expression profile of postnatal, adult, old and geriatric MuSCs highlight how different staged niches are characterized by distinct MuSCs pool composition.

4.2.2. Epigenetic remodeling accompanies postnatal muscle stem cells to the adult road.

It is well known that chromatin organization is critical in the transition from quiescence to activation in MuSCs (Boonsanay et al., 2016; L. Liu et al., 2013; Shi & Garry, 2006). To better understand how epigenetic regulation affects MuSCs in postnatal and adult life, we first exploited our RNA-seq data of chromatin-associated epigenetic modifiers.

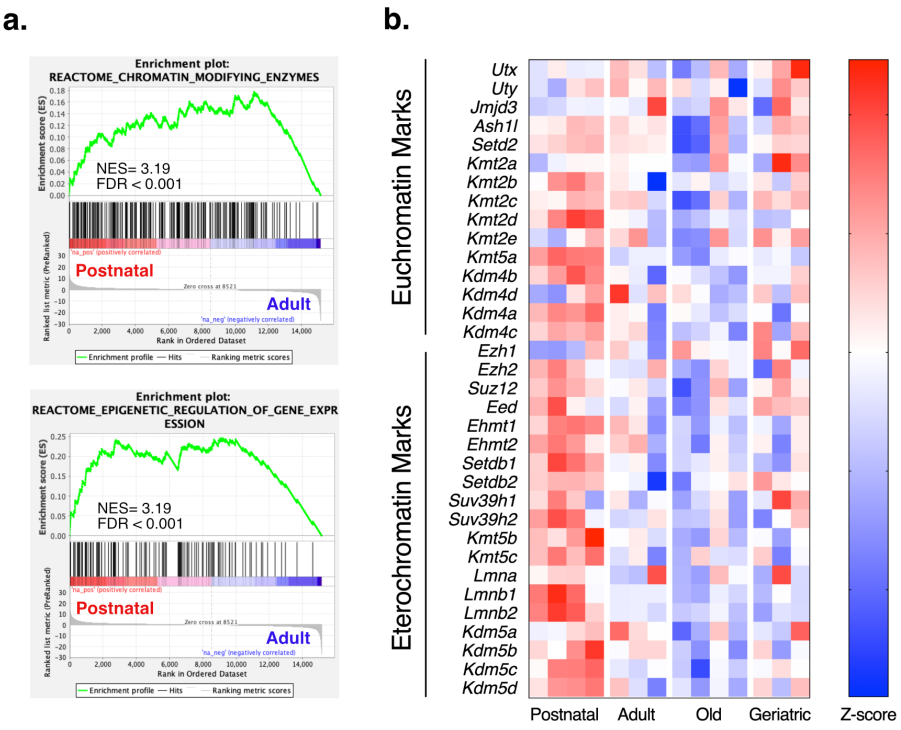

Figure 6. Postnatal MuSCs compared with adult MuSCs display upregulation of genes involved in chromatin remodelling. Pre-ranked GSEA (metric = -log10Pvalue x sign log fold change) from postnatal versus adult MuSCs (a). Heatmap of gene expression for methyltransferase and chromatin enzymes in postnatal, adult, old and geriatric muscle stem cells plotted as Z score (b).

Pre-ranked Gene set enrichment analysis (GSEA) highlighted a positive correlation in postnatal MuSCs with terms linked to Epigenetic regulation of gene expression and Chromatin Modifying Enzymes (Fig. 6a).

Given the importance of histone modifications in gene expression regulation, we analysed the expression of genes involved in the deposition and removal of histone modifications related to open and closed chromatin, such as the trimethylation of lysine 4 and 36 of histone 3 (Euchromatin) (e.g., *Kmt2a-e, Setd2)*, and the trimethylation of lysine 9 and 27 of histone 3 (Heterochromatin) (e.g., *Ehmt1-2, Ezh2*) (Fig. 6b). The majority of histone methyltransferase and demethylase (*Suv39h1, Suv39h2, Setdb1, Kdm4a, Kdm5c*) and nuclear lamina proteins (*Lmna, Lmnb1/2)* were downregulated in Adult MuSCs respect to the postnatal stage (Fig. 6b), confirming an epigenetic activity that sustain MuSCs activation and proliferation.

To better characterize epigenetic changes in postnatal and adult MuSCs we performed chromatin immunoprecipitation-sequencing (ChIP-seq) on muscle stem cells isolated from muscles of postnatal and adult mice with antibodies specific for H3K36me3, H3K4me3 (markers of active transcription) or H3K9me3, H3K27me3 (marker of constitutive and facultative heterochromatin, respectively).

Firstly, we investigated by ChIP-seq the distribution of H3K36me3. Quality control, performed by a bioinformatics tool called ChiC (Livi et al., 2020), shows that, as expected, the

distribution of enrichment for H3K36me3, both in postnatal and adult MuSCs (Suppl. Fig. 3a, b, respectively) is preferentially at the body gene level.

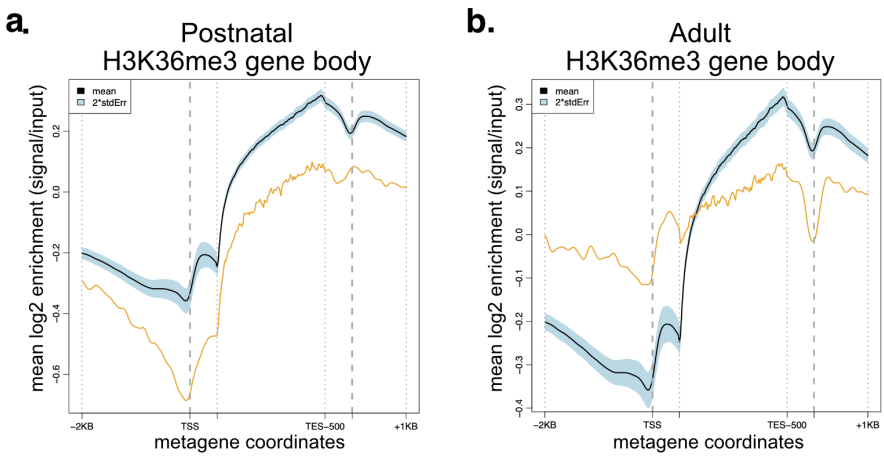

Supplementary Figure 3 Quality control H3K36me3 ChIP-seq. ChIP-seq metaprofile enrichment from H3K36me3 in postnatal and adult muscle stem cells generated by ChIP-seq quality Control framework (ChIC) (Livi et al., 2020). Average log2 transform normalized (ChIP over input) enrichment signals are shown for postnatal (a) and adult (b). Muscle stem cell (yellow line) compared to the mean signal of reference compendium datasets for the same chromatin mark (black line) along with its ±2 standard error interval (blue shadow).

Genome-wide analysis shows a diminished percentage of genome covered by H3K36me3, but a higher number of peaks in adult MuSCs (Fig.7 a, b). Peak calling and annotation of genes, performed with the GENCODE vM25 (Frankish et al., 2021), uniquely covered in postnatal and adult MuSCs revealed 1405 and 2355 genes enriched in postnatal and adult MuSCs, respectively (Fig. 7c). Gene Ontology analysis of postnatal-

specific H3K36me3 peaks was enriched for terms associated

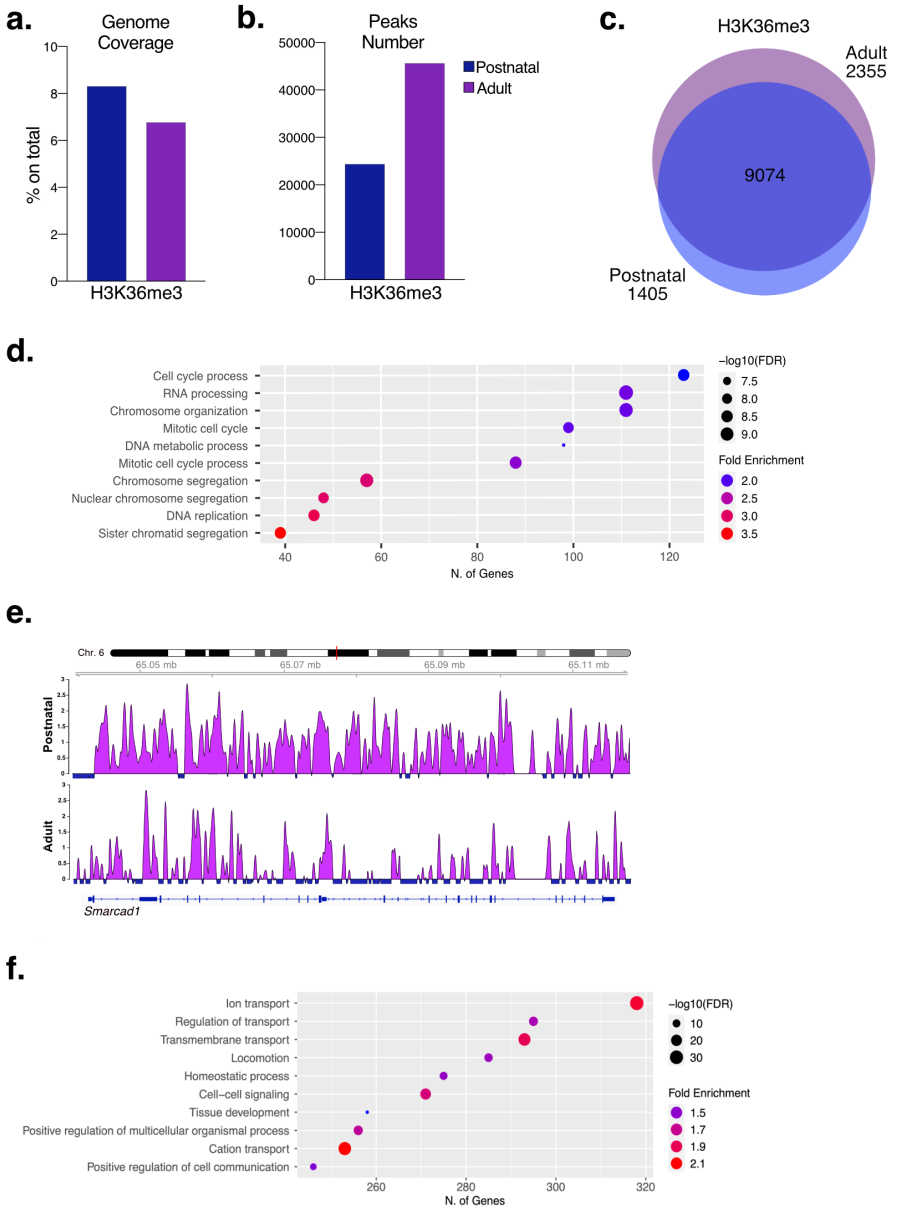

Figure 7. H3K36me3 profile in postnatal and adult muscle stem cells. Percentage of the genome covered by H3K36me3 in postnatal and adult MuSCs (a). The number of H3K36me3 Peaks enriched in postnatal and adult MuSCs, analysis performed with epic2 (Stovner & Sætrom, 2019) (b). Proportional Venn diagram (Hulsen et al., 2008) of genes covered by h3k36me3 in postnatal and adult MuSCs (c). Enriched pathways analysis of biological process for H3K36me3-unique genes in postnatal MuSCs (d). Visualization of representative genes, Smarcad1, of H3K36me3 signal over input in

postnatal and adult MuSCs (e). Enriched pathways analysis of biological process for H3K36me3-unique genes in adult MuSCs (f).

with cell cycle, chromosome segregation and DNA metabolic process (Fig. 7d), confirming RNA-seq data (Fig. 4c) and track analysis of H3K36me3 coverage at specific genes related to the cell cycle, such as *Smarcad1* (Bantele et al., 2017) (Fig. 7e). On the other hand, adult-specific H3K36me3 peaks cover genes involved in homeostatic processes, cell-cell communication, and regulation of transport (Fig. 7f).

Then, we analysed the distribution of H3K9me3. By visual inspection of signal tracks, we noticed a general decrease of chromatin occupancy from postnatal to adult MuSCs (Fig.8a).

Genome-wide analysis confirms a lower number of peaks and a diminished percentage of genome covered by H3K9me3 in adult MuSCs (Fig. 8b, 8c). To further confirm the difference in H3K9me3 levels, we isolated fresh MuSCs from postnatal and adult mice and we performed immunofluorescence analysis (Fig. 8d). We found a decline, although not significant, in H3K9me3 signal intensity (Fig. 8e). Then, we analysed the differentially enriched H3K9me3 peaks in the postnatal or adult MuSCs: we identified genes with promoter included in these peaks and we performed Gene Ontology enrichment analysis of biological processes. Postnatal-specific H3K9me3 peaks are enriched in terms related to neuro/head developmental processes (*Tnr, Fezf2, Foxp2, Tbr1*) (Chiu et al., 2014; Kolk et al., 2006; Tsai et al., 2014; Zuccotti et al., 2014) (Fig. 8f, g), suggesting the

repression of alternative pathways during muscle differentiation. In adult MuSCs most of the terms were associated with the regulation of transcription (Fig. 8h), that is maintained at a low level in quiescence (van Velthoven et al., 2017).

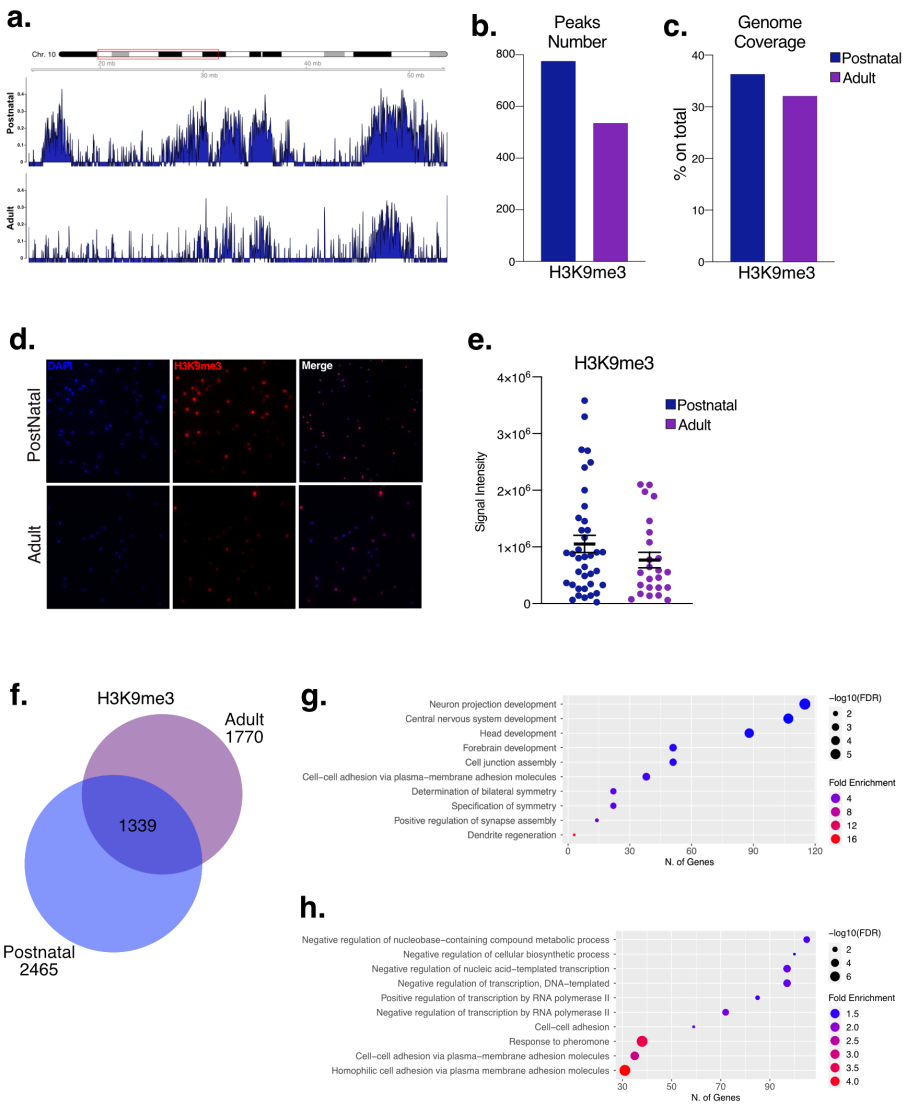

Figure 8. H3K9me3 profile in postnatal and adult MuSCs. Visualization of a representative genomic region on chromosome 10 (chr10:13,532,784-54,862,636) of H3K9me3 signal over input in postnatal and adult MuSCs (a). The number of H3K9me3 Peaks enriched in postnatal and adult MuSCs, analysis performed with epic2 *(Stovner & Sætrom, 2019)* (b). Percentage of genome covered by H3K9me3 in postnatal and

adult muscle stem cell (c). Representative image of H3K9me3 IF in postnatal and adult MuSCs (d), and respective quantification of signal intensity. Data are shown as mean ± SEM (e). Proportional Venn diagram (Hulsen et al., 2008) of genes covered by H3K9me3 in postnatal and adult muscle stem cell (f). Enriched pathways analysis of biological process of genes included in H3K9me3-unique peaks in postnatal and adult MuSCs (g, h).

Among the genes, enriched in adult-specific H3K9me3 peaks we found pathways important for embryonic (*Irx2, Hnrnpk, Cnot2, Hoxd9*) (Bakhmet et al., 2019; Bernstein et al., 2006; Taniguchi et al., 2011; Zheng et al., 2012), osteogenic (*Bmp7, Foxf2*) (Shen et al., 2009; Tanaka et al., 2022), hematopoietic (*Gata3, Myb*) (Baker et al., 2014; Ku et al., 2012), mesenchymal (*Sox5, Fsn*) (Beites et al., 2009; Xu et al., 2018) and cardio (*Gata6*) (Gharibeh et al., 2021) development.

Thereafter, we analysed the already published ChIP-seq dataset for H3K4me3 and H3K27me3 in postnatal and adult MuSCs (Bianchi et al., 2020; Liu et al., 2013; Machado et al., 2017). We first verified the quality of the published datasets by analysing the metaprofile with ChIC (Livi et al., 2020). As expected, H3K4me3, in both postnatal and adult MuSCs, exhibited a very sharp profile at the transcription start site (TSS) in both datasets (Suppl. Fig. 4a, b) while H3K27me3 presented a broader distribution that includes the region upstream the TSS (Suppl. Fig. 4d, e). Peak calling and annotation analysis of H3K4me3 doesn't emphasize significant changes in the number and identity of genes marked in postnatal and adult MuSCs (Suppl. Fig. 4c). On the other hand, Adult MuSCs are characterized by a significantly inferior number

of genes marked by H3K27me3 (Suppl. Fig. 4f), in agreement

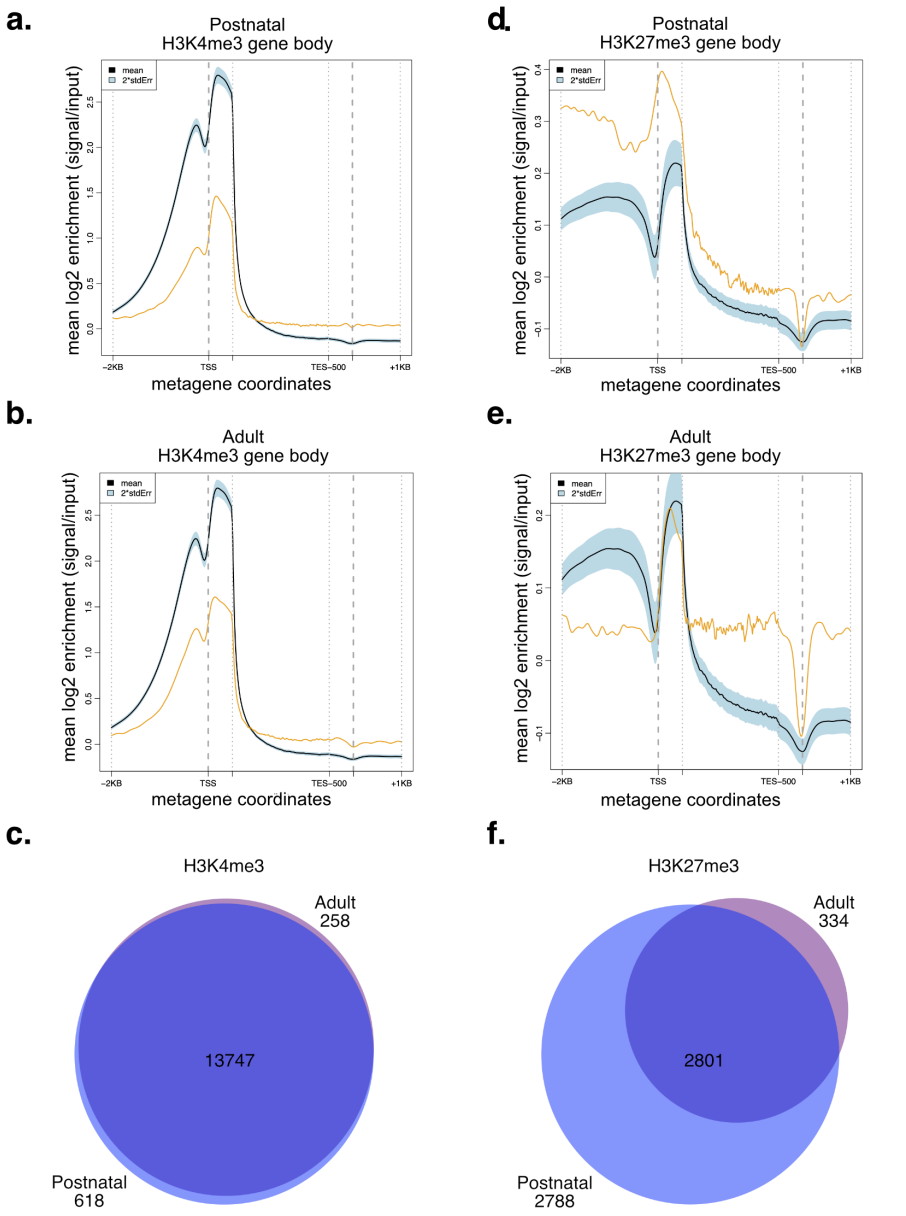

Supplementary Figure 4. ChIP-seq Quality controls. ChIP-seq metaprofile enrichment from published datasets H3K4me3 (a, b) and H3K27me3 (d, e) in postnatal and adult MuSCs (Bianchi et al., 2020a; L. Liu et al., 2013; Machado et al., 2017) executed by ChIP-seq quality Control framework (ChIC) (Livi et al., 2020). Average log2 transform normalized (ChIP over input) enrichment signals are shown for tested ChIP-seq samples (yellow line) compared to the mean signal of reference compendium datasets for the same chromatin mark (grey line) along with its ±2 standard error interval (blue

shadow) (a, b). Proportional Venn diagram (Hulsen et al., 2008) of genes marked by H3K4me3 (c) and by H3K27me3 (f) in postnatal and adult MuSCs.

with the downregulation of the methyltransferase *Ezh2* and the upregulation of the histone demethylase *Utx (*Fig. 6b). Gene ontology enrichment analysis of biological process in postnatal-specific genes covered by H3K27me3 highlights term related to muscle development and morphogenesis (*Pax7, Myf5, Hey2, Bmpr1a*), but also extracellular matrix assembly and cell adhesion (*Col1a1, Chd2, Itga8, Egfl6*) (Suppl. Fig. 5). On the contrary, adult MuSCs genes marked by H3K27me3 were not enriched for any significant term.

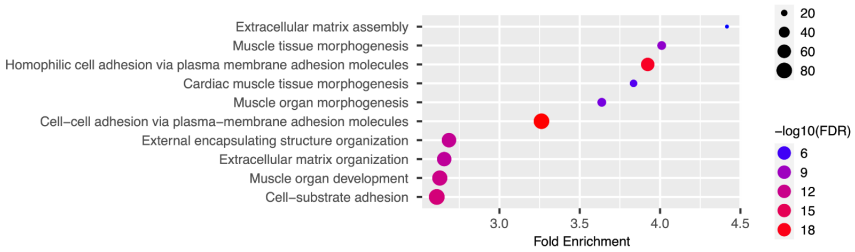

Supplementary Figure 5. H3K27me3 in postnatal MuSCs. Enriched pathways analysis of biological process of genes included in H3K27me3-unique peaks in postnatal MuSCs.

Taken together, these observations confirm the importance of epigenetic remodelling in the passage from the postnatal to adult life.

4.2.3. Four fractions Sequential Analysis of MacroMolecules accessibilitY (4fSAMMY-seq) as a tool for studying euchromatin and heterochromatin regions in human fibroblasts.

(Manuscript in preparation)

Our recently published technology (Sebestyén et al., 2020), SAMMY-seq or Sequential Analysis of Macromolecules Accessibly-sequencing is a valuable tool for studying chromatin organization. The technology is based on biochemical methods for the extraction of different fractions containing DNA-sensitive (S2), salt-sensitive (S3), and salt-resistant (S4) chromatin. After sequencing, pairwise comparison between the most insoluble and more accessible fraction (S4vsS2 or S3vsS2) allowed the mapping of heterochromatic regions strongly associated with Nuclear Lamina (NL). This first available protocol is characterized by three fractions (3fSAMMY-seq), all enriched of heterochromatic genomic regions, consequently to the use of a DNA digestion enzyme such as DNAse Turbo, which is very aggressive and leads to the digestion of all accessible chromatin. To recover both euchromatin and heterochromatin, we developed a new protocol, called 4fSAMMY-seq (four fractions SAMMY-seq), on three million primary human fibroblasts (Fig. 9). By modulating the step of DNAse digestion, using a milder enzyme like DNAse I, we captured the open chromatin regions, together with more insoluble chromatin fraction (manuscript in preparation). The ratio among the fractions then allowed the

identification of both eu- and heterochromatin. The different steps between the two protocols are briefly explained in Fig. 9a. The use of a milder-acting DNase-I in S2 fraction generated two different DNA size ranges (Suppl. Fig. 6a).

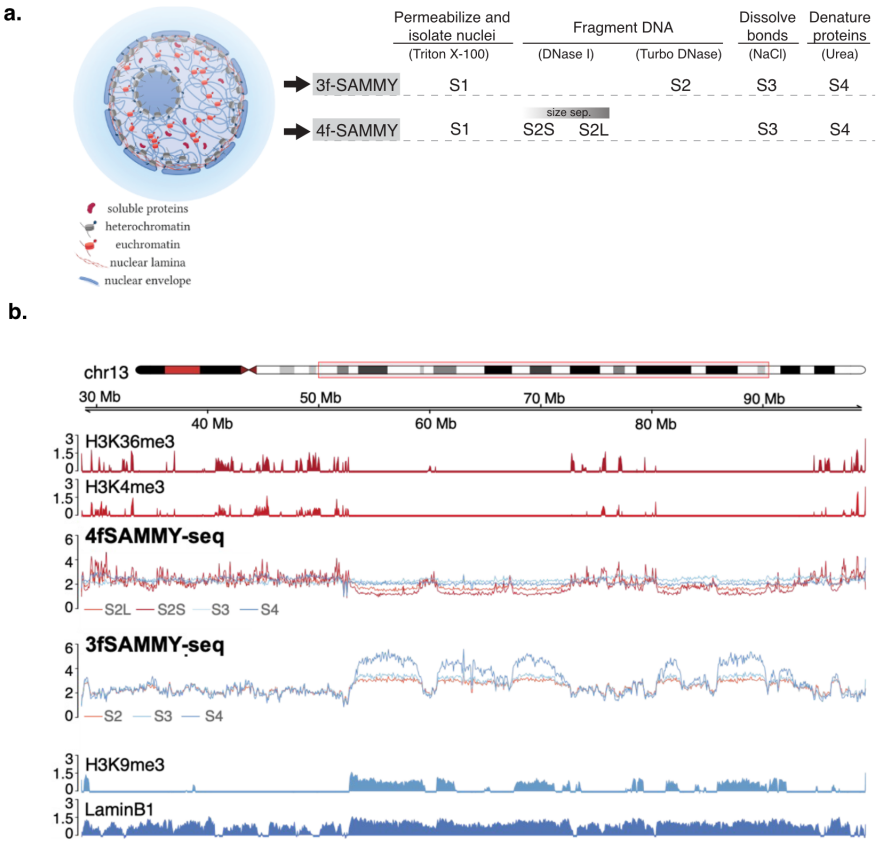

Figure 9. Three and Four fraction SAMMY-seq: Schematic representation of the 3f/4fSAMMY-seq protocol (a). Distribution of 4fSAMMY-seq and 3fSAMMY-seq reads in each sequenced fraction of healthy skin primary fibroblast along a representative genomic region (chr13:28,643,272-99,222,399). Library size normalized read counts over 10 kb genomic bins are shown for each sequenced fraction. From top to bottom: ChIP-seq tracks for histone marks (HMs) associated with active chromatin (H3K36me3 and H3K4me3 - red); 4fSAMMY-seq linear tracks (S2L - orange, S2S - dark red, S3 - light blue, S4 – blue); 3fSAMMY-seq linear tracks (S2 - red, S3 - light blue, S4 – blue); ChIP-seq tracks of heterochromatin mark (H3K9me3 –blue and LaminB1- dark blue).

Taking advantage of the SPRI affinity beads system we separated the two fragments pools based on length, namely S2 small (S2S) and S2 larger (S2L) (Suppl. Fig. 6b, c).

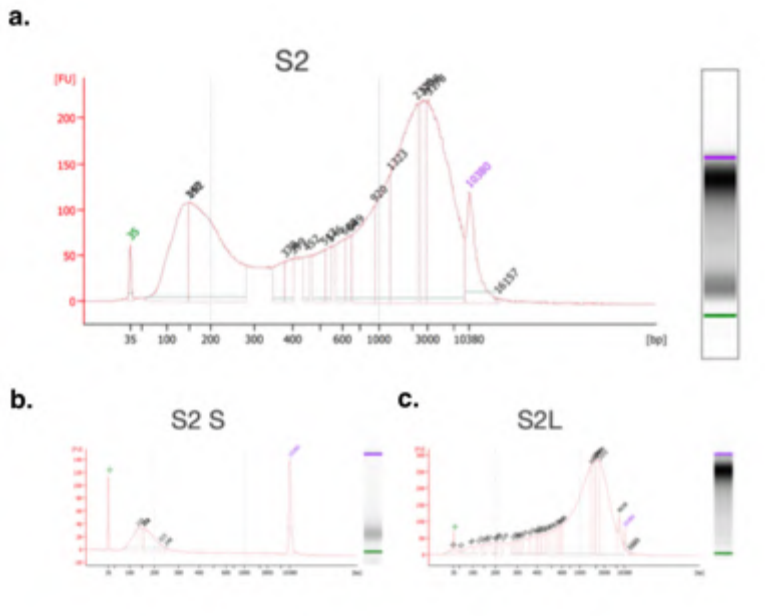

Supplementary Figure 6. Separation of S2S (short) and S2L (large) fraction. Representative bioanalyzer assay of S2 purified DNA before size-selection (a) and after separation of S2S (b) and S2L (c) subfractions. The lower marker (35bp) and the upper marker (10.380bp) are labeled in green and purple, respectively.

Then, while S2S was directly used for subsequent steps, the S2L was further sonicated to obtain fragments of the appropriate length for library preparation.

As already described, 3fSAMMY-seq presents mega-scale bumps in genomic regions enriched in LaminB1 and H3K9me3 in fractions S4, S3, and to a lesser extent in S2 (Fig. 9b) (Sebestyén et al., 2020). On the other hand, read coverage profiles of each 4fSAMMY sequenced fraction highlighted enrichments in S2S and S2L fractions in open chromatin regions

(H3K4me3, H3K36me3) and valleys in heterochromatin regions (LaminB1, H3K9me3) (Fig.9b).

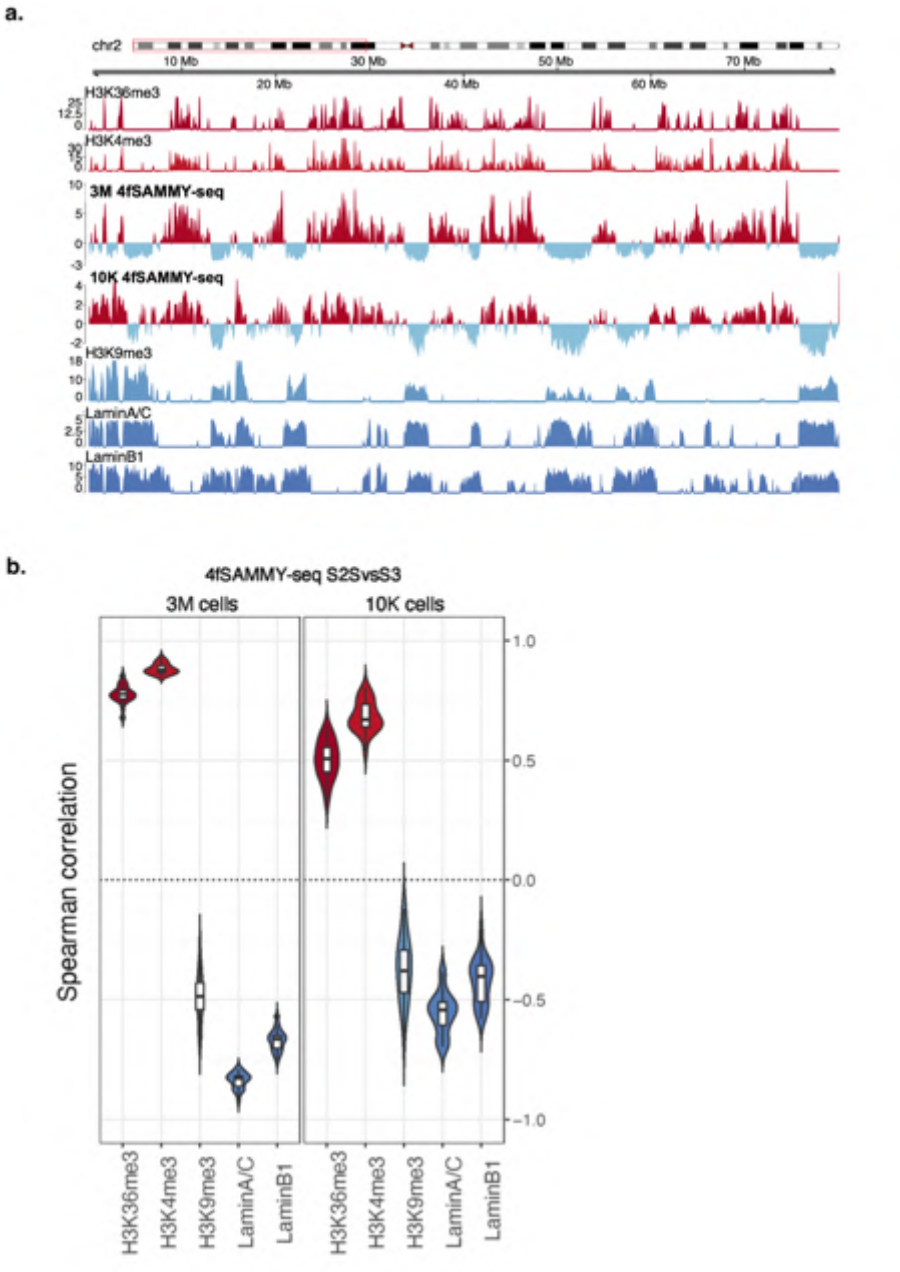

Figure 10. 4fSAMMY-seq in healthy human fibroblast. Differential read distributions across the pairwise comparison of 4fSAMMY-seq fractions (S2SvsS3) in primary human fibroblasts aligned on a representative region of chromosome 2 (80Mb on

chr2:1-80.055.066). The smoothed differential signal is calculated with the SPP package. Positive signals are marked in red and represent the S2S enriched regions, whereas negative signals are marked in light blue and represent the S3 enrichments. ChIP-seq tracks of euchromatin marks H3K36me3 and H3K4me3 (red) and heterochromatin mark H3K9me3 (blue), Lamin A/C and Lamin B (dark blue) of the same region are shown (a). Box-Violin plot showing the Spearman correlation coefficient of 4fSAMMY-seq S2SvsS3 comparison with euchromatin-associated histone marks (HMs) (H3K36me3 and H3K4me3), heterochromatin-associated HM (H3K9me3) and ChIP-seq of LaminA/C and LaminB1 (b).

To highlight eu- and heterochromatin enrichment of 4fSAMMY-seq we used pairwise comparison of more accessible fraction S2S versus more insoluble fraction S3, obtaining a positive enrichment that match with euchromatin marks and a negative enrichment that coincide with heterochromatin marks (Fig. 10a). Spearman correlation analysis of the pairwise comparison S2SvsS3 confirms at the genome-wide level the high correlation with euchromatin-associated histone marks, and the anti-correlation with heterochromatin-associated marks (Fig. 10b).

To be able to employ 4fSAMMY-seq even in contexts characterized by low cell availability, such as FACS-sorted primary cells, we adapted the protocol to ten thousand primary fibroblasts (10k). The results show that despite the low number of cells it is possible to efficiently separate euchromatin and heterochromatin regions (Fig. 10 a, b).

To fully leverage our sequencing data, we try to estimate A/B compartments as seen by Hi-C (Lieberman-Aiden et al., 2009) (Fig. 11). Taking advantages of the Calder algorithm (Y. Liu et al., 2021), we used all the SAMMY-seq fractions for the calculation of the solubility matrix, based on the Fisher's z-transformed correlation. Subsequently, the A/B compartments

were estimated by eigenvector analysis of the genome solubility matrix. By visual inspection of the HI-C and SAMMY-seq matrices and relative eigenvector, it is possible to appreciate their similarity (Fig. 11).

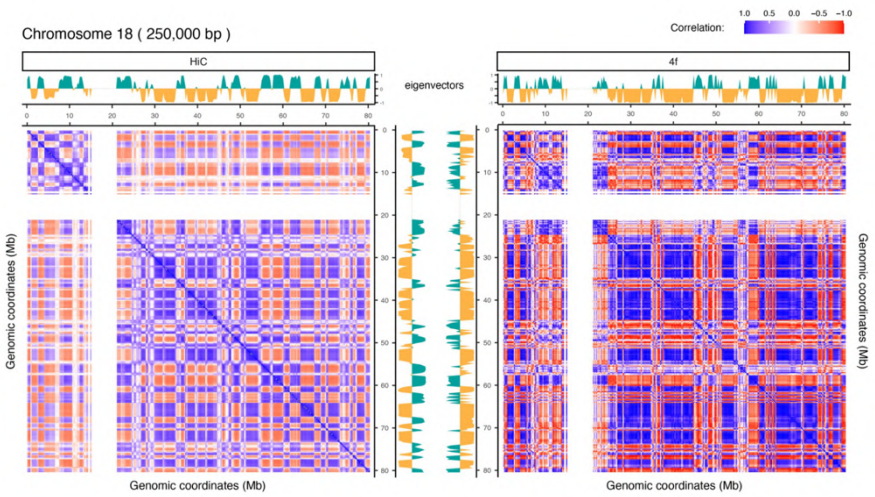

Figure 11. 3D genome organization in Human Fibroblasts. Normalized Hi-C contact matrix of Primary human fibroblast for chr18 at 250 kb resolution (left). Normalized Solubility matrix of Primary human fibroblast for chr18 at 250 kb resolution (right). Shown above and on the side of each matrix are the respective eigenvectors.

Differences between two methods included specific Polycomb-associated sequencing (data not shown) and are currently under investigation (manuscript in preparation).

In conclusion, the novel 4fSAMMY-seq enables genome-wide mapping of lamina-associated heterochromatin, active euchromatin regions, and the estimation of A/B compartment in a single assay on non-fixed cells, thereby providing a complete picture of the 3D nuclear genome organization.

4.2.4. 4fSAMMY-seq efficiently identifies chromatin solubility states in a low number of muscle stem cells

Considering the advantage of our technology in discriminating euchromatin and heterochromatin regions and the vast epigenetic profile that we generated in postnatal and adult muscle stem cells, we decided to apply 4fSAMMY-seq to study euchromatin and heterochromatin organization in MuSCs.

We initially optimized the protocol using 250K MuSCs modulating the sonication conditions (Suppl. Fig. 7 a, b, c).

DNA quantification of the different fractions after sonication (Suppl. Fig. 7d), showed variable concentrations of fraction-associated DNA (0.118-5 ng/ul), with S2L and S3 representing the most concentrated fractions, and S4 the less, in some cases undetectable. Next, we applied the protocol on 10-20K MuSCs, finding all fractions not quantifiable. Starting from fraction-associated DNA, even undetectable by Qubit assay, we generated libraries for subsequent sequencing, and we checked the quality on Bioanalyzer or Tape station instruments (Suppl. Fig. 7e).

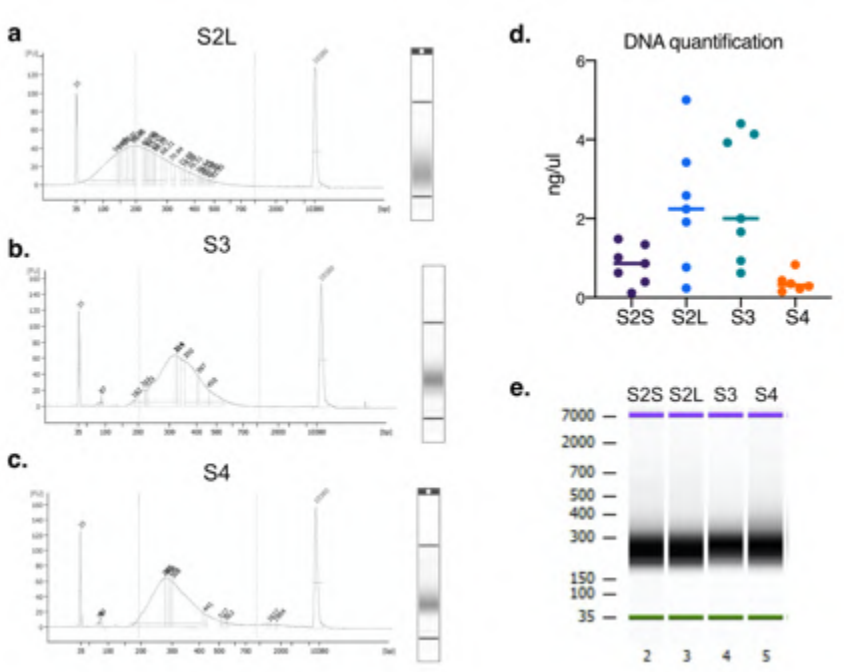

Supplementary Figure 7. 4fSAMMY-seq optimization in MuSCs. Representative bioanalyzer assay of Optimization of sonication in S2L (a), S3 (b), S4 (c) fractions. The lower marker is at 35bp and the upper marker at 10.380bp. DNA quantification of post-sonicated fractions in 250k MuSCs (d). Representative bioanalyzer assay of prepared Library starting from 10k MuSCs (S2S, S2L, S3, S4) (e).

We initially sequenced a mean yield of 35 million reads per fraction, in 250K and 10K MuSCs extracted from the same mouse and in two additional 10K samples. 4fSAMMY-seq comparisons of soluble S2S versus insoluble S3 revealed that despite the low number of cells, we successfully detected a conserved presence of differentially enriched genomic regions in

MuSCs corresponding to euchromatin and heterochromatin (Fig. 12a).

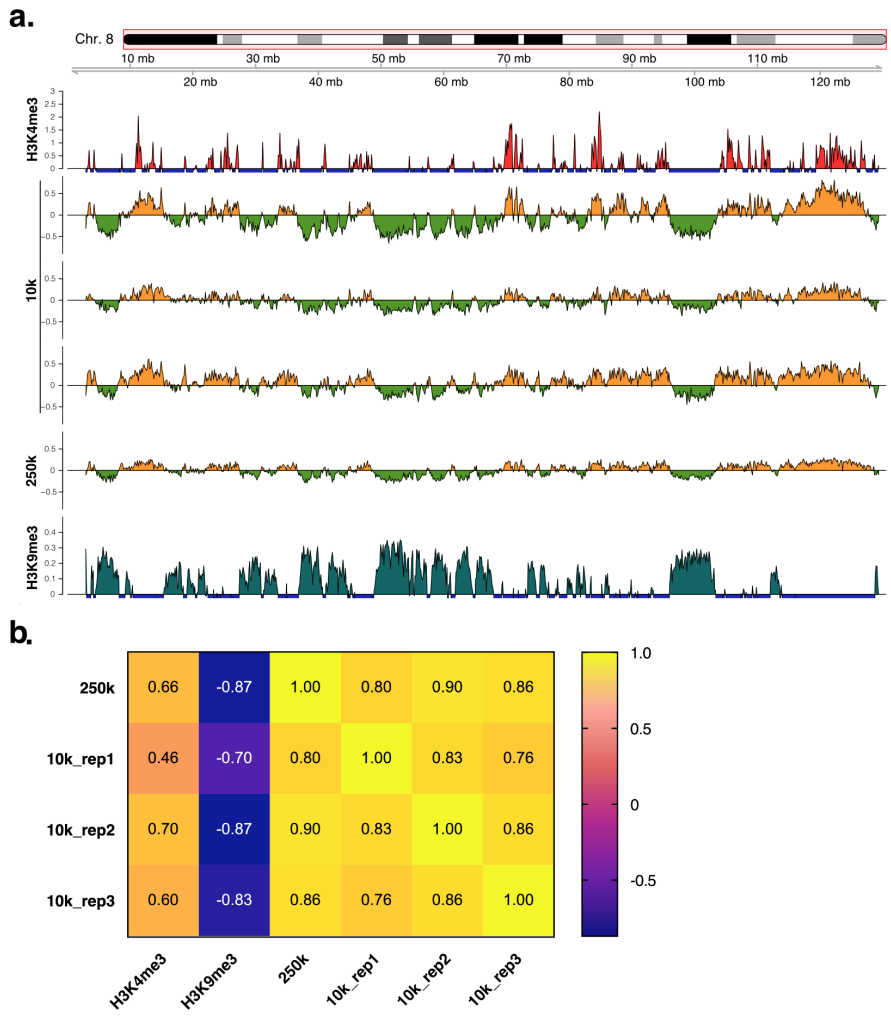

Figure 12. 4fSAMMY-seq on different amount of postnatal muscle stem cells. Differential read distributions across pairwise comparison of 4fSAMMY-seq fractions (S2SvsS3) in primary MuSCs aligned on chromosome 8 (128Mb). The smoothed differential signal is calculated with the SPP package. Positive signals are marked in orange and represent the S2S enriched regions, whereas negative signals are marked in green and represent the S3 enrichments. ChIP-seq tracks of euchromatin marks H3K4me3 (red) and heterochromatin mark H3K9me3 (dark green) (of the same region are shown (a).

Genome-wide analysis of pairwise comparison S2S versus S3 confirms at the genome-wide level, the high correlation between 250k and 10k replicate deriving from the same batch of MuSCs (10k_rep1) (r = 0.80) and between 10k replicates (average r=0.82) (Fig. 12b). A slightly lower correlation was found between 10K-rep2 and 10k_rep3 (r = 0.76): this may be partly due to biological variability among the different mice used. Moreover, we found a high correlation of S2S soluble regions with H3K4me3, euchromatin-associated histone mark, and a high anti-correlation with H3K9me3, heterochromatin-associated mark (Fig. 12b).

Taken together these data suggest that 4fSAMMY-seq is a suitable tool to analyse chromatin dynamics using a limited number of muscle stem cells.

4.2.5. 4fSAMMY-seq chromatin solubility profile in postnatal Muscle Stem Cells.

We applied 4fSAMMY-seq on three samples of muscle stem cells extracted from postnatal mice 19 days after birth. Again, we observed a clear enrichment of soluble, S2SvsS3 regions with open chromatin marks (H3K4me3, H3K36me3) and transcription and an inverse correlation with broad regions of the H3K9me3 heterochromatin mark (Fig. 13a). We validate these results at the genome-wide level by the pairwise correlation between 4fSAMMY-seq (S2SvsS3 comparison) and ChIP-seq signals of the different histone marks (Fig. 13b). We found a strong anti-correlation (-0,72 < r < -0,87) of soluble domains with constitutive H3K9me3 heterochromatin mark and correlation between the S2S fraction with the active promoters H3K4me3 mark (0,56 < r < 0,67). Interestingly, facultative heterochromatin, marked by the Polycomb related H3K27me3, correlated with open soluble regions (0,56 < r < 0,60). Finally, we found a weak association of soluble regions with the transcription elongation H3K36me3 mark (average r = 0,29) (Fig. 13b).

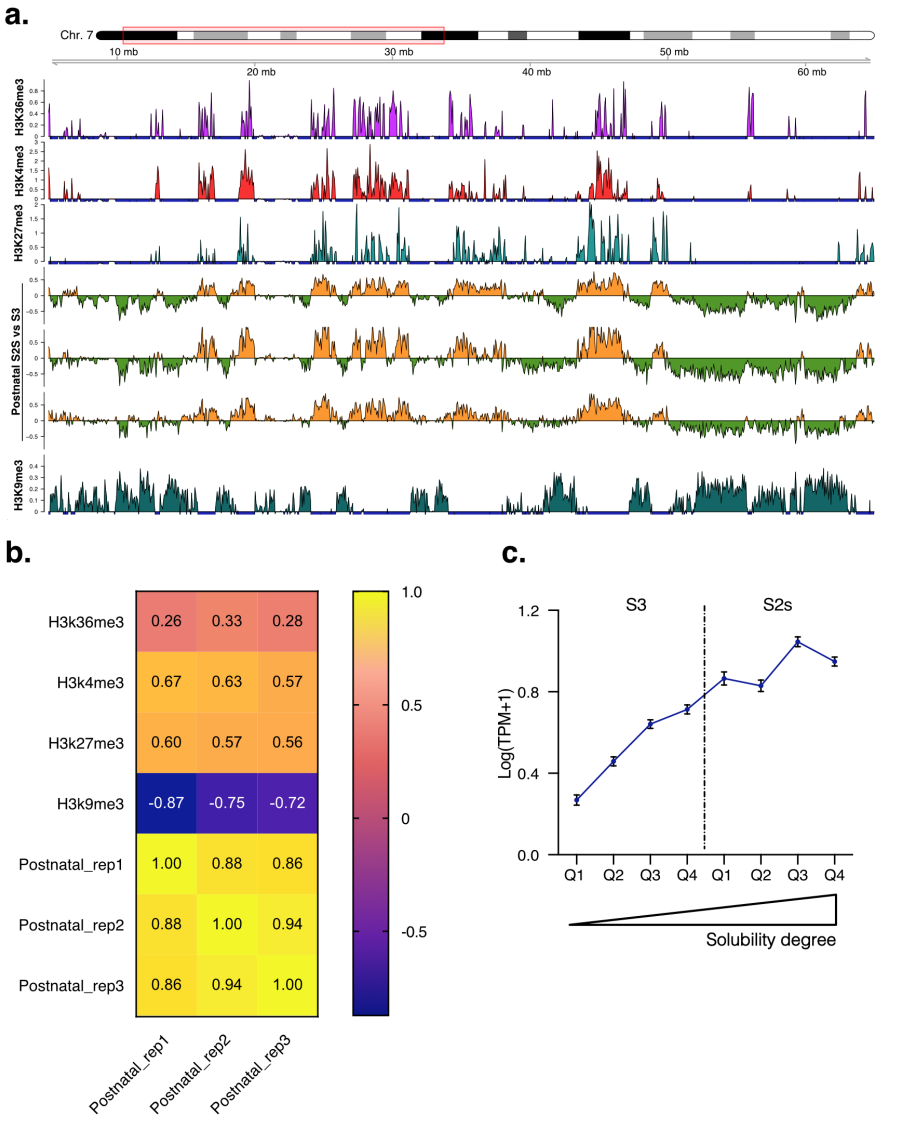

Figure 13. 4fSAMMY-seq on Postnatal Muscle Stem Cells. Differential read distributions across a pairwise comparison of 4fSAMMY-seq fractions (S2SvsS3) in postnatal MuSCs aligned on a representative region of chromosome 7 (chr7:4,070,191-68,514,866). The smoothed differential signal is calculated with the SPP package. Positive signals are marked in orange and represent the S2S enriched regions, whereas negative signals are marked in green and represent the S3 enrichments. ChIP-seq tracks in postnatal MuSCs of euchromatin marks H3K36me3 (purple), H3K4me3 (red), heterochromatin mark H3K27me3 (aqua green), H3K9me3 (dark green) of the same region are shown (a). Spearman correlation heatmap of chromosome-by-chromosome correlation coefficient of 4fSAMMY-seq S2SvsS3 comparison with euchromatin-associated histone marks (HMs) (H3K36me3 and

H3K4me3), heterochromatin- associated HM (H3K9me3, H3K27me3) (b). Plots showing the median log(TPM+1) value of gene expression (Y-axis) across the distinct quartile of solubility in each sample (X-axis) in postnatal MuSCs. The line extends the 95% confidence interval for the median labeled as dot (c).

Next, to finely assess the correspondence between chromatin solubility and transcriptional activity, we quantitively subdivided the solubility scale *in silico*. To this end, the degree of solubility has been ranked according to the 4fSAMMY-seq (S2SvsS3 comparison) negative and positive enrichments at 100 kb resolution. Then, the S2S and S3 coverage were both divided into quartile ranges. In postnatal MuSCs, the level of gene expression, measured as transcripts per million (TPM), increases progressively from the highest insoluble S3 quartile to the most soluble quartile in S2, suggesting a direct correlation between solubility and transcription (Fig. 13c).

4.2.6.Adult muscle stem cells display decreased solubility of muscle-specific regions

To understand if adult muscle stem cells show a different chromatin solubility profile, in line with the diverse epigenetic landscape, we apply 4SAMMY-seq on three samples of adult muscle stem cells (Fig. 14a). Spearman correlation analysis underlines an elevated correlation between the different replicates (average r = 0.88), confirming again the reliability of the technology. At the genome-wide level, we noticed some differences to previous analysis postnatal MuSCs (Fig. 13b). In particular, the correlation of soluble domains (S2S) with the transcription-associated H3K36me3 mark increases from an average r of 0.29 in postnatal MuSCs to 0.84 in adult MuSCs, in line with the homogeneity of the quiescent cell population. In parallel, we observed a decrease in the anti-correlation values with the constitutive (H3K9me3) and facultative (H3K27me3) heterochromatin marks: H3K9me3, that goes from an r average of 0.78 in postnatal MuSCs to 0.41 in adult MuSCs; H3K27me3, from an average r of 0.58 in postnatal MuSCs to an average r of -0.11 in adult MuSCs (Fig. 14b). Despite the difference in epigenetic landscapes, we observed the same transcription trends in the different quartiles of solubility (Fig 14c).

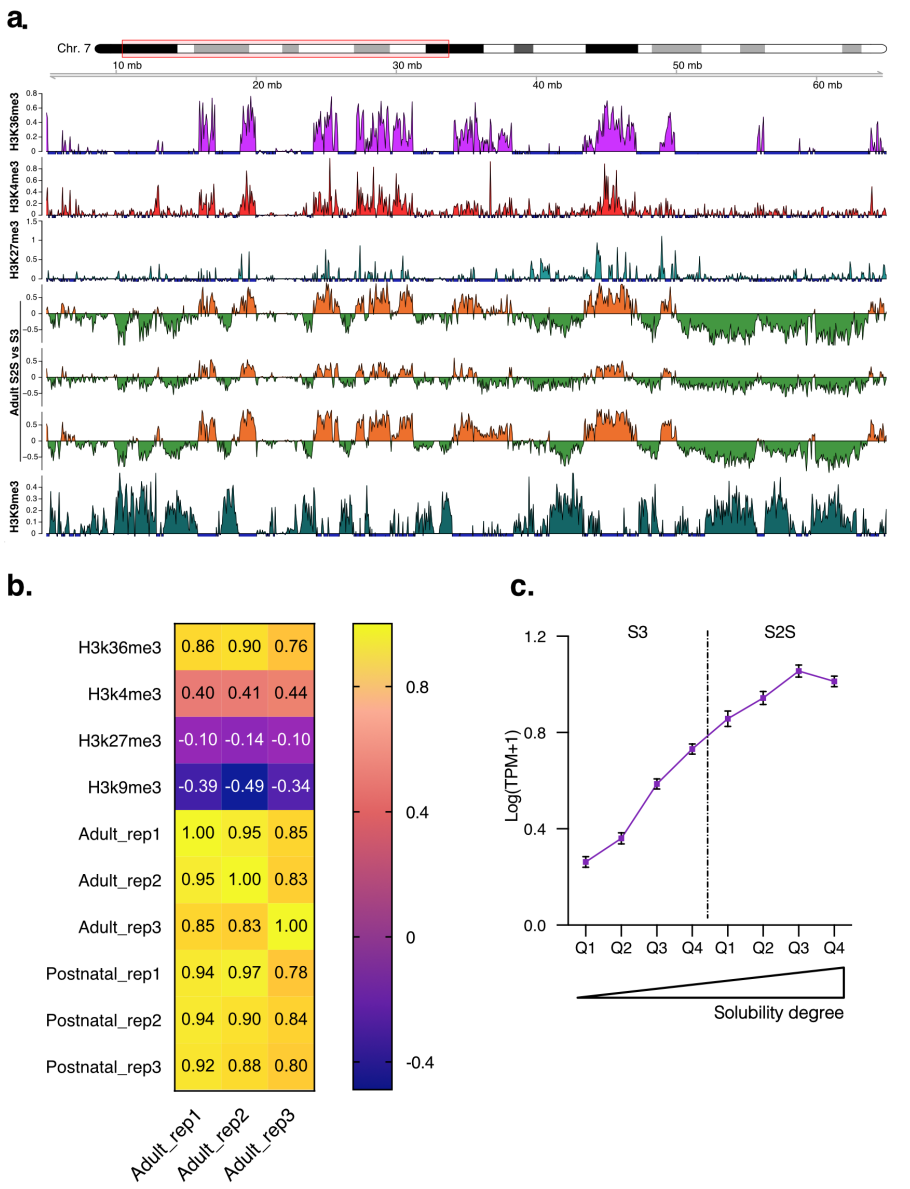

Figure 14. 4fSAMMY-seq on adult Muscle Stem Cells. Differential read distributions across a pairwise comparison of 4fSAMMY-seq fractions (S2SvsS3) in adult MuSCs aligned on a representative region of chromosome 7 (chr7:4,070,191-68,514,866). The smoothed differential signal is calculated with the SPP package. Positive signals are marked in orange and represent the S2S enriched regions, whereas negative signals are marked in green and represent the S3 enrichments. ChIP-seq tracks in adult MuSCs of euchromatin marks H3K36me3 (purple), H3K4me3 (red), heterochromatin mark H3K27me3 (aqua green), H3K9me3 (dark green) and of the same region are shown (a). Spearman correlation heatmap of chromosome-by-chromosome correlation coefficient of 4fSAMMY-seq S2SvsS3 comparison with euchromatin-

associated histone marks (HMs) (H3K36me3 and H3K4me3), heterochromatin-associated HM (H3K9me3, H3K27me3) and postnatal 4fSAMMY-seq S2Svs S3 comparison (b). Plots showing the median log(TPM+1) value of gene expression (Y-axis) across the distinct quartile of solubility of the three replicates (X-axis) in Adult MuSCs. The line extends the 95% confidence interval for the median labelled as dot (c).

Spearman correlation of 4fSAMMY-seq signal tracks between postnatal and adult MuSCs showed a high degree of similarity (average r=0.89) (Fig. 14b). These observations suggest that although histone marks present different distributions probably linked to the MuSCs state (activated or quiescent), the overall solubility profile in postnatal and adult MuSCs is maintained.

To dig deeper inside the solubility differences of MuSCs, we generate consensus signals for the S2S and S3 fractions of postnatal and adult MuSCs, dividing the genome into discrete units of 10kb, called bins, and calculating the mean of the signals and the confidence intervals in all bins for each time point (Fig. 15a). Subsequently, we compared the two S2S consensus signals of postnatal and adult MuSCs for each fraction and we identified high or low soluble regions in adult MuSCs those genomic regions with a non-overlapping confidence interval respect to postnatal MuSCs. We found overall 4807 genes inside the differentially soluble genomic regions (Fig. 15b). Next, we take advantage of our transcriptome data set intersecting the low

soluble genes in adult versus postnatal MuSCs with downregulated genes (Fig. 15c).

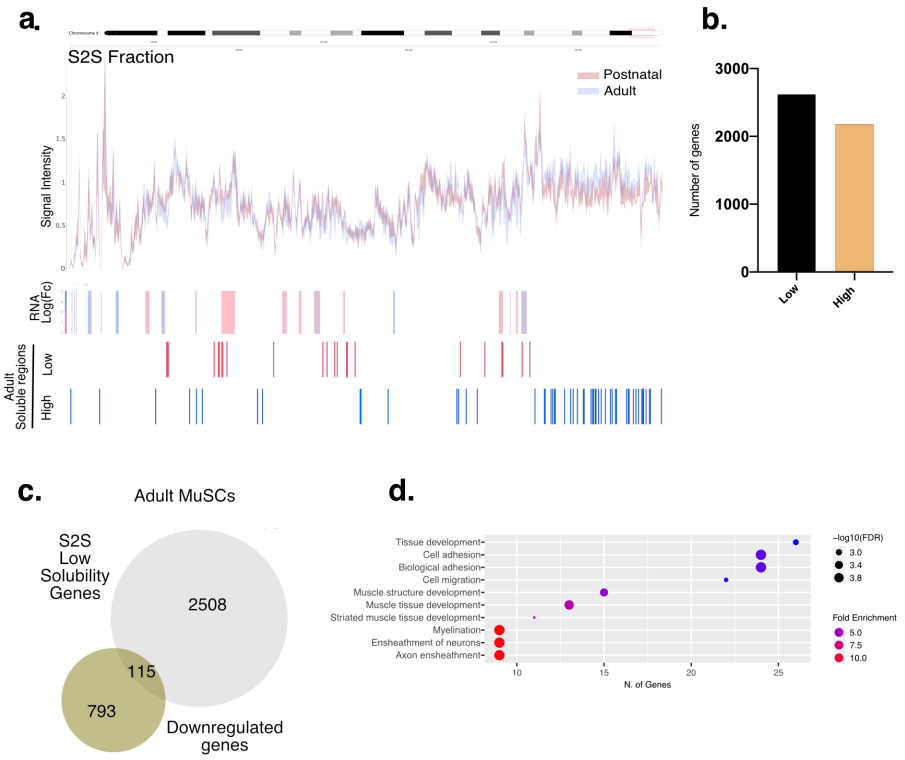

Figure 15. Solubility changes in adult muscle stem cells. 4fSAMMY-seq consensus signal (y-axis) of postnatal and adult S2S fractions using a 10 kb bins size on a representative genomic region on chromosome 4 (chr4:146,434,366-154,464,166). From the top: RNA-seq Log fold change of DEGs in the comparison of adult versus postnatal; differentially soluble regions in adult MuSCs, low (red) and high (blue) solubility (a). Bar plot of the number of genes enriched in the adult differentially soluble region (b). Proportional Venn diagram (Hulsen et al., 2008) of adult S2S low solubility genes (in respect to the postnatal S2S) intersect with downregulated genes in adult versus postnatal MuSCs (c). Enriched pathways analysis of the biological process for the 115 genes derived from the previous intersection (c) in adult MuSCs (d).

A total of 115 genes were found, suggesting that chromatin solubility dynamics are not directly followed by transcriptional changes. However, Gene Ontology enrichment analysis of biological processes underlines terms related to striated muscle

and muscle structure development, in line with lower developmental activity in adult quiescent MuSCs (Fig. 15d). Altogether, these data suggest that only a subset of genes undergoes a complete change of the epigenetic status.

4.2.7. Alteration of body and muscle morphology in Old and Geriatric mice

Aging is a physiological process associated with alterations in body composition (St-Onge & Gallagher, 2010). To have a deeper comprehension of how aging phenotypically affects the body and skeletal muscle of mice at different ages, we used different types of examinations on total mice body or tibialis anterior muscle: micro-computer tomography for evaluation of bone and fat volumes (Fig. 16), magnetic resonance imaging and spectroscopy (Fig. 17) to study muscle environment and metabolite alterations. Adult, old, and geriatric mice were weighed before each examination, revealing a dramatic fluctuation in body weight across age transitions (Fig.16a). In fact, mice showed a significant increase in body weight during aging, followed by a drop in geriatric mice (Fig.16a). Micro-computed tomography measured no alteration of the bone volume at the different stage (Fig. 16b, c), however, the total and abdominal fat volumes in old and geriatric mice are different (Fig. 16d, e), mirroring the alterations depicted in the body weights (Fig. 16a). Proton Magnetic Resonance Spectroscopy (^{1}H-MRS) enables a non-invasive *in vivo* quantification of metabolites (Takashima et al., 2018). In skeletal muscle, such as tibialis

anterior, allows the relative

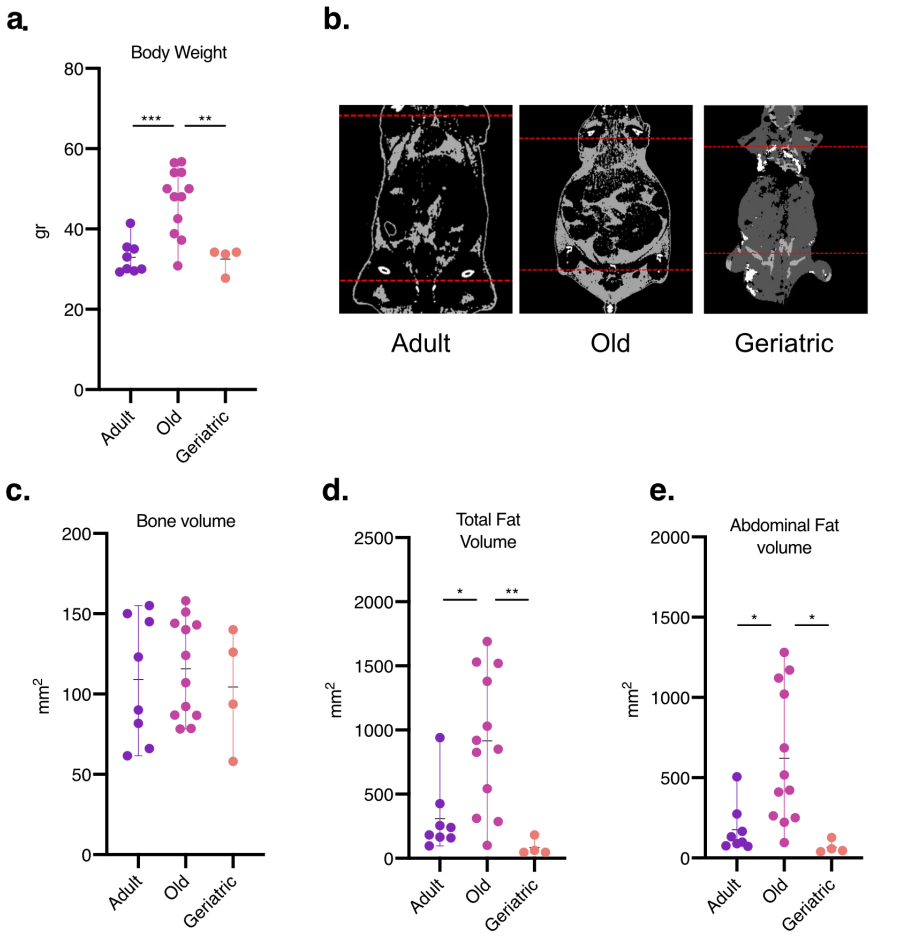

Figure 16. Micro-computed tomography analysis in adult, old and geriatric mice. Effect of aging in body weight in adult (n=8), old (n=12) and geriatric (n=4) mice (a). Representative Micro CT slice containing mouse total body. The greyscale image illustrates the different attenuation of mineralized bone compared to the surrounding non-mineralized tissue. Redline defines the analysis area (b.). Quantification of bone, total fat, and abdominal fat volume, normalized on tibia length, in adult, old and geriatric mice (c, d, e). Data are shown as mean ± SEM; *p<0.05, **p<0.01, ***p<0.001 calculated by 1way ANOVA, Tukey's multiple comparison test (a, c, d, e)

quantification of intramyocellular and extramyocellular lipids (IMCL, EMCL, respectively), together with other metabolites,

such as choline and taurine, important for the regulation of calcium and muscle contraction (Moretti et al., 2020; Spriet & Whitfield, 2015) (Fig. 17a). The IMCL measures did not depict variations during aging (Fig. 17b). On the other hand, EMCL and total lipids display a sinusoidal trend starting from the adult mice (Fig. 17 c, d), reminiscent of the body weight alteration (Fig. 16a).

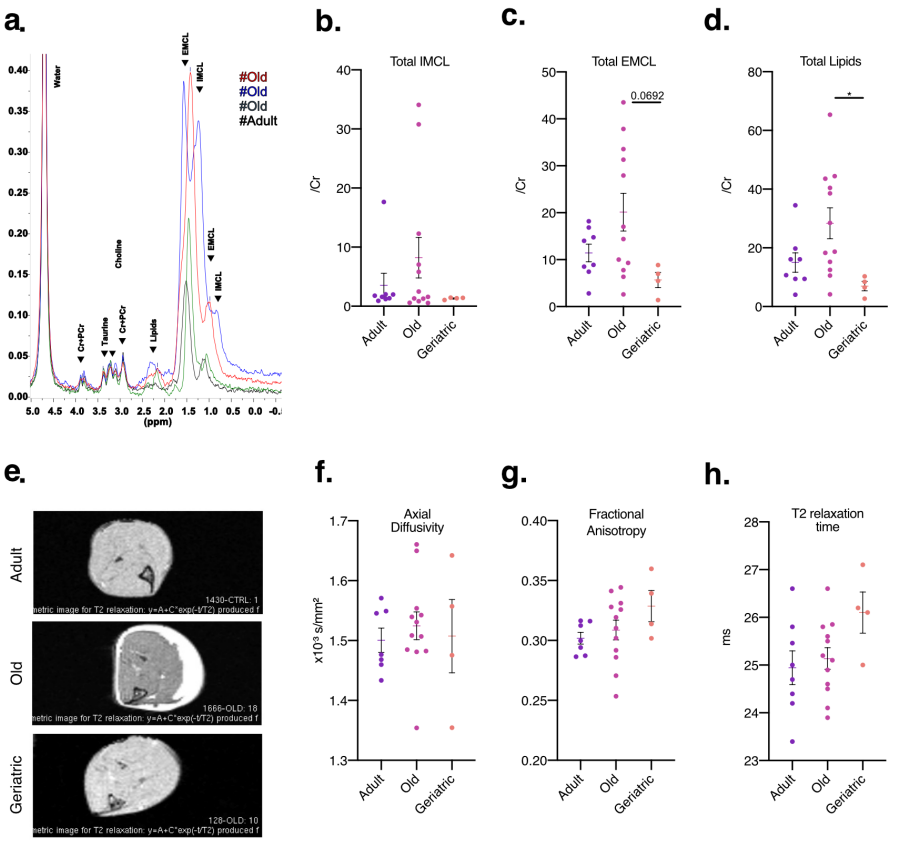

Figure 17. Representative ^{1}H spectra acquired in the voxel from TAs are shown for adult (black) and old (blue, red, green) mice. Cr+PCr, total creatine plus Phosphocreatine; IMCL, intramyocellular lipid; EMCL, extramyocellular lipid (a). Quantification of total IMCL, EMCL, and lipids normalized on total creatine in adult (n=8), old (n=12), and geriatric (n=4) mice (b, c, d). Representative axial MR images of a TA in adult, old, and geriatric animals, acquired without fat suppression (e). Quantification of axial diffusivity, fractional anisotropy, and T2 time of relaxation

(ms=millisecond) in adult (n=8), old (n=12), and geriatric (n=4) mice (f, g, h). Data are shown as mean ± SEM; *p<0.05 calculated by 1way ANOVA, Tukey's multiple comparison test (b, c, d, f, g, h).

T2 relaxation time and diffusion tensor imaging (DTI) analysis through MRI (see methods for details), detect changes in the microenvironment of the muscle (Martins-Bach et al., 2015). Axial diffusivity, which denotes the magnitude of diffusion parallel to myofibers, was not altered during aging (Fig. 17e, f). However, fractional anisotropy and T2 relaxation time, markers of fiber damage and edema, display a pattern of progressive increment, although not significant, in old and geriatric mice (Fig. 17g, h, respectively). In summary, these results reveal a dysfunctional macro and microenvironment of the aged and geriatric skeletal muscle.

4.2.8.Geriatric Muscle Stem Cells display decreased 4fSAMMY-seq signal

Skeletal muscle aging is accompanied by a loss of muscle stem cells, a phenomenon that affects not only their number but also their function (Bernet et al., 2014; Chakkalakal et al., 2012; Sousa-Victor et al., 2014). The study of these cells during physiological aging is often limited by the number of cells required in most epigenomic-related techniques. 4fSAMMY-seq is a robust novel technology that works with a minimum of 10K cells. For this reason, we decided to analyse the epigenome of MuSCs obtained from old (21-24 months) and geriatric (more than 27 months) mice with 4fSAMMY-seq. Correlation analysis between the different replicates emphasizes a high degree of similarity in old MuSCs (average r = 0.95), whereas geriatric MuSCs display a lower degree of correlation (between 0.70 and 0.89) (Fig. 18a). Genomic tracks of the 4fSAMMY-seq showing the S2SvsS3 comparison underlined overall similar chromatin compartmentalization, supported also by the high correlation at the genome-wide level (Fig. 18a). However, geriatric MuSCs are shown by a slight, but consistent decrease in both S2S and S3 amplitude, suggesting an intermingle between chromatin compartments (Fig. 18b).

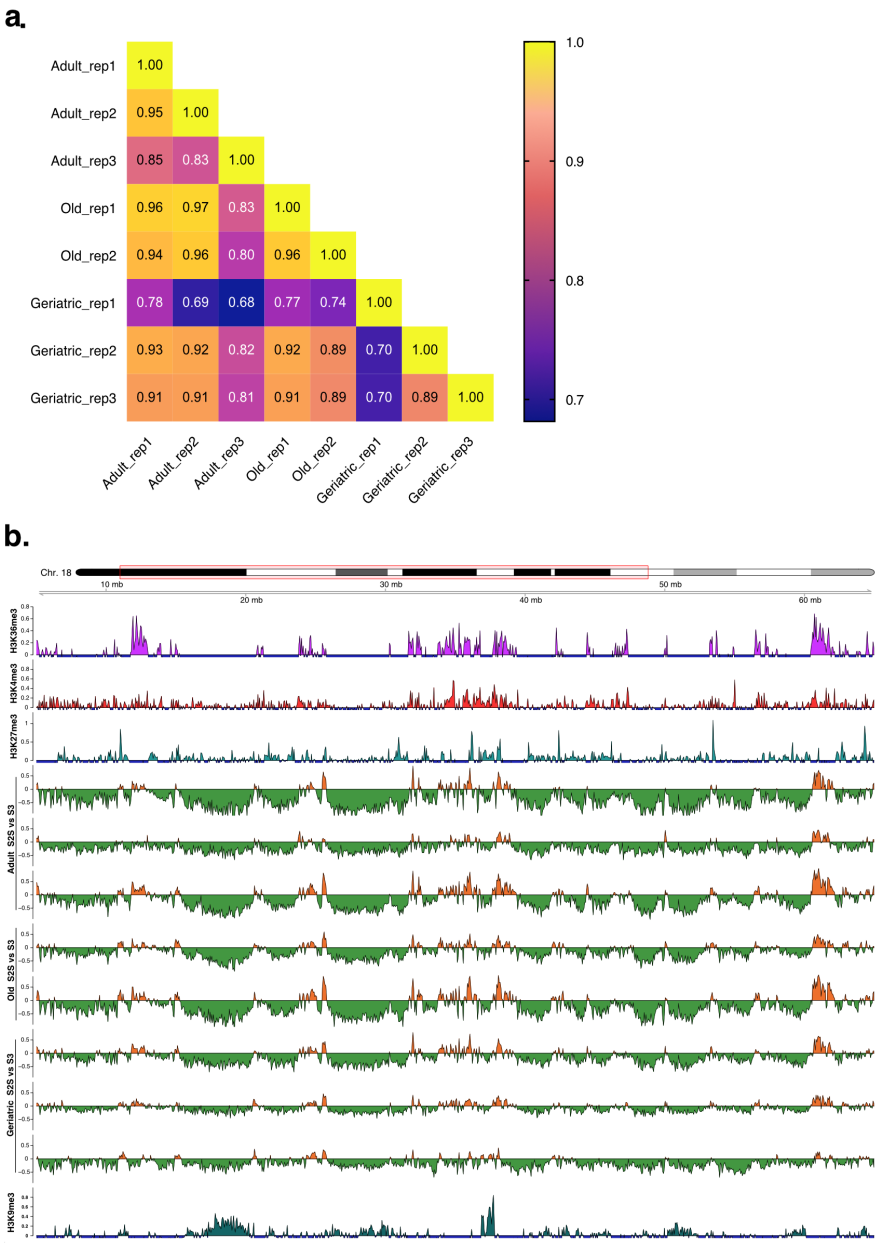

Figure 18. 4fSAMMY-seq in old and geriatric muscle stem cells. Spearman correlation heatmap of correlation coefficient of adult old and geriatric 4fSAMMY-seq S2Svs S3 comparison (a). Differential read distributions across a pairwise comparison of 4fSAMMY-seq fractions (S2SvsS3) in adult, old and geriatric MuSCs aligned on a representative region of chromosome 18 (chr18:4,484,366-65,488,659). Positive

signals are marked in orange and represent the S2S enriched regions, whereas negative signals are marked in green and represent the S3 enrichments. ChIP-seq tracks in adult MuSCs of euchromatin marks H3K36me3 (purple), H3K4me3 (red), heterochromatin mark H3K27me3 (aqua green), H3K9me3 (dark green) of the same region are shown (b).

We take advantage of the quantitative analysis described above (Fig.15) to generate the consensus signal for the adult, old and geriatric MuSCs. We found 1562 common genes that display a lower solubility in geriatric MuSCs with respect to adult and old MuSCs (Fig.19a). Preliminary enrichment analysis performed on the KEGG database revealed that these genes are highly enriched for pathways important for the regulation of MuSCs, as MAPK, PI3K-AKT, CAMP signaling pathways (Fig.19b).

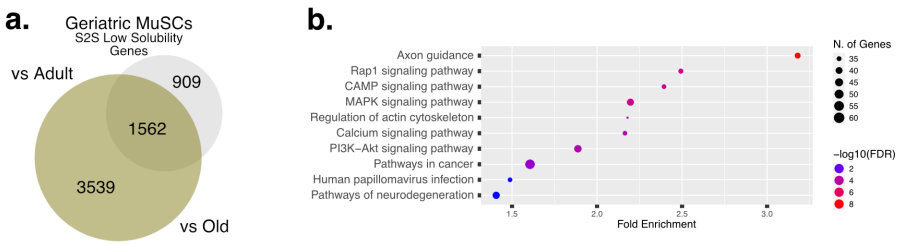

Figure 19 Altered solubility in geriatric muscle stem cells. Proportional Venn diagram (Hulsen et al., 2008) of geriatric S2S low solubility genes (in respect to the adult S2S) intersected with S2S low solubility genes (in respect to the old S2S) (a). Enriched pathways analysis of the biological process for the 1562 genes derived from the previous intersection (b).

Despite the observed solubility alterations, gene expression analysis of genes associated with the enriched pathways showed no fluctuations in geriatric MuSCs (data not shown). Altogether, these data suggest that geriatric MuSCs are characterized by

solubility alterations in genes important for preserving the proper cell state.

4.2.9. Solubility Compartment Analysis in Muscle Stem Cell

To further understand how MuSCs 3D genome organization is modified during the life course, we took advantage of the analysis described above (Fig.11) to investigate euchromatin/heterochromatin compartmentalization.

We generated solubility matrices of muscle stem cells, starting from the S2S, S2L, and S3 fractions at all ages. Despite the failure to employ the S4 fraction in this analysis due to the scarce DNA starting material, the matrices showed the correct chromatin compartmentalization (Fig. 20a).

In fact, by analyzing the first eigenvector of the correlation matrices at 250 kb resolution, we found a concurrence of the soluble S2S with euchromatin compartment (A) and insoluble S3 fraction with repressive (B) compartment (Fig. 20b). Muscle stem cells at the different stages of life exhibited overall conserved chromatin compartmentalization (Fig. 20c), in line with recent literature in other cellular models (C. Chen et al., 2019; Dixon et al., 2015). The genome was portioned in A and B compartments on a ratio of 46,4 ± 0.3/53,6 ±0.3 on the total genome in postnatal, adult, old and geriatric MuSCs (Fig. 20 c, d, e). In the transition from postnatal to adult MuSCs, we detected an A -> B

compartment shift of 0,83% of the genome, and a B -> A compartment shift of 0,56% of the genome (Fig. 20c).

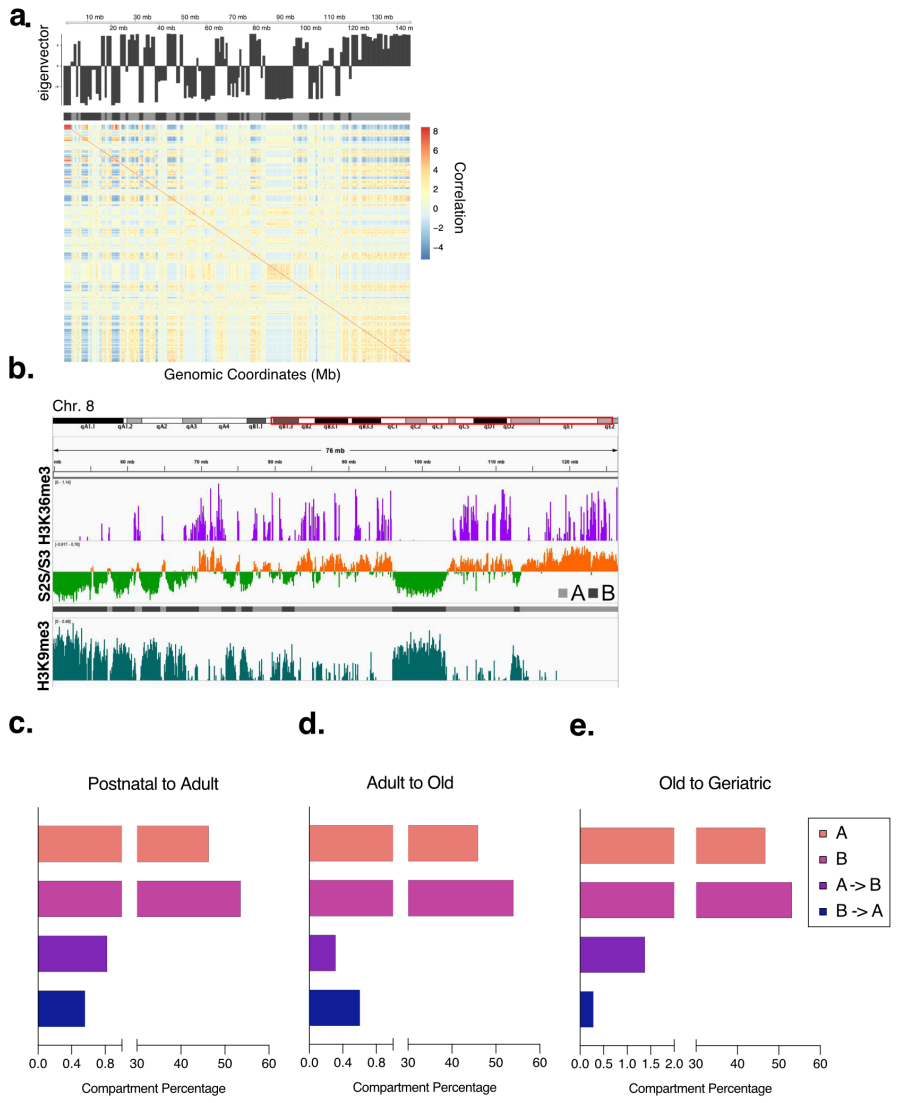

Figure 20. 3D genome organization in postnatal, adult, old and geriatric MuSCs. Normalized Solubility matrix of MuSCs for chromosome 7 at 250 kb resolution (a). Shown above and on the side of the matrix, it is shown the respective eigenvectors. Differential read distributions across a pairwise comparison of 4fSAMMY-seq fractions (S2SvsS3) in postnatal MuSCs aligned on a representative region of chromosome 8 (chr8:49,732,556-126,021,330). The smoothed differential signal is calculated with the SPP package. Positive signals are marked in orange and represent the S2S enriched

regions, whereas negative signals are marked in green and represent the S3 enrichments. A and B compartments are represented as grey or black line, respectively, under the S2SvsS3 comparison. ChIP-seq tracks in postnatal MuSCs of euchromatin mark H3K36me3 (purple) and heterochromatin mark H3K9me3 (dark green) (b). Bar plots showing the percentage of A/B compartment conserved and shifting in the transition postnatal to adult (c), adult to old (d), old to geriatric (e). Genome was divided in 250 kb bins.

During aging, we witnessed an interesting trend toward A compartment (0.60%) in old MuSCs respect to the adult (Fig. 20d) while between old and geriatric MuSCs we found a substantial increase in the switch from A to B compartment (1.4%) (Fig. 20e). These apparent opposite data suggest a more open chromatin environment in old MuSCs and a subsequent expansion of heterochromatin structure in geriatric MuSCs.

Although bioinformatic annotation analysis of the re-arranged genomic regions is still ongoing, visual inspection of the compartments allows in regions switching from B to A compartment in old and geriatric MuSCs the identification of genes important for proliferation and migration (Fig. 21), such as *Dock2* and *Spdl1* (Kodama et al., 2019; L. Wang et al., 2010), suggesting a functional role of these re-arrangement in the altered profile of MuSCs in aging.

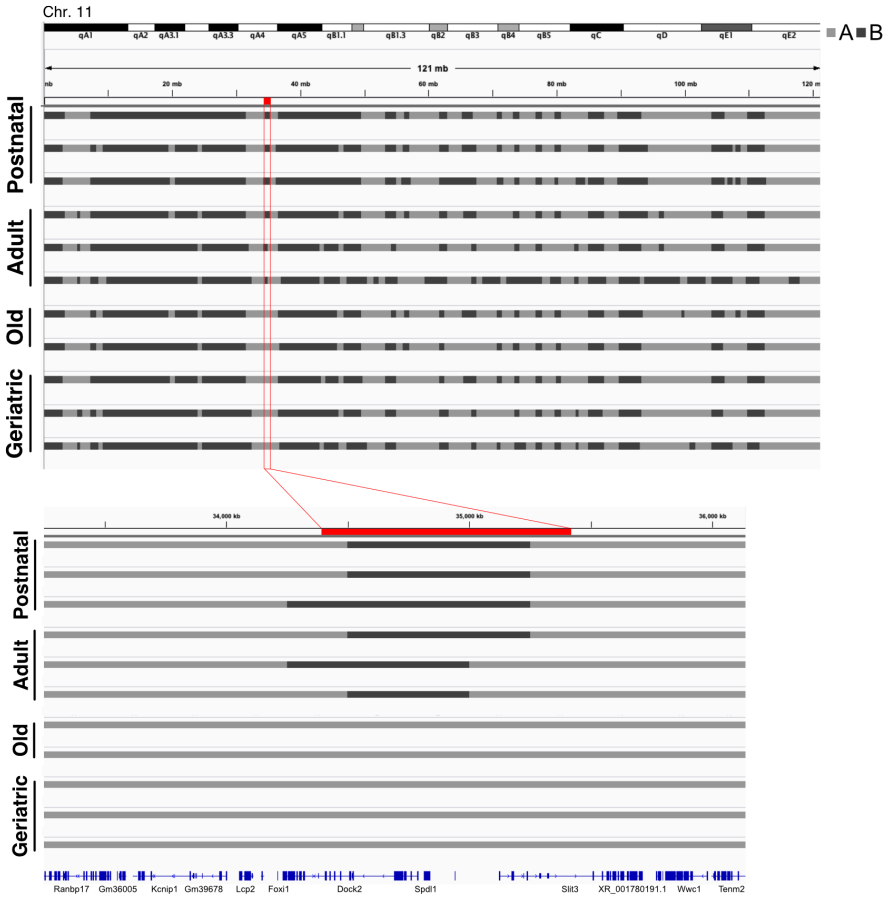

Figure 21. A and B compartments in MuSCs at all stages on chromosome 11. Below: A and B compartment on the zoomed region highlighted in red on chromosome 11 (chr11:33,237,396-36,158,655).

4.2.10. Geriatric muscle resident Fibroadipogenic progenitors (FAPs) present an altered transcriptional profile

Skeletal muscle is populated by a wide variety of cell populations that contribute to its homeostasis and regeneration (Dell'Orso et al., 2019; Oprescu et al., 2020b). Due to the dramatic fluctuation of the muscle environment during physiological aging (Fig. 16-17), we investigate the transcriptional profile of muscle resident PDGFRα^{+} cells or Fibroadipogenic progenitor cells (FAPs). This cell population is characterized by clonal expansions and the ability to undertake different fate choices, such as fibrogenic, osteogenic, and adipogenic(Joe et al., 2010b; Uezumi et al., 2010b).

We sequenced three replicates for each time point (adult, old and geriatric), obtaining at least 20 million uniquely mapped reads in each replicate (Suppl. Fig. 8a). We observed a high correlation degree ($r > 0.9$) across all biological replicates, confirming the purity of our sorted samples (Suppl. Fig. 8b).

Principal Component Analysis (PCA) showed that old and geriatric FAPs segregate in two distinct groups (Fig. 22a), whereas the lack of clear clustering of replicates in the adult, in line with the heterogeneity of FAP subpopulations reported in the unperturbed muscle (Malecova et al., 2018b), suggest a clonal selection of FAPs during aging.

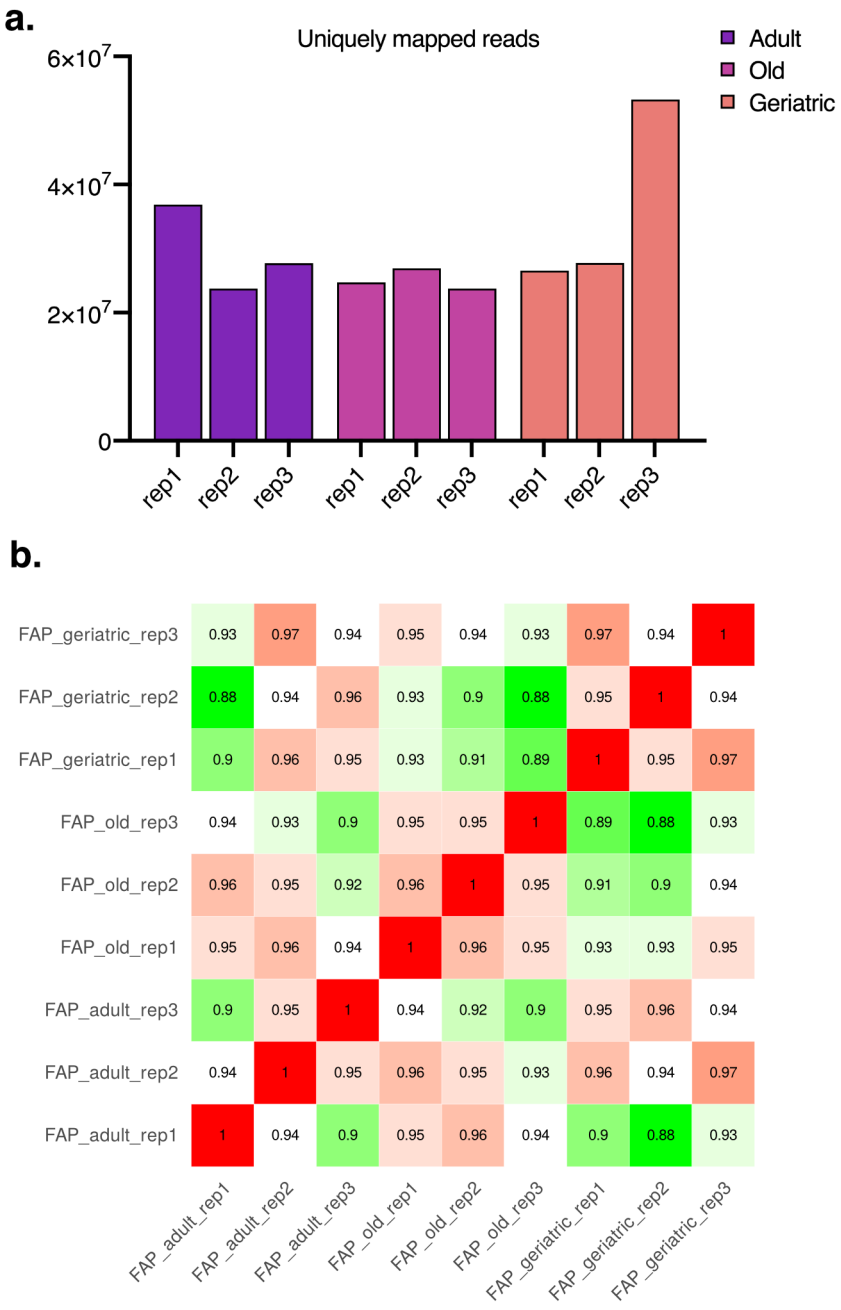

Supplementary Figure 8. Supplementary Figure 8 RNA-seq quality control. Millions of RNA-seq uniquely mapped reads per sequenced sample (a). Spearman Correlation Analysis between replicates and samples (b).

Differential Expression (DE) analysis shows an increase in transcriptional diversity related to increasing age (Fig.22 b, c, e).

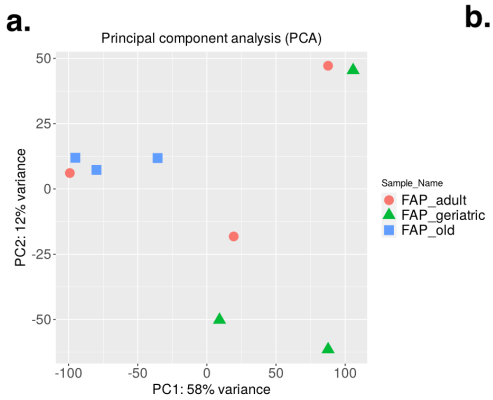

b.

	Total DEG	Up	Down
Old vs adult	98	41	57
Geriatric vs Adult	491	302	189
Geriatric vs Old	1999	1291	708

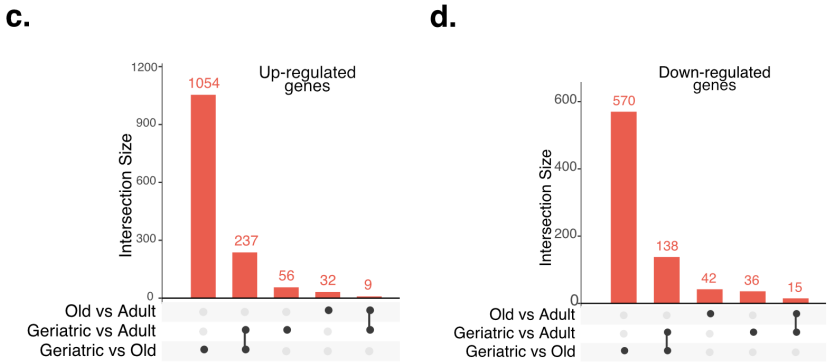

Figure 22. Transcriptional profile of adult, old and geriatric FAPs. Principal Component Analysis (PCA) of the values of gene expression among the three indicated groups. Each dot represents a biological replicate (a). Table with total DEGs in all the comparison (b). The upSet plot shows the intersections of the three datasets of upregulated or downregulated genes in the combination matrix (bottom) and the columns show how many genes are in each intersection (c, d respectively).

As for MuSCs, we focused the attention on the transition from adult to old, and from old to geriatric FAPs. We found that 98 genes were dysregulated in old, concerning adult FAPs (Fig. 21b). In particular, we highlight 41 upregulated and 57 downregulated genes in old versus adult FAPs (Fig. 21 c, d,

respectively). Beside the low number of DEGs, enrichment analysis of biological process of downregulated genes in old FAPs, with respect to adult, shows terms related to Positive regulation of molecular function and metabolic process (*Ccnd2, Hk2, Cd36, Pank3, Plk2*), suggesting dysregulation of proliferation and metabolism in old FAPs (Fig. 23a).

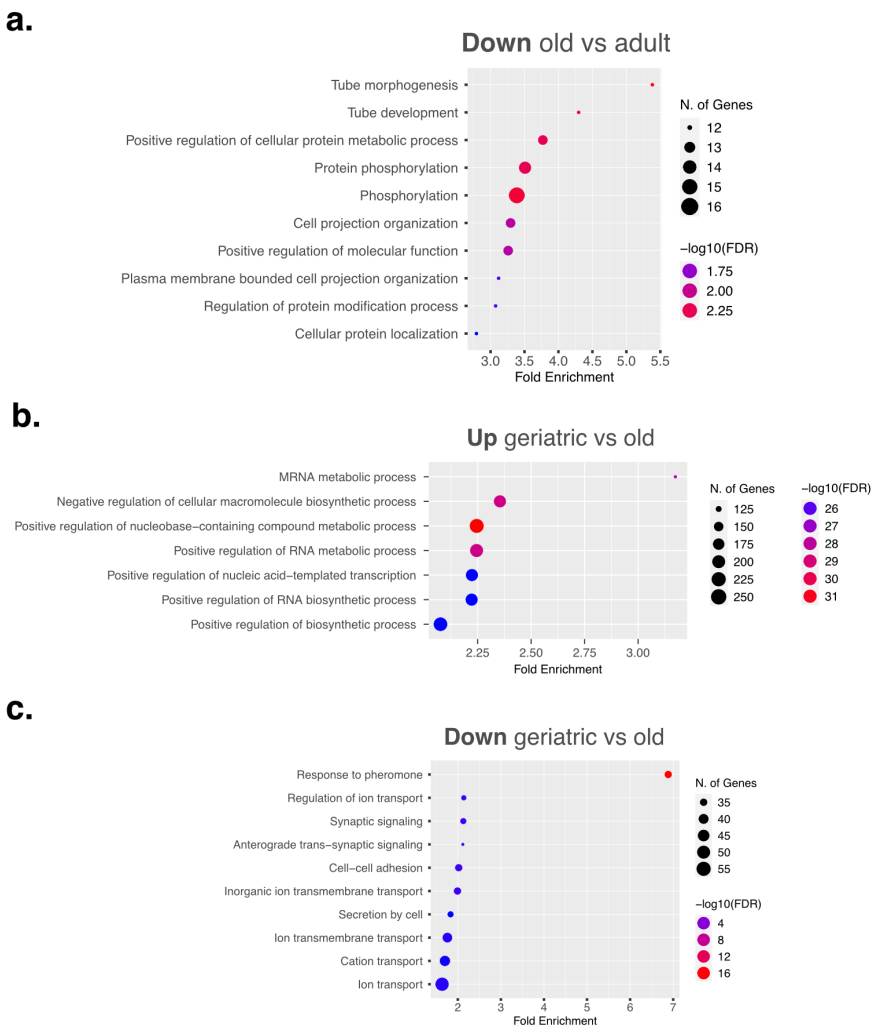

Figure 23. Enriched pathways analysis of biological process for DEGs in the comparison of old versus adult (a), and geriatric versus old (b, c) FAPs.

Up-regulated genes in old FAPs did not display any enrichment in gene ontology analysis, probably while of 41 genes up-regulated, 50% were non-coding RNA (data not shown).

As we advance with age, the number of dysregulated genes increases to a total of 1999 DEGs in the geriatric-old comparison (Fig. 22b). Up-regulated genes in geriatric concerning old FAPs, were enriched for terms related to Positive regulation of RNA and nucleic acid metabolic process (Fig. 23b). Geriatric FAPs exhibit upregulation of PcG genes (*Ezh2, Bmi, Suz12*), H3K36 methyltransferase enzyme (*Nsd1, Setd2*), heterochromatin protein (*Cbx1, Lbr, Lmnb1*), and DNA damage related genes (*Cdkn1a, Trp53inp1*) (el Husseini & Hales, 2018; Hérault et al., 2021; Martin-Herranz et al., 2019; Solovei et al., 2013; Sousa-Victor et al., 2014; Tauc et al., 2021; L. Wang et al., 2018). On the other hand, down-regulated genes show enrichment in term related to cell-cell adhesion (*Rhoh, Cdh8*), ion transport (*Cacna1e, Scn9a*) and secretion (*Nmb, Glp1r*) (Fig. 23c) (Brock & Ingber, 2005; Z. Li et al., 2021; Warnier et al., 2018).

Altogether, these data suggest that Geriatric FAPs undergo a dramatic transcriptional alteration that might be associated with severe epigenetic remodeling. For these reasons, we proceeded in applying our 4fASAMMY-seq protocol, on adult, old and geriatric FAPs obtained from the same mice described during the work. Bioinformatic evaluations are currently proceeding.

4.3. Materials and Methods

4.3.1.Mice

Wild-type C57BL/6 mice from “The Jackson Laboratories” were used. Mice were bred and maintained according to the standard facility procedure (San Raffaele hospital, DIBIT 1, Milan) and all the experimental protocols were approved accordingly by the Italian Ministry of Health (IACUC 952). Mice were sacrificed at different timing (P19-21, 3-7 months, 21-24 months, 28 months) by cervical dislocation.

4.3.2.Micro-computerized tomography

In vivo micro-computerized tomography (µCT) scans were carried out to quantify bone and fat volumes *in vivo*. µCT imaging was performed using the IVIS SpectrumCT Pre-clinical in Vivo Imaging System (Perkin-Elmer, Waltham, MA, USA). µCT images were acquired without any contrast medium, with the following parameters: x-ray tube voltage = 50 kV, tube current = 1 mA, x-ray focal spot size = 50 µm. The µCT images, calibrated in Hounsfield unit (HU), were reconstructed with a voxel size of 75 μm^3. Threshold-based image segmentation using ITK –snap was performed to obtain a 3D reconstruction and quantification

of the bone and fat volumes. The tibia length was also measured using ITK –snap and used to normalize the data.

4.3.3.Magnetic Resonance Imaging and Spectroscopy

In vivo MRI experiments were conducted on a 7-Tesla scanner for rodents, fully equipped for high-resolution MRI/MRS *(Biospec*, Paravision 6.0.1 Software Bruker-Biospin) with 450/675 mT/m gradients (slew-rate: 3400-4500T/m/s; rise-time 140µs) and a circularly polarized mouse body volume coil with an inner diameter of 40 mm.

For each MRI exam, a mixture of IsoVet (isoflurane 1-2%) with oxygen was used to anesthetize animals, and breath rate was constantly monitored to regulate the level of anesthesia. The body temperature of the mice was maintained through warm water circulating inside the bed where the animal was placed during the MRI exam.

For muscle anatomy localization, T2 weighted MR images were acquired with axial, coronal, and sagittal sections of 0.8 mm and an in-plane resolution of 100 µm (FOV = 16 mm) using a fast-spin-echo sequence (TR/TE = 2500/30 ms, rare factor = 8, average = 3, 3 minutes of acquisition).

For quantitative analysis of tissue muscles, maps of T2 relaxation times were acquired at the tibia level (TR = 3000 ms, Echo Images =12, TE= 8.30 to 99.6 ms, average = 2, 9.30 minutes of

acquisition) with axial-sections of 1mm and in-plane resolution of 188x125 µm (FOV = 24x16 mm). Diffusion tensor imaging (DTI) was also acquired with an echo planar imaging sequence (TR/TE = 2800/26 ms; matrix = 128 × 128) with diffusion gradients applied in 30 directions (b = 900 s/mm2 and duration/separation = 5/11 ms) or without (n = 5, b = 0). From DTI, the main diffusion directions and the magnitude of diffusivity were calculated in all 3 directions using standard algorithms (Bruker-Paravision 6.0) that generate maps of the fractional anisotropy (FA), mean diffusivity (MD), axial diffusivity ($\lambda_{||}$), and radial diffusivity ($\lambda_{\perp}$). For each exam, MRI parameters were measured by manual drawing of regions of interest (ROIs) in the anterior tibialis (TA) muscle.

To assess muscle metabolism, proton MR spectroscopy (^{1}H-MRS) was used. In detail, a PRESS sequence was applied with the selection of a voxel in the anterior tibialis (size = 1.6 × 1.6 × 3 mm3) with water-suppression (VAPOR) and fixed TR/TE (2000/16.6 ms). The signal was accumulated 300 times leading to a total acquisition time of 10 minutes. For each acquisition, the magnetic field homogeneity was specifically optimized by automatic map-shim calculation from a B0 map initially acquired (Bruker, Paravision 6.0). A spectrum with no water suppression was also acquired and used for metabolites concentration calculation using the LCModel program (http://s-provencher.com/lcmodel.shtml). All acquired spectra were obtained with a suitable signal-to-noise ratio (>4) allowing the quantification of the most abundant metabolites present in TA

muscle. Metabolites with an estimated standard deviation (Cramer-Rao lower bounds, %SD) higher than 25% were excluded.

4.3.4.Muscle embedding and Immunofluorescence

TA muscles were embedded in Killik (Bio-Optica, 05-9801), immediately frozen in pre-cooled isopentane, and cryosectioned at 10 um thin.

Immunofluorescence were performed as described previously (Bianchi et al., 2020a), with minor adjustment. Sections were fixed for 20 minutes in PFA 4% ((Sigma 30525-89) and washed 3x5 minutes in PBS 1X. Pre-cooled methanol at -20° for 6 minutes was used for the permeabilization. Antigen retrieval was performed 2x5 minutes in hot citric acid (75°C) pH6.0 and washed 2x5 minutes in PBS 1X. Sections were blocked for 1 h in BSA 5% followed by incubation for 45 minutes with FAB mouse fragment 1:100 in DPBS (Jackson Immuno Research, 115-007-003). Primary antibodies were diluted in BSA 5% and incubated O/N at 4°C. Primary antibodies: MyoD 1:100 (Thermo-Fisher, PAS23078), KI67 1:100 (Abcam, ab115580), Laminin 1:100 (Invitrogen, MA106100). The day after, sections were washed 3x5 minutes in PBS 1X complemented with 0,1% BSA and incubated with secondary antibodies (Invitrogen, anti-Rabbit AF647 #A31573, anti-Rat AF568 #A11077) in BSA 5% 1h at RT

in the dark. Then, sections were washed for 3x5 minutes in PBS 1X complemented with 0,1% BSA and incubated with Pax7 1:20 (Developmental Studies Hybridoma Bank). After washing 3x5 minutes in PBS 1X complemented with 0,1% BSA sections were incubated for 45 minutes with primary antibody Biotin (1:500) (Jackson Immuno Research, 115-065-205) for Pax7 signal amplification. After washing 3x5 minutes in PBS 1X, sections were incubated for 30 minutes with secondary antibodies 488-streptavidin 1:1250 (Jackson Immuno Research, AB_2337249). The sections were washed 3x5 minutes in PBS 1X, stained 8 minutes with DAPI (1:1000 in PBS 1X), washed 3x5 minutes in PBS 1X and mounted on slide with a drop of Prolong Glass (Invitrogen, P36980).

4.3.5.Image acquisition

Images were acquired using a Leica Sp5 confocal microscope using 40x objectives and analyzed using Fiji (Schindelin et al., 2012).

4.3.6.Muscle Stem Cell and Fibroadipogenic Precursor extraction and FACS sorting

Hind and Fore-limb muscles were isolated from sacrificed mice and digested 60/75 minutes in 2,4 U/ml of Dispase II (Roche, 04942078001), 2 mg/ml of Collagenase A (Roche, 1013586001), 0,4 mM CaCl2 (Sigma, C5670), 5 mM MgCl2 (Sigma, M8266), 0,1 mg/mL DNase I (Roche, 1014159001) in PBS 1X at 37°C in a water bath. The samples were resuspended in HBSS (Gibco, 14025-050) and implemented with 0,2% BSA (Sigma, A7030) to stop the enzymatic digestion. The cell suspension was serially filtered with 70 µm and 40 µm cells strainers and resuspended in HBBS +++ (0,2% BSA, 1% DNase I, 1% PenStrep (Euroclone, ECB3001) for the night. The day after, cell suspension was stained 30 minutes at 4°C with the following antibodies: PB-CD45 1:50 (eBioscience 48-0451), PB-CD31 1:50 (eBioscience 48-0311), PB-Ter119 1:50 (eBioscience 48-5921), FITC-Sca1 1:50 (eBioscience 11-5981), APC 7integrin 1:100 (AbLab, 67-001-05) and sorted with BD FACS ARIA SORP for: PB-CD45$^-$/ PB-CD31$^-$/ PB-Ter119$^-$/ FITC-Sca1$^-$/APC-7integrin$^+$ (Muscle Stem Cell) and PB-CD45$^-$/ PB-CD31$^-$/ PB-Ter119$^-$/ FITC-Sca1$^+$/APC-7integrin$^-$ (Fibroadipogenic Precursor).

4.3.7.Immunofluorescence on Muscle Stem Cells

To preserve the integrity of chromatin architecture, Skeletal muscle cell suspension was fixed in 1:10 formaldehyde solution (50mM Hepes-KOH pH7.5, 100mM NaCl, 1mM EDTA, 0.5mM EGTA, 11% formaldehyde - in H2O) for 9 minutes at room temperature in mild agitation and quenched with 125 mM Glycine before FACS sorting. Sorted muscle stem cells (MuSCs) were adhered on poly-L-lysine (Sigma, P8920) pre-coated coverslips for 30 minutes at RT. Then, they were fixed with 4% paraformaldehyde (PFA) (Sigma 30525-89) dissolved in PBS, for 7 minutes at RT. After 3 washes in PBS of 5 minutes each, MuSCs were permeabilized in 0.5% Triton X-100/PBS for 10 minutes at RT in mild agitation. Blocking was performed with 5% BSA/PBS for 1 hour at RT. Samples were incubated with a rabbit primary antibody anti-H3K9me3 (Abcam, ab8898) diluted 1:1000 in 50% of blocking solution at 4 °C overnight. After 6 washes in PBS of 3 minutes each, samples were incubated with an anti-rabbit secondary antibody conjugated with Alexa Fluor 568 (Invitrogen, A11036) diluted 1:1000 in Blocking solution, for 2 hours at RT in the dark. After 6 washes in PBS of 3 minutes each, DNA was stained with DAPI (1:1000) in PBS for 10 minutes at RT in the dark. After 6 washes with PBS, coverslips were mounted on a slide with Prolong diamond antifade mountant (Thermo Fisher Scientific, P36961).

4.3.8.Image acquisition

Images were acquired using a Nikon Crest microscope using 40x objectives and analyzed using Fiji (Schindelin et al., 2012).

4.3.9.Sammy-seq protocol

Chromatin fractionation on CTRL004 (10 thousand to 3 million cells), sorted Muscle Stem Cells (10k-250k) was performed with minor adaptations to the protocol described in (Sebestyén et al., 2020). Cells were counted, washed in cold PBS and resuspended in cold cytoskeleton buffer CSK: 10 mM PIPES pH 6,8; 100 mM NaCl; 1 mM EGTA; 300 mM Sucrose; 3 mM $MgCl_2$; 1X Protease Inhibitor Cocktail (Roche, 04693116001); 1 mM PMSF (Sigma-Aldrich, 93482) supplemented with 1 mM DTT and 0,5% Triton X-100. After 10 minutes on a wheel at 4°C, samples were centrifugated for 3 minutes at 900g at 4°C and cytoplasmic and nucleoplasmic components were collected as S1 fraction. Pellets were washed for 10 minutes on the wheel at 4°C with an additional volume of the same CSK buffer (supplemented with 1 mM DTT and 0,5% Triton X-100). Chromatin was then digested by using 25 U DNase I (Invitrogen, AM2222) in CSK buffer for 60 minutes at 37°C. To stop digestion, ammonium sulfate was added to samples to a final concentration of 250 mM and, after 5 minutes on ice, samples were pelleted at 900g for 3 minutes at 4°C and the supernatant was collected as S2 fraction. After a

wash in CSK buffer, the pellet was further extracted with 2M NaCl in CSK buffer for 10 minutes at 4°C, centrifuged at 2300 g for 3 minutes at 4°C and the supernatant was conserved as S3 fraction. Pellets were washed twice for 10 minutes on the wheel at 4°C with a double volume of 2M NaCl CSK buffer. Finally, after 3 minutes of 3000g centrifugation at 4°C, pellets were solubilized in 8M urea for 10 minutes at RT to denature any remaining protein and dissolve membranes and labeled as S4. Fractions were stored at – 80°C until DNA extraction.

4.3.10.DNA extraction, library preparation and sequencing

Fractions were diluted 1:2 in TE buffer (10mM TrisHCl pH 8.0, 1 mM EDTA) and incubated with 61,5 U of RNAse cocktail (Ambion, AM2286) at 37° for 90 minutes, followed by 40µg of Proteinase K (Invitrogen, AM2548), at 55° for 150 minutes. Genomic DNA was then isolated using phenol/chloroform/isoamyl (Sigma-Aldrich, 77617) extraction followed by back extraction of phenol/chloroform/isoamyl with an additional volume of TE buffer. DNA was precipitated adding 20ug glycogen (Ambion AM9510), in 0.3M sodium acetate with 3 volumes of cold ethanol. Precipitating DNA were then incubated for 1 hour in dry ice or overnight at -20° and centrifuged 30 minutes at 23000g. After a wash in 80% ethanol, dry pellets were resuspended in 50 µl (S2) or 15 ul (S3 and S4) of nuclease-free

water and incubated at 4°C overnight. On the next day, S2 was further purified using PCR DNA Purification Kit (Qiagen, 28106) and separated using AMPure XP paramagnetic beads (Beckman Coulter, A63880) with the ratio of 0,90/0,95 to obtain smaller fragments conserved as S2S (< 300 bp) and larger fragments labeled as S2L (> 300bp) fractions. Both were suspended in 15 ul of nuclease-free water. S2L, S3 and S4 fractions were sonicated in a Covaris M220 focused-ultrasonicator using screw cap microTUBEs (Covaris, 004078) to obtain a smear of DNA fragments peaking at 150-350 bp (water bath 20°C, peak power 30.0, duty factor 20.0, cycles/burst 50). MuSCs: 150 seconds for S2L and 175 seconds for S3 and S4; Fibroblasts: 125 seconds for S2L and S3, 150 seconds for S4. Fractions were quantified using Qubit 4 fluorometer with Qubit dsDNA HS Assay Kit (Invitrogen, Q32854) and run on an Agilent 2100 Bioanalyzer using High Sensitivity DNA Kit (Agilent, 5067-4626). Libraries were created from each sample using NEBNext Ultra II DNA Library Prep Kit for Illumina (NEB, E7645L) and Unique Dual Index NEBNextMultiplex Oligos for Illumina (NEB, E6440S); libraries were then qualitatively and quantitatively checked on Bioanalyzer 2100 using High Sensitivity DNA Kit (Agilent, 5067-4626). Libraries with distinct adapter indexes were then multiplexed and, after cluster generation on FlowCell, sequenced for 50 bases in paired-ends mode on an IlluminaNovaSeq 6000 instrument at the IEO Genomic Unit in Milan or in one-end mode at the Division of Pathology of Fondazione IRCCS Ca' Granda-

Ospedale Maggiore, Policlinico of Milan. A sequencing depth of at least 25-35 millions of reads was obtained for each sample.

4.3.11.RNA extraction, library preparation and sequencing

10-20K of Muscle Stem cell/Fibroadipogenic Progenitors from the FACS-sorting were stabilized in 200µl of 1-Thioglycerol/Homogenization Solution of the Maxwell® RSC miRNA Tissue Kit (Promega, AS1460) and stored frozen at -80°C for later total RNA automated purification using Maxwell® RSC 48 Instrument (Promega, AS8500) according to manufacturer's instructions. Total RNA was quantified by Qubit 4 fluorometer with Qubit RNA HS Assay Kit (Invitrogen, Q32852) and assessed by Agilent 2100 Bioanalyzer using Agilent RNA 6000 Pico Kit (Agilent, 5067-1513) to inspect RNA integration. For each sample, 1 ng of total RNA was used to construct strand-specific RNAseq library with SMARTer Stranded Total RNA-Seq Kit - Pico Input (Takara, 634487). The yield and quality of the libraries were evaluated on Agilent 2100 Bioanalyzer using High Sensitivity DNA Kit (Agilent, 5067-4626). RNAseq libraries were sequenced on the Illumina NextSeqTM 550 system at the sequencing facilities of Humanitas or Division of Pathology of Fondazione IRCCS Ca' Granda-Ospedale Maggiore, Policlinico of Milan to a minimum target of 40 million for 75-100 bases in paired-ends mode.

4.3.12.Chromatin Immunoprecipitation, library preparation and sequencing

To preserve the integrity of chromatin architecture, Skeletal muscle cell suspension was fixed as described in the above paragraph (“Immunofluorescence on Muscle Stem Cells”) before FACS sorting. Isolated Muscle Stem cells derived from different mice of the same age were pulled together and stored at -80°C. For ChIP analysis, 1.5 million fixed cells (derived from 15-20 mice) were thawed on ice and resuspended in fresh SDS buffer (10 mM Tris-HCl pH 8.0, 2 mM EDTA, 0.25% SDS, 1X PMSF, 1X protease inhibitors) and sonication was performed using a Covaris M220 focused-ultrasonic with following settings: water bath 7 °C, peak power 75.0, duty factor 10.0, cycles/burst 250, duration: 720 seconds. A small aliquot of chromatin (5ul) was purified and used for a chromatin shearing check. For IP, equilibration buffer (10mM Tris pH 8.0, 233mM NaCl, 1.66% Triton X-100, 0.166% DOC, 1mM EDTA, 1X PMSF, 1X protease inhibitors) was added to the shared chromatin, followed by the incubation with 2 µg of the antibody of interest on a rotating wheel at 4°C overnight. A minimum of 1% of the chromatin was stored as input sample. Primary antibodies: H3K9me3 (Abcam, ab8898), H3K36me3 (Abcam, ab9050)). The next day, protein G beads (Life Technology,1004D) were added, and the samples were incubated for additional 2 hours on the rotating wheel at 4°C. Samples containing the beads-antibody-protein/DNA

complexes were washed twice with IP buffer, high-salt IP buffer (500 mM NaCl in IP buffer), RIPA-LiCl buffer (10 mM TrisHCl pH 8.0, 1mM EDTA, 250 mM LiCl, 0.5% DOC, 0.5% NP-40, 1x PMSF, 1x Protease inhibitors), and TrisHCl pH 8,0. Between each wash the samples were incubated for 5 minutes at 4 °C on the wheel. Finally, protein-DNA complexes were eluted with the Elution buffer (10 mM TrisHCl pH 8.0, 5 mM EDTA, 300 mM NaCl, 0.4% SDS). The cross-links were reverted by incubating the samples (included the input previously stored) overnight at 65°C. DNA was isolated through standard phenol/chloroform extraction, followed by precipitation and resuspension in 10 mM TrisHCl pH8.0. Fractions were quantified using Qubit 4 fluorometer with Qubit dsDNA HS Assay Kit (Invitrogen, Q32854) and run on an Agilent 2100 Bioanalyzer using High Sensitivity DNA Kit (Agilent, 5067-4626). Libraries were created from each sample using NEBNext Ultra II DNA Library Prep Kit for Illumina (NEB, E7645L) and Unique Dual Index NEBNextMultiplex Oligos for Illumina (NEB, E6440S); libraries were then qualitatively and quantitatively checked on Bioanalyzer 2100. Libraries with distinct adapter indexes were then multiplexed and, after cluster generation on FlowCell, sequenced for 50 bases in paired-ends mode on an IlluminaNovaSeq 6000 instrument at the IEO Genomic Unit in Milan. A sequencing depth of at least 30 million reads was obtained for each sample.

4.3.13.Literature data (Human Fibroblast/Murine Muscle Stem Cells)

For Human Fibroblasts, we collected publicly available datasets from the following sources: Lamin A/C ChIP-seq (McCord et al., 2013)(SRR605493, SRR605494, SRR605495 and SRR605496), Lamin B1 ChIP-seq (Dou et al., 2015) (SRR2119331, SRR2119332, SRR2119335 and SRR2119336) and H3K9me3, H3K4me1, H3K36me3, H3K27ac, H3K4me3 from Roadmap Epigenomics (fibroblast sample: E055).
The ChIP-seq data of Muscle Stem Cells have been downloaded from the following publicly datasets available: GSE47362 (H3K27me3, H3K36me3, H3K4me3), GSE123725 (H3K4me3, H3K27me3), GSE103163 (H3K27me3, H3K4me3) (Bianchi et al., 2020a; L. Liu et al., 2013; Machado et al., 2017).
All the data have been downloaded as raw data and analyzed as described in the next sections.

4.3.14.RNA -seq Analysis

The sequenced reads were analyzed with the pipeline nf-core/rnaseq (Baylis, 2020) (v3.8) using Nextflow (J. Zhang et al., 2011) (v21.10.6). Quality reports of raw reads and pre-processed reads are generated by FastQC (Babraham Bioinformatics) (v0.11.9). Quality trimming and adapter clipping are performed by cutadapt (Martin, 2011) (v3.4) and trimmed reads were

cleaned of ribosomal RNA (rRNA) sequences with SortMeRNA (Kopylova et al., 2012) (v4.3.4) considering all the available databases. Reads were then mapped with HISAT2 (Y. Zhang et al., 2021) (v2.7.10a) on mouse genome build mm10 and gene and transcript expression levels were quantified using Salmon (Patro et al., 2017) on GENCODE (Frankish et al., 2021) (vM25) Basic gene annotation. Differential expression analysis and Gene Ontology among age groups were performed with iDEP tool (Ge et al., 2018). Gene Set Enrichment Analysis (GSEA) tool was used in pre-ranked mode as suggested for RNA-seq experiments using the following metric -log10Pvalue*signLogFC for all genes in the annotation as input and the *"classic"* metric for gene ranking (Mootha et al., 2003; Subramanian et al., 2005).

4.3.15.Sammy-seq sequencing read analysis

Sequenced reads were quality evaluated with FastQC (v0.11.9) and trimmed with Trimmomatic (Bolger et al., 2014) (v0.39) with the following parameters: 2 for seed_mismatch, 30 for palindrome_threshold, 10 for simple_threshold, and 4:15 for sliding-window. The sequence minimum length threshold of 36 base pairs has been applied for all data. As clip file has been used the trimmomatic provided dataset "TruSeq3-SE.fa" (for single end) and "TruSeq3-PE-2.fa" (for paired end). After trimming, reads were aligned with BWA (H. Li & Durbin, 2009)

(v0.7.17-r1188) with -n 2 -k 2 parameters using as reference genome UCSC mm10 (Stolarczyk et al., 2020). Duplicates are marked and removed with Picard (v2.22) (https://github.com/broadinstitute/picard) MarkDuplicates option and then filtered using Samtools (H. Li et al., 2009) (v1.11). We further filtered all the reads with a mapping quality lower than 1. From the alignment output, a coverage analysis was performed using Deeptools (Ramírez et al., 2014) (v3.5.0) bamCoverage function (single track). For this analysis the genome was binned at 50bp, the reads extended to 250 bp and the RPKM normalization method has been used. Mouse genome size was considered of 2652783500 bp (value suggested in the Deeptools (manualhttps://deeptools.readthedocs.io/en/latest/content/feature/effectiveGenomeSize.html). From the analysis, were excluded regions known to be problematic in terms of sequencing (the list has been downloaded from ENCODE blacklisted regions https://www.encodeproject.org/files/ENCFF547MET). SAMMY-seq smoothed differential signal enrichment (comparison analysis) has been calculated using SPP (Kharchenko et al., 2008) (v 1.16.0) R (Hahne & Ivanek, 2016) (v4.1.2) library. The bam files were imported with the "read.bam.tags" function, then they were filtered using “remove.local.tag.anomalies”, finally comparisons were computed using “get.smoothed.enrichment.mle” function, with setting “tag.shift = 0” and “background.density.scaling = TRUE ” , then converted to bigwig data format with UCSC tool wigToBigWig (Kent et al.,

2010) (v4). The analysis was performed with the same parameters for all the datasets.

4.3.16.Correlation Analysis

Genome-wide Spearman correlations between SAMMY-seq samples and all the dataset was conducted using Deeptools (Ramírez et al., 2014) (v3.5.0) using the function "plotCorrelation" with the following settings: "—corData --corMethod spearman -p heatmap --skipZeros --plotNumbers". Before the analysis, the smoothed differential signal enrichment (see section “SAMMY-seq sequencing read analysis”) is rebinned with Deeptools (Ramírez et al., 2014) (v3.5.0) "multiBigwigSummary" at 100Kb with the setting "–bs 100000". The analysis was performed identically for all the datasets.

4.3.17.Consensus Track generation

The consensus signal, necessary for subsequent analysis, is generated using the results of Deeptools (Ramírez et al., 2014) (v3.5.0) "multiBigwigSummary" at 10kb, with -bs option 1000 on Single tracks (see section “SAMMY-seq sequencing read analysis”). Signals are further normalized by removing all bins with no signal and computing quantile normalization with the preprocessCore (*GitHub - Bmbolstad/PreprocessCore*, n.d.)

(v1.56.0) library using the function "normalize.quantiles". After data normalization, the consensus track is generated by computing the mean of the signals and the confidence intervals.

4.3.18.Track Visualization

Tracks visualization was performed with the Gviz(Hahne & Ivanek, 2016) R library (v1.38.0). The track profiles are computed using the function "DataTrack". The comparisons (see section “SAMMY-seq sequencing read analysis”) were plotted using the mountain plots with "polygon", along with the function "plotTracks" settings the value "window = 900". To visualize the consensus tracks, (see method consensus track generation) samples of each time point have been overlayed with "OverlayTrack" and plotted with “DataTrack” function.

4.3.19.A/B compartment analysis

Pairwise Fisher’s z-transformed correlations were computed between each SAMMY-seq fraction at 250kb resolution. The resulting correlation matrix was used to calculate the euclidean distance between pairs of points defined in the n-dimensional space, where n is the number of fractions. A/B compartments were identified from the first eigenvectors of Fisher’s z-transformed correlation matrices of 250kb-resolution solubility

matrices. The sign of the first eigenvector was oriented by the gene density of each domain (Lieberman-Aiden et al., 2009b) such that domains with higher gene density were assigned positive signs (A compartment) while domains with lower gene density were assigned negative signs (B compartment). The compartment eigenvector BED files were then exported and analyzed in R to identify compartments that were steady or switched between the following comparison: postnatal vs adult, adult vs old, and old vs geriatric MuSCs. Analysis was performed with R (v.4.1.2) applying functions deriving from the Calder algorithm (Y. Liu et al., 2021).

4.3.20.ChiP-seq read analysis

After sequencing, reads were qualitatively checked with FastQC (v0.11.8) and trimmed with Trimmomatic (Bolger et al., 2014) (v0.39), to remove adapters and low-quality bases. An additional Fast QC quality control was performed to evaluate the quality of the reads after trimming. Reads were then aligned in single-end to the mouse reference genome (mm10) (Stolarczyk et al., 2020), using BWA (H. Li & Durbin, 2009) (v0.7.17). Aligned reads were stored as SAM format and then transformed into a BAM file, using SAMtools (H. Li et al., 2009) (v1.13) PCR duplicates were removed with Picard (version 2.23.9; http://broadinstitute.github.io/picard) and only reads with mapping quality > 1 were kept. The downstream analyses of

quality control were performed with the R package ChIC (Livi et al., 2020) (ChIP-seq quality Control) (v1.10.0).

4.3.21.ChiP-seq Peak calling and annotation

Peak calling for H3K4me3 datasets was performed using macs2 (Y. Zhang et al., 2008) (v2.2.7.1) with options -q 0.05 to filter peaks with q-values higher than 0.05. For Broad ChIP-seq data (H3K9me3, H3K36me3, H3K27me3), peak calling was performed using epic2 (Stovner & Sætrom, 2019) (0.0.52), setting the FDR ≤ 0.05. Unwanted chromosomes were removed with the option -d '(GL|JH|M)'. The following settings were used for each histone mark analysis: H3K36me3 peaks --bin-size and --gaps-allowed were left to auto-mode; H3K27me3, the --bin-size 200 and --gaps-allowed 3; H3K9me3 --bin-size 600 --gaps-allowed 30. ChiP-seq peaks are annotated on the GENCODE vM25 basic gene annotation (Frankish et al., 2021). For H3K4me3 and H3K27me3 histone marks, peaks were associated with the genes on ±1Kb around TSS. For H3K36me3, we selected genes based on the presence of peaks inside gene bodies. Finally, for H3K9me3, genes are selected if the TSS are inside a peak. Peak biological replicas, where present, were merged to ensure reproducibility.

4.3.22.Statistical Analysis

All the data are represented as mean with S.E.M. (Standard Error of the Mean) using Graph Pad prism. The sample size (n) is described for each experiment in the relative figure legend. Multiple comparisons between three or more groups were made using one-way Anova or two-way Anova with significance as P value <0,05 (*), P value < 0,01 (**), P value <0,001 (***), P value <0,0001 (****).

4.4. Reference to Chapter 4

Bachman, J. F., Klose, A., Liu, W., Paris, N. D., Blanc, R. S., Schmalz, M., Knapp, E., & Chakkalakal, J. v. (2018). Prepubertal skeletal muscle growth requires Pax7-expressing satellite cell-derived myonuclear contribution. *Development*, *145*(20). https://doi.org/10.1242/dev.167197

Baker, S. J., Ma'ayan, A., Lieu, Y. K., John, P., Reddy, M. V. R., Chen, E. Y., Duan, Q., Snoeck, H.-W., & Reddy, E. P. (2014). B-myb is an essential regulator of hematopoietic stem cell and myeloid progenitor cell development. *Proceedings of the National Academy of Sciences of the United States of America*, *111*(8), 3122–3127. https://doi.org/10.1073/pnas.1315464111

Bakhmet, E. I., Nazarov, I. B., Gazizova, A. R., Vorobyeva, N. E., Kuzmin, A. A., Gordeev, M. N., Sinenko, S. A., Aksenov, N. D., Artamonova, T. O., Khodorkovskii, M. A., Alenina, N., Onichtchouk, D., Wu, G., Schöler, H. R., & Tomilin, A. N. (2019). hnRNP-K Targets Open Chromatin in Mouse Embryonic Stem Cells in Concert with Multiple Regulators. *Stem Cells*, *37*(8), 1018–1029. https://doi.org/10.1002/stem.3025

Bantele, S. C., Ferreira, P., Gritenaite, D., Boos, D., & Pfander, B. (2017). Targeting of the Fun30 nucleosome remodeller by the Dpb11 scaffold facilitates cell cycle-regulated DNA end resection. *ELife*, *6*. https://doi.org/10.7554/eLife.21687

Baylis, F. (2020). Competing interests The nf-core framework for community-curated bioinformatics pipelines. *Nature Biotechnology*, *38*. https://doi.org/10.1038/s41587-020-0446-y

Beites, C. L., Hollenbeck, P. L. W., Kim, J., Lovell-Badge, R., Lander, A. D., & Calof, A. L. (2009). Follistatin modulates a BMP autoregulatory loop to control the size and patterning of sensory domains in the developing tongue. *Development*, *136*(13), 2187–2197. https://doi.org/10.1242/dev.030544

Bernet, J. D., Doles, J. D., Hall, J. K., Kelly Tanaka, K., Carter, T. A., & Olwin, B. B. (2014). P38 MAPK signaling underlies a cell-autonomous loss of stem cell self-renewal in skeletal muscle of aged mice. *Nature Medicine*, *20*(3), 265–271. https://doi.org/10.1038/nm.3465

Bernstein, B. E., Mikkelsen, T. S., Xie, X., Kamal, M., Huebert, D. J., Cuff, J., Fry, B., Meissner, A., Wernig, M., Plath, K., Jaenisch, R., Wagschal, A., Feil, R., Schreiber, S. L., & Lander, E. S. (2006). A Bivalent Chromatin Structure Marks Key Developmental Genes in Embryonic Stem Cells. *Cell*, *125*(2), 315–326. https://doi.org/10.1016/j.cell.2006.02.041

Bianchi, A., Mozzetta, C., Pegoli, G., Lucini, F., Valsoni, S., Rosti, V., Petrini, C., Cortesi, A., Gregoretti, F., Antonelli, L., Oliva, G., de Bardi, M., Rizzi, R., Bodega, B., Pasini, D., Ferrari, F., Bearzi, C., & Lanzuolo, C. (2020). Dysfunctional polycomb transcriptional repression contributes to lamin A/C–dependent muscular dystrophy. *Journal of Clinical Investigation*, *130*(5), 2408–2421. https://doi.org/10.1172/JCI128161

Bolger, A. M., Lohse, M., & Usadel, B. (2014). Trimmomatic: a flexible trimmer for Illumina sequence data. *Bioinformatics*, *30*(15), 2114–2120. https://doi.org/10.1093/BIOINFORMATICS/BTU170

Boonsanay, V., Zhang, T., Georgieva, A., Kostin, S., Qi, H., Yuan, X., Zhou, Y., & Braun, T. (2016). Regulation of Skeletal Muscle Stem Cell Quiescence by Suv4-20h1-Dependent Facultative Heterochromatin Formation. *Cell Stem Cell*, *18*(2), 229–242. https://doi.org/10.1016/j.stem.2015.11.002

Brack, A. S., Bildsoe, H., & Hughes, S. M. (2005). Evidence that satellite cell decrement contributes to preferential decline in nuclear number from large fibres during murine age-related muscle atrophy. *Journal of Cell Science*, *118*(20), 4813–4821. https://doi.org/10.1242/JCS.02602

Brock, A. L., & Ingber, D. E. (2005). Control of the direction of lamellipodia extension through changes in the balance between Rac and Rho activities. *Molecular & Cellular Biomechanics : MCB*, *2*(3), 135–143.

Carlson, M. E., & Conboy, I. M. (2007). Loss of stem cell regenerative capacity within aged niches. *Aging Cell*, *6*(3), 371–382. https://doi.org/10.1111/J.1474-9726.2007.00286.X

Chakkalakal, J. v., Jones, K. M., Basson, M. A., & Brack, A. S. (2012). The aged niche disrupts muscle stem cell quiescence. *Nature*, *490*(7420), 355–360. https://doi.org/10.1038/nature11438

Chen, C., Yu, W., Tober, J., Gao, P., He, B., Lee, K., Trieu, T., Blobel, G. A., Speck, N. A., & Tan, K. (2019). Spatial Genome Re-organization between Fetal and Adult Hematopoietic Stem Cells. *Cell Reports*, *29*(12), 4200. https://doi.org/10.1016/J.CELREP.2019.11.065

Chiu, Y.-C., Li, M.-Y., Liu, Y.-H., Ding, J.-Y., Yu, J.-Y., & Wang, T.-W. (2014). Foxp2 regulates neuronal differentiation and neuronal subtype specification. *Developmental Neurobiology*, *74*(7), 723–738. https://doi.org/10.1002/dneu.22166

Dell'Orso, S., Juan, A. H., Ko, K.-D., Naz, F., Gutierrez-Cruz, G., Feng, X., & Sartorelli, V. (2019). Single-cell analysis of adult skeletal muscle stem cells in homeostatic and regenerative conditions. *Development*, *146*(12). https://doi.org/10.1242/dev.174177

Dixon, J. R., Jung, I., Selvaraj, S., Shen, Y., Antosiewicz-Bourget, J. E., Lee, A. Y., Ye, Z., Kim, A., Rajagopal, N., Xie, W., Diao, Y., Liang, J., Zhao, H., Lobanenkov, V. v., Ecker, J. R., Thomson, J. A., & Ren, B. (2015). Chromatin architecture reorganization during stem cell differentiation. *Nature*, *518*(7539), 331–336. https://doi.org/10.1038/nature14222

Dou, Z., Xu, C., Donahue, G., Shimi, T., Pan, J.-A., Zhu, J., Ivanov, A., Capell, B. C., Drake, A. M., Shah, P. P., Catanzaro, J. M., Daniel Ricketts, M., Lamark, T., Adam, S. A., Marmorstein, R., Zong, W.-X., Johansen, T., Goldman, R. D., Adams, P. D., & Berger, S. L. (2015). Autophagy mediates degradation of nuclear lamina. *Nature*, *527*(7576), 105–109. https://doi.org/10.1038/nature15548

el Husseini, N., & Hales, B. F. (2018). The Roles of P53 and Its Family Proteins, P63 and P73, in the DNA Damage Stress Response in Organogenesis-Stage Mouse Embryos. *Toxicological Sciences*, *162*(2), 439–449. https://doi.org/10.1093/toxsci/kfx270

Frankish, A., Diekhans, M., Jungreis, I., Lagarde, J., Loveland, J. E., Mudge, J. M., Sisu, C., Wright, J. C., Armstrong, J., Barnes, I., Berry, A., Bignell, A., Boix, C., Carbonell Sala, S., Cunningham, F., Di Domenico, T., Donaldson, S., Fiddes, I. T., García Girón, C., … Flicek, P. (2021). GENCODE 2021. *Nucleic Acids Research*, *49*(D1), D916–D923. https://doi.org/10.1093/nar/gkaa1087

Gattazzo, F., Laurent, B., Relaix, F., Rouard, H., & Didier, N. (2020). Distinct Phases of Postnatal Skeletal Muscle Growth Govern the Progressive Establishment of Muscle Stem Cell Quiescence. *Stem Cell Reports*, *15*(3), 597–611. https://doi.org/10.1016/j.stemcr.2020.07.011

Ge, S. X., Son, E. W., & Yao, R. (2018). iDEP: an integrated web application for differential expression and pathway analysis of RNA-Seq data. *BMC Bioinformatics*, *19*(1), 534. https://doi.org/10.1186/s12859-018-2486-6

Gharibeh, L., Yamak, A., Whitcomb, J., Lu, A., Joyal, M., Komati, H., Liang, W., Fiset, C., & Nemer, M. (2021). GATA6 is a regulator of sinus node development and heart rhythm. *Proceedings of the National Academy of Sciences of the United States of America*, *118*(1), e2007322118. https://doi.org/10.1073/pnas.2007322118

GitHub - bmbolstad/preprocessCore. (n.d.). Retrieved 3 October 2022, from https://github.com/bmbolstad/preprocessCore

Gong, C., Kim, Y. K., Woeller, C. F., Tang, Y., & Maquat, L. E. (2009). SMD and NMD are competitive pathways that contribute to myogenesis: effects on PAX3 and myogenin mRNAs. *Genes & Development*, *23*(1), 54–66. https://doi.org/10.1101/gad.1717309

Hahne, F., & Ivanek, R. (2016). Visualizing Genomic Data Using Gviz and Bioconductor. In *Methods in Molecular Biology* (Vol. 1418, pp. 335–351). Humana Press Inc. https://doi.org/10.1007/978-1-4939-3578-9_16

Hérault, L., Poplineau, M., Mazuel, A., Platet, N., Remy, É., & Duprez, E. (2021). Single-cell RNA-seq reveals a concomitant delay in differentiation and cell cycle of aged hematopoietic stem cells. *BMC Biology*, *19*(1), 19. https://doi.org/10.1186/s12915-021-00955-z

Hulsen, T., de Vlieg, J., & Alkema, W. (2008). BioVenn – a web application for the comparison and visualization of biological lists using area-proportional Venn diagrams. *BMC Genomics*, *9*(1), 488. https://doi.org/10.1186/1471-2164-9-488

Joe, A. W. B., Yi, L., Natarajan, A., le Grand, F., So, L., Wang, J., Rudnicki, M. A., & Rossi, F. M. v. (2010). Muscle injury activates resident fibro/adipogenic progenitors that facilitate

myogenesis. *Nature Cell Biology*, *12*(2), 153–163. https://doi.org/10.1038/ncb2015
Kent, W. J., Zweig, A. S., Barber, G., Hinrichs, A. S., & Karolchik, D. (2010). BigWig and BigBed: enabling browsing of large distributed datasets. *Bioinformatics*, *26*(17), 2204–2207. https://doi.org/10.1093/bioinformatics/btq351
Kharchenko, P. v, Tolstorukov, M. Y., & Park, P. J. (2008). Design and analysis of ChIP-seq experiments for DNA-binding proteins. *Nature Biotechnology*, *26*(12), 1351–1359. https://doi.org/10.1038/nbt.1508
Kodama, T., Marian, T. A., Lee, H., Kodama, M., Li, J., Parmacek, M. S., Jenkins, N. A., Copeland, N. G., & Wei, Z. (2019). MRTFB suppresses colorectal cancer development through regulating SPDL1 and MCAM. *Proceedings of the National Academy of Sciences*, *116*(47), 23625–23635. https://doi.org/10.1073/pnas.1910413116
Kolk, S. M., Whitman, M. C., Yun, M. E., Shete, P., & Donoghue, M. J. (2006). A unique subpopulation of Tbr1-expressing deep layer neurons in the developing cerebral cortex. *Molecular and Cellular Neuroscience*, *32*(1–2), 200–214. https://doi.org/10.1016/j.mcn.2005.08.022
Kopylova, E., Noé, L., & Touzet, H. (2012). SortMeRNA: fast and accurate filtering of ribosomal RNAs in metatranscriptomic data. *Bioinformatics (Oxford, England)*, *28*(24), 3211–3217. https://doi.org/10.1093/BIOINFORMATICS/BTS611
Ku, C.-J., Hosoya, T., Maillard, I., & Engel, J. D. (2012). GATA-3 regulates hematopoietic stem cell maintenance and cell-cycle entry. *Blood*, *119*(10), 2242–2251. https://doi.org/10.1182/blood-2011-07-366070
Lepper, C., Conway, S. J., & Fan, C. M. (2009). Adult satellite cells and embryonic muscle progenitors have distinct genetic requirements. *Nature*, *460*(7255), 627–631. https://doi.org/10.1038/nature08209
Li, H., & Durbin, R. (2009). Fast and accurate short read alignment with Burrows-Wheeler transform. *Bioinformatics*, *25*(14), 1754–1760. https://doi.org/10.1093/bioinformatics/btp324
Li, H., Handsaker, B., Wysoker, A., Fennell, T., Ruan, J., Homer, N., Marth, G., Abecasis, G., & Durbin, R. (2009). The Sequence

Alignment/Map format and SAMtools. *Bioinformatics*, *25*(16), 2078–2079. https://doi.org/10.1093/bioinformatics/btp352

Li, Z., Chen, X., Vong, J. S. L., Zhao, L., Huang, J., Yan, L. Y. C., Ip, B., Wing, Y. K., Lai, H.-M., Mok, V. C. T., & Ko, H. (2021). Systemic GLP-1R agonist treatment reverses mouse glial and neurovascular cell transcriptomic aging signatures in a genome-wide manner. *Communications Biology*, *4*(1), 656. https://doi.org/10.1038/s42003-021-02208-9

Lieberman-Aiden, E., van Berkum, N. L., Williams, L., Imakaev, M., Ragoczy, T., Telling, A., Amit, I., Lajoie, B. R., Sabo, P. J., Dorschner, M. O., Sandstrom, R., Bernstein, B., Bender, M. A., Groudine, M., Gnirke, A., Stamatoyannopoulos, J., Mirny, L. A., Lander, E. S., & Dekker, J. (2009a). Comprehensive mapping of long-range interactions reveals folding principles of the human genome. *Science*, *326*(5950), 289–293. https://doi.org/10.1126/SCIENCE.1181369/SUPPL_FILE/LIEBERMAN-AIDEN.SOM.PDF

Lieberman-Aiden, E., van Berkum, N. L., Williams, L., Imakaev, M., Ragoczy, T., Telling, A., Amit, I., Lajoie, B. R., Sabo, P. J., Dorschner, M. O., Sandstrom, R., Bernstein, B., Bender, M. A., Groudine, M., Gnirke, A., Stamatoyannopoulos, J., Mirny, L. A., Lander, E. S., & Dekker, J. (2009b). Comprehensive Mapping of Long-Range Interactions Reveals Folding Principles of the Human Genome. *Science*, *326*(5950), 289–293. https://doi.org/10.1126/science.1181369

Liu, L., Cheung, T. H., Charville, G. W., Hurgo, B. M. C., Leavitt, T., Shih, J., Brunet, A., & Rando, T. A. (2013). Chromatin Modifications as Determinants of Muscle Stem Cell Quiescence and Chronological Aging. *Cell Reports*, *4*(1), 189–204. https://doi.org/10.1016/j.celrep.2013.05.043

Liu, Y., Nanni, L., Sungalee, S., Zufferey, M., Tavernari, D., Mina, M., Ceri, S., Oricchio, E., & Ciriello, G. (2021). Systematic inference and comparison of multi-scale chromatin sub-compartments connects spatial organization to cell phenotypes. *Nature Communications*, *12*(1), 2439. https://doi.org/10.1038/s41467-021-22666-3

Livi, C. M., Tagliaferri, I., Pal, K., Sebestyén, E., Lucini, F., Bianchi, A., Valsoni, S., Lanzuolo, C., & Ferrari, F. (2020). A ChIC

solution for ChIP-seq quality assessment. *BioRxiv*, 2020.05.19.103887. https://doi.org/10.1101/2020.05.19.103887

Lou, C.-H., Chousal, J., Goetz, A., Shum, E. Y., Brafman, D., Liao, X., Mora-Castilla, S., Ramaiah, M., Cook-Andersen, H., Laurent, L., & Wilkinson, M. F. (2016). Nonsense-Mediated RNA Decay Influences Human Embryonic Stem Cell Fate. *Stem Cell Reports*, *6*(6), 844–857. https://doi.org/10.1016/j.stemcr.2016.05.008

Machado, L., Esteves de Lima, J., Fabre, O., Proux, C., Legendre, R., Szegedi, A., Varet, H., Ingerslev, L. R., Barrès, R., Relaix, F., & Mourikis, P. (2017). In Situ Fixation Redefines Quiescence and Early Activation of Skeletal Muscle Stem Cells. *Cell Reports*, *21*(7), 1982–1993. https://doi.org/10.1016/j.celrep.2017.10.080

Malecova, B., Gatto, S., Etxaniz, U., Passafaro, M., Cortez, A., Nicoletti, C., Giordani, L., Torcinaro, A., de Bardi, M., Bicciato, S., de Santa, F., Madaro, L., & Puri, P. L. (2018). Dynamics of cellular states of fibro-adipogenic progenitors during myogenesis and muscular dystrophy. *Nature Communications*, *9*(1), 3670. https://doi.org/10.1038/s41467-018-06068-6

Martin, M. (2011). Cutadapt removes adapter sequences from high-throughput sequencing reads. *EMBnet.Journal*, *17*(1), 10. https://doi.org/10.14806/ej.17.1.200

Martin-Herranz, D. E., Aref-Eshghi, E., Bonder, M. J., Stubbs, T. M., Choufani, S., Weksberg, R., Stegle, O., Sadikovic, B., Reik, W., & Thornton, J. M. (2019). Screening for genes that accelerate the epigenetic aging clock in humans reveals a role for the H3K36 methyltransferase NSD1. *Genome Biology*, *20*(1), 1–19. https://doi.org/10.1186/S13059-019-1753-9/FIGURES/3

Martins-Bach, A. B., Malheiros, J., Matot, B., Martins, P. C. M., Almeida, C. F., Caldeira, W., Ribeiro, A. F., de Sousa, P. L., Azzabou, N., Tannús, A., Carlier, P. G., & Vainzof, M. (2015). Quantitative T2 combined with texture analysis of nuclear magnetic resonance images identify different degrees of muscle involvement in three mouse models of muscle dystrophy: Mdx, Largemydand mdx/Largemyd. *PLoS ONE*, *10*(2). https://doi.org/10.1371/journal.pone.0117835

McCord, R. P., Nazario-Toole, A., Zhang, H., Chines, P. S., Zhan, Y., Erdos, M. R., Collins, F. S., Dekker, J., & Cao, K. (2013).

Correlated alterations in genome organization, histone methylation, and DNA–lamin A/C interactions in Hutchinson-Gilford progeria syndrome. *Genome Research*, *23*(2), 260–269. https://doi.org/10.1101/gr.138032.112

Mootha, V. K., Lindgren, C. M., Eriksson, K.-F., Subramanian, A., Sihag, S., Lehar, J., Puigserver, P., Carlsson, E., Ridderstråle, M., Laurila, E., Houstis, N., Daly, M. J., Patterson, N., Mesirov, J. P., Golub, T. R., Tamayo, P., Spiegelman, B., Lander, E. S., Hirschhorn, J. N., … Groop, L. C. (2003). PGC-1alpha-responsive genes involved in oxidative phosphorylation are coordinately downregulated in human diabetes. *Nature Genetics*, *34*(3), 267–273. https://doi.org/10.1038/ng1180

Moretti, A., Paoletta, M., Liguori, S., Bertone, M., Toro, G., & Iolascon, G. (2020). Choline: An Essential Nutrient for Skeletal Muscle. *Nutrients*, *12*(7), 2144. https://doi.org/10.3390/nu12072144

Oprescu, S. N., Yue, F., Qiu, J., Brito, L. F., & Kuang, S. (2020). Temporal Dynamics and Heterogeneity of Cell Populations during Skeletal Muscle Regeneration. *IScience*, *23*(4), 100993. https://doi.org/10.1016/j.isci.2020.100993

Patro, R., Duggal, G., Love, M. I., Irizarry, R. A., & Kingsford, C. (2017). Salmon provides fast and bias-aware quantification of transcript expression. *Nature Methods*, *14*(4), 417–419. https://doi.org/10.1038/nmeth.4197

Ramírez, F., Dündar, F., Diehl, S., Grüning, B. A., & Manke, T. (2014). deepTools: a flexible platform for exploring deep-sequencing data. *Nucleic Acids Research*, *42*(W1), W187–W191. https://doi.org/10.1093/nar/gku365

Relaix, F., Bencze, M., Borok, M. J., der Vartanian, A., Gattazzo, F., Mademtzoglou, D., Perez-Diaz, S., Prola, A., Reyes-Fernandez, P. C., Rotini, A., & Taglietti. (2021). Perspectives on skeletal muscle stem cells. *Nature Communications 2021 12:1*, *12*(1), 1–11. https://doi.org/10.1038/s41467-020-20760-6

Sambasivan, R., Yao, R., Kissenpfennig, A., van Wittenberghe, L., Paldi, A., Gayraud-Morel, B., Guenou, H., Malissen, B., Tajbakhsh, S., & Galy, A. (2011). Pax7-expressing satellite cells are indispensable for adult skeletal muscle regeneration. *Development*, *138*(17), 3647–3656. https://doi.org/10.1242/DEV.067587

Schindelin, J., Arganda-Carreras, I., Frise, E., Kaynig, V., Longair, M., Pietzsch, T., Preibisch, S., Rueden, C., Saalfeld, S., Schmid, B., Tinevez, J.-Y., White, D. J., Hartenstein, V., Eliceiri, K., Tomancak, P., & Cardona, A. (2012). Fiji: an open-source platform for biological-image analysis. *Nature Methods*, *9*(7), 676–682. https://doi.org/10.1038/nmeth.2019

Sebestyén, E., Marullo, F., Lucini, F., Petrini, C., Bianchi, A., Valsoni, S., Olivieri, I., Antonelli, L., Gregoretti, F., Oliva, G., Ferrari, F., & Lanzuolo, C. (2020). SAMMY-seq reveals early alteration of heterochromatin and deregulation of bivalent genes in Hutchinson-Gilford Progeria Syndrome. *Nature Communications*, *11*(1). https://doi.org/10.1038/S41467-020-20048-9

Shen, B., Wei, A., Whittaker, S., Williams, L. A., Tao, H., Ma, D. D. F., & Diwan, A. D. (2009). The role of BMP-7 in chondrogenic and osteogenic differentiation of human bone marrow multipotent mesenchymal stromal cells in vitro. *Journal of Cellular Biochemistry*, *109*(2), n/a-n/a. https://doi.org/10.1002/jcb.22412

Shi, X., & Garry, D. J. (2006). Muscle stem cells in development, regeneration, and disease. *Genes & Development*, *20*(13), 1692–1708. https://doi.org/10.1101/gad.1419406

Solovei, I., Wang, A. S., Thanisch, K., Schmidt, C. S., Krebs, S., Zwerger, M., Cohen, T. V., Devys, D., Foisner, R., Peichl, L., Herrmann, H., Blum, H., Engelkamp, D., Stewart, C. L., Leonhardt, H., & Joffe, B. (2013). LBR and Lamin A/C Sequentially Tether Peripheral Heterochromatin and Inversely Regulate Differentiation. *Cell*, *152*(3), 584–598. https://doi.org/10.1016/j.cell.2013.01.009

Sousa-Victor, P., Gutarra, S., García-Prat, L., Rodriguez-Ubreva, J., Ortet, L., Ruiz-Bonilla, V., Jardí, M., Ballestar, E., González, S., Serrano, A. L., Perdiguero, E., & Muñoz-Cánoves, P. (2014). Geriatric muscle stem cells switch reversible quiescence into senescence. *Nature*, *506*(7488), 316–321. https://doi.org/10.1038/nature13013

Spriet, L. L., & Whitfield, J. (2015). Taurine and skeletal muscle function. *Current Opinion in Clinical Nutrition and Metabolic Care*, *18*(1), 96–101. https://doi.org/10.1097/MCO.0000000000000135

Stolarczyk, M., Reuter, V. P., Smith, J. P., Magee, N. E., & Sheffield, N. C. (2020). Refgenie: a reference genome resource manager. *GigaScience*, *9*(2), 1–6. https://doi.org/10.1093/gigascience/giz149

St-Onge, M.-P., & Gallagher, D. (2010). Body composition changes with aging: The cause or the result of alterations in metabolic rate and macronutrient oxidation? *Nutrition*, *26*(2), 152–155. https://doi.org/10.1016/j.nut.2009.07.004

Stovner, E. B., & Sætrom, P. (2019). epic2 efficiently finds diffuse domains in ChIP-seq data. *Bioinformatics*, *35*(21), 4392–4393. https://doi.org/10.1093/bioinformatics/btz232

Subramanian, A., Tamayo, P., Mootha, V. K., Mukherjee, S., Ebert, B. L., Gillette, M. A., Paulovich, A., Pomeroy, S. L., Golub, T. R., Lander, E. S., & Mesirov, J. P. (2005). Gene set enrichment analysis: a knowledge-based approach for interpreting genome-wide expression profiles. *Proceedings of the National Academy of Sciences of the United States of America*, *102*(43), 15545–15550. https://doi.org/10.1073/pnas.0506580102

Takashima, H., Takebayashi, T., Ogon, I., Yoshimoto, M., Morita, T., Imamura, R., Nakanishi, M., Nagahama, H., Terashima, Y., & Yamashita, T. (2018). Analysis of intra and extramyocellular lipids in the multifidus muscle in patients with chronic low back pain using MR spectroscopy. *The British Journal of Radiology*, 20170536. https://doi.org/10.1259/bjr.20170536

Tanaka, T., Takahashi, A., Kobayashi, Y., Saito, M., Xiaolong, S., Jingquan, C., Ito, Y., Kato, T., Ochi, H., Sato, S., Yoshii, T., Okawa, A., Carlsson, P., & Inose, H. (2022). Foxf2 represses bone formation via Wnt2b/β-catenin signaling. *Experimental & Molecular Medicine*, *54*(6), 753–764. https://doi.org/10.1038/s12276-022-00779-z

Taniguchi, Y., Tanaka, O., Sekiguchi, M., Takekoshi, S., Tsukamoto, H., Kimura, M., Imai, K., & Inoko, H. (2011). Enforced expression of the transcription factor HOXD3 under the control of the Wnt1 regulatory element modulates cell adhesion properties in the developing mouse neural tube. *Journal of Anatomy*, *219*(5), 589–600. https://doi.org/10.1111/j.1469-7580.2011.01425.x

Tauc, H. M., Rodriguez-Fernandez, I. A., Hackney, J. A., Pawlak, M., Ronnen Oron, T., Korzelius, J., Moussa, H. F., Chaudhuri,

S., Modrusan, Z., Edgar, B. A., & Jasper, H. (2021). Age-related changes in polycomb gene regulation disrupt lineage fidelity in intestinal stem cells. *ELife*, *10*. https://doi.org/10.7554/eLife.62250

Tsai, H.-L., Chiu, W.-T., Fang, C.-L., Hwang, S.-M., Renshaw, P. F., & Lai, W.-F. T. (2014). Different Forms of Tenascin-C with Tenascin-R Regulate Neural Differentiation in Bone Marrow-Derived Human Mesenchymal Stem Cells. *Tissue Engineering Part A*, *20*(13–14), 1908–1921. https://doi.org/10.1089/ten.tea.2013.0188

Uezumi, A., Fukada, S., Yamamoto, N., Takeda, S., & Tsuchida, K. (2010). Mesenchymal progenitors distinct from satellite cells contribute to ectopic fat cell formation in skeletal muscle. *Nature Cell Biology*, *12*(2), 143–152. https://doi.org/10.1038/ncb2014

van Velthoven, C. T. J., de Morree, A., Egner, I. M., Brett, J. O., & Rando, T. A. (2017). Transcriptional Profiling of Quiescent Muscle Stem Cells In Vivo. *Cell Reports*, *21*(7), 1994–2004. https://doi.org/10.1016/j.celrep.2017.10.037

Wang, L., Nishihara, H., Kimura, T., Kato, Y., Tanino, M., Nishio, M., Obara, M., Endo, T., Koike, T., & Tanaka, S. (2010). DOCK2 regulates cell proliferation through Rac and ERK activation in B cell lymphoma. *Biochemical and Biophysical Research Communications*, *395*(1), 111–115. https://doi.org/10.1016/j.bbrc.2010.03.148

Wang, L., Niu, N., Li, L., Shao, R., Ouyang, H., & Zou, W. (2018). H3K36 trimethylation mediated by SETD2 regulates the fate of bone marrow mesenchymal stem cells. *PLOS Biology*, *16*(11), e2006522. https://doi.org/10.1371/journal.pbio.2006522

Warnier, M., Flaman, J.-M., Chouabe, C., Wiel, C., Gras, B., Griveau, A., Blanc, E., Foy, J.-P., Mathot, P., Saintigny, P., van Coppenolle, F., Vindrieux, D., Martin, N., & Bernard, D. (2018). The SCN9A channel and plasma membrane depolarization promote cellular senescence through Rb pathway. *Aging Cell*, *17*(3), e12736. https://doi.org/10.1111/acel.12736

Xu, L., Zheng, L., Wang, Z., Li, C., Li, S., Xia, X., Zhang, P., Li, L., & Zhang, L. (2018). TNF-α-Induced SOX5 Upregulation Is Involved in the Osteogenic Differentiation of Human Bone Marrow Mesenchymal Stem Cells Through KLF4 Signal

Pathway. *Molecules and Cells*, *41*(6), 575–581. https://doi.org/10.14348/molcells.2018.2359

Zhang, J., Baran, J., Cros, A., Guberman, J. M., Haider, S., Hsu, J., Liang, Y., Rivkin, E., Wang, J., Whitty, B., Wong-Erasmus, M., Yao, L., & Kasprzyk, A. (2011). International Cancer Genome Consortium Data Portal--a one-stop shop for cancer genomics data. *Database*, *2011*(0), bar026–bar026. https://doi.org/10.1093/database/bar026

Zhang, Y., Liu, T., Meyer, C. A., Eeckhoute, J., Johnson, D. S., Bernstein, B. E., Nusbaum, C., Myers, R. M., Brown, M., Li, W., & Liu, X. S. (2008). Model-based Analysis of ChIP-Seq (MACS). *Genome Biology*, *9*(9), R137. https://doi.org/10.1186/gb-2008-9-9-r137

Zhang, Y., Park, C., Bennett, C., Thornton, M., & Kim, D. (2021). Rapid and accurate alignment of nucleotide conversion sequencing reads with HISAT-3N. *Genome Research*, *31*(7), 1290–1295. https://doi.org/10.1101/gr.275193.120

Zheng, X., Dumitru, R., Lackford, B. L., Freudenberg, J. M., Singh, A. P., Archer, T. K., Jothi, R., & Hu, G. (2012). Cnot1, Cnot2, and Cnot3 Maintain Mouse and Human ESC Identity and Inhibit Extraembryonic Differentiation. *STEM CELLS*, *30*(5), 910–922. https://doi.org/10.1002/stem.1070

Zuccotti, A., le Magueresse, C., Chen, M., Neitz, A., & Monyer, H. (2014). The transcription factor *Fezf2* directs the differentiation of neural stem cells in the subventricular zone toward a cortical phenotype. *Proceedings of the National Academy of Sciences*, *111*(29), 10726–10731. https://doi.org/10.1073/pnas.1320290111

Chapter 5 Final Consideration

5.1. Discussion

The increase in the population over age 65 has fielded several challenges, such as reduced adaptation to stressors and an increase in frailty (Lipsitz, 2004; Mitnitski et al., 2001; Yates, 2002), which is typified by a decrease in skeletal muscle volume, force and regeneration, namely sarcopenia (Cesari et al., 2014). Maintenance of homeostasis in skeletal muscle is carried out by a resident stem population (Cheung & Rando, 2013), whose numbers and functions are severely impacted during aging (Brack et al., 2005; Carlson & Conboy, 2007; Sousa-Victor et al., 2014). Physiological muscular decay during life includes declines in the functionality of multiple pathways, but how these different systems converge to alter genome organization in tissue-resident stem cells has not yet been explored. The focus of our laboratory is the study of chromatin organization and related alterations that arise from pathologies, such as laminopathies and cancer, or from the natural physiological course, i.e., aging. During my Ph.D., I had the opportunity to work on both physiological and pathological contexts, videlicet aging, Progeria, and Emery Dreifuss Muscular Dystrophy.

In the first described work (chapter 2) (Pegoli et al., 2021), we demonstrated how the deletion of the *Cdkn2a* locus improved the cardiac function in a murine model of Emery Dreifuss Muscular Dystrophy ($LMNA^{\Delta 8-11}$–/–). This murine strain is characterized in the postnatal stage by dilated cardiomyopathy (DCM) with limited

compensatory hypertrophy, mirroring the pathology in humans (Lu et al., 2011). We previously reported that the genetic ablation of the *Cdkn2a* locus, in the same murine model, restores MuSCs properties affected by the dysregulation of the interplay between Polycomb group of proteins (PcG) and Lamin A, which leads to loss of cell identity and the appearance of senescent traits (i.e., $p16^{INK4a}$ expression) (Bianchi et al., 2020; Cesarini et al., 2015). We further characterized the cardiac phenotype and function, during the postnatal stage, in LMNA $^{\Delta 8–11}$ –/– mice, with or without the deletion of *Cdkn2a* locus. We observed that LMNA $^{\Delta 8–11}$ –/– Cdkn2a -/- exhibits improve survival and ameliorated cardiac contraction performance measured through echocardiography. At the cellular level, the ablation of the *Cdkn2a* locus reduced the number of apoptotic cardiomyocytes, revealing an essential role of *Cdkn2a* in the preservation of cardiomyocytes in the absence of Lamin A during postnatal development.

In a parallel work (chapter 3) (Rosti V. et al., 2022) we set up an experimental protocol to simultaneously isolate fibromuscular stromal populations from different tissues, such as the aorta, skin and skeletal muscle. We selected a panel of markers for fluorescent-activated cell sorting (FACS) to derive the stromal portion of the aforementioned tissues. We defined the appropriate experimental conditions to preserve the nuclear and chromatin structures of the cells.

Overall, these first two papers were of importance in laying the practical and theoretical foundations that enabled me to conduct the work set outlined in Chapter 4.

In the last work, my first-name project (Chapter 4), we used a multi-OMICs approach to evaluate the complex interaction between chromatin organization and gene expression in the skeletal muscle stem cell niche during the murine life course. In normal muscle, a healthy MuSC compartment ensures a fine regulation of quiescence, differentiation, and self-renewal of the stem cell population (Ghadiali et al., 2017; Rayagiri et al., 2018; Sampath et al., 2018). The composition of the muscle stem cell niche reflects the requirements specific to the life stage and sees a fine integration of intrinsic and extrinsic signals derived from the entire surrounding environment, including myofibers, resident populations, and extracellular matrix (Mashinchian et al., 2018).

We investigated the evolution of the myogenic stem cell niche across four life stages – postnatal, adult, old and geriatric – characterizing the proportion of quiescent, cycling and activated MuSCs (Fig. 2,3), their transcriptional profile (Fig.4,5,6) and the muscle macro and microenvironment progression (Fig. 16,17).

We observed that aging is accompanied by a common fluctuation at the muscle level of most of the parameters we evaluated. In fact, in old mice, compared with adult and geriatric, in addition to the increase in body weight and muscle and fat (Fig 16,17), there was an increase in the percentage of activated MuSCs and muscle volume (Fig.2). This condition was accompanied by a

progressive increment of inflammation and edema that is even higher in geriatric stage (Fig. 17). Then, only 50% of old mice reached the geriatric age. Interestingly in geriatric mice, while the weight and lipid accumulation dropped or was negatively selected (Fig. 16) the inflammation and edema persisted (Fig. 17), suggesting a detrimental trajectory that could lead to muscle stem niche alteration. Still, as for the early life stage, the limitation of our study was the inability to perform micro-computed tomography and magnetic resonance analysis to identify muscle environmental changes in the postnatal mice, characterized by high levels of activated muscle stem cells (Fig. 2).

Gene expression profile confirmed that the muscle stem cell pool at the postnatal stage is composed of 50 % activated MuSCs, as previously reported (Gattazzo et al., 2020), with a transcriptional profile focused on the cell cycle progression (Fig.2, 3, 4). On the other hand, adult muscle stem cells showed an expression profile prone to post-transcriptional and translational regulation (Fig.4). These data further corroborate recent publications emphasizing how post-transcriptional regulatory mechanisms, such as intron retention or Staufen-mediated mRNA decay (de Morrée et al., 2017; Hausburg et al., 2015; Yue et al., 2020), are critical for maintaining quiescence, placing non-sense mediated decay (NMD) as a possible new mechanism to investigate. From the analysis of RNA-seq we also found that old and geriatric MuSCs are sensitive to the muscle environment changes described above (Fig. 16, 17), leading to inappropriate activation of the old

MuSCs and loss of transcriptional integrity in the geriatric MuSCs (Fig.5).

Fine regulation of chromatin reorganization is critical for the proper balance of the muscle stem cell pool (Bianchi et al., 2020; Boonsanay et al., 2016; Liu et al., 2013). In the last twenty years, the generation of high-throughput sequencing (NGS)-based techniques allowed the improvement of our 3D genome organization knowledge (Yan et al., 2015). Specific methods have arisen to address the understanding of cell functions (RNA-seq, scRNA-seq) (Johnson et al., 2007; Tang et al., 2009), to determine genome-wide transcription factor binding (ChIP-seq, Cut&Run) (Schmidt et al., 2009; Skene & Henikoff, 2017), to map chromatin accessibility (DNase-seq and ATAC-seq) (Boyle et al., 2008; Buenrostro et al., 2013), to analyse the heterochromatin (Protect-seq) (Spracklin & Pradhan, 2020) and to comprehend higher-order chromatin conformation (3C-based technologies) (Dostie et al., 2006; Lieberman-Aiden et al., 2009; Simonis et al., 2006). Most of these technologies rely on large numbers of cells, the use of antibodies to immunoprecipitate specific factors, and formaldehyde fixation of nuclei, making the use of the above-described methods difficult to apply to rare tissue-derived cell populations. We optimized our previously published 3f-SAMMY protocol (Sebestyén et al., 2020), which allows easy identification of heterochromatin regions associated with the nuclear lamina. The novel technology, the 4fSAMMY-seq, provides a global snapshot of the solubility and compartmentalization of the entire

chromatin (Fig. 9 and 11) (manuscript in preparation). The use of milder digestion conditions and the separation of the resulting soluble S2 fraction allowed the recognition of peaks associated with euchromatin and signal depletions (valley) associated with the heterochromatin. Importantly, 4fSAMMY-seq works on a limited number of cells (10K), both cell culture and primary cells (Fig. 10 and 12). We performed 4fSAMMY-seq in muscle stem cells at different stages of the murine lifespan. In line with studies performed in other experimental models (Chen et al., 2019; Dixon et al., 2012), we found that the global organization of the genome remains stable over the years, despite activation processes predominant in postnatal age or the occurrence of intrinsic alterations due to aging (Fig 13, 14, 18). However, with a tailored computational analysis we were able to identify chromatin regions with higher and lower solubilities in all categories of mice age. In the first comparison of postnatal vs adult MuSCs, we found that alterations in chromatin solubility do not directly trigger changes in transcription, compatible with the multiple and simultaneous epigenetic mechanisms acting on chromatin. However, the genomic regions affected are enriched in regions important for muscle differentiation (Fig.15), suggesting a role for chromatin biochemical properties in muscle stem cell activation.

The context-dependent relationship between biochemical properties, accessibility, chromatin compartmentalization, and functional outcomes, like transcription, is under intense

investigation in the last decade (Hansen et al., 2021). Accessible and soluble may acquire different meanings in the context of an open/closed chromatin state. Accessible chromatin, depending on the applied assay (DNase-seq, ATAC-seq, and MNase-seq) (Boyle et al., 2008; Buenrostro et al., 2013; Mieczkowski et al., 2016), often defines those portions of DNA that are nucleosome-depleted or characterized by a high turnover of nucleosomes, which includes regulatory elements such as promoters and enhancers(Klemm et al., 2019). However, the solubility, depending on the concentrations of transcriptional and regulatory factors may differ (Lundgren et al., 2000).

Heterochromatin has been proposed to serve as a driver of compartmentalization (Solovei et al., 2009; van Steensel & Belmont, 2017). In our model, we showed how the genomic organization of the stem cell is maintained by a different chorus of histone markers (Fig 7,8). In the postnatal phase, characterized by the presence of an activated and quiescent MuSC pool, we highlighted how the sharp solubility profiles found in the S2S versus S3 comparisons are characterized by two heterochromatin histone markers (Fig.13). In fact, we found S2S enrichment highly correlated with the H3K27me3 facultative heterochromatin mark, whereas the insoluble fraction with constitutive the H3K9me3 heterochromatin mark. A recent study has proposed a model of compartmental antagonism between Lamin-associated and Polycomb-dependent regions, suggesting that the different spatial segregation in A and B of the different

forms of heterochromatin avoids the constitutive repression of PcG-regulated genes (Siegenfeld et al., 2022). The substantial change in the postnatal and adult compartmentalization is characterized by the increased correlation, in S2S and S3, with H3K36me3 and the loss of correlation with H3K27me3 (Fig.14). Considering that H3K27me3 and H3K36me3 modifications are mutually exclusive and Polycomb proteins coordinate the complex relationship between these two histone modifications (Alabert et al., 2020; Schmitges et al., 2011), the opposite expression of PRC2 members, Ezh1 and Ezh2, in postnatal and adult MuSCs (Fig.6), suggests that in adult MuSCs PRC2 may play a role in the spatial organization that has not been yet investigated.

Recent evidence suggests that fundamental transcription factors of muscle stem cell identity, such as PAX7 and MYOD, are involved in specific chromatin looping dynamics necessary for cell fate and differentiation, regulating the temporal re-organization of sub-compartment interaction (Wang et al., 2022; Zhang et al., 2020).

The simultaneous change in the expression of PAX7 and MYOD suggests the profound connection between chromatin re-organization and expression fundamental to the proper initiation or maintenance of activation and quiescence events. In geriatric stem cells *Pax7*, critical for the maintenance of a compact chromatin configuration in quiescence (Günther et al., 2013), is strongly down-regulated (Fig. 5). Concomitantly, we underlined a

substantial switch from A to B compartment between old and geriatric MuSCs, suggesting an expansion of heterochromatin structure (Fig.20). The path from old to geriatric state in the muscle stem cell is accompanied by a conversion to a pre-senescent state (Sousa-Victor et al., 2014). Pura-Cánoves group demonstrated how this switch to a pre-senescent state is accompanied by altered transcriptional regulation of Polycomb-target genes. Consistent with this evidence, in our work geriatric MuSCs show transcriptional upregulation of alternative differentiation pathways and silencing of the myogenic program (Fig.5). It is, therefore, tempt to speculate that redistribution of Polycomb may entrain this compartmental change through a less permissive chromatin state, which would lead under regenerative pressure to an inability of the geriatric muscle stem cell to proliferate and activate successfully. In parallel with heterochromatin changes, we found a marked decrease in S2SvsS3 signalling of geriatric MuSCs with respect to adult and old mice (Fig. 18). Regions with altered biochemical properties included pathways important for the maintenance of quiescence (Fig.19), such as the MAPK signaling pathway involved in asymmetric division and differentiation (Bernet et al., 2014; Price et al., 2014). Despite the fact that gene expression data did not show direct gene expression alteration of the involved genes, it is possible that in a situation of environmental pressure demand, such as muscle injury, the transcriptional defects related to the

transition from quiescence to activation that characterizes this age becomes evident.

Overall, our results suggest that the correct maintenance of the chromatin compartment, in term of epigenetic modification and biochemical properties, allow the proper unfolding of processes leading to quiescence and activation in MuSCs and that alteration in chromatin solubility lead during aging to an improper organization of genomic regions important for stem cell function. The complex network of signals, which maintains a healthy and functioning muscle niche, is enabled by the interplay of different cell populations (Mashinchian et al., 2018). During our work, we demonstrated how one of these populations, the Fibroadipogenic precursors (FAPs), during aging exhibits a dramatic dysregulation of transcriptional processes, which sees an overexpression of terms related to transcriptional regulation (Fig 22). Specifically, geriatric FAPs presented an upregulation of many Polycomb members (Ezh2, Bmi1, Suz12), suggesting a key role of these proteins in FAPs during aging, that to date has not yet been investigated. We already processed 4fSAMMY-seq on FAPs extracted from the same mice analyzed above. Future bioinformatic analyses will integrate the complex thread linking transcriptional control, epigenetic regulation and the MuSCs/FAPs crosstalk.

5.2. Future Perspective

The concept of skeletal muscle epi-memory was introduced by Sharples in 2016 and defined as the ability of the skeletal muscle to respond more or less effectively to a stimulus, based on a previous encounter with it, mediated and inherited through epigenetic mechanisms (Sharples et al., 2016). Different types of studies, such as epidemiological research on the association of sarcopenia and underweight birth weight (Patel et al., 2012), studies on mouse models of exposure/removal to specific nutritional factors *in utero* (Dunlop et al., 2015) or research on exercise characterized by extended periods of training, detraining, retraining and the association with DNA-methylation (Seaborne et al., 2018) have highlighted the profound plasticity of skeletal muscle and its populations, beginning to expand our knowledge of the epigenetic factors involved in this memory capability. In our work, we demonstrated how the muscle and its niche can experience period-specific needs - growth, maintenance, aging - through fine modulation of the environment and MuSCs nuclear characteristics. One of the features of our dataset is the characterization in individual mice, at different time points, of muscle environment, chromatin structure and gene expression at the level of single populations, namely MuSCs and FAPs. Future efforts will be directed at understanding their close association. Through the integration of bioinformatic analyses focused on identifying an interconnection between chromatin

solubility, epigenetic modification, transcription in distinct cell populations we aim to trace loss and gain trajectories that define not only the transitional state from one age to the next but that attempt to define individual variability in the epigenetic landscape. The ultimate goal of the illustrated work is to define new pathways of investigation for understanding not only chronological aging but also diseases characterized by premature senescence, such as progeria and EDMD.

5.3. Reference to Chapter 5

Alabert, C., Loos, C., Voelker-Albert, M., Graziano, S., Forné, I., Reveron-Gomez, N., Schuh, L., Hasenauer, J., Marr, C., Imhof, A., & Groth, A. (2020). Domain Model Explains Propagation Dynamics and Stability of Histone H3K27 and H3K36 Methylation Landscapes. *Cell Reports*, *30*(4), 1223-1234.e8. https://doi.org/10.1016/j.celrep.2019.12.060

Bernet, J. D., Doles, J. D., Hall, J. K., Kelly Tanaka, K., Carter, T. A., & Olwin, B. B. (2014). P38 MAPK signaling underlies a cell-autonomous loss of stem cell self-renewal in skeletal muscle of aged mice. *Nature Medicine*, *20*(3), 265–271. https://doi.org/10.1038/nm.3465

Bianchi, A., Mozzetta, C., Pegoli, G., Lucini, F., Valsoni, S., Rosti, V., Petrini, C., Cortesi, A., Gregoretti, F., Antonelli, L., Oliva, G., de Bardi, M., Rizzi, R., Bodega, B., Pasini, D., Ferrari, F., Bearzi, C., & Lanzuolo, C. (2020). Dysfunctional polycomb transcriptional repression contributes to lamin A/C–dependent muscular dystrophy. *Journal of Clinical Investigation*, *130*(5), 2408–2421. https://doi.org/10.1172/JCI128161

Boonsanay, V., Zhang, T., Georgieva, A., Kostin, S., Qi, H., Yuan, X., Zhou, Y., & Braun, T. (2016). Regulation of Skeletal Muscle Stem Cell Quiescence by Suv4-20h1-Dependent Facultative Heterochromatin Formation. *Cell Stem Cell*, *18*(2), 229–242. https://doi.org/10.1016/j.stem.2015.11.002

Boyle, A. P., Davis, S., Shulha, H. P., Meltzer, P., Margulies, E. H., Weng, Z., Furey, T. S., & Crawford, G. E. (2008). High-Resolution Mapping and Characterization of Open Chromatin across the Genome. *Cell*, *132*(2), 311–322. https://doi.org/10.1016/j.cell.2007.12.014

Brack, A. S., Bildsoe, H., & Hughes, S. M. (2005). Evidence that satellite cell decrement contributes to preferential decline in nuclear number from large fibres during murine age-related muscle atrophy. *Journal of Cell Science*, *118*(20), 4813–4821. https://doi.org/10.1242/JCS.02602

Buenrostro, J. D., Giresi, P. G., Zaba, L. C., Chang, H. Y., & Greenleaf, W. J. (2013). Transposition of native chromatin for fast and sensitive epigenomic profiling of open chromatin, DNA-

binding proteins and nucleosome position. *Nature Methods*, *10*(12), 1213–1218. https://doi.org/10.1038/nmeth.2688
Carlson, M. E., & Conboy, I. M. (2007). Loss of stem cell regenerative capacity within aged niches. *Aging Cell*, *6*(3), 371–382. https://doi.org/10.1111/J.1474-9726.2007.00286.X
Cesari, M., Landi, F., Vellas, B., Bernabei, R., & Marzetti, E. (2014). Sarcopenia and Physical Frailty: Two Sides of the Same Coin. *Frontiers in Aging Neuroscience*, *6*. https://doi.org/10.3389/fnagi.2014.00192
Cesarini, E., Mozzetta, C., Marullo, F., Gregoretti, F., Gargiulo, A., Columbaro, M., Cortesi, A., Antonelli, L., di Pelino, S., Squarzoni, S., Palacios, D., Zippo, A., Bodega, B., Oliva, G., & Lanzuolo, C. (2015). Lamin A/C sustains PcG protein architecture, maintaining transcriptional repression at target genes. *Journal of Cell Biology*, *211*(3), 533–551. https://doi.org/10.1083/jcb.201504035
Chen, C., Yu, W., Tober, J., Gao, P., He, B., Lee, K., Trieu, T., Blobel, G. A., Speck, N. A., & Tan, K. (2019). Spatial Genome Re-organization between Fetal and Adult Hematopoietic Stem Cells. *Cell Reports*, *29*(12), 4200. https://doi.org/10.1016/J.CELREP.2019.11.065
Cheung, T. H., & Rando, T. A. (2013). Molecular regulation of stem cell quiescence. *Nature Reviews Molecular Cell Biology*, *14*(6), 329–340. https://doi.org/10.1038/nrm3591
de Morrée, A., van Velthoven, C. T. J., Gan, Q., Salvi, J. S., Klein, J. D. D., Akimenko, I., Quarta, M., Biressi, S., & Rando, T. A. (2017). Staufen1 inhibits MyoD translation to actively maintain muscle stem cell quiescence. *Proceedings of the National Academy of Sciences of the United States of America*, *114*(43), E8996–E9005. https://doi.org/10.1073/pnas.1708725114
Dixon, J. R., Selvaraj, S., Yue, F., Kim, A., Li, Y., Shen, Y., Hu, M., Liu, J. S., & Ren, B. (2012). Topological domains in mammalian genomes identified by analysis of chromatin interactions. *Nature*, *485*(7398), 376–380. https://doi.org/10.1038/nature11082
Dostie, J., Richmond, T. A., Arnaout, R. A., Selzer, R. R., Lee, W. L., Honan, T. A., Rubio, E. D., Krumm, A., Lamb, J., Nusbaum, C., Green, R. D., & Dekker, J. (2006). Chromosome Conformation Capture Carbon Copy (5C): A massively parallel

solution for mapping interactions between genomic elements. *Genome Research*, *16*(10), 1299–1309. https://doi.org/10.1101/gr.5571506

Dunlop, K., Cedrone, M., Staples, J., & Regnault, T. (2015). Altered Fetal Skeletal Muscle Nutrient Metabolism Following an Adverse In Utero Environment and the Modulation of Later Life Insulin Sensitivity. *Nutrients*, *7*(2), 1202–1216. https://doi.org/10.3390/nu7021202

Gattazzo, F., Laurent, B., Relaix, F., Rouard, H., & Didier, N. (2020). Distinct Phases of Postnatal Skeletal Muscle Growth Govern the Progressive Establishment of Muscle Stem Cell Quiescence. *Stem Cell Reports*, *15*(3), 597–611. https://doi.org/10.1016/j.stemcr.2020.07.011

Ghadiali, R. S., Guimond, S. E., Turnbull, J. E., & Pisconti, A. (2017). Dynamic changes in heparan sulfate during muscle differentiation and ageing regulate myoblast cell fate and FGF2 signalling. *Matrix Biology*, *59*, 54–68. https://doi.org/10.1016/j.matbio.2016.07.007

Günther, S., Kim, J., Kostin, S., Lepper, C., Fan, C.-M., & Braun, T. (2013). Myf5-Positive Satellite Cells Contribute to Pax7-Dependent Long-Term Maintenance of Adult Muscle Stem Cells. *Cell Stem Cell*, *13*(5), 590–601. https://doi.org/10.1016/j.stem.2013.07.016

Hansen, J. C., Maeshima, K., & Hendzel, M. J. (2021). The solid and liquid states of chromatin. *Epigenetics & Chromatin*, *14*(1), 50. https://doi.org/10.1186/s13072-021-00424-5

Hausburg, M. A., Doles, J. D., Clement, S. L., Cadwallader, A. B., Hall, M. N., Blackshear, P. J., Lykke-Andersen, J., & Olwin, B. B. (2015). Post-transcriptional regulation of satellite cell quiescence by TTP-mediated mRNA decay. *ELife*, *4*(4). https://doi.org/10.7554/eLife.03390

Johnson, D. S., Mortazavi, A., Myers, R. M., & Wold, B. (2007). Genome-Wide Mapping of in Vivo Protein-DNA Interactions. *Science*, *316*(5830), 1497–1502. https://doi.org/10.1126/science.1141319

Klemm, S. L., Shipony, Z., & Greenleaf, W. J. (2019). Chromatin accessibility and the regulatory epigenome. *Nature Reviews. Genetics*, *20*(4), 207–220. https://doi.org/10.1038/s41576-018-0089-8

Lieberman-Aiden, E., van Berkum, N. L., Williams, L., Imakaev, M., Ragoczy, T., Telling, A., Amit, I., Lajoie, B. R., Sabo, P. J., Dorschner, M. O., Sandstrom, R., Bernstein, B., Bender, M. A., Groudine, M., Gnirke, A., Stamatoyannopoulos, J., Mirny, L. A., Lander, E. S., & Dekker, J. (2009). Comprehensive mapping of long-range interactions reveals folding principles of the human genome. *Science*, *326*(5950), 289–293. https://doi.org/10.1126/SCIENCE.1181369/SUPPL_FILE/LIEBERMAN-AIDEN.SOM.PDF

Lipsitz, L. A. (2004). Physiological Complexity, Aging, and the Path to Frailty. *Science of Aging Knowledge Environment*, *2004*(16), pe16–pe16. https://doi.org/10.1126/sageke.2004.16.pe16

Liu, L., Cheung, T. H., Charville, G. W., Hurgo, B. M. C., Leavitt, T., Shih, J., Brunet, A., & Rando, T. A. (2013). Chromatin Modifications as Determinants of Muscle Stem Cell Quiescence and Chronological Aging. *Cell Reports*, *4*(1), 189–204. https://doi.org/10.1016/j.celrep.2013.05.043

Lu, J. T., Muchir, A., Nagy, P. L., & Worman, H. J. (2011). LMNA cardiomyopathy: cell biology and genetics meet clinical medicine. *Disease Models & Mechanisms*, *4*(5), 562–568. https://doi.org/10.1242/dmm.006346

Lundgren, M., Chow, C.-M., Sabbattini, P., Georgiou, A., Minaee, S., & Dillon, N. (2000). Transcription Factor Dosage Affects Changes in Higher Order Chromatin Structure Associated with Activation of a Heterochromatic Gene. *Cell*, *103*(5), 733–743. https://doi.org/10.1016/S0092-8674(00)00177-X

Mashinchian, O., Pisconti, A., le Moal, E., & Bentzinger, C. F. (2018). The Muscle Stem Cell Niche in Health and Disease. In *Current topics in developmental biology* (Vol. 126, pp. 23–65). Curr Top Dev Biol. https://doi.org/10.1016/bs.ctdb.2017.08.003

Mieczkowski, J., Cook, A., Bowman, S. K., Mueller, B., Alver, B. H., Kundu, S., Deaton, A. M., Urban, J. A., Larschan, E., Park, P. J., Kingston, R. E., & Tolstorukov, M. Y. (2016). MNase titration reveals differences between nucleosome occupancy and chromatin accessibility. *Nature Communications 2016 7:1*, *7*(1), 1–11. https://doi.org/10.1038/ncomms11485

Mitnitski, A. B., Mogilner, A. J., & Rockwood, K. (2001). Accumulation of deficits as a proxy measure of aging.

TheScientificWorldJournal, *1*, 323–336. https://doi.org/10.1100/tsw.2001.58

Patel, H. P., Jameson, K. A., Syddall, H. E., Martin, H. J., Stewart, C. E., Cooper, C., & Sayer, A. A. (2012). Developmental Influences, Muscle Morphology, and Sarcopenia in Community-Dwelling Older Men. *The Journals of Gerontology Series A: Biological Sciences and Medical Sciences*, *67A*(1), 82–87. https://doi.org/10.1093/gerona/glr020

Pegoli, G., Milan, M., Manti, P. G., Bianchi, A., Lucini, F., Santarelli, P., Bearzi, C., Rizzi, R., & Lanzuolo, C. (2021). Role of Cdkn2a in the Emery–Dreifuss Muscular Dystrophy Cardiac Phenotype. *Biomolecules*, *11*(4), 538. https://doi.org/10.3390/biom11040538

Price, F. D., von Maltzahn, J., Bentzinger, C. F., Dumont, N. A., Yin, H., Chang, N. C., Wilson, D. H., Frenette, J., & Rudnicki, M. A. (2014). Inhibition of JAK-STAT signaling stimulates adult satellite cell function. *Nature Medicine*, *20*(10), 1174–1181. https://doi.org/10.1038/nm.3655

Rayagiri, S. S., Ranaldi, D., Raven, A., Mohamad Azhar, N. I. F., Lefebvre, O., Zammit, P. S., & Borycki, A.-G. (2018). Basal lamina remodeling at the skeletal muscle stem cell niche mediates stem cell self-renewal. *Nature Communications*, *9*(1), 1075. https://doi.org/10.1038/s41467-018-03425-3

Rosti V., Gorini F., Santarelli P., Sarnicola M.L., Magnani S., & Lanzuolo C. (2022). Polycomb bodies detection in murine fibromuscular stroma from skin, skeletal muscles and aortic tissues. *Methods Mol Biol - IN PRESS*.

Sampath, S. C., Sampath, S. C., Ho, A. T. V., Corbel, S. Y., Millstone, J. D., Lamb, J., Walker, J., Kinzel, B., Schmedt, C., & Blau, H. M. (2018). Induction of muscle stem cell quiescence by the secreted niche factor Oncostatin M. *Nature Communications*, *9*(1), 1–9. https://doi.org/10.1038/s41467-018-03876-8

Schmidt, D., Wilson, M. D., Spyrou, C., Brown, G. D., Hadfield, J., & Odom, D. T. (2009). ChIP-seq: Using high-throughput sequencing to discover protein–DNA interactions. *Methods*, *48*(3), 240–248. https://doi.org/10.1016/j.ymeth.2009.03.001

Schmitges, F. W., Prusty, A. B., Faty, M., Stützer, A., Lingaraju, G. M., Aiwazian, J., Sack, R., Hess, D., Li, L., Zhou, S., Bunker, R.

D., Wirth, U., Bouwmeester, T., Bauer, A., Ly-Hartig, N., Zhao, K., Chan, H., Gu, J., Gut, H., … Thomä, N. H. (2011). Histone Methylation by PRC2 Is Inhibited by Active Chromatin Marks. *Molecular Cell*, *42*(3), 330–341. https://doi.org/10.1016/j.molcel.2011.03.025

Seaborne, R. A., Strauss, J., Cocks, M., Shepherd, S., O'Brien, T. D., van Someren, K. A., Bell, P. G., Murgatroyd, C., Morton, J. P., Stewart, C. E., & Sharples, A. P. (2018). Human Skeletal Muscle Possesses an Epigenetic Memory of Hypertrophy. *Scientific Reports*, *8*(1), 1898. https://doi.org/10.1038/s41598-018-20287-3

Sebestyén, E., Marullo, F., Lucini, F., Petrini, C., Bianchi, A., Valsoni, S., Olivieri, I., Antonelli, L., Gregoretti, F., Oliva, G., Ferrari, F., & Lanzuolo, C. (2020). SAMMY-seq reveals early alteration of heterochromatin and deregulation of bivalent genes in Hutchinson-Gilford Progeria Syndrome. *Nature Communications*, *11*(1). https://doi.org/10.1038/S41467-020-20048-9

Sharples, A. P., Stewart, C. E., & Seaborne, R. A. (2016). Does skeletal muscle have an 'epi'-memory? The role of epigenetics in nutritional programming, metabolic disease, aging and exercise. *Aging Cell*, *15*(4), 603–616. https://doi.org/10.1111/acel.12486

Siegenfeld, A. P., Roseman, S. A., Roh, H., Lue, N. Z., Wagen, C. C., Zhou, E., Johnstone, S. E., Aryee, M. J., & Liau, B. B. (2022). Polycomb-lamina antagonism partitions heterochromatin at the nuclear periphery. *Nature Communications*, *13*(1), 4199. https://doi.org/10.1038/s41467-022-31857-5

Simonis, M., Klous, P., Splinter, E., Moshkin, Y., Willemsen, R., de Wit, E., van Steensel, B., & de Laat, W. (2006). Nuclear organization of active and inactive chromatin domains uncovered by chromosome conformation capture–on-chip (4C). *Nature Genetics*, *38*(11), 1348–1354. https://doi.org/10.1038/ng1896

Skene, P. J., & Henikoff, S. (2017). An efficient targeted nuclease strategy for high-resolution mapping of DNA binding sites. *ELife*, *6*. https://doi.org/10.7554/eLife.21856

Solovei, I., Kreysing, M., Lanctôt, C., Kösem, S., Peichl, L., Cremer, T., Guck, J., & Joffe, B. (2009). Nuclear Architecture of Rod Photoreceptor Cells Adapts to Vision in Mammalian Evolution. *Cell*, *137*(2), 356–368. https://doi.org/10.1016/j.cell.2009.01.052

Sousa-Victor, P., Gutarra, S., García-Prat, L., Rodriguez-Ubreva, J., Ortet, L., Ruiz-Bonilla, V., Jardí, M., Ballestar, E., González, S., Serrano, A. L., Perdiguero, E., & Muñoz-Cánoves, P. (2014). Geriatric muscle stem cells switch reversible quiescence into senescence. *Nature*, *506*(7488), 316–321. https://doi.org/10.1038/nature13013

Spracklin, G., & Pradhan, S. (2020). Protect-seq: genome-wide profiling of nuclease inaccessible domains reveals physical properties of chromatin. *Nucleic Acids Research*, *48*(3), e16–e16. https://doi.org/10.1093/nar/gkz1150

Tang, F., Barbacioru, C., Wang, Y., Nordman, E., Lee, C., Xu, N., Wang, X., Bodeau, J., Tuch, B. B., Siddiqui, A., Lao, K., & Surani, M. A. (2009). mRNA-Seq whole-transcriptome analysis of a single cell. *Nature Methods*, *6*(5), 377–382. https://doi.org/10.1038/nmeth.1315

van Steensel, B., & Belmont, A. S. (2017). Lamina-Associated Domains: Links with Chromosome Architecture, Heterochromatin, and Gene Repression. *Cell*, *169*(5), 780–791. https://doi.org/10.1016/j.cell.2017.04.022

Wang, R., Chen, F., Chen, Q., Wan, X., Shi, M., Chen, A. K., Ma, Z., Li, G., Wang, M., Ying, Y., Liu, Q., Li, H., Zhang, X., Ma, J., Zhong, J., Chen, M., Zhang, M. Q., Zhang, Y., Chen, Y., & Zhu, D. (2022). MyoD is a 3D genome structure organizer for muscle cell identity. *Nature Communications*, *13*(1), 205. https://doi.org/10.1038/s41467-021-27865-6

Yan, H., Tian, S., Slager, S. L., Sun, Z., & Ordog, T. (2015). Genome-Wide Epigenetic Studies in Human Disease: A Primer on -Omic Technologies. *American Journal of Epidemiology*, *183*(2), kwv187. https://doi.org/10.1093/aje/kwv187

Yates, F. E. (2002). Complexity of a human being: changes with age. *Neurobiology of Aging*, *23*(1), 17–19. https://doi.org/10.1016/S0197-4580(01)00261-5

Yue, L., Wan, R., Luan, S., Zeng, W., & Cheung, T. H. (2020). Dek Modulates Global Intron Retention during Muscle Stem Cells

Quiescence Exit. *Developmental Cell*, 1–16. https://doi.org/10.1016/j.devcel.2020.05.006

Zhang, N., Mendieta-Esteban, J., Magli, A., Lilja, K. C., Perlingeiro, R. C. R., Marti-Renom, M. A., Tsirigos, A., & Dynlacht, B. D. (2020). Muscle progenitor specification and myogenic differentiation are associated with changes in chromatin topology. *Nature Communications*, *11*(1). https://doi.org/10.1038/S41467-020-19999-W

Publication

Rosti V., Gorini F., Santarelli P., Sarnicola M.L., Magnani S., & Lanzuolo C. (2022). Polycomb bodies detection in murine fibromuscular stroma from skin, skeletal muscles and aortic tissues. *Methods Mol Biol - IN PRESS*.

Pegoli, G., Milan, M., Manti, P. G., Bianchi, A., Lucini, F., Santarelli, P., Bearzi, C., Rizzi, R., & Lanzuolo, C. (2021). Role of Cdkn2a in the Emery–Dreifuss Muscular Dystrophy Cardiac Phenotype. *Biomolecules*, *11*(4), 538. https://doi.org/10.3390/biom11040538